



UNIONE EUROPEA
Fondo Sociale Europeo



UNIVERSITÀ DEGLI STUDI DELL'AQUILA
DIPARTIMENTO DI INGEGNERIA E SCIENZE DELL'INFORMAZIONE E
MATEMATICA (DISIM)

Dottorato di Ricerca in **Matematica e Modelli**

XXXV ciclo

Titolo della tesi

New Frontiers in Cable Mechanics: Modeling and Design of a Smart Cable

SSD ICAR/08 SCIENZA DELLE COSTRUZIONI

Dottorando

Mahadeb Kumar Das

Coordinatore del corso

Prof. Davide Gabrielli

Tutore

Prof. Angelo Luongo

Co-supervisore

Prof. Manuel Ferretti

Supervisore

Prof. Francesco D'Annibale

A.A. 2021/2022

New Frontiers in Cable Mechanics: Modeling and Design of a Smart Cable

Submitted By

Mahadeb Kumar Das
Student ID: 269100

DISIM-Dipartimento di Ingegneria e Scienze dell'Informazione e
Matematica

Submitted To

DISIM-Dipartimento di Ingegneria e Scienze dell'Informazione e
Matematica

in partial fulfillment of the requirements for the degree of
Doctor of Philosophy

Supervised by

Prof. Angelo Luongo

Co-supervised by

Prof. Manuel Ferretti & Prof. Francesco D'Annibale
DICEAA-Dipartimento di Ingegneria civile, edile - architettura e
ambientale



UNIVERSITÀ
DEGLI STUDI
DE L'AQUILA

University of L'Aquila, Italy, 2023

This PhD research work is co-financed with the resources from the 2014-2020 National Operational Program (CCI 2014IT16M2OP005), European Social Fund, Action I.1 "Innovative Doctorates with an industrial framework"



(a)



(b)



(c)

ACKNOWLEDGMENTS

At first I express my greatest and deepest gratitude to the almighty, the supreme of the universe, to whom all praises go for enabling me to complete my PhD research work.

It gives me great pleasure to express my deepest gratitude and appreciation to my supervisor **Prof. Angelo Luongo** and co-supervisors **Prof. Manuel Ferretti** and **Prof. Francesco D'Annibale**, DICEAA-Dipartimento di Ingegneria civile, edile - architettura e ambientale, and coordinator **Prof. Davide Gabrielli**, DISIM-Dipartimento di Ingegneria e Scienze dell'Informazione e Matematica, University of L'Aquila, Italy, for their willingness to accept me as research student and for their constant supervision, effective guidance, invaluable instructions and endless encouragement in preparing this thesis. I would also like to thank my supervisors for their earnest feelings and enthusiasm, which help in matters concerning my research affairs, and above all for always being there as my mentors. Their suggestions drove me towards better ways of thinking, their reviews enriched me in solving problems, and their support gave me strength at the time of my disappointment. I take this opportunity to express my great indebtedness to the authority of the PON scholarship including the administrative staff and all the honorable and respected teachers at the University of L'Aquila, Italy, for giving me such a great opportunity to learn and acquire knowledge.

Finally, I wish to express my deepest sense of gratitude and love to my mother **Mandari Das**, who was died on 27th of April 2017.

Above all, I am lucky to get Prof. Angelo Luongo, Prof. Manuel Ferretti and Prof. Francesco D'Annibale as my supervisors and for this, I am very grateful to the supreme almighty who enabled us to reach a successful end and also wish for my supervisors longevity.

ABSTRACT

The galloping instability of a suspended shallow flexible cable (possibly ice-accreted) has been studied via a linear continuum model. The cable is suspended from the same level of two supports and modeled as a linear one-dimensional structure embedded in a three-dimensional space. External and internal damping are considered according to the Rayleigh model of damping, and the aerodynamic forces are modeled under the assumption of quasi-steady theory. Two critical galloping modes, in-plane and out-of-plane components, have been studied through an exact analysis by solving a boundary value problem. An analytical analysis, through a straight-forward perturbation method has been applied to analyze the galloping phenomenon in three resonance conditions: non-resonant, one-one resonant and one-one-one resonant cases. Lastly, two numerical approaches have also been employed, and the outcomes have been compared with the exact and analytical solutions, presented with figures and tables. The insight is that the coupling leads to either lower or higher critical velocities compared with the prediction made by the simplified planar model. Parallely, a piezoelectric damper has been designed to control the vibration of a straight single cable structure, tuned with the shunt circuits. The optimal placement of the damper, and optimization of geometrical and mechanical parameters have been described. The control procedure and performance of the damper in terms of longitudinal and transversal vibrations are presented. It is noticed that the LR and NC-R shunts show remarkable suppression of vibrations. An energy harvester has also been designed and the energy has been harvested from the structure as electric power. The harvester has been analyzed in terms of frequency, electric load resistance, and acceleration dependence. The amount of energy extracted from the PVDF energy harvester is low as the input mechanical energy is low due to the hardness of the flexible cable to transfer deformation to the piezoelectric tube and the dissipation of energy through the circuit.

NOMENCLATURE

$\mathbf{a}_\alpha, \bar{\mathbf{a}}_\alpha$	Unit vectors of the bases \mathcal{B}_f and $\bar{\mathcal{B}}_f, (\alpha = t, n, b)$, respectively
$\mathbf{a}_i, \bar{\mathbf{a}}_i$	Unit vectors of the bases \mathcal{B} and $\bar{\mathcal{B}}, (i = 1, 2, 3)$, respectively
\mathbf{x}	Position vector in the current configuration
$\bar{\mathbf{x}}$	Position vector in the reference configuration
$\mathcal{B}, \bar{\mathcal{B}}, \mathcal{B}_e$	current, reference and external bases
$\bar{\mathcal{B}}_f$	Frenet basis
\mathbf{t}_0	Internal stress
$\mathbf{p}_0, \mathbf{P}_{0H}$	Preloads
\mathbf{p}	Linear force density
\mathbf{P}_H	End force
\mathbf{u}	Displacements
$u(s, t)$	Tangential displacement
$v(s, t)$	Normal displacement
$w(s, t)$	Out-of-plane displacement
T_0	Prestress of the cable
EA	Axial stiffness
m	Mass per unit length of iced cable
l	Length of the cable
$\bar{\kappa}$	Prestress curvature
$e(t)$	Dynamic unit extension
f_n^d	Damping forces
f_n^a	Aerodynamic forces
c_e	Damping coefficient
η, ζ	Viscosity coefficient

ρ	Air density
b	Characteristic length of the cross-section
ω	Modal frequency
U_c	Critical wind velocity
c_d	Drag coefficient
c_l	Lift coefficient
ϵ	Perturbation parameter
d	Sag of the suspended cable
Λ^2	Irvine parameter
$\hat{c}_{a1}, \hat{c}_{22}^a, \hat{c}_{23}^a, \hat{c}_{32}^a, \hat{c}_{33}^a$	Aerodynamic coefficients
ω_c	Modal frequency
P	Applied force
q_j	Generalized coordinates
ϕ_j	Trial functions
δ_{ij}	Kronecker delta
α, γ	Initial attack angles

Overmarks

- $(\cdot)'$ space-derivative
- $(\dot{\cdot})$ time-derivative
- $(\cdot)_0$ preload and prestress
- $(\tilde{\cdot})$ incremental load or stress

TABLE OF CONTENTS

	Page
List of Tables	ix
List of Figures	x
1 Introduction	1
1.1 Research Motivation	1
1.2 Research Background and Historical Review of Literature	2
1.3 Objectives of the Research, Summary, and Organization	9
1.3.1 Objectives	9
1.3.2 Summary	9
1.3.3 Organization of the Thesis	9
2 Literature Review: Aeroelastic Stability	11
2.1 Introduction	11
2.2 Aerodynamic Forces	11
2.3 Galloping of single-degree-of-freedom systems	15
2.3.1 Model	15
2.3.2 Linear Stability analysis	17
2.3.3 Nonlinear analysis: the limit cycle	21
2.4 Galloping of strings	27
2.4.1 Strings	28
3 Development of the model of a shallow flexible cable	30
3.1 Introduction	30
3.2 Basic Assumptions	30
3.3 Prestressed Cables	31
3.3.1 Quasi-exact model	31
3.3.2 The Linearized Theory	37
3.3.3 Shallow cables	38

4	A Continuum Approach to the Nonlinear In-Plane Galloping of Shallow Flexible Cables	41
4.1	Introduction	41
4.2	Continuum Model	42
4.2.1	Governing Equations	42
4.2.2	Damping Model	43
4.2.3	The Linear Problem	44
4.2.4	The Space Eigenvalue Problem	44
4.2.5	The Adjoint Eigenvalue Problem and the Solvability Condition	46
4.3	The Nonlinear Problem	47
4.3.1	Multiple Scale Analysis	47
4.4	Finite-Dimensional Models	52
4.4.1	Finite Difference Method	52
4.4.2	Galerkin Method	53
4.5	Numerical Results	56
4.6	Conclusion	63
5	Spatial galloping analysis of shallow cables via a linear continuum model	64
5.1	Introduction	64
5.2	Mathematical Modeling	64
5.2.1	Equation of Motion	65
5.2.2	Damping Model	65
5.2.3	Aerodynamic Forces	67
5.3	The “Exact” Galloping Analysis	68
5.4	The Asymptotic Galloping Analysis	71
5.4.1	The Non-resonant Case	75
5.4.2	The 1:1 Resonant Case	76
5.4.3	The 1:1:1 Resonant Case	81
5.5	Numerical Results	85
5.5.1	The non-resonant case	88
5.5.2	One - One resonant case	89
5.5.3	The 1:1:1 resonant case	98
5.6	Conclusions	111
6	Vibration control of a cable structure via a flexible piezoelectric damper and energy harvesting	113
6.1	Introduction	113
6.1.1	Piezoelectric devices to control vibration of structures	114

6.1.2	Piezoelectric devices for harvesting energy	116
6.2	Modeling	117
6.2.1	Finite element modeling of the smart cable	118
6.2.2	Tube-shaped PVDF damping component modeling and design	119
6.2.3	Geometric parameters optimization	122
6.2.4	Positioning of the PVDF tube	124
6.3	Shunt circuit design	126
6.3.1	The LR shunt circuit	126
6.3.2	The NC-R shunt circuit	126
6.4	Numerical Results	128
6.4.1	Damping characteristics	128
6.4.2	Analysis of the longitudinal vibration of a single cable structure	128
6.4.3	Analysis of the transverse vibration of a single-cable structure	130
6.5	Configuration of the model for energy harvester	133
6.6	Discussion of results	133
6.7	Conclusion	136
7	Conclusions and future development	137
	Bibliography	139

LIST OF TABLES

TABLE	Page
2.1 Values of $C'_{y0} := C_{d0} + C'_{l0}$ for different cross-section shapes of a long cylinder, subject to laminar flow, horizontally incident; negative values indicate aerodynamically unstable cross-sections [66].	20
5.1 Critical modal conditions for exact and numerical solutions: velocity (ms^{-1})	86
5.2 Critical modal conditions for exact and numerical solutions: frequency (rad/s)	86
5.3 Critical modal conditions for analytical and numerical solutions: velocity (ms^{-1})	88
5.4 Critical modal conditions for analytical and numerical solutions: frequency (rad/s)	88
5.5 Critical modal conditions for analytical and numerical solutions: velocity (ms^{-1})	90
5.6 Critical modal conditions for analytical and numerical solutions: velocity (ms^{-1})	95
5.7 Critical modal conditions for analytical and numerical solutions with common modal frequency $\omega_{0j} = 3.42\text{rad/s}$: velocity (ms^{-1}); (Non-resonant part)	99
5.8 Critical modal conditions for analytical and numerical solutions with common frequency $\omega_{0j} = 4.017\text{rad/s}$: velocity (ms^{-1})	100
5.9 Critical modal conditions for analytical and numerical solutions with common modal frequency $\omega_{0j} = 1.94\text{rad/s}$: velocity (ms^{-1}); (Non-resonant part)	105
5.10 Critical modal conditions for analytical and numerical solutions with common frequency $\omega_{0j} = 1.361\text{rad/s}$: velocity (ms^{-1})	105
6.1 The natural frequency of the longitudinal vibrating structure and the parameters for the shunt circuits	129
6.2 The natural frequency of transverse vibrating structure and the parameters for the shunt circuits	132

LIST OF FIGURES

FIGURE	Page
2.1 Aerodynamic forces on fixed rigid cylinder, taken from [66]: (a) aerodynamic cross-section; (b) squat cross-section; (c) cross-section subject to a flow roated by an angle $\alpha > 0$ (counterclockwise); (d) cross-section rotated by an angle $-\alpha$, subject to horizontal wind.	13
2.2 Qualitative form of the aerodynamic coefficients vs the angle of attack [66]: (a) generic cross-section; (b) cross-section symmetric with respect with respect to the $\alpha = 0$ axis.	14
2.3 Aerodynamic forces on a symmetric cross-section [66]: (a) generic condition; (b) overturning around the symmetric axis	14
2.4 Single degree of freedom system, subject to wind [66].	16
2.5 Orientation of the cross-section with respect to the horizontal flow [66]: (a) material axis \mathbf{a}_{x0} aligned with \mathbf{a}_x ; (b) material axis \mathbf{a}_{x0} deviated from \mathbf{a}_x by an (clockwise) angle $-\alpha$; (c) aerodynamic coefficients evaluated at α_0 (i.e., relative to the orientation $-\alpha_0$ of the cross-section).	21
2.6 Bifurcation diagrams for the Rayleigh-Duffing equation [66]: (a) limit cycle frequency-amplitude relationship; (b) amplitude of the limit cycle vs the wind velocity (solid line: stable, dashed line: unstable)	26
2.7 Limit cycles for the Rayleigh-Duffing equation [66]: (a) stable (super-critical) limit cycle; (b) unstable (sub-critical) limit cycle; (c) family of stable limit cycles, parameterized by $U > U_c$; (d) family of unstable limit cycle, parameterized by $U < U_c$	27
3.1 Prestressed cable [54]: (a) kinematics: reference prestressed configuration S , current configuration \hat{S} , displacement \mathbf{u} ; (b) dynamics: preloads \mathbf{p}_0 , \mathbf{P}_{0H} , prestress \mathbf{t}_0 , current loads \mathbf{p} , \mathbf{P}_H	31
3.2 Shallow cable [54]: (a) reference configuration; centerline S in the $(\mathbf{i}_1, \mathbf{i}_2)$ -plane, sag d ; (b) current configuration, centerline \hat{S} and its horizontal projection, displacement components u_t, u_n, u_b	38

4.1	Shallow horizontal cable under normal wind flow. Thin line: in-plane equilibrium position under self-weight; thick line: current configuration under the action of both self-weight and wind.	42
4.2	Case study 1: Approximated initial first linear mode	56
4.3	Case study 1: (a) First linear symmetric mode; (b, c, d) Second order corrections; figures are taken from [21].	57
4.4	Case study 1: (a) Bifurcation diagram, solid line: stable, dashed line: unstable; (b) Reconstituted displacement $v(s, t)$ of the cable for $\frac{U_2}{U_c} = 0.11$, taken from [21].	58
4.5	Case study 1: reconstituted time evolution of the displacement $v(s, t)$ for $\frac{U_2}{U_c} = 0.11$ at (a) half-span; (b) quarter-span (green line: multiple scale method; blue line: Galerkin method; orange line: finite difference method) [21].	59
4.6	Case study 1: reconstituted phase plot (v, \dot{v}) for $\frac{U_2}{U_c} = 0.11$ at (a) half-span; (b) quarter-span (green line: multiple scale method; blue line: Galerkin method; orange line: finite difference method)[21].	59
4.7	Case study 2: Approximated initial first linear mode.	60
4.8	Case study 2: (a) Anti-symmetric mode; (b, c, d) Second order corrections [21].	60
4.9	Case study 2: (a) Bifurcation diagram, solid line: stable, dashed line: unstable; (b) Reconstituted displacement $v(s, t)$ of the cable for $\frac{U_2}{U_c} = 0.09$, taken from [21].	61
4.10	Case study 2: reconstituted time evolution of the displacement $v(s, t)$ for $\frac{U_2}{U_c} = 0.09$ at (a) half-span; (b) quarter-span (green line: multiple scale method; blue line: Galerkin method; orange line: finite difference method) [21].	62
4.11	Case study 2: reconstituted phase plot (v, \dot{v}) for $\frac{U_2}{U_c} = 0.09$ at quarter-span (green line: multiple scale method; blue line: Galerkin method; orange line: finite difference method) [21].	62
5.1	Shallow horizontal cable under normal wind flow. Thin line: in-plane equilibrium position under self-weight; thick line: current configuration under the action of both self-weight and wind.	65
5.2	Spectrum of the planar \hat{v}_j (continuous lines) and out-of-plane \hat{w}_k (dashed lines) frequencies of the cable as function of the Irvine parameter. Odd indexes denote symmetric modes, even indexes antisymmetric modes. Points <i>A</i> to <i>D</i> are representative of different resonance conditions, taken from [42].	74

5.3	Eigenvalues $\lambda_{1j} = \pm i\omega_{0j} + \epsilon\lambda_{1j}^{(1,2)}$ in the plane of the invariants of the modal damping matrix \mathbf{B} : (a) eigenvalue sketches in each region, (b) eigenvalue paths for increasing wind velocity U , according to the signs of $\text{tr}\mathbf{B}^a$, $\det\mathbf{B}^a$; the parabola has equation $\text{tr}^2\mathbf{B} = 4\det\mathbf{B}$, taken from [60].	79
5.4	Aerodynamic coefficients, taken from [9, 120]: (a) Drag and lift coefficients; (b) Values of $C_d + C_l'$	86
5.5	critical mode for case S: (a) Real parts of \hat{v} ; (b) imaginary parts of \hat{v}	87
5.6	critical mode for case S: (a) real parts of \hat{w} ; (b) imaginary parts of \hat{w}	87
5.7	critical mode for case L: (a) real parts of \hat{v} ; (b) imaginary parts of \hat{v}	87
5.8	critical mode for case L: (a) real parts of \hat{w} ; (b) imaginary parts of \hat{w}	88
5.9	critical mode for case S: (a) real parts of \hat{v} ; (b) imaginary parts of \hat{v}	89
5.10	critical mode for case L: (a) real parts of \hat{v} ; (b) imaginary parts of \hat{v}	89
5.11	modal shapes for (case I in Figure 5.3-(b)): (a) real parts of \hat{v} ; (b) imaginary parts of \hat{v}	91
5.12	modal shapes for (case I in Figure 5.3-(b)): (a) real parts of \hat{w} ; (b) imaginary parts of \hat{w}	91
5.13	modal shapes for (case II in Figure 5.3-(b)): (a) real parts of \hat{v} ; (b) imaginary parts of \hat{v}	91
5.14	modal shapes for (case II in Figure 5.3-(b)): (a) real parts of \hat{w} ; (b) imaginary parts of \hat{w}	92
5.15	modal shapes for (case III in Figure 5.3-(b)): (a) real parts of \hat{v} ; (b) imaginary parts of \hat{v}	92
5.16	modal shapes for (case III in Figure 5.3-(b)): (a) real parts of \hat{w} ; (b) imaginary parts of \hat{w}	92
5.17	modal shapes for (case IV, curve (a), in Figure 5.3-(b)): (a) real parts of \hat{v} ; (b) imaginary parts of \hat{v}	93
5.18	modal shapes for (case IV, curve (a), in Figure 5.3-(b)): (a) real parts of \hat{w} ; (b) imaginary parts of \hat{w}	93
5.19	modal shapes for (case IV, curves (b), in Figure 5.3-(b)): (a) real parts of \hat{v} ; (b) imaginary parts of \hat{v}	93
5.20	modal shapes for (case IV, curves (b), in Figure 5.3-(b)): (a) real parts of \hat{w} ; (b) imaginary parts of \hat{w}	94
5.21	modal shapes for (case I in Figure 5.3-(b)): (a) real parts of \hat{v} ; (b) imaginary parts of \hat{v}	95
5.22	modal shapes for (case I in Figure 5.3-(b)): (a) real parts of \hat{w} ; (b) imaginary parts of \hat{w}	95
5.23	modal shapes for (case II in Figure 5.3-(b)): (a) real parts of \hat{v} ; (b) imaginary parts of \hat{v}	96

5.24 modal shapes for (case II in Figure 5.3-(b)): (a) real parts of \hat{w} ; (b) imaginary parts of \hat{w}	96
5.25 modal shapes for (case III in Figure 5.3-(b)): (a) real parts of \hat{v} ; (b) imaginary parts of \hat{v}	96
5.26 modal shapes for (case III in Figure 5.3-(b)): (a) real parts of \hat{w} ; (b) imaginary parts of \hat{w}	97
5.27 modal shapes for (case IV, curve (a), in Figure 5.3-(b)): (a) real parts of \hat{v} ; (b) imaginary parts of \hat{v}	97
5.28 modal shapes for (case IV, curve (a), in Figure 5.3-(b)): (a) real parts of \hat{w} ; (b) imaginary parts of \hat{w}	97
5.29 modal shapes for (case IV, curves (b), in Figure 5.3-(b)): (a) real parts of \hat{v} ; (b) imaginary parts of \hat{v}	98
5.30 modal shapes for (case IV, curves (b), in Figure 5.3-(b)): (a) real parts of \hat{w} ; (b) imaginary parts of \hat{w}	98
5.31 modal shapes for the non-resonant part of (case I in Figure 5.3-(b)): (a) real and (b) imaginary parts of \hat{v}	100
5.32 modal shapes for (case I in Figure 5.3-(b)): (a) real parts of \hat{v} ; (b) imaginary parts of \hat{v}	100
5.33 modal shapes for (case I in Figure 5.3-(b)): (a) real parts of \hat{w} ; (b) imaginary parts of \hat{w}	101
5.34 modal shapes for the non-resonant part of (case II in Figure 5.3-(b)): (a) real and (b) imaginary parts of \hat{v}	101
5.35 modal shapes for (case II in Figure 5.3-(b)): (a) real parts of \hat{v} ; (b) imaginary parts of \hat{v}	101
5.36 modal shapes for (case II in Figure 5.3-(b)): (a) real parts of \hat{w} ; (b) imaginary parts of \hat{w}	102
5.37 modal shapes for non-resonant part of (case III in Figure 5.3-(b)): (a) real and (b) imaginary parts of \hat{v}	102
5.38 modal shapes for (case III in Figure 5.3-(b)): (a) real parts of \hat{v} ; (b) imaginary parts of \hat{v}	102
5.39 modal shapes for (case III in Figure 5.3-(b)): (a) real parts of \hat{w} ; (b) imaginary parts of \hat{w}	103
5.40 modal shapes for non-resonant part of (case IV in Figure 5.3-(b)): (a) real and (b) imaginary parts of \hat{v}	103
5.41 modal shapes for (case IV, curve (a), in Figure 5.3-(b)): (a) real parts of \hat{v} ; (b) imaginary parts of \hat{v}	103
5.42 modal shapes for (case IV, curve (a), in Figure 5.3-(b)): (a) real parts of \hat{w} ; (b) imaginary parts of \hat{w}	104

5.43	modal shapes for (case IV, curves (b), in Figure 5.3-(b)): (a) real parts of \hat{v} ; (b) imaginary parts of \hat{v}	104
5.44	modal shapes for (case IV, curves (b), in Figure 5.3-(b)): (a) real parts of \hat{w} ; (b) imaginary parts of \hat{w}	104
5.45	modal shapes for the non-resonant part of (case I in Figure 5.3-(b)): (a) real and (b) imaginary parts of \hat{v}	106
5.46	modal shapes for (case I in Figure 5.3-(b)): (a) real parts of \hat{v} ; (b) imaginary parts of \hat{v}	106
5.47	modal shapes for (case I in Figure 5.3-(b)): (a) real parts of \hat{w} ; (b) imaginary parts of \hat{w}	107
5.48	modal shapes for the non-resonant part of (case II in Figure 5.3-(b)): (a) real and (b) imaginary parts of \hat{v}	107
5.49	modal shapes for (case II in Figure 5.3-(b)): (a) real parts of \hat{v} ; (b) imaginary parts of \hat{v}	107
5.50	modal shapes for (case II in Figure 5.3-(b)): (a) real parts of \hat{w} ; (b) imaginary parts of \hat{w}	108
5.51	modal shapes for non-resonant part of (case III in Figure 5.3-(b)): (a) real and (b) imaginary parts of \hat{v}	108
5.52	modal shapes for (case III in Figure 5.3-(b)): (a) real parts of \hat{v} ; (b) imaginary parts of \hat{v}	108
5.53	modal shapes for (case III in Figure 5.3-(b)): (a) real parts of \hat{w} ; (b) imaginary parts of \hat{w}	109
5.54	modal shapes for non-resonant part of (case IV in Figure 5.3-(b)): (a) real and (b) imaginary parts of \hat{v}	109
5.55	modal shapes for (case IV, curve (a), in Figure 5.3-(b)): (a) real parts of \hat{v} ; (b) imaginary parts of \hat{v}	109
5.56	modal shapes for (case IV, curve (a), in Figure 5.3-(b)): (a) real parts of \hat{w} ; (b) imaginary parts of \hat{w}	110
5.57	modal shapes for (case IV, curves (b), in Figure 5.3-(b)): (a) real parts of \hat{v} ; (b) imaginary parts of \hat{v}	110
5.58	modal shapes for (case IV, curves (b), in Figure 5.3-(b)): (a) real parts of \hat{w} ; (b) imaginary parts of \hat{w}	110
6.1	The smart cable: a single cable of length L , left end of which encircled by piezoelectric PVDF tube of length l	118
6.2	Geometry of the smart cable.	119
6.3	A schematic of the PVDF tube [111]: (a) under longitudinal tension; (b) under pure bending	120

6.4	Charge distribution in the PVDF tube [111]: (a) under an axial tension; (b) under a pure bending	121
6.5	Relationship between the electrical energy and the thickness.	124
6.6	Transverse displacement and strain	125
6.7	LR shunt circuit system taken from [111].	126
6.8	NC-R shunt circuit system taken from [111].	127
6.9	Single cable structure with the tube shaped PVDF damping system. . .	129
6.10	The longitudinal vibration response of the single cable structure with the tube-shaped PVDF damping system: (a) Frequency response of the right endpoint; (b) time-history response of the right endpoint under forced vibration.	130
6.11	Single cable structure with the tube shaped PVDF damping system. . .	131
6.12	The transverse vibration response of the single cable structure with the tube-shaped PVDF damping system: (a) Frequency response of the midpoint; (b) time-history response of the midpoint under forced vibration.	132
6.13	Energy harvester: (a) The peak of induced voltage across the PVDF tube; (b) The mechanical power input in the harvester; (c) The harvested power from the mechanical power input.	134
6.14	Energy harvested depending on electrical load resistance: (a) Induced voltage across the PVDF tube; (b) The mechanical power input in the harvester; (c) The harvested power from the mechanical power input. . .	135
6.15	Energy harvested dependance on mechanical acceleration: (a) Induced voltage across the PVDF tube; (b) The mechanical power input in the harvester; (c) The harvested power from the mechanical power input. . .	136

CHAPTER 1

INTRODUCTION

1.1 Research Motivation

For tension structures, cables are broadly used, which is one of the most important and mechanically efficient structural elements. They can be made of Copper, Silver, Steel, fiberglass, and polyester. Suspended cable materials are light weight, flexible, resistance of high tension, and these mechanical and physical properties are taken into account to use them in different mechanical, civil, ocean, electrical and other engineering applications by way of illustration in suspension and cable-stayed bridges, guyed towers and mooring structures. They are the best media to carry loads, transmit forces, and conduct of signals within long distances. The research focuses on the modeling, design and implementation of cables with intelligent functions.

The static and dynamic behavior of cables include free vibrations, reaction to driving excitation, and experimental observations of the oscillation. For a long time and in recent years, the study of cable problems in terms of the modes of vibration and natural frequencies has been an important subject and has received much attention among the researchers. Investigations by these time were conducted by various researchers on suspended cables e.g. [21, 42, 44, 52, 56, 58, 61, 71, 90, 91, 120], the theory of vibration has been refined considerably. Many works had done previously on this topic of the theory of cable vibration was restricted with predefined conditions, such as cable was considered inextensible and purely flexible. In recent years, the development of cable dynamics has got some enforcement by considering the elasticity effect, sag-to-span ratio, and wind attack angles.

1.2 Research Background and Historical Review of Literature

We represent here, a historical review based on the references described in [42], and then the development of theories as well as recent studies on this relevant topic of suspended cables.

From the sketches of Leonardo da Vinci in fifteenth century, the notion of catenary system has been found [86]. It predicted the result of loaded strings and other related things such as the idea of mechanism of the collapse of voussoir arch. From the description in the book "A span of bridges: an illustrated history", Stevin [34] carried out experiments of strings with loaded mass. From the experiments, he developed the theory of the formation of triangle forces. The study of the above book was for the suspension bridges that stated "a cable hangs in a parabolic arc". According to Truesdell [101] and Irvine [42], Beeckman solved the suspension bridge problem by 1615 for the uniformly distributed loads. Contrary to this study, in mid-seventeenth century, Leibnitz and Huygens, James Bernoulli and John Bernoulli came to a conclusion that the shape of a hanging cable is catenary. They used different approaches to discover the catenary, for example, Bernoulli brothers and Leibnitz used calculus, and Huygen followed the geometrical approach. The vibration of taut strings was studied extensively in the early part of the eighteenth century. Daniel Bernoulli studied transverse oscillations of a hanging uniform cable under the self weight whose one end was supported. Later, the same problem was analyzed by L. Euler as mentioned in [101]. They proposed the solution of the natural frequency in terms of infinite series. On that period, a lot of attention had received of the investigation on discrete systems. In 1788, by Lagrange, described in [106], a solution was proposed for vibrations of a massless, extensible string whose both ends were fixed and many dead loads were hung. A configuration, like this of suspended masses described the cable as the uniform self-loading. To describe the cable vibration, a breakthrough contribution was given by Poisson in 1820, see [42]. He established the equation of motion, in the form of partial differential equations, of a cable taking in consideration of general loading system. These equations were used to improve the previously obtained solutions of the problem of taut strings and vertically suspended cable. So that, the correct form of solutions of the linear natural vibrations of the uniform suspended cable were presented by restricting in stationary form of catenary. Till then except Lagrange's work, the theory of cable vibration taking in consideration of cable sag was not presented. With the help of general equations of Poisson's correct to the first order, Rohrs [93] consulting with Stokes, has developed an approximate solution of symmetric-vertical vibrations taking into account a small sag-to-span

ratio of a uniform suspended inextensible cable. Routh [94] in 1868, gave an exact solution for the symmetric and asymmetric in-plane vibrations of an inextensible heterogeneous sagging cable suspended vertically in a cycloid form. His results for the vibration of cycloid cable reduced the solution obtained by Rohr's for small sag-to-span ratio of uniform cable. His analysis did not cover the taut cable case as he limiting his study for the inextensible cable. Gradually, the study of cable vibration got a diverse applied field to investigate. Also a short review of cable dynamics was presented by Starossek [97] describing the beginning of the modern mechanics. Den Hartog [17] proposed a vertical galloping mechanism for the vibrating ice-coated cables by studying experimentally the transmission line oscillations. He observed high amplitudes for low frequency vibrations of the transverse wind action on transmission lines. Rannie and Von Karman [95] in 1941, studied a three-span inextensible cable and attained separately the natural frequencies for the symmetric and anti-symmetric in-plane modes of vibrations. The cable's elasticity was used for the first time by Kloppel and Lie [50] in 1942. Later in 1945, Vincent taking in consideration of cable elasticity, developed Rannie and Von Karman's work for the symmetric modes [105]. Pugsley [83] studied a uniformly suspended chain by giving emphasize on the first three planar modes in 1949 and proposed a semi-empirical theory to describe its natural frequency. He compared the obtained solution with experimental results and his previous work as well as Routh's work, and allowed the sag-to-span ratio from 1 : 10 up to 1 : 4. Bleich et al. [2] in 1950, contributed to improve the theory of suspension bridge vibration taking in consider of the elasticity of cable. But the obtained results for the effects of elasticity are not percipient comparing with geometrical point of view, because of the large sag-to-span ratio of the cable. For inextensible cable with effective sag, Saxon and Cahn [96] conferred theoretical solutions in 1953. These solutions also improved the previous solutions for the inextensible cable with small sag-to-span ratio, and using this, the accuracy of asymptotic solution improves with the mode number, when the sag-to-span ratio is large. In 1961, Goodey [31] investigated the natural modes and frequencies of dig-sag cables suspended from the same level of two fixed ends. He used different methods to get the solutions. He obtained the similar expressions proposed by Saxon and Cahn, using angular displacement as independent variable. Initially deformed cable vibrating between two fixed supports was studied by Soler [98] and obtained solution in closed form for the mode shapes and frequencies. There are some significant discrepancies of natural frequencies between the symmetric planar modes of inextensible sagged cables and taut strings. There were no experimental work found until 1970s to describe this situation. In 1974, Irvine and Caughey [44] showed an accurate description that the transition range of these two forms needs to include compatible cable

elasticity. They studied the linear theory of shallow elastic cable and got a solution in closed form. Their study, first time, gave an immense perception about the linear theory of free oscillations of fixed rigid supported cable horizontally suspended from same level of two ends having the sag-to-span ratio from 1 : 8 to zero approximately. They suggested a parameter combining cable elasticity and geometry to explain the extensibility of it as well as they gave explanation of cables symmetric and anti-symmetric in-plane motions. From the experimental results of symmetric and anti-symmetric planar modes, they predicted about the modal cross-over points. West et al. [110] studied the natural frequencies and vibration modes of suspended cables, where a discrete model is used. The cable is considered as a linked structure consists of some straight bars, which are connected by frictionless pins with concentrated masses. They have also discussed about the modal cross-over phenomena and the discrepancies found previously for the inextensible cables. Later, Irvine together with Griffin [43] extended his work to explore the impact of the fundamental geometric and elastic parameter known as Irvine parameter Λ^2 , in the response to the dynamic loading of a suspended cable causes by support excitement due to earthquake. They presented wave-type and modal solutions to describe the phenomena. The problem further includes the analysis of the effects of aerodynamic instabilities. Yamaguchi [113] investigated large sagged flat and inclined cables using Galerkin method and got approximated results with great accuracy. He formulated the model of the cable as a flexible and extensible continuum. The linearized model was solved by formulating a generalized eigenvalue problem discretizing into a finite-DOF system and presented obtained natural frequencies and shape of modes of the suspended cable. Rega and Luongo [90] examined in-plane vibrations of inextensible cables with symmetric movable supports and observed the cross-over points where the sag-to-span ratio has a wide range of values. For the linear dynamics, they described the way to insert a spring at one end of a cable, and it is possible to alter the effective value of Λ^2 , that interact with the cables low order frequency dynamics.

Nonlinear model of suspended cables was also considered by many researchers [21, 22, 23, 32, 35, 48, 49, 52, 56, 62, 63, 64, 71, 79, 85, 91, 120]. Owing to cables quadratic and cubic nonlinearities, to understand the multi-modal dynamics of the cable, it is important to analyze the internal resonances. Hanghold and Russel [36] proposed a system of nonlinear equations for the cable structures, which includes geometric nonlinearity accounting elastic deformation. They studied steady deflection, natural frequency measurements for small vibrations. For the transmission lines oscillations having low frequencies and large amplitudes, Hagedorn and Schäfer [35] investigated non-linear terms effects in the governing equations of an elastic flexible suspended cable, taking into account of quadratic and cubic

nonlinearities. They used Ritz-Galerkin method to approximate the solution of the first normal modes of vibration. These motion components are coupled by cubic nonlinearities caused by stretching cable and quadratic nonlinearities occurred by the curvature of equilibrium cable to provide a complete 3-dimensional reaction of the cable known as modal interaction. Nonlinear effects in the governing equation of a two-degree-of-freedom elastic model of cable suspended by its self-weight, also investigated by Luongo et al. [62]. They analyzed geometric nonlinearities of monofrequent vibrations to study the motion amplitude and frequency adjustment of the modal oscillations when the internal resonance is absent. They solved the quadratic and cubic nonlinearities by multiple time scale perturbation technique. Later, Luongo et al. [63] developed nonlinear model of an initially deformed elastic cable continuum through a Lagrangian description and a discrete model is developed by applying Galerkin method. They also investigated the proper approximate solution procedure which is consistent to the system. Lee and Perkins [71] developed a flexible elastic suspended cable model considering the planar excitation to investigate the interaction of symmetric planar and out-of-plane modes with two-to-one internal resonances. They used second order perturbation analysis to study the existence and stability of the solution, where the first order solution exhibits saturation and jump phenomenon, and cubic and higher order nonlinearities interrupt saturation. The effect of geometric nonlinearity of elastic cables suspended horizontally was studied in the work of Perkins [85] by addressing the modal interactions of in-plane and out-of-plane frequencies, which is at 2 : 1 ratio. By multiple scale method of analysis, it is observed that the first order terms include small damping parameters, and the parametric terms and second order terms are the external terms. Luongo and Piccardo [56] studied the aeroelastic phenomenon of a suspended flexible cable subjected by its own weight from two fixed supports, where the linear eigenfrequencies assumed in 1 : 2 ratio. They creatively considered the geometric nonlinearity effect along with aerodynamic effect, while it was neglected in the previous work of Lee and Perkins [71]. They also presented the effects of some parameters e.g., geometric cable parameters to study the critical and post-critical behaviour of the system. One can find a full description on the different critical conditions and the postcritical behaviour of a flexible elastic suspended cable in the research work of Luongo et al. [61], where multiple scale perturbation method was employed to study the internal resonances and multimodal galloping. Ferretti et al. [23] studied the effects of a single moving load combined with geometric nonlinearities on Kirchhoff taut strings taking into account the changing tension. The moving force is considered very small resulting small displacement and small increment in dynamic tension. They analyzed the model through analytical and numerical approaches and compared the results.

On the other hand, Triantafyllou [100] studied linear dynamics of taut inclined cables and derived a general asymptotic solution in 1984. He noticed modal cross-over phenomena while studying the horizontal cable which coincides with the prediction of Irvine and Caughey. But for the inclined cable, he did not observe the cross-over phenomena. Jones [47] derived linearized coupled horizontal and vertical equations of motion in terms of drag and lift forces. The aerodynamic parameters of the iced conductor also determined and compared with Den Hartog's criterion. A three-degree-of-freedom model is developed in the work of Yu et al. [114] by analyzing an iced electrical transmission line to study the galloping phenomenon. They used perturbation technique to develop the bifurcation equations assuming weak nonlinearity. Their study includes one non-resonant and nine internal resonant cases. They have taken in consideration of axial stress and torsion but neglected the curvature of the cable. A global model and a solution methodology were proposed by Piccardo [84] to study the aeroelastic phenomena. The onset of aerodynamic instability with any aeroelastic phenomenon of a system can be studied by linearizing the model. Two solution approaches of perturbation analysis were taken into account in the work of Pakdemirli et al. [87], one is direct approach, applied to governing partial differential equations of suspended cables with corresponding boundary conditions, and another approach of multiple scale method, is applied after discretizing the partial differential equations. They compared the results of both approaches, and discrepancies appear on the first level of approximated solutions. Van Oudheusden [104] described the quasi-steady aerodynamic modeling concept and the validity conditions of the similar systems with two assumptions. Rega et al. [92] used two analytical approaches to develop an asymptotic model to study the dynamic response of an elastic shallow suspended cable excited by a harmonic motion. The second order solution may be not unique, resulting the problem's inconsistency to apply the method of multiple scale analysis. An effective method of analyzing the impacts of wind force action on cables is wind tunnel test. The test generally focused on the evaluation of aerodynamic coefficients with respect to different wind attack angles. The wind tunnel tests has done by many researchers e.g., [16, 30, 33, 67, 69, 76], in order to investigate the response characteristics of cables, and presenting the galloping mechanisms. Novak et al. [76] in 1978, studied the aerodynamic properties by experimenting some iced guy cables to analyze their aeroelastic instability mechanisms in terms of wind tunnel test and presented drag and lift coefficients with respect to wind attack angles. Experimental investigation was done by Loredo-Souza and Davenport [67] to study the aeroelastic modes of transmission lines through wind tunnel tests. They compared the wind response in the transmission lines with the theoretical predictions predicted by using statistical method. After consistency of the theory

with the experiment, they proposed a modeling approach to model the conductor cables of transmission lines.

Recently, researchers are contributing to develop improved model and different richer solution techniques of the model of suspended cable considering different geometrical and aeroelastic properties. Among them some contributed works are presented through the references [42, 54, 55, 58, 62, 79, 91]. Irvine [46] proposed general solutions to study the response of a horizontal, freely hanged cable, assuming parabolic profile with small sag-to-span ratio, and subjected to a point load or/and a distributed load. Later, Irvine with Sinclair [45] gave an exact solution for developed non-dimensional equations of an elastic suspended cable subjected to vertical point loads. Approximate numerical integration, using Gauss quadrature formula [25], and Newton-Raphson method [25, 120], finite difference formulation [21, 52, 73] were used to solve nonlinear equations of cable vibration. Regarding the nonlinear vibrations of elastic suspended cables, Rega [91] summarized in three parts of the review to model the cable structure and methods to analyze the mechanical system via the continuum and their discretized models. Taking in consideration of bending and torsional stiffness, Luongo et al. [55] developed a stiff linear model of prestressed curved beam analyzing the galloping of suspended cables. By using a magnitude order analysis, they simplified the equation of motion of cables. Based on various types of ice-coated cable shapes, it is important to emphasize the study on the coupling effect between along-wind and cross-wind responses. Recently, improved models have been proposed, such as, Luongo and Piccardo [60] have developed analytical model dealing with bifurcation phenomenon of the coupled flexural galloping in resonant and non-resonant cases, and provide qualitative explanations for the coupled translational galloping mechanism through perturbation solution for both conditions. As described in [52], a stiff model is able to take into account the bending and torsional stiffness in a consistent way, whereas in many research works, it was ignored. In their investigation, they considered the multimodal galloping in the nonlinear regime and accounting quasi-steady aerodynamic forces. They have employed two numerical methods and an analytical method to study the model. Luongo and Piccardo [58], later, proposed an improved analytical approach for the equations of the suspended cable taking into account the cable rotation and the passive modes of the cables. The effects of internal resonances are also described for the continuous and discrete models. In the study of galloping vibrations of suspended, small sag-to-span ice-coated cables, Luongo et al. [64] pointed out the importance of cross-sectional torsion and bending, based on a curved, prestressed elastic beam. As a result of the self-weight and mean wind speed, the torsional rotation can be separated into

static and dynamic components. With considering the similar effect of bending, Kang et al. [49] studied linear and nonlinear dynamics of suspended cables. They analyzed the first and third order planar symmetric mode's frequencies when they are in 3 : 1 ratio, by applying multiple scale method. Bending stiffness remarkably changes the natural frequencies and shapes of mode. In research work conducted by Luongo and Zulli [53], has included the simultaneous effect of rain and wind flow on stay cable in cable-stayed bridges. They presented the obtained results in terms of in-plane and out-of-plane motion describing through bifurcation diagrams. Very recent researches are expanding with various external effects e.g., thermal effects on suspended cables. An analytical model is developed and studied the thermal effects by Lepidi and Gattulli [70]. An improved perturbation scheme has been proposed in the research of Luongo and Zulli [57], involves perturbing all the parameters in the parameter space along straight lines. And, since the exploring straight line can be freely selected, the parameters can be varied independently. In [57], new developments of perturbation technique have been proposed for the statics of cables subjected vertical forces distributed arbitrarily, and then extended the scheme to the general 3D-loading case [59]. Ferretti et al. [21] have investigated a continuum model of horizontally suspended shallow ice-coated cable taking into account external and internal damping to study the aeroelastic stability of the structure. The contribution of internal and external damping has presented by proposing the damping scheme following Kelvin-Voigt rheological model. To study the post-critical behavior, they have employed multiple scale method and compared the results with numerical solutions. The nonlinear effect of a string which traveled by a moving load is investigated and proposed a developed semi-analytical approach to separate the total response into a quasi-steady and an incremental dynamic part [22]. Nonlinear effects on horizontally suspended cable also investigated by Zulli et al. [120] to study the critical aeroelastic behavior taking in consideration of external and internal damping. They have considered the steady swing of the cable and presented the solution in terms of frequencies and mode shapes, and compared the analytical results with numerical one. Besides, a detailed introduction of modeling and designing of a smart cable to control vibration is presented in chapter 6.

1.3 Objectives of the Research, Summary, and Organization

1.3.1 Objectives

The objective of the research is to strengthen existing cable infrastructures due to scientific and technological advancement in terms of:

1. Modeling of damping properties and air interaction effects
2. Non-destructive monitoring of structures
3. Energy harvesting using piezoelectric devices
4. Improving efficiency in passenger and freight transport through structural control
5. Cost reduction and maintaining high levels of efficiency and environmental sustainability.

1.3.2 Summary

Since cables are slender structures with a low damping coefficient that are prone to galloping with the wind flow. This phenomena is known as aeroelastic phenomenon caused by wind action on ice-coated suspended cables having non-circular cross-sections. We assume that the cable is suspended by its own weight and is a self-excited dynamical system. According to the quasi-steady theory, the excitation is presented by forces proportional to the structural velocity and in a linear field. By Den Hartog criterion, for one-degree-of-freedom system, the critical velocity of the wind can be determined by applying the condition that total damping is zero. For the system having more than one-degree-of-freedom, we study the eigenvalue problem to obtain the least wind speed in which an eigenvalue from left crosses the imaginary axis in the complex plane. Analytical analysis of such a model is more complicated compared with a numerical analysis. On the other hand, this type of model is effective to get closed form solutions which can enable to study the bifurcation mechanism.

1.3.3 Organization of the Thesis

The research work from the last three years is summarized in this thesis. This thesis consists of seven chapters. This chapter represents the introduction, describing the background, motivation, objectives, and scope of the research. The second

chapter depicts the literature review of aeroelastic stability, followed by [66]. The formulation of the problem of galloping of a shallow flexible suspended cable is presented in Chapter 3. In-plane galloping of a shallow flexible cable modeled and analyzed in a continuum approach is presented in Chapter 4, followed by [21]. Chapter 5 represents and analyzes a linear spatial galloping analysis of shallow cables. A smart cable to suppress vibration is designed and modeled in chapter 6 by following the concept described in [111], and then an energy harvester is also designed to harvest energy from the cable vibration. In chapter 7, we have concluded the thesis and illustrated the future development of the model.

LITERATURE REVIEW: AEROELASTIC STABILITY**2.1 Introduction**

When a flexible structure having non-circular cross-section e.g., because of ice-accretion, subjected to a wind force, results change in its orientation according to flow direction. Upon vibration in the structure, the acting wind force oscillates accordingly. When the oscillating wind force accelerates the vibration in structure, results aerodynamic instability, which can lead to high-magnitude vibration. In other words, the dynamic aeroelastic instability can occur when a lift-generating structure subject to aerodynamic loads. When aerodynamic forces and structure's natural modes are coupled, large amplitude diverging motion may occur. In this chapter, aerodynamic forces, related aerodynamic coefficients, the application of quasi-static theory, and other relevant topics, as well as the aeroelastic bifurcation mechanism, have been illustrated by following A. Luongo, M. Ferretti and S. Di Nino [66].

2.2 Aerodynamic Forces

When a load is exerted on an elastic structure, results structure-wind interaction and loss of stability of that structure can happen. A rigid cylindrical structure fixed on the ground is taken as a sample to describe the mechanism. The \mathbf{a}_z -axis of the cylinder is submerged in laminar wind flow having velocity $\mathbf{U} = U\mathbf{a}_d$ perpendicular to \mathbf{a}_z , described in Figure 2.1 (a). We can neglect the effect of edge when the cylinder is very long and we can also consider the fluid's velocity field as planar which is perpendicular to \mathbf{a}_z . If the cross-section of the cylinder is a contour curve with no corners, variable curvature (slow), i.e., the structure having an aerodynamic shape, the threads of the fluid attached without smashing on the body. In such a case, we can evaluate the normal and tangential fields of pressure that acts on the body, by applying equations of motion of fluid, and integrating on the lateral surface

of cylinder, we can determine the resultant force \mathbf{f}^a and couple \mathbf{c}^a measuring per unit length of the cylinder, where the forces are known as aerodynamic forces. The projection of the forces on the basis $(\mathbf{a}_d, \mathbf{a}_l, \mathbf{a}_z)$, having the relation $\mathbf{a}_l := \mathbf{a}_z \times \mathbf{a}_d$, we can have,

$$\mathbf{f}^a := f_d \mathbf{a}_d + f_l \mathbf{a}_l, \quad \mathbf{c}^a := c_z \mathbf{a}_z. \quad (2.1)$$

where, f_d is drag force or force of resistance which acts in the flow direction and has a positive value if the orientation directed on \mathbf{a}_d ; f_l is the lift force which acts on perpendicular to the direction of the flow, and is positive if it is oriented as $\mathbf{a}_z \times \mathbf{a}_d$; and c_z is known as aerodynamic couple which is defined in a manner to a predefined center, and is positive when it is oriented as \mathbf{a}_z . They are expressed as follows,

$$f_d = \frac{1}{2} \rho_a U^2 D C_d, \quad (2.2a)$$

$$f_l = \frac{1}{2} \rho_a U^2 D C_l, \quad (2.2b)$$

$$c_z = \frac{1}{2} \rho_a U^2 D^2 C_m, \quad (2.2c)$$

with the air density ρ_a , cross-sectional characteristic dimension D , kinetic force $\frac{1}{2} \rho_a U^2$, and C_d, C_l and C_m are the drag, lift and moment coefficients respectively, and they are known as aerodynamic coefficients. Generally, these coefficients depend on the cross-sectional shapes and wind-interaction directions. By imposing some conditions on the system, e.g., considering idealized airfoils, we can obtain aerodynamic coefficients analytically. But most of the cases, they are determined experimentally by fixing the structure in a wind tunnel, known as wind tunnel tests, e.g., bluff bodies of which the edges are sharp and high variable curvatures, see Figure 2.1 (b). And these create high differences of pressure between the wind direction and opposite part of the structure, as a result, vortices produce.

Angle of attack

The angle formed in between the cross-sectional axis (e.g., a reference line on the body) and the acting relative wind flow direction is known as the angle of attack. The angle of attack denoted by α , formed with the direction of the cross-section of body \mathbf{a}_x by the flow direction of wind \mathbf{a}_d , and the value of the angle is positive if \mathbf{a}_x and \mathbf{a}_d coincide and rotates anti-clockwise with an angle smaller than π , see Figure 2.1 (c). We are interested to evaluate the laws $C_h(\alpha)$, aerodynamic coefficients. To determine the laws, wind tunnel tests employed where the flow direction kept fixed and the cylinder is rotated clockwise around its axis by an angle α , see Figure 2.1 (d). By approaching with the small increments of angle α ,

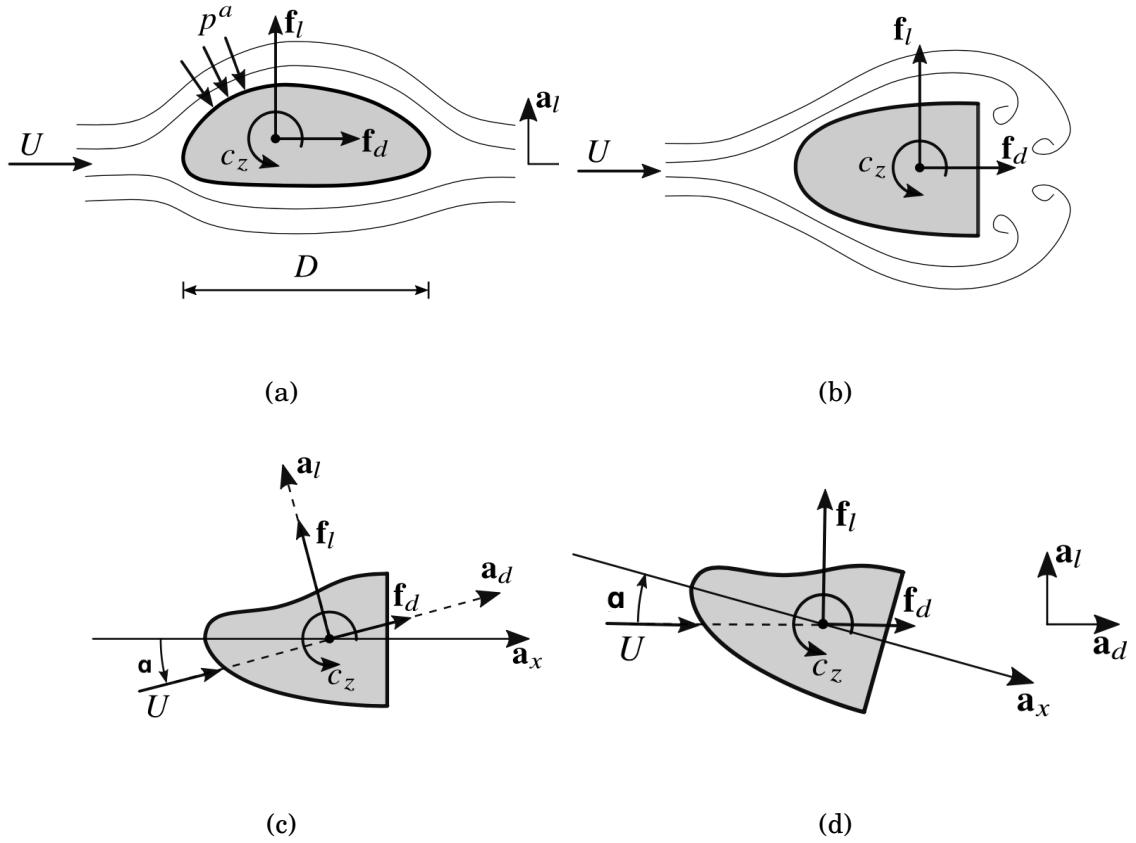


Figure 2.1: Aerodynamic forces on fixed rigid cylinder, taken from [66]: (a) aerodynamic cross-section; (b) squat cross-section; (c) cross-section subject to a flow rotated by an angle $\alpha > 0$ (counterclockwise); (d) cross-section rotated by an angle $-\alpha$, subject to horizontal wind.

and using Equations 2.2 for the forces with related attack angles, the laws $C_h(\alpha)$ are determined by points, as qualitatively depicted in Figure 2.2.

For the cross-sections, in general, the aerodynamic coefficients are of 1st ordered. For any attack angle α , it is noticed that the drag coefficient $C_d > 0$, as the air medium resists at the entrance by the structure. Contrarily, the coefficients C_l and C_m can be positive or negative. Particularly, a lift force $f_l > 0$ shows that the direction of the aerodynamic reaction is vertical when the flow is horizontal and directed on \mathbf{a}_x and, it is downward, if the lift force is negative. If the cross-section is symmetric on the basis of the structural axis \mathbf{a}_x , then the laws $C_h(\alpha)$ can be symmetric or anti-symmetric, if the forces are taken according to the attack angle α , as in Figure 2.3 (a), and the tension is reversed about to the axis of symmetry, see Figure 2.3 (b), the forces are certainly obtained corresponding to the attack angle $-\alpha$, as the cross-section shape is not altered. Referencing the basis $(\mathbf{a}_d, \mathbf{a}_l)$, intrinsic to flow direction, it is noticed that $f_d(-\alpha) = f_d(\alpha)$, $f_l(-\alpha) = -f_l(\alpha)$ and $c_z(-\alpha) = -c_z(\alpha)$. In the conclusion, $C_d(\alpha)$ is symmetric and $C_l(\alpha), C_m(\alpha)$ are anti-

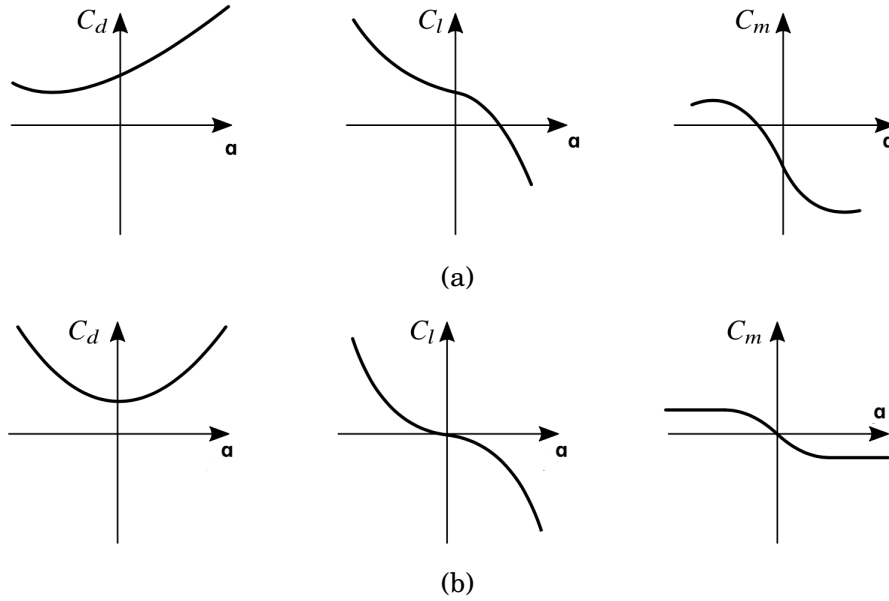


Figure 2.2: Qualitative form of the aerodynamic coefficients vs the angle of attack [66]: (a) generic cross-section; (b) cross-section symmetric with respect with respect to the $\alpha = 0$ axis.

symmetric functions, see Figure 2.2 (b). When the cross-section is circular, and the axes are symmetric, then $C_l(\alpha) = C_m(\alpha) \equiv 0$.

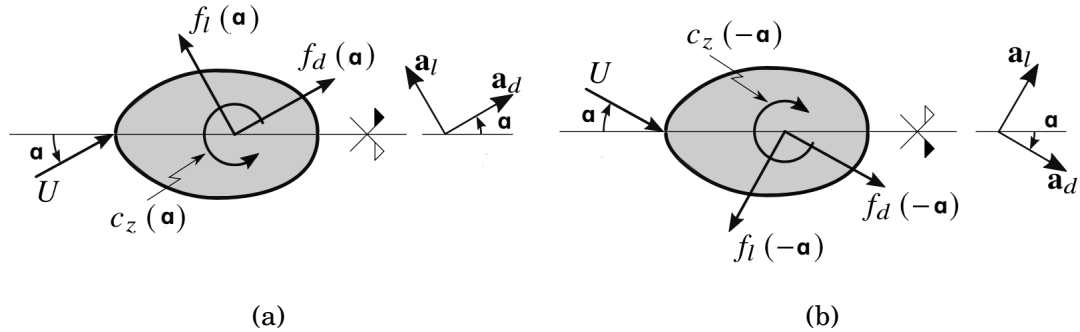


Figure 2.3: Aerodynamic forces on a symmetric cross-section [66]: (a) generic condition; (b) overturning around the symmetric axis

Quasi-steady Theory

It is cumbersome to determine the aerodynamic forces, because of the vibration of the cylinder owing to its elastic behavior, under the influence of wind flow rather than remaining static. Which can be disseminated in the structure, or can be absorbed through the ground, taking as a constraint. Indeed, the vibration of the structure can change the nature of the flow, as a result, the forces are changed from steady to unsteady varying with time as a function of the structures dynamic reaction. It is also complex to evaluate the unsteady forces, which can be evaluated by some approximated methods. The related aerodynamic coefficients can be found

by wind tunnel tests and quasi-steady theory allows to use them to evaluate the forces.

The concept of the quasi-steady theory is formed on the basis of the subsequent hypothesis. If the movement of the body is slow comparing to the fluid material particles that surround it, at an instance t , the aeroelastic forces have the same value as they are determined on the body when it was fixed under the flow with constant attack angle $\alpha(t)$, at the fixed time t . This is known as instantaneous attack angle $\alpha(t)$. The angle of attack varies over time, because of the vibration of the structure, and consequently, the quasi-steady theory does not follow the dynamics of the mechanism. Under this hypothesis, the expression for the aeroelastic forces in equation (2.2) can be rewritten as follows:

$$f_d = \frac{1}{2}\rho_a U_r^2(t) DC_d(\alpha(t)), \quad (2.3a)$$

$$f_l = \frac{1}{2}\rho_a U_r^2(t) DC_l(\alpha(t)), \quad (2.3b)$$

$$c_z = \frac{1}{2}\rho_a U_r^2(t) D^2 C_m(\alpha(t)), \quad (2.3c)$$

where, it is replaced the flow with $U_r(t)$, instantaneous velocity; and $\alpha(t)$, instantaneous angle of attack.

2.3 Galloping of single-degree-of-freedom systems

The loss of stability of an aeroelastic single -degree-of-freedom (SDOF) system exhibits by itself with a phenomenon known as galloping. In a wind flow field, galloping is defined as the low frequency and self-excited large vertical oscillation of an elastic body (in general, cold region) e.g., iced electric lines, suspended cables.

2.3.1 Model

Let us assume, a rigid cylinder having length l , fixed horizontally and is constrained in a way that it can transform oscillations vertically, when an external force is applied to it. A horizontal static wind of magnitude U is acting orthogonally to the axis of the cylinder, illustrated in Figure 2.4. The governing equation of motion of the system with the vertical displacement $v(t)$, reads:

$$M\ddot{v} = F_y^{el}(v) + F_y^v(\dot{v}) + F_y^a(\dot{v}; U), \quad (2.4)$$

where, M is the body mass; depending on the displacement, F_y^{el} is the elastic forces applied by constraint; depending on the structural velocity, $F_y^v(\dot{v})$ is the viscous force; $F_y^a(\dot{v}; U)$ is vertical component of aeroelastic force, depends on structural velocity.

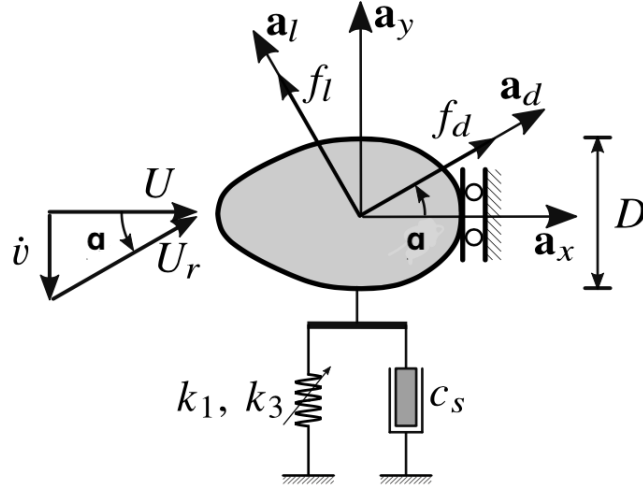


Figure 2.4: Single degree of freedom system, subject to wind [66].

Assuming that the spring (see Figure 2.4) is non-linear and symmetric, the constitutive law reads:

$$F_y^{el} = -(k_1 v + k_3 v^3), \quad (2.5)$$

with the linear stiffness $k_1 > 0$ and cubic stiffness $k_3 \geq 0$. When $k_3 > 0$, i.e., the nonlinear regain force is larger modulus comparing with linear one, the spring is known as ‘hardening’ and if $k_3 < 0$, it is called ‘softening’. On the other hand, the viscous damper is considered linear with the structural coefficient c_s , as,

$$F_y^v = -c_s \dot{v}. \quad (2.6)$$

Then the equation of motion (2.4) becomes,

$$\ddot{v} + 2\xi_s \omega_s \dot{v} + \omega_s^2 v + \kappa_s v^3 = \frac{1}{M} F_y^a(\dot{v}; U), \quad (2.7)$$

with $\omega_s := \sqrt{\frac{k_1}{M}}$, circular frequency of undamped body; $\kappa_s := \frac{k_3}{M}$, nonlinear coefficient (structural); and $\xi_s := \frac{c_s}{2\omega_s M}$, structural damping coefficient.

Aeroelastic forces

It is prerequisite to determine the instantaneous angle of attack $\alpha(t)$ and relative wind U_r acting on the structure, at instance t , along with the direction of the material axis \mathbf{a}_x . The vector difference between relative velocity to the ground,

$U\mathbf{a}_x$ and the velocity of the body $\dot{v}\mathbf{a}_y$, is the relative wind velocity to the body, $U_r\mathbf{a}_d$, namely

$$U_r\mathbf{a}_d = U\mathbf{a}_x - \dot{v}\mathbf{a}_y.$$

We have, $\mathbf{a}_d = \cos\alpha\mathbf{a}_x + \sin\alpha\mathbf{a}_y$, then the above relation can be written as,

$$\begin{aligned} U_r(\cos\alpha\mathbf{a}_x + \sin\alpha\mathbf{a}_y) &= U\mathbf{a}_x - \dot{v}\mathbf{a}_y, \\ \Rightarrow (U - U_r\cos\alpha)\mathbf{a}_x - (U_r\sin\alpha + \dot{v})\mathbf{a}_y &= 0. \end{aligned}$$

From which, we have

$$U_r = \frac{U}{\cos\alpha}, \quad (2.8a)$$

$$\tan\alpha = -\frac{\dot{v}}{U}. \quad (2.8b)$$

Figure 2.4 represents the relative velocity, U_r with the attack angle α , for the structural velocity $-\dot{v}\mathbf{a}_y$, and as a result, α is positive following equation (2.8b). So, the body movement has the following effects:

(i) the movement of the body modifies velocity magnitude, by following equation (2.8a); and (ii) it also modifies the attack angle.

As a result, both effects depend on structural velocity and are implicit functions of time t , which illustrates why the aeroelastic forces rely on the velocity of the structure, even in a simplified theory such as the quasi-steady theory. Now using equations (2.3a), (2.3b) and equations (2.8), and projecting them onto \mathbf{a}_y , we have the vertical component of the force,

$$F_y^\alpha = f_d l \sin\alpha + f_l l \cos\alpha = \frac{1}{2}\rho_a U^2 D l C_y(\alpha), \quad (2.9)$$

where,

$$C_y(\alpha) := \frac{1}{\cos^2\alpha} [C_d(\alpha)\sin\alpha + C_l(\alpha)\cos\alpha], \quad (2.10)$$

is another aerodynamic coefficient.

2.3.2 Linear Stability analysis

In this subsection, an initial linear analysis is attained on the commence of the aeroelastic instability phenomenon. Assuming that the velocity (structural) \dot{v} is smaller than the wind velocity U , we have from the Equation (2.8b), the attack angle α is small as well. By series expansion of the trigonometric functions, we get

$$\alpha = -\frac{\dot{v}}{U} + \dots, \quad (2.11)$$

along with, $C_y(\alpha) = C_l(\alpha) + C_d(\alpha)\alpha$. Expansion of the aerodynamic coefficients on the neighborhood of $\alpha = 0$, we have

$$C_h(\alpha) = C_{h0} + C'_{h0}\alpha + \dots, \quad h = d, l, \quad (2.12)$$

the prime, here indicates the derivative with respect to α and the subscript 0 denotes the laws evaluated at $\alpha = 0$, and hence, C'_{h0} is slope of the curve $C_h(\alpha)$ at origin. Following equation (2.11), linearizing equation (2.12) in α , we get

$$C_y(\alpha) = C_{l0} - (C_{d0} + C'_{l0}) \frac{\dot{v}}{U}. \quad (2.13)$$

Neglecting elastic and aeroelastic nonlinearities and using equation (2.9) and equation (2.13), the Equation of motion (2.7) becomes,

$$\ddot{v} + 2\xi_s\omega_s\dot{v} + \omega_s^2v = \frac{1}{2} \frac{\rho_a U^2 D l}{M} \left[C_{l0} - (C_{d0} + C'_{l0}) \frac{\dot{v}}{U} \right]. \quad (2.14)$$

In the above equation, the existence of a static force, which is independent of \dot{v} , and a time varying force, which is proportional to \dot{v} , is obvious. The static force and the force which exerted at rest on the structure coincides. As it only modifies the equilibrium position, it has no contribution to stability. The next force, instead, proportional to \dot{v} , a viscous force, which can be merged with the structural damping. Hence, the equation of motion reads,

$$\ddot{v} + 2\omega_s(\xi_s + U\zeta_1)\dot{v} + \omega_s^2v = 0, \quad (2.15)$$

where,

$$\zeta_1 := \frac{\rho_a D l}{4\omega_s M} (C_{d0} + C'_{l0}). \quad (2.16)$$

The aerodynamic damping factor is defined as $\xi_a := U\zeta_1$, proportional to the velocity of the wind and whose values depend on ζ_1 . There are two contributions of this coefficient, they are: (i) drag coefficient $C_{d0} > 0$, measures the medium resistance at the static position of the structure, and the derivative of lift coefficient $C'_{l0} \gtrless 0$ measures the lift coefficients slope at the origin. There are two cases can arise:

- (a) $C_{d0} + C'_{l0} \geq 0$ (that is, (i) $C'_{l0} \geq 0$; or (ii) $C'_{l0} < 0$, but $|C'_{l0}| \leq C_{d0}$); resulting $\zeta_1 \geq 0$, which means stabilizing or neutralizing the aerodynamic damping and added with structural damping, the system in this case is called aerodynamically stable.
- (b) $C_{d0} + C'_{l0} < 0$ (that is, $C'_{l0} < 0$, and in addition $|C'_{l0}| > C_{d0}$); in this case, it is instabilizing the aerodynamic damping, as it is deducted itself from structural damping and the system is aerodynamically unstable.

The following outcomes are originated from the above analysis: the 1st derivative of lift coefficient at $\alpha = 0$, must be (i) negative and (ii) large enough in modulus to occur the aeroelastic instability. Due to the proportional relationship between aerodynamic damping and U , a critical velocity U_c exists, called critical galloping velocity, that total damping $\xi_t := \xi_s + U\zeta_1$ zeroes, we have $U_c := -\frac{\xi_s}{\zeta_1}$, or,

$$U_c = \frac{4\omega_s M}{\rho_a D l} \frac{\xi_s}{|C_{d0} + C'_{l0}|}, \quad \text{if } C_{d0} + C'_{l0} < 0. \quad (2.17)$$

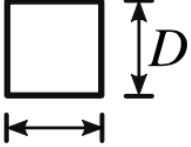
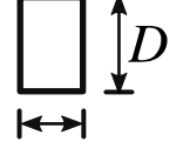
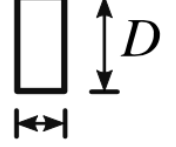
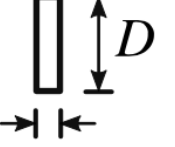
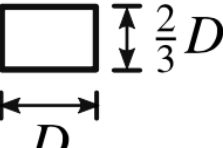
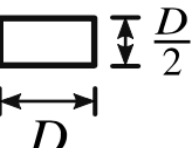
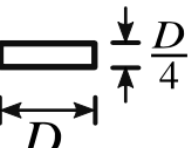
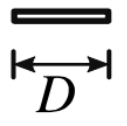
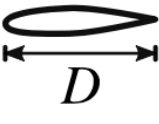
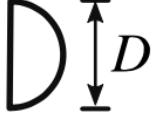
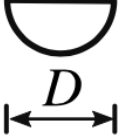
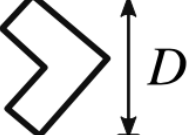
The critical galloping velocity is also known as Den Hartog velocity. In critical condition, when $U = U_c$, then $\lambda = \pm i\omega_s$, i.e., a pair of purely imaginary eigenvalues appear, where ω_s is the natural frequency. As a result, there occurs a Hopf bifurcation. The equilibrium is asymptotically stable when $U < U_c$, and unstable when $U > U_c$.

Numerical values of the galloping aerodynamic coefficient

A long cylinder was considered whose aerodynamic coefficients were studied in the case of various cross-sectional shapes and some numerical and experimental analyses [1]. The results are discussed in details in the book by A. Luongo, M. Ferretti and S. Di Nino [66]. Due to some inevitable errors in evaluations or inaccuracies in numerical modeling, the obtained results in some cases are discordant, e.g., the flow behavior, such as turbulent or laminar; the length of cylinder; different shapes of cross-sections affect the results. In general, the summation $C'_{y0} := C_{d0} + C'_{l0}$ is affected more than their separate values of C_{d0} and C'_{l0} . In the Table 2.1, taken from [1, 66], for different cross-sectional shapes which represents the values of C'_{y0} . The observed results are described in below:

"the square shape is unstable; the vertically long rectangles are stable; the horizontally long rectangles are unstable if the ratio of thickness-to-width is larger than 1/4, otherwise stable. For the airfoil, the coefficient $C'_{y0} \simeq 2\pi$, and is stable; D-section is also stable but the L-profile is not stable."

Table 2.1: Values of $C'_{y_0} := C_{d0} + C'_{l_0}$ for different cross-section shapes of a long cylinder, subject to laminar flow, horizontally incident; negative values indicate aerodynamically unstable cross-sections [66].

			
D	$2D/3$	$D/2$	$D/4$
$C'_{y_0} = -3.0$	$C'_{y_0} = 0$	$C'_{y_0} = 0.5$	$C'_{y_0} = 0.15$
<hr/>			
			
D	D	D	D
$C'_{y_0} = -1.3$	$C'_{y_0} = -2.8$	$C'_{y_0} = 10$	$C'_{y_0} = 6.3$
<hr/>			
			
D	D	D	D
$C'_{y_0} = 6.3$	$C'_{y_0} = 0.1$	$C'_{y_0} = 0.5$	$C'_{y_0} = -0.66$
<hr/>			

Influence of the orientation of the cross-section with respect to the flow

We assumed in the previous section, to formulate the laws $C_h(\alpha)$, the aerodynamic coefficients, that the direction of the body which is the reference direction and the direction of flow \mathbf{a}_x coincide. Now, we concern to the case where the material direction, \mathbf{a}_{x_0} (say), does not coincide with the flow direction \mathbf{a}_x , but makes an angle $-\alpha_0$, described by Figure 2.5.

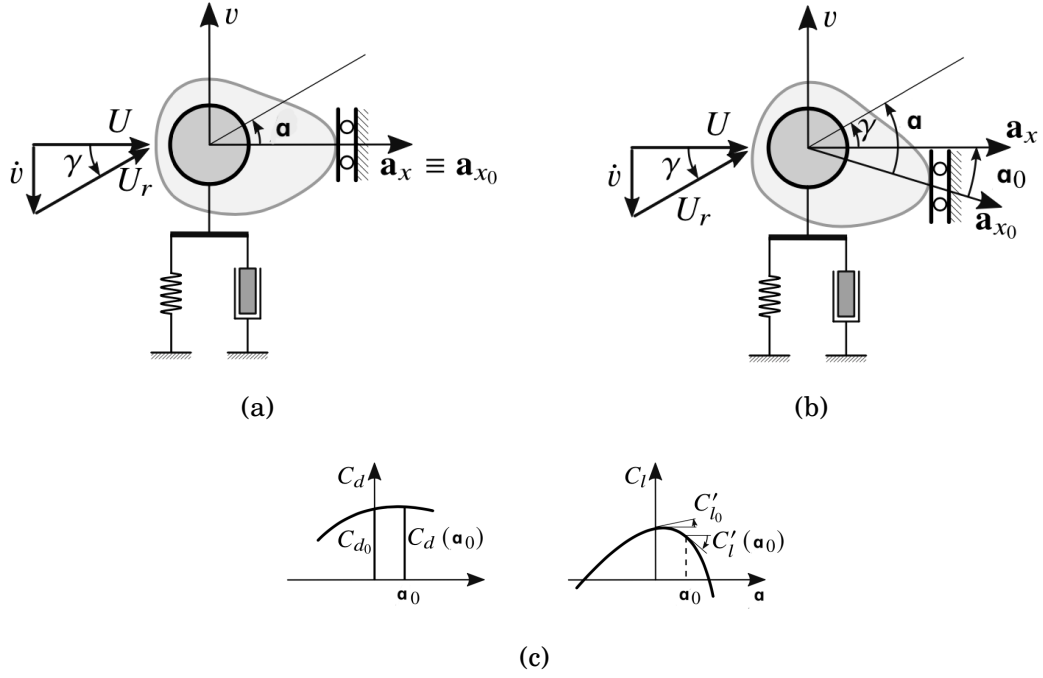


Figure 2.5: Orientation of the cross-section with respect to the horizontal flow [66]: (a) material axis \mathbf{a}_{x0} aligned with \mathbf{a}_x ; (b) material axis \mathbf{a}_{x0} deviated from \mathbf{a}_x by an (clockwise) angle $-\alpha$; (c) aerodynamic coefficients evaluated at α_0 (i.e., relative to the orientation $-\alpha_0$ of the cross-section).

Such a condition arises, for instance, when attempting to evaluate the frozen electric ducts dynamics that subjected to horizontal wind flow and whose annexation is capable of assuming any orientation regarding the flow. By applying the previous outcomes, we can determine the aerodynamic force which acts on cylinder. The angle $\alpha = 0$ should be replaced with new angle $\alpha = \alpha_0$, as the aerodynamic force depends on drag coefficient and the derivative of lift coefficient, which are determined when the body is at rest and on the direction of the flow. So that, $C_{d0} + C'_{l0} \equiv C_d(0) + C'_l(0)$ in the equation (2.16), have to be replaced by $C_d(\alpha_0) + C'_l(\alpha_0)$.

2.3.3 Nonlinear analysis: the limit cycle

From the linear analysis, we get the critical velocity U_c and in this velocity, the instability condition occurs. Oscillations which are exponentially divergent, predicted in the zone of instability, but no fact is provided regarding the limit cycles existence that constrain the amplitudes of the oscillation, and about the dependence of these limit cycles on U . To find out the information of these problems, we need to perform a nonlinear analysis accounting both the aeroelastic and structural nonlinearities. In order to achieve this, the elastic spring's cubic contribution is once more taken into account, (which was neglected previous analysis), from the equation of motion (2.7), and in addition, the higher order terms of the aeroelastic

force in the expansion in Taylor series, are considered again.

Nonlinear aeroelastic forces

The vertical aerodynamic coefficient $C_y(\alpha)$ is precisely expressed in equation (2.10), where the angle α can be found from equation (2.8b). It is necessary to take into account not only the linear term but also the quadratic, cubic and other higher order terms by expanding the angle in series with small enough but finitesimal terms in $\frac{\dot{v}}{U}$. The similar operation needs to be done for the lift and drag coefficients. We have then,

$$\alpha = -\frac{\dot{v}}{U} + \frac{1}{3}\left(\frac{\dot{v}}{U}\right)^3 + \dots, \quad (2.18a)$$

$$C_h(\alpha) = C_{h0} + C'_{h0}\alpha + \frac{1}{2}C''_{h0}\alpha^2 + \frac{1}{6}C'''_{h0}\alpha^3 + \dots, \quad h = d, l. \quad (2.18b)$$

Substituting equation (2.18) in equation (2.10), and also expanding the circular functions in series up to cubic terms, we have

$$\begin{aligned} C_y(\alpha) = C_{l0} - \left(\frac{\dot{v}}{U}\right)(C_{d0} + C'_{l0}) + \left(\frac{\dot{v}}{U}\right)^2 \left(\frac{1}{2}C_{l0} + C'_{d0} + \frac{1}{2}C''_{l0}\right) \\ - \left(\frac{\dot{v}}{U}\right)^3 \left(\frac{1}{2}C_{d0} + \frac{1}{6}C'_{l0} + \frac{1}{2}C''_{d0} + \frac{1}{6}C'''_{l0}\right). \end{aligned} \quad (2.19)$$

Then, from equation (2.9), we get

$$F_y = \frac{1}{2}\rho_\alpha U^2 D l \left[A_0 - A_1 \frac{\dot{v}}{U} + A_2 \left(\frac{\dot{v}}{U}\right)^2 - A_3 \left(\frac{\dot{v}}{U}\right)^3 + \dots \right], \quad (2.20)$$

where, we define

$$\begin{aligned} A_0 &:= C_{l0}, \\ A_1 &:= C_{d0} + C'_{l0}, \\ A_2 &:= \frac{1}{2}C_{l0} + C'_{d0} + \frac{1}{2}C''_{l0}, \\ A_3 &:= \frac{1}{2}C_{d0} + \frac{1}{6}C'_{l0} + \frac{1}{2}C''_{d0} + \frac{1}{6}C'''_{l0}. \end{aligned} \quad (2.21)$$

Here A_i 's are the nondimensional aerodynamic coefficients.

For the case of cross-sectional symmetry, as $C_d(\alpha)$ is symmetric and $C_l(\alpha)$ is anti-symmetric, we have $C'_{d0} = C'''_{d0} = \dots = 0$, and $C_{l0} = C''_{l0} = \dots = 0$. Hence, $A_0 = A_2 = \dots = 0$, agreeing that F_y has to be an odd function of $\frac{\dot{v}}{U}$, so that

$$F_y = -\frac{1}{2}\rho_\alpha U^2 D l \left[A_1 + A_3 \left(\frac{\dot{v}}{U}\right)^3 + \dots \right]. \quad (2.22)$$

Nonlinear equation of motion

Considering the symmetric cross-section regarding the flow, the equation of motion (2.7) can be rewritten as:

$$\ddot{v} + 2\omega_s(\xi_s + U\zeta_1)\dot{v} + \omega_s^2 v + \kappa_s v^3 + \frac{1}{U}\zeta_3 \dot{v}^3 = 0, \quad (2.23)$$

where the terms higher than cubic, are neglected. Equation (2.23) is known as Rayleigh-Duffing equation. The following conditions hold for a cross-section which is aerodynamically unstable, as defined:

$$\zeta_1 := \frac{\rho_a D l}{4\omega_s M} A_1 < 0, \quad \zeta_3 := \frac{\rho_a D l}{2M} A_3. \quad (2.24)$$

There are two types of nonlinearities in equation (2.23), one is structural type (Duffing-like), which is presented by cubic term in displacement, and other one is aeroelastic type (Rayleigh-like), which is expressed by cubic term in structural velocity.

Lindstedt-Poincaré method

Because of the nonlinearities in the Rayleigh-Duffing equation, in the closed form, the equation is unsolvable. But the equation becomes weakly nonlinear and allows it to be solved via a perturbation approach when the motion amplitude is small and finite, which results smallness in the nonlinearities. We approach with the Lindstedt-Poincaré method, one can get in details by following [66]. The following actions must be taken in order to use the approach, which entails finding the periodic solutions to the equation of motion (2.23). We now introduce a dimensionless time $\tau := \Omega t$, where Ω is unknown circular frequency. Hence, equation (2.23) becomes,

$$\Omega^2 \ddot{v} + 2\Omega\omega_s(\xi_s + U\zeta_1)\dot{v} + \omega_s^2 v + \kappa_s v^3 + \frac{\Omega^3}{U}\zeta_3 \dot{v}^3 = 0. \quad (2.25)$$

The dot here denotes the time derivative with respect to the new time τ . We are interested to find the periodic solution to the above equation of one parameter family of the form $v = v(\tau; \epsilon)$, $\Omega = \Omega(\epsilon)$, $U = U(\epsilon)$, where ϵ is a perturbation parameter. Accounting the symmetry property of the system, we can expand the above parameters in Taylor series as:

$$v(\tau; \epsilon) = \epsilon v_1(\tau) + \epsilon^3 v_3(\tau) + \dots, \quad (2.26a)$$

$$\Omega(\epsilon) = \Omega_0 + \epsilon^2 \Omega_2 + \dots, \quad (2.26b)$$

$$U(\epsilon) = U_0 + \epsilon^2 U_2 + \dots. \quad (2.26c)$$

In the above expansions, the coefficients are unknown. Substituting equations (2.26) into equation (2.25), and separating the similar order terms of ϵ , we get the following perturbation equations:

$$\text{order } \epsilon: \quad \Omega_0^2 \ddot{v}_1 + 2\Omega_0 \omega_s (\xi_s + U_0 \zeta_1) \dot{v}_1 + \omega_s^2 v_1 = 0, \quad (2.27a)$$

$$\begin{aligned} \text{order } \epsilon^2: \quad \Omega_0^2 \ddot{v}_3 + 2\Omega_0 \omega_s (\xi_s + U_0 \zeta_1) \dot{v}_3 + \omega_s^2 v_3 = & -2\Omega_0 \Omega_2 \ddot{v}_1 - \kappa_s v_1^3 - 2\Omega_0 \omega_s U_2 \zeta_1 \dot{v}_1 \\ & - 2\Omega_2 \omega_s (\xi_s + U_0 \zeta_1) \dot{v}_1 - \frac{\Omega_0^3}{U_0} \zeta_3 \dot{v}_1^3. \end{aligned} \quad (2.27b)$$

Because of the periodicity with period 2π of the solution on τ scale, we have $v(2\pi) = v(0)$, $\dot{v}(2\pi) = \dot{v}(0)$. Then from equation (2.26a), we get

$$v_k(2\pi) = v_k(0), \quad \dot{v}_k(2\pi) = \dot{v}_k(0), \quad k = 1, 3, \dots \quad (2.28)$$

Next, we introduce the normalization condition $v(0; \epsilon) = \epsilon$, $\dot{v}(0; \epsilon) = 0$, characterizes to ϵ the amplitude of the limit cycle. From equation (2.26a), we have

$$\begin{aligned} v_1(0) = 1, \quad \dot{v}_1(0) = 0, \\ v_k(0) = 0, \quad \dot{v}_k(0) = 0, \quad k = 3, 5, \dots \end{aligned} \quad (2.29)$$

Solution to the perturbation equations

The 1st order perturbation equation admits the periodic solutions iff it vanishes the total damping $\xi_s + U_0 \zeta_1$. Consequently, we have $U_0 = -\frac{\xi_s}{\zeta_1} \equiv U_c$, the critical velocity. Besides, $\omega_0 = \omega_s$ for the period 2π . From the equations (2.32b) and (2.32c), with the initial values, inferring that the family of limit cycles bifurcates from the equilibrium position at Hopf bifurcation. According to the normalization condition and the above results, we have the solution for 1st order equation:

$$v_1 = \cos \tau. \quad (2.30)$$

Substituting the solution (2.30) into equation (2.27b) and performing some calculations, we get

$$\begin{aligned} \omega_s^2 (\ddot{v}_3 + v_3) = 2\omega_s \Omega_2 \cos \tau + 2\omega_s^2 U_2 \zeta_1 \sin \tau - \frac{1}{4} \kappa_s (3 \cos \tau + \cos(3\tau)) \\ + \frac{1}{4} \frac{\omega_s^3}{U_c} \zeta_3 (3 \sin \tau - \sin(3\tau)). \end{aligned} \quad (2.31)$$

Removing the resonant terms, and taking the coefficients of $\cos \tau$ and $\sin \tau$, we have

$$\begin{aligned} 2\omega_s\Omega_2 - \frac{3}{4}\kappa_s &= 0, \\ 2\omega_s^2U_2\zeta_1 + \frac{3}{4}\frac{\omega_s^3}{U_c}\zeta_3 &= 0. \end{aligned} \quad (2.32)$$

Solving equations (2.32), we get

$$\Omega_2 = \frac{3\kappa_s}{8\omega_s}, \quad U_2 = -\frac{3\omega_s\zeta_3}{8U_c\zeta_1}. \quad (2.33)$$

Using the above results in equations (2.26), we have

$$v(\tau; \epsilon) = \epsilon \cos(\tau), \quad (2.34a)$$

$$\Omega(\epsilon) = \omega_s \left(1 + \epsilon^2 \frac{3\kappa_s}{8\omega_s^2} \right), \quad (2.34b)$$

$$U(\epsilon) = U_c \left(1 - \epsilon^2 \frac{3\omega_s\zeta_3}{8U_c^2\zeta_1} \right). \quad (2.34c)$$

Since $\tau = \Omega t$, we can come back to the true time, accounting $\zeta_1 < 0$,

$$v(t; \epsilon) = \epsilon \cos \left(\left(1 + \epsilon^2 \frac{3\kappa_s}{8\omega_s^2} \right) \omega_s t \right), \quad (2.35a)$$

$$U(\epsilon) = U_c \left(1 + \epsilon^2 \frac{3\omega_s\zeta_3}{8U_c^2|\zeta_1|} \right). \quad (2.35b)$$

Now, after the elimination of ϵ , we get

$$v(t; U) = \sqrt{\frac{8U_c|\zeta_1|(U - U_c)}{3\omega_s\zeta_3}} \cos \left(\left(1 + \frac{\kappa_s U_c |\zeta_1| (U - U_c)}{\omega_s^3 \zeta_3} \right) \omega_s t \right). \quad (2.36)$$

Equations (2.34) represent the limit cycles of the system, where ϵ is amplitude with $\Omega = \Omega(\epsilon)$ a frequency, and $U = U(\epsilon)$ a wind velocity. On the other hand, equation (2.36) represents the limit cycle as a function of U instead of ϵ .

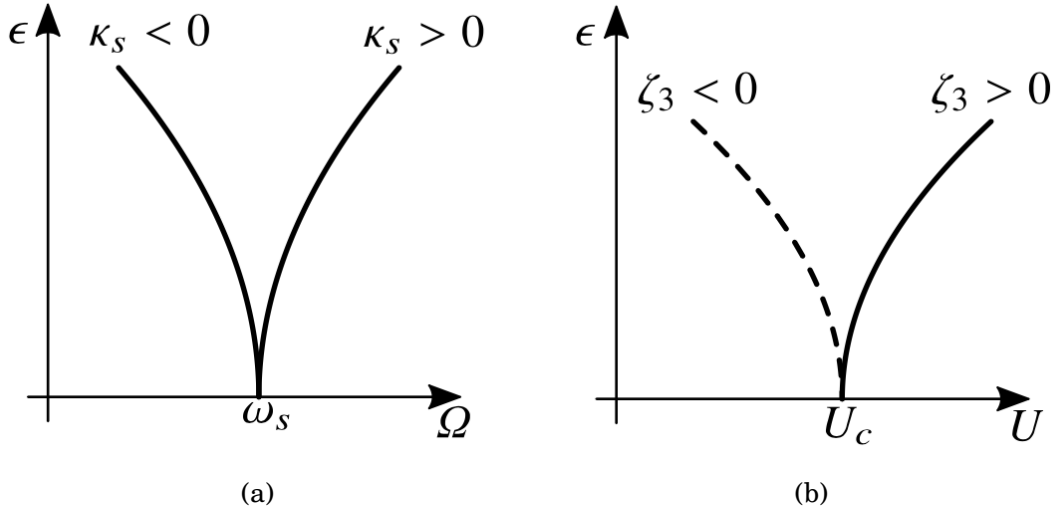


Figure 2.6: Bifurcation diagrams for the Rayleigh-Duffing equation [66]: (a) limit cycle frequency-amplitude relationship; (b) amplitude of the limit cycle vs the wind velocity (solid line: stable, dashed line: unstable)

Bifurcation diagrams for the expression of frequency and velocity of wind against the amplitude are drawn in the Figure 2.6. From the figure, we can observe that: (i) if $\kappa_s > 0$, that is, hardening of the spring, then $\Omega > \omega_s$, meaning that, with a higher frequency (comparing with natural frequency), the cycle is completed; and if $\kappa_s < 0$, that is, softening the spring, then $\Omega < \omega_s$; (ii) if $\zeta_3 > 0$, that is, in equation (2.21), $A_3 > 0$, then we have, super-critical limit cycle, i.e., it exists for $U > U_c$; and if $\zeta_3 < 0$, that is, in equation (2.21), $A_3 < 0$, then we have sub-critical limit cycle, i.e., it exists for $U < U_c$; (iii) at this order, there is no effect of structural nonlinearity on the limit cycles amplitude but has only effect on frequency; also, there is no effect of aeroelastic nonlinearity on frequency, but has effect on amplitude.

The closed orbit, which is described by the system, is an ellipse in the phase plane (v, \dot{v}) , for the physical parameters of the system and for an assigned ϵ , from the equations (2.34), which moves clockwise (see Figure 2.7 (a), (b)). We can prove that, if the bifurcation is super-critical then the orbit is stable, and if sub-critical, then unstable. The stable limit cycle attracts the trajectories, described in Figure 2.7(a), constrains the exponential development of the motion which is predicted by linear theory. Whereas, the unstable cycle repels the trajectories, see Figure 2.7(b). If it is higher magnitude than ϵ in the second case, the motion diverges, even though for the stable equilibrium position. A 3-dimensional representation of the limit cycles is described in Figures 2.7(c), (d). For each velocity U (fixed), which is super-critical or sub-critical, there is a limit cycle whose amplitude grows with $|U - U_c|$, as expresses by equation (2.34).

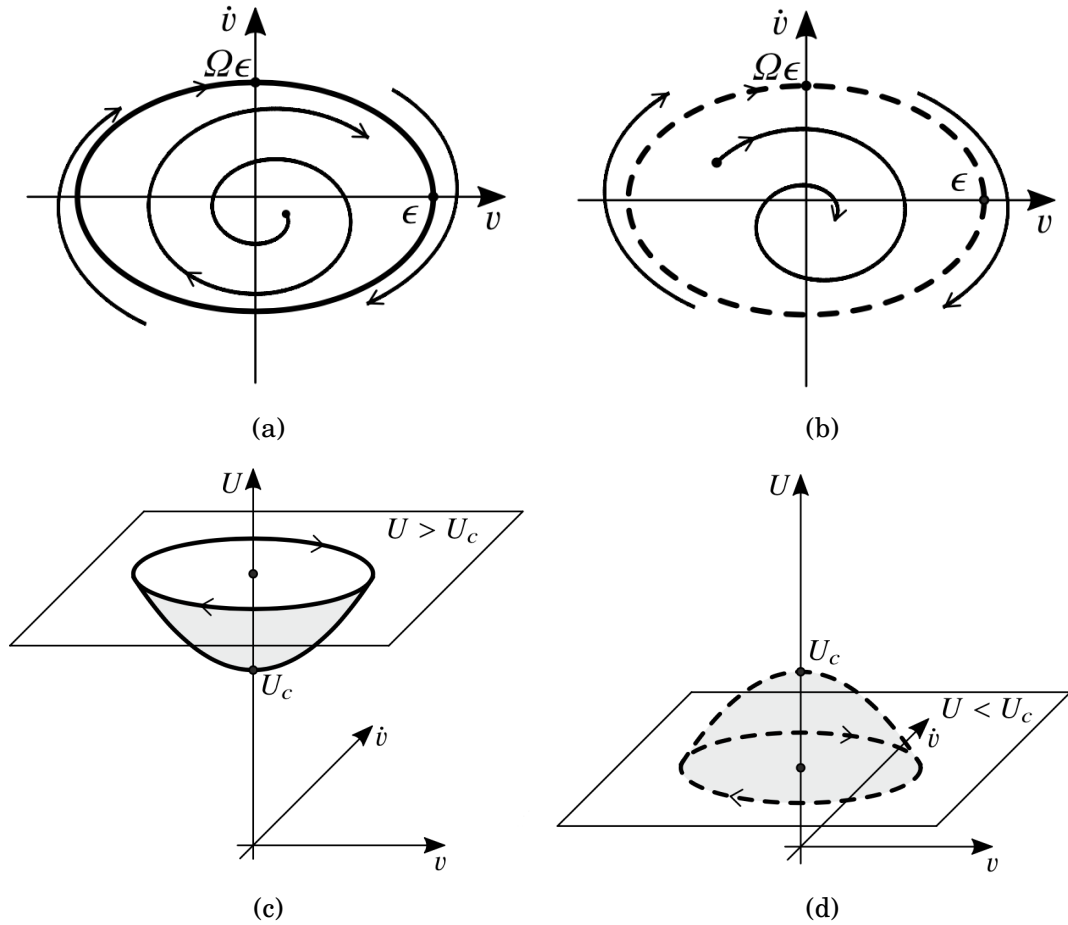


Figure 2.7: Limit cycles for the Rayleigh-Duffing equation [66]: (a) stable (super-critical) limit cycle; (b) unstable (sub-critical) limit cycle; (c) family of stable limit cycles, parameterized by $U > U_c$; (d) family of unstable limit cycle, parameterized by $U < U_c$

2.4 Galloping of strings

Previously, we determined a rigid cylinder's motion on which static flow acts, and the wind action was considered similar on all cross-sections, excluding the neighboring ends of the cylinder. On the other hand, if the cylinder is deformable, such as a taut string whose cross-sectional motion $v(z, t)$ is irregular and has different magnitude, where the aeroelastic forces f_y^a are the function of z . The aeroelastic forces depend on the deflection at z as well as on the deflection in the close field at z and makes it non-planar as the motion of which affects the flow. By excluding the non-local part of the phenomena and focusing just on the impact of the local motion of the string, or by the assumption $f_y^a(z, t) = f_y^a(v(z, t))$, the problem becomes simplified. On the basis of the assumption, we stated the following hypothesis: "the aeroelastic forces act on z of the string, are similar of the forces those applied on the infinitely long rigid cylinder, experiencing at the certain abscissa of the

cross-section with the equivalent translational velocity."

Consequently, the string's curvature and interaction between cross-sectional velocities (structural) are neglected. Considering the effect of structural nonlinearities, a linear structural model can be formulated under the condition of nonlinear aeroelastic forces. Then the equation of motion takes the form:

$$m\ddot{v} + c_e\dot{v} + \left(1 + \hat{\eta}\frac{\partial}{\partial t}\right)\mathcal{K}v = f_y^a(z, t), \quad (2.37)$$

with the related boundary conditions. Where, $v = v(z, t)$ is transversal displacement; m is linear mass density; c_e is external damping coefficient; \mathcal{K} is total stiffness operator, which are elastic and geometric stiffnesses; $\hat{\eta}$ is internal damping coefficient, which is formulated on the basis of the rheological Kelvin-Voigt model, describes internal viscous force, and $f_y^a(z, t)$ are aeroelastic forces per unit length; under the conditions of symmetry, we have from equation (2.22),

$$f_y(z, t) = -\frac{1}{2}\rho_a U^2 D \left[A_1 \frac{\dot{v}(z, t)}{U} + A_3 \left(\frac{\dot{v}(z, t)}{U} \right)^3 + \dots \right]. \quad (2.38)$$

To solve equation (2.37), we need numerical schemes e.g., finite element method or finite difference method. If we use Galerkin method, the problem will be simplified, we consider

$$v(z, t) = \phi(z)q(t), \quad (2.39)$$

where, $\phi(z)$ is deflection, considered as reference function and $q(t)$ is time dependent amplitude. This weak formulation of the equilibrium gives an ODE with unknown Lagrangian parameter q .

2.4.1 Strings

We consider a string which is taut and fixed at the supports A, B ($z = 0, l$), and a wind of velocity $U\mathbf{a}_x$ acts on it. It is assumed that the cross-section of the string is non-circular e.g., because of ice-coation, which is symmetric along \mathbf{a}_x -axis and can oscillate freely on the transverse direction \mathbf{a}_y . The associated equation of motion with the boundary condition reads:

$$\begin{aligned} m\ddot{v} + c_e\dot{v} - \eta A_s \dot{v}'' - T_0 v'' &= f_y^a(z, t), \\ v(0, t) &= 0, \\ v(l, t) &= 0, \end{aligned} \quad (2.40)$$

with $v = v(z, t)$ is the displacement on transverse direction, m is the mass per unit length of iced string, c_e is the external damping coefficient, η is the internal

damping coefficient, A_s is the structural cross-sectional area of the non-iced string, T_0 is the string's tension, defined as $T := \sigma_0 A_s$, and f_y^a is the aeroelastic forces per unit length of the string.

If it is resricsted that the oscillation of the string happens in it's first natural mode, then we have

$$v(z, t) = q(t) \sin\left(\frac{\pi z}{l}\right). \quad (2.41)$$

This is the exact solution of the equation of motion regarding linear part. By applying the orthogonality condition of the residual of field equation with the reference shape function, we have the weak formulation of the equilibrium:

$$\int_0^l [m\ddot{v} + c_e \dot{v} - \eta A_s v'' - T_0 v'' - f_y^a(z, t)] \sin\left(\frac{\pi z}{l}\right) dz = 0. \quad (2.42)$$

Using equation (2.41) and then integrating, we obtain an ODE, known as Rayleigh oscillator,

$$M\ddot{q} + (c_s + Ub_1)\dot{q} + k_1 q + \frac{1}{U} b_3 \dot{q}^3 = 0, \quad (2.43)$$

where,

$$\begin{aligned} M &:= m \int_0^l \sin^2\left(\frac{\pi z}{l}\right) dz = \frac{1}{2} ml, \\ k_1 &:= T_0 \frac{\pi^2}{l^2} \int_0^l \sin^2\left(\frac{\pi z}{l}\right) dz = T_0 \frac{\pi^2}{2l}, \\ c_s &:= \left(c_e + \eta A_s \frac{\pi^2}{l^2}\right) \int_0^l \sin^2\left(\frac{\pi z}{l}\right) dz = \frac{1}{2} \left(c_e l + \eta A_s \frac{\pi^2}{l^2}\right), \\ b_1 &:= \frac{1}{2} \rho_a D A_1 \int_0^l \sin^2\left(\frac{\pi z}{l}\right) dz = \frac{1}{4} \rho_a D l A_1, \\ b_3 &:= \frac{1}{2} \rho_a D A_3 \int_0^l \sin^4\left(\frac{\pi z}{l}\right) dz = \frac{3}{16} \rho_a D l A_3. \end{aligned} \quad (2.44)$$

The equation (2.43) and equation (2.23) are same when $\omega_s^2 = \frac{k_1}{M}$, $\xi_s = \frac{c_s}{2\omega_s M}$, $\kappa_s = 0$, $\zeta_1 = \frac{b_1}{2\omega_s M}$ and $\zeta_3 = \frac{b_3}{M}$.

CHAPTER 3

DEVELOPMENT OF THE MODEL OF A SHALLOW FLEXIBLE CABLE

3.1 Introduction

In this chapter, we have developed a mathematical model of shallow flexible cable, suspended between two fixed points. It is assumed that the cable subject to an uniform wind. The torsional and flexural stiffnesses are neglected. Firstly, we have considered the prestressed cable model; and successively, we have presented the linearized theory; and lastly, we have obtained the required model for shallow cables.

3.2 Basic Assumptions

The derivation of the mathematical model of a suspended cable is performed based on the work of H. M. Irvine [42] and A. Luongo and D. Zulli [54].

To develop the model of a suspended cable, the following assumptions are taken into account through this thesis work:

- i. The cable is flexible and the bending stiffness is neglected.

Through the study in this work, we neglect the effect of bending stiffness because of smallness. Some authors have discussed about this topic, one can find the work [21, 22, 23, 52, 53, 54, 55, 56, 57, 58, 59, 60, 61,62, 63, 64, 65 120]. Our cable systems in this work are mainly affected more by axial stiffness compared to bending stiffness. And, these cables are considered perfectly flexible.

- ii. The cable is subjected to tensile forces only. The cable is assumed only to transmit the large amplitude of tensile forces and no resistance acts against bending and compression.

iii. The supports are fixed and the material of the cable follows the Hooke's law.

3.3 Prestressed Cables

We have considered a suspended cable, which is prestressed by static forces, to develop a mathematical model representing the reaction of it, when embedded in a three-dimensional space. The cable is in equilibrium under its own weight, which is the reference configuration. We are interested in oscillations around equilibrium configuration that have small amplitude.

3.3.1 Quasi-exact model

Prestressed reference state: A suspended flexible cable, considered lying on curve S in the three-dimensional space and expressed by the parametric equations

$$\bar{\mathbf{x}} = \bar{\mathbf{x}}(s),$$

where s denotes the arclength of the curve S . The Frenet triad is then defined as,

$$\bar{\mathcal{B}}_f = (\bar{\mathbf{a}}_t(s), \bar{\mathbf{a}}_n(s), \bar{\mathbf{a}}_b(s)),$$

where the unit vectors satisfy the Frenet formulas:

$$\bar{\mathbf{a}}_t' = \bar{\kappa} \bar{\mathbf{a}}_n, \bar{\mathbf{a}}_n' = \bar{\tau} \bar{\mathbf{a}}_b - \bar{\kappa} \bar{\mathbf{a}}_t, \bar{\mathbf{a}}_b' = -\bar{\tau} \bar{\mathbf{a}}_n.$$

Assuming that the cable is in equilibrium position subjected to internal stress $\mathbf{t}_0(s)$ and static external forces $\mathbf{p}_0(s), \mathbf{P}_{0H}$, here $H = A, B$ the fixed points of the supports. Therefore, the balance equations with the boundary conditions read:

$$\begin{aligned} \mathbf{t}_0' + \mathbf{p}_0 &= 0, \\ \mp \mathbf{t}_{0H} &= \mathbf{P}_{0H}. \end{aligned} \tag{3.1}$$

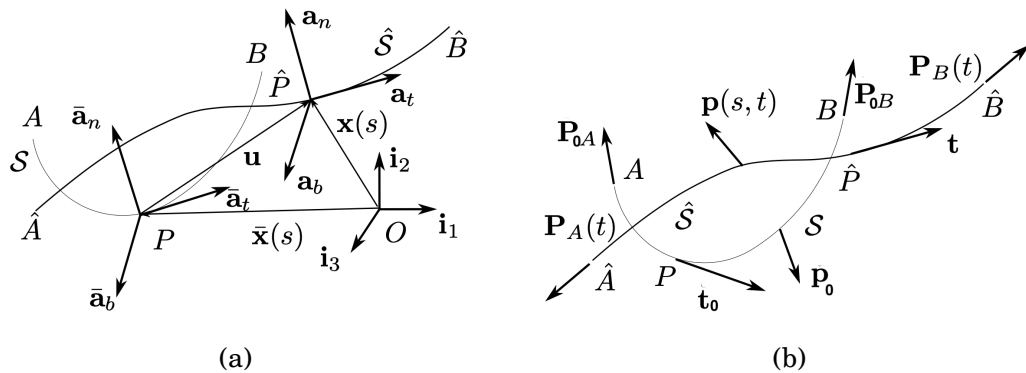


Figure 3.1: Prestressed cable [54]: (a) kinematics: reference prestressed configuration S , current configuration \hat{S} , displacement \mathbf{u} ; (b) dynamics: preloads $\mathbf{p}_0, \mathbf{P}_{0H}$, prestress \mathbf{t}_0 , current loads \mathbf{p}, \mathbf{P}_H .

Kinematics: Let us consider, the (non-natural) parametric equations $\mathbf{x} = \mathbf{x}(s, t)$, at time $t > 0$ represent the current configuration of the cable. Denoting the relevant Frenet triad,

$$\mathcal{B} := (\mathbf{a}_t(s, t), \mathbf{a}_n(s, t), \mathbf{a}_b(s, t)),$$

satisfying the following, taking the stretch as unity:

$$\mathbf{a}'_t = \kappa \mathbf{a}_n, \mathbf{a}'_n = \tau \mathbf{a}_b - \kappa \mathbf{a}_t, \mathbf{a}'_b = -\tau \mathbf{a}_n, \quad (3.2)$$

where,

$$\mathbf{a}_t = \mathbf{x}', \mathbf{a}_n = \frac{1}{\kappa} \mathbf{x}'', \mathbf{a}_b = \frac{1}{\kappa} (\mathbf{x}' \times \mathbf{x}''), \quad (3.3)$$

and, $\kappa = \|\mathbf{x}''\|$, $\tau = \frac{\mathbf{x}' \times \mathbf{x}'' \cdot \mathbf{x}'''}{\|\mathbf{x}''\|^2}$.

Let us consider the displacement measured from the reference configuration, to express the current configuration with it, as follows:

$$\mathbf{u} := \mathbf{x}(s, t) - \bar{\mathbf{x}}(s), \quad (3.4)$$

with the geometric boundary conditions

$$\mathbf{u}_H = \check{\mathbf{u}}_H. \quad (3.5)$$

We have, the unique scalar strain component (unit extension), defined as: $e = \|\mathbf{x}'\| - 1$. Taking into account the relation $\bar{\mathbf{x}}' = \bar{\mathbf{a}}_t$ and using equation (3.4), we have

$$e = \sqrt{1 + 2\mathbf{u}' \cdot \bar{\mathbf{a}}_t + \mathbf{u}' \cdot \mathbf{u}'} - 1. \quad (3.6)$$

Now, defining the displacement vector in terms of external basis, as follows:

$$\mathbf{u} := \sum_{j=1}^3 u_j \mathbf{i}_j. \quad (3.7)$$

As $\bar{\mathbf{a}}_t = \sum_{j=1}^3 \bar{x}'_j \mathbf{i}_j$, we have

$$e = \sqrt{1 + 2 \left(\sum_{j=1}^3 \bar{x}'_j u'_j + \frac{1}{2} \sum_{j=1}^3 u'^2_j \right)} - 1. \quad (3.8)$$

On the other hand, representing the displacement vector in the intrinsic reference basis, as:

$$\mathbf{u} := u_t \bar{\mathbf{a}}_t + u_n \bar{\mathbf{a}}_n + u_b \bar{\mathbf{a}}_b, \quad (3.9)$$

then, we have the derivative of \mathbf{u} :

$$\begin{aligned} \mathbf{u}' &= u'_t \bar{\mathbf{a}}_t + u_t \bar{\mathbf{a}}'_t + u'_n \bar{\mathbf{a}}_n + u_n \bar{\mathbf{a}}'_n + u'_b \bar{\mathbf{a}}_b + u_b \bar{\mathbf{a}}'_b, \\ &= u'_t \bar{\mathbf{a}}_t + u_t \bar{\kappa} \bar{\mathbf{a}}_n + u'_n \bar{\mathbf{a}}_n + u_n (\bar{\tau} \bar{\mathbf{a}}_b - \bar{\kappa} \bar{\mathbf{a}}_t) + u'_b \bar{\mathbf{a}}_b - u_b \bar{\tau} \bar{\mathbf{a}}_n. \end{aligned}$$

So that,

$$\mathbf{u}' = (u'_t - \bar{\kappa}u_n) \bar{\mathbf{a}}_t + (u'_n + \bar{\kappa}u'_t - \bar{\tau}u_b) \bar{\mathbf{a}}_n + (u'_b + \bar{\tau}u_n) \bar{\mathbf{a}}_b. \quad (3.10)$$

Using equation (3.10), equation (3.6) becomes,

$$e = \sqrt{1 + 2(u'_t - \bar{\kappa}u_n) + (u_t - \bar{\kappa}u_n)^2 + (u'_n + \bar{\kappa}u'_t - \bar{\tau}u_b)^2 + (u'_b + \bar{\tau}u_n)^2} - 1. \quad (3.11)$$

Dynamics: Let us assume the cable is subjected to external forces acting on its domain, whose linear density is $\mathbf{p}(s, t)$, and at the boundaries H , other forces $\mathbf{P}_H(t)$ are applied.

A virtual motion \mathbf{v} is superimposed to the current state to express the internal and external virtual powers, as:

$$P_{internal} := \int_S \mathbf{t} \cdot d\mathbf{s},$$

$$P_{external} := \int_S \mathbf{p} \cdot \mathbf{v} ds + \sum_{H=A}^B \mathbf{P}_H \cdot \mathbf{v}_H,$$

where \mathbf{t} is a forced-stress acting to the stretching velocity gradient $\mathbf{d} := (\mathbf{v}_l \cdot \mathbf{a}_t) \mathbf{a}_t$. Since \mathbf{d} is collinear to \mathbf{a}_t , we have

$$\mathbf{t} = T \mathbf{a}_t,$$

with T , the tension of the cable. Now, we have

$$\int_S \mathbf{p} \cdot \mathbf{v} ds + \sum_{H=A}^B \mathbf{P}_H \cdot \mathbf{v}_H = \int_S \mathbf{t} \cdot \mathbf{v}' ds \quad \forall \mathbf{v}.$$

Integrating by parts,

$$\int_S (\mathbf{t}' + \mathbf{p}) \cdot \mathbf{v} ds + \sum_{H=A}^B [(\mathbf{P}_H \pm \mathbf{t}_H) \cdot \mathbf{v}_H] = 0 \quad \forall \mathbf{v}.$$

From which, we get the local balance equation as follows:

$$\mathbf{t}' + \mathbf{p} = \mathbf{0}.$$

Through the d'Alembert principle, the inertial effects is taking into consideration and the above field equation modifies to,

$$\mathbf{t}' + \mathbf{p} = m \ddot{\mathbf{x}},$$

and the associated boundary conditions,

$$(\mathbf{P}_H \pm \mathbf{t}_H) \cdot \mathbf{v}_H = 0.$$

The incremental balance equations: Accounting the displacement vector, we have the balance equations (for details, one can see the book "Mathematical models of Beams and Cables" [54]):

$$\begin{aligned}\mathbf{t}' + \mathbf{p} &= m\ddot{\mathbf{u}}, \\ \mp \mathbf{t}_H &= \mathbf{P}_H,\end{aligned}\tag{3.12}$$

where, $\mathbf{t}(s, t)$ is stress and $\mathbf{p}(s, t)$ is the acting force on the current configuration. Subtracting equation (3.1) from equation (3.12), we can get the incremental balance equations with respect to reference configuration:

$$\begin{aligned}(\mathbf{t} - \mathbf{t}_0)' + \tilde{\mathbf{p}} &= m\ddot{\mathbf{u}}, \\ \mp (\mathbf{t} - \mathbf{t}_0)_H &= \tilde{\mathbf{P}}_H,\end{aligned}\tag{3.13}$$

where $\tilde{\mathbf{p}} := \mathbf{p} - \mathbf{p}_0$ and $\tilde{\mathbf{P}}_H := \mathbf{P}_H - \mathbf{P}_{0H}$ are incremental loads.

As we have $\mathbf{t} = T\mathbf{a}_t$ and $\mathbf{t}_0 = T_0\bar{\mathbf{a}}_t$, i.e., they are not parallel. From equation (3.3),

$$\begin{aligned}\mathbf{a}_t &= \mathbf{x}', \\ &= \mathbf{u}' + \bar{\mathbf{x}}', \\ &= \mathbf{u}' + \bar{\mathbf{a}}_t,\end{aligned}$$

and,

$$\mathbf{t} - \mathbf{t}_0 = T\mathbf{a}_t - T_0\bar{\mathbf{a}}_t = T(\mathbf{u}' + \bar{\mathbf{a}}_t) - T_0\bar{\mathbf{a}}_t.\tag{3.14}$$

Now from equation (3.13), we get

$$\begin{aligned}[T(\bar{\mathbf{a}}_t + \mathbf{u}') - T_0\bar{\mathbf{a}}_t]' + \tilde{\mathbf{p}} &= m\ddot{\mathbf{u}}, \\ \Rightarrow [(T - T_0)\bar{\mathbf{a}}_t + T\mathbf{u}']' + \tilde{\mathbf{p}} &= m\ddot{\mathbf{u}}.\end{aligned}$$

Which implies with the boundary conditions,

$$\begin{aligned}[\tilde{T}\bar{\mathbf{a}}_t + T\mathbf{u}']' + \tilde{\mathbf{p}} &= m\ddot{\mathbf{u}}, \\ \mp [\tilde{T}\bar{\mathbf{a}}_t + T\mathbf{u}']_H &= \tilde{\mathbf{P}}_H,\end{aligned}\tag{3.15}$$

where, $\tilde{T} = T - T_0$.

Projecting equation (3.15) onto external basis, we have

$$[\tilde{T}\bar{x}'_j + Tu'_j]' + \tilde{T}_j = m\ddot{u}_j, \quad j = 1, 2, 3\tag{3.16}$$

and, boundary conditions

$$\mp [\tilde{T}\bar{x}'_j + Tu'_j]_H = \tilde{P}_{jH}, \quad j = 1, 2, 3.\tag{3.17}$$

From equation (3.15), we have

$$\tilde{T}'\bar{\mathbf{a}}_t + \tilde{T}\bar{\mathbf{a}}'_t + T'\mathbf{u}' + T\mathbf{u}'' + \tilde{\mathbf{p}} = m\ddot{\mathbf{u}}.\tag{3.18}$$

We have, using equation (3.10), the second derivative of \mathbf{u} :

$$\begin{aligned} \mathbf{u}'' = & \left[(u'_t \bar{\kappa} u_n)' - \bar{\kappa} (u'_n + \bar{\kappa} u_t - \bar{\tau} u_b) \right] \bar{\mathbf{a}}_t + \left[(u'_n + \bar{\kappa} u_t - \bar{\tau} u_b)' + \bar{\kappa} (u'_t - \bar{\kappa} u_n) \right. \\ & \left. - \bar{\tau} (u'_b + \bar{\tau} u_n) \right] \bar{\mathbf{a}}_n + \left[(u'_b + \bar{\tau} u_n)' + \bar{\tau} (u'_n + \bar{\kappa} u_t - \bar{\tau} u_b) \right] \bar{\mathbf{a}}_b. \end{aligned} \quad (3.19)$$

Equation (3.18) becomes, with the help of equation (3.19):

$$\begin{aligned} & \tilde{T}' \bar{\mathbf{a}}_t + \tilde{T} \bar{\kappa} \bar{\mathbf{a}}_n + T' \left[(u'_t - \bar{\kappa} u_n) \bar{\mathbf{a}}_t + (u'_n + \bar{\kappa} u'_t - \bar{\tau} u_b) \bar{\mathbf{a}}_n + (u'_b + \bar{\tau} u_n) \bar{\mathbf{a}}_b \right] \\ & + T \left[(u'_t \bar{\kappa} u_n)' - \bar{\kappa} (u'_n + \bar{\kappa} u_t - \bar{\tau} u_b) \right] \bar{\mathbf{a}}_t \\ & + T \left[(u'_n + \bar{\kappa} u_t - \bar{\tau} u_b)' + \bar{\kappa} (u'_t - \bar{\kappa} u_n) - \bar{\tau} (u'_b + \bar{\tau} u_n) \right] \bar{\mathbf{a}}_n \\ & + T \left[(u'_b + \bar{\tau} u_n)' + \bar{\tau} (u'_n + \bar{\kappa} u_t - \bar{\tau} u_b) \right] \bar{\mathbf{a}}_b + \tilde{\mathbf{p}} = m \ddot{\mathbf{u}}. \end{aligned}$$

Rewriting

$$\begin{aligned} & \left[\tilde{T}' + T' (u'_t - \bar{\kappa} u_n) + T (u'_t - \bar{\kappa} u_n)' - \bar{\kappa} T (u'_n + \bar{\kappa} u_t - \bar{\tau} u_b) \right] \bar{\mathbf{a}}_t \\ & + \left[\bar{\kappa} \tilde{T} + T' (u'_n + \bar{\kappa} u_t - \bar{\tau} u_b) + T (u'_n + \bar{\kappa} u_t - \bar{\tau} u_b)' + \bar{\kappa} T (u'_t - \bar{\kappa} u_n) - \bar{\tau} T (u'_b + \bar{\tau} u_n) \right] \bar{\mathbf{a}}_n \\ & + \left[T' (u'_b + \bar{\tau} u_n) + T (u'_b + \bar{\tau} u_n)' + \bar{\tau} T (u'_n + \bar{\kappa} u_t - \bar{\tau} u_b) \right] \bar{\mathbf{a}}_b + \tilde{\mathbf{p}} = m \ddot{\mathbf{u}}. \end{aligned} \quad (3.20)$$

Projecting equation (3.20) onto the intrinsic reference basis, we obtain

$$\begin{aligned} & \tilde{T}' + \left[T (u'_t - \bar{\kappa} u_n) \right]' - \bar{\kappa} T (u'_n + \bar{\kappa} u_t - \bar{\tau} u_b) + \tilde{p}_t = m \ddot{u}_t, \\ & \bar{\kappa} \tilde{T} + \left[T (u'_n + \bar{\kappa} u_t - \bar{\tau} u_b) \right]' + \bar{\kappa} T (u'_t - \bar{\kappa} u_n) - \bar{\tau} T (u'_b + \bar{\tau} u_n) + \tilde{p}_n = m \ddot{u}_n, \\ & \left[T (u'_b + \bar{\tau} u_n) \right]' + \bar{\tau} T (u'_n + \bar{\kappa} u_t - \bar{\tau} u_b) + \tilde{p}_b = m \ddot{u}_b, \end{aligned} \quad (3.21)$$

and, the associate boundary conditions:

$$\begin{aligned} & \mp \left[\tilde{T} + T (u'_t - \bar{\kappa} u_n) \right]_H = \tilde{P}_t, \\ & \mp \left[T (u'_n + \bar{\kappa} u_t - \bar{\tau} u_b) \right]_H = \tilde{P}_n, \\ & \mp \left[T (u'_b + \bar{\tau} u_n) \right]_H = \tilde{P}_b. \end{aligned} \quad (3.22)$$

The elastic law: We consider the cable is made of hyperelastic materials. Let us consider a potential,

$$\phi = T_0 e + \frac{1}{2} EA e^2,$$

which is non-homogeneous and quadratic, where EA is the axial stiffness of the flexible cable. We have,

$$\frac{\partial \phi}{\partial e} = T_0 + EA e.$$

By Green law, $T = \frac{\partial \phi}{\partial e}$, so that

$$T = T_0 + EA e. \quad (3.23)$$

The fundamental problem: The following set of equations are important to construct the fundamental problem of the cable model:

- the strain-displacement relationship i.e., equation (3.6)
- the incremental balance equations i.e., equation (3.13a)
- the elastic law i.e., equation (3.23)
- the related geometric and mechanical boundary conditions i.e., equation (3.5) and equation (3.13b)

Now we have from equation (3.13),

$$\begin{aligned} (\mathbf{t} - \mathbf{t}_0)' + \tilde{\mathbf{p}} &= m\ddot{\mathbf{u}}, \\ \Rightarrow [T(\bar{\mathbf{x}}' + \mathbf{u}') - T_0\bar{\mathbf{x}}']' + \tilde{\mathbf{p}} &= m\ddot{\mathbf{u}}, \\ \Rightarrow [(T_0 + EAe)\bar{\mathbf{x}}' + (T_0 + EAe)\mathbf{u}' - T_0\bar{\mathbf{x}}']' + \tilde{\mathbf{p}} &= m\ddot{\mathbf{u}}. \end{aligned}$$

Therefore,

$$[EAe\bar{\mathbf{x}}' + (T_0 + EAe)\mathbf{u}']' + \tilde{\mathbf{p}} = m\ddot{\mathbf{u}}. \quad (3.24)$$

When the above equation is projected on the external basis, we have

$$[EAe\bar{x}'_j + (T_0 + EAe)u'_j]' + \tilde{p}_j = m\ddot{u}_j, \quad j = 1, 2, 3 \quad (3.25)$$

and, the related boundary conditions,

$$\mp [EAe\bar{x}'_j + (T_0 + EAe)u'_j]_H = \tilde{P}_{jH}, \quad j = 1, 2, 3. \quad (3.26)$$

Taking into account the intrinsic basis, we have from equation (3.24):

$$\begin{aligned} [EAe\bar{\mathbf{a}}_t + (T_0 + EAe)\mathbf{u}']' + \tilde{\mathbf{p}} &= m\ddot{\mathbf{u}}, \\ \Rightarrow (EAe)' \bar{\mathbf{a}}_t + EAe\bar{\mathbf{a}}'_t + (T_0 + EAe)\mathbf{u}' + (T_0 + EAe)\mathbf{u}'' + \tilde{\mathbf{p}} &= m\ddot{\mathbf{u}}, \\ \Rightarrow (EAe)' \bar{\mathbf{a}}_t + EAe\bar{\kappa}\bar{\mathbf{a}}_n + (T_0 + EAe)' [(u'_t - \bar{\kappa}u_n)\bar{\mathbf{a}}_t + (u'_n + \bar{\kappa}u_t - \bar{\tau}u_b)\bar{\mathbf{a}}_n + (u'_b + \bar{\tau}u_n)\bar{\mathbf{a}}_b] \\ &+ (T_0 + EAe) [(u'_t - \bar{\kappa}u_n)' - \bar{\kappa}(u'_n + \bar{\kappa}u_t - \bar{\tau}u_b)] \bar{\mathbf{a}}_t \\ &+ (T_0 + EAe) [(u'_n + \bar{\kappa}u_t - \bar{\tau}u_b)' + \bar{\kappa}(u'_t - \bar{\kappa}u_n) - \bar{\tau}(u'_b + \bar{\tau}u_n)] \bar{\mathbf{a}}_n \\ &+ (T_0 + EAe) [(u'_b + \bar{\tau}u_n)' + \bar{\tau}(u'_n + \bar{\kappa}u_t - \bar{\tau}u_b)] \bar{\mathbf{a}}_b + \tilde{\mathbf{p}} = m\ddot{\mathbf{u}}. \end{aligned}$$

After projecting on intrinsic basis, we have

$$\begin{aligned} (EAe)' + [(T_0 + EAe)(u'_t - \bar{\kappa}u_n)]' - \bar{\kappa}(T_0 + EAe)(u'_n + \bar{\kappa}u_t - \bar{\tau}u_b) + \tilde{p}_t &= m\ddot{u}_t, \\ (EAe)\bar{\kappa} + [(T_0 + EAe)(u'_n + \bar{\kappa}u_t - \bar{\tau}u_b)]' \\ &+ (T_0 + EAe) [\bar{\kappa}(u'_t - \bar{\kappa}u_n) - \bar{\tau}(u'_b + \bar{\tau}u_n)] + \tilde{p}_n = m\ddot{u}_n, \\ [(T_0 + EAe)(u'_b + \bar{\tau}u_n)]' + \bar{\tau}(T_0 + EAe)(u'_n + \bar{\kappa}u_t - \bar{\tau}u_b) + \tilde{p}_b &= m\ddot{u}_b, \end{aligned} \quad (3.27)$$

and, the boundary conditions:

$$\begin{aligned} \mp [EAe + (T_0 + EAe)(u'_t - \bar{\kappa}u_n)]_H &= \tilde{P}_t, \\ \mp [(T_0 + EAe)(u'_n + \bar{\kappa}u_t - \bar{\tau}u_b)]_H &= \tilde{P}_n, \\ \mp [(T_0 + EAe)(u'_b + \bar{\tau}u_n)]_H &= \tilde{P}_b. \end{aligned} \quad (3.28)$$

3.3.2 The Linearized Theory

After Linearizing,

from equation (3.6), we have the strain

$$e = \mathbf{u}' \cdot \bar{\mathbf{a}}_t, \quad (3.29)$$

and, the incremental balance equations (3.15) take the form

$$\begin{aligned} [\tilde{T}\bar{\mathbf{a}}_t + T_0\mathbf{u}']' + \tilde{\mathbf{p}} &= m\ddot{\mathbf{u}}, \\ [\tilde{T}\bar{\mathbf{a}}_t + T_0\mathbf{u}']_H &= \tilde{\mathbf{P}}_H. \end{aligned} \quad (3.30)$$

The constitutive law can be written as

$$\tilde{T} = EAe. \quad (3.31)$$

Now, we have from equation (3.30a),

$$\begin{aligned} & [EAe\bar{\mathbf{a}}_t + T_0\mathbf{u}']' + \tilde{\mathbf{p}} = m\ddot{\mathbf{u}}, \\ \Rightarrow & [EA(\mathbf{u}' \cdot \bar{\mathbf{a}}_t)\bar{\mathbf{a}}_t + T_0\mathbf{u}']' + \tilde{\mathbf{p}} = m\ddot{\mathbf{u}}, \\ \Rightarrow & [EA(\mathbf{u}' \cdot \bar{\mathbf{a}}_t)]'\bar{\mathbf{a}}_t + [EA(\mathbf{u}' \cdot \bar{\mathbf{a}}_t)]\bar{\mathbf{a}}_t' + [T_0\mathbf{u}']' + \tilde{\mathbf{p}} = m\ddot{\mathbf{u}}, \\ \Rightarrow & [EA((u_t' - \bar{\kappa}u_n)\bar{\mathbf{a}}_t + (u_n' + \bar{\kappa}u_t - \bar{\tau}u_b)\bar{\mathbf{a}}_n + (u_b' + \bar{\tau}u_n)\bar{\mathbf{a}}_b) \cdot \bar{\mathbf{a}}_t]'\bar{\mathbf{a}}_t \\ & + [EA((u_t' - \bar{\kappa}u_n)\bar{\mathbf{a}}_t + (u_n' + \bar{\kappa}u_t - \bar{\tau}u_b)\bar{\mathbf{a}}_n + (u_b' + \bar{\tau}u_n)\bar{\mathbf{a}}_b) \cdot \bar{\mathbf{a}}_t]\bar{\kappa}\bar{\mathbf{a}}_n \\ & + [T_0((u_t' - \bar{\kappa}u_n)\bar{\mathbf{a}}_t + (u_n' + \bar{\kappa}u_t - \bar{\tau}u_b)\bar{\mathbf{a}}_n + (u_b' + \bar{\tau}u_n)\bar{\mathbf{a}}_b)]' + \tilde{\mathbf{p}} = m\ddot{\mathbf{u}}, \\ \Rightarrow & [EA(u_t' - \bar{\kappa}u_n)]'\bar{\mathbf{a}}_t + [EA(u_t' - \bar{\kappa}u_n)]\bar{\kappa}\bar{\mathbf{a}}_n' + [T_0(u_t' - \bar{\kappa}u_n)]'\bar{\mathbf{a}}_t + [T_0(u_t' - \bar{\kappa}u_n)]\bar{\mathbf{a}}_t' \\ & + [T_0(u_n' + \bar{\kappa}u_t - \bar{\tau}u_b)]'\bar{\mathbf{a}}_n + [T_0(u_n' + \bar{\kappa}u_t - \bar{\tau}u_b)]\bar{\mathbf{a}}_n' + [T_0(u_b' + \bar{\tau}u_n)]'\bar{\mathbf{a}}_b \\ & + [T_0(u_b' + \bar{\tau}u_n)]\bar{\mathbf{a}}_b' + \tilde{\mathbf{p}} = m\ddot{\mathbf{u}}, \\ \Rightarrow & [EA(u_t' - \bar{\kappa}u_n)]'\bar{\mathbf{a}}_t + [EA(u_t' - \bar{\kappa}u_n)]\bar{\kappa}\bar{\mathbf{a}}_n' + [T_0(u_t' - \bar{\kappa}u_n)]'\bar{\mathbf{a}}_t + [T_0(u_t' - \bar{\kappa}u_n)]\bar{\kappa}\bar{\mathbf{a}}_n \\ & + [T_0(u_n' + \bar{\kappa}u_t - \bar{\tau}u_b)]'\bar{\mathbf{a}}_n + [T_0(u_n' + \bar{\kappa}u_t - \bar{\tau}u_b)](\bar{\tau}\bar{\mathbf{a}}_b - \bar{\kappa}\bar{\mathbf{a}}_t) + [T_0(u_b' + \bar{\tau}u_n)]'\bar{\mathbf{a}}_b \\ & + [T_0(u_b' + \bar{\tau}u_n)]\bar{\tau}\bar{\mathbf{a}}_n + \tilde{\mathbf{p}} = m\ddot{\mathbf{u}}. \end{aligned}$$

Projecting the above equation onto the intrinsic basis, we obtain

$$\begin{aligned} & [EA(u_t' - \bar{\kappa}u_n)]' + [T_0(u_t' - \bar{\kappa}u_n)]' - \bar{\kappa}T_0(u_n' + \bar{\kappa}u_t - \bar{\tau}u_b) + \tilde{p}_t = m\ddot{u}_t, \\ & EA\bar{\kappa}(u_t' - \bar{\kappa}u_n) + [T_0(u_n' + \bar{\kappa}u_t - \bar{\tau}u_b)]' + T_0[\bar{\kappa}(u_t' - \bar{\kappa}u_n) - \bar{\tau}(u_b' + \bar{\tau}u_b)] \\ & \quad + \tilde{p}_n = m\ddot{u}_n, \\ & [T_0(u_b' + \bar{\tau}u_n)]' + \bar{\tau}T_0(u_n' + \bar{\kappa}u_t - \bar{\tau}u_b) + \tilde{p}_b = m\ddot{u}_b, \end{aligned} \quad (3.32)$$

with the related boundary conditions,

$$\begin{aligned} \mp [EA(u_t' - \bar{\kappa}u_n) + T_0(u_t' - \bar{\kappa}u_n)]_H &= \tilde{P}_t, \\ \mp [T_0(u_n' + \bar{\kappa}u_t - \bar{\tau}u_b)]_H &= \tilde{P}_n, \\ [T_0(u_b' + \bar{\tau}u_n)]_H &= \tilde{P}_b. \end{aligned} \quad (3.33)$$

3.3.3 Shallow cables

We will now develop an approximated mathematical model for the shallow cables, one can get details from A. Luongo and D. Zulli [54], Irvine [42]. First, we will drive an approximated nonlinear model and then we will linearize it.

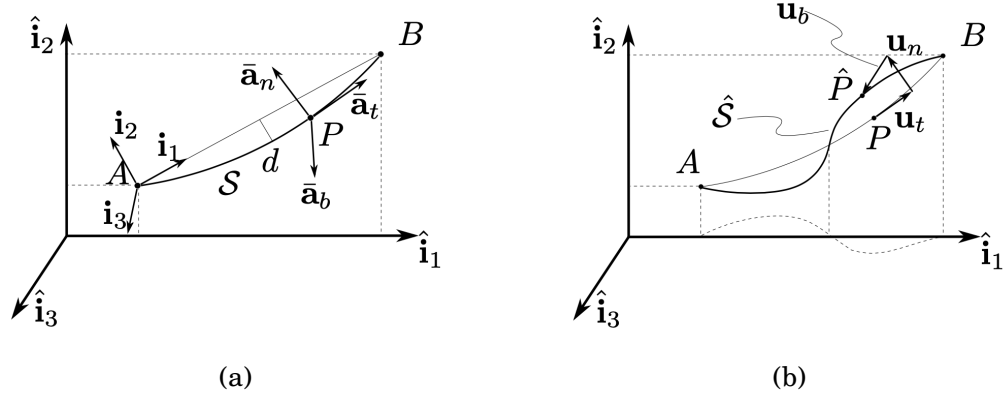


Figure 3.2: Shallow cable [54]: (a) reference configuration; centerline S in the $(\hat{\mathbf{i}}_1, \hat{\mathbf{i}}_2)$ -plane, sag d ; (b) current configuration, centerline \hat{S} and its horizontal projection, displacement components u_t, u_n, u_b .

Hypotheses: The cable hangs under its self-weight and no wind effects on it. As long it hangs under the effect of gravity, the cable lies in a certain plane and have a small sag-to-span ratio, mathematically $\delta := d/l$, of order $O(10^{-1})$ and we neglect torsional rigidity. The curvature $\bar{\kappa}$ and pretension T_0 is taken constant along the cable. The ratio T_0/EA is small as of order $O(10^{-3})$, or smaller, which describes that, the celerity of transverse wave of the cable, $c_t = \sqrt{\frac{T_0}{m}}$ is the much smaller comparing with the longitudinal one $c_l = \sqrt{\frac{EA}{m}}$. The displacements are varied on a scale length of cable length order, that is, $u'_\alpha = O(u_\alpha/l)$. The tangential displacement is considered to be smaller, as $u_t/l = O(\delta^2)$, whereas, the transverse displacements are considered the order of the order of sag, i.e., $u_n/l = O(\delta), u_b/l = O(\delta)$. And, the additive forces are transverse, that is, $\tilde{p}_t = 0$.

By the series expansion of the unit extension for a small displacement and taking $\bar{\tau} = 0$, we have from equation (3.11),

$$e = u'_t - \bar{\kappa}u_n + \frac{1}{2} \left[(u'_t - \bar{\kappa}u_n)^2 + (u'_n + \bar{\kappa}u_t)^2 + u_b'^2 \right] + H.O.T. \quad (3.34)$$

Accounting to Biot approximation, we can omit the linear squared term and we can neglect $\bar{\kappa}u_t$ comparing with u'_n , because of their ratio $O(\delta^2)$, and lastly neglecting the higher order terms,

$$e = u'_t - \bar{\kappa}u_n + \frac{1}{2} (u_n'^2 + u_b'^2). \quad (3.35)$$

The static condensation of the tangential displacement : From the 1st equation of (3.27), the leading term among the internal forces, $(EAe)' = O(EAu_t')$, and the other terms have δ^2 - times smaller. Also, the terms with a characteristic time $O(l/c_t)$, we have

$$m\ddot{u}_t = O\left(mu_t \frac{c_t^2}{l^2}\right) = O\left(\frac{T_0 u_t}{l^2}\right) \ll O\left(\frac{EAu_t}{l^2}\right) = (EAe)'. \quad (3.36)$$

So, the tangential inertia can be neglected, and the equation simplified as

$$(EAe)' = 0, \quad (3.37)$$

which implies that

$$e(s, t) = e_0(t), \quad (3.38)$$

which expresses that the unit extension is constant along the cable but changes with time.

Integrating equation (3.35),

$$\int_{s_A}^s e ds = \int_{s_A}^s u_t' ds - \bar{\kappa} \int_{s_A}^s u_n ds + \frac{1}{2} \int_{s_A}^s (u_n'^2 + u_b'^2) ds.$$

We get,

$$u_t = u_{tA}(t) + e_0(t)(s - s_A) + \bar{\kappa} \int_{s_A}^s u_n ds - \frac{1}{2} \int_{s_A}^s (u_n'^2 + u_b'^2) ds. \quad (3.39)$$

From the above equation, it is clear that the tangential displacement condensed statically. Equation (3.39) becomes with the two fixed ends, A and B,

$$\begin{aligned} u_{tB} &= u_{tA}(t) + e_0(t)(s_B - s_A) + \bar{\kappa} \int_{s_A}^{s_B} u_n ds - \frac{1}{2} \int_{s_A}^{s_B} (u_n'^2 + u_b'^2) ds, \\ \Rightarrow u_{tB} &= u_{tA}(t) + e_0(t)l + \bar{\kappa} \int_{s_A}^{s_B} u_n ds - \frac{1}{2} \int_{s_A}^{s_B} (u_n'^2 + u_b'^2) ds. \end{aligned}$$

Applying the geometric boundary conditions $u_{tA} = u_{tB} = 0$, we obtain

$$e_0(t) = -\frac{\bar{\kappa}}{l} \int_{s_A}^{s_B} u_n ds + \frac{1}{2l} \int_{s_A}^{s_B} (u_n'^2 + u_b'^2) ds. \quad (3.40)$$

The transverse motion: Now again, the balance equations taking $\bar{\tau} = 0$, we have the equations at the normal and binormal directions:

$$\begin{aligned} (EAe_0)\bar{\kappa} + [(T_0 + EAe_0)(u_n' + \bar{\kappa}u_t)'] + (T_0 + EAe_0)[\bar{\kappa}(u_t' - \bar{\kappa}u_n)] + \tilde{p}_n &= m\ddot{u}_n, \\ [(T_0 + EAe_0)u_b'] + \tilde{p}_b &= m\ddot{u}_b. \end{aligned}$$

We have $T_0 + EAe_0 = \text{const.}$, from the hypothesis and previous analysis. From the equation along the normal direction, we note that $\frac{\bar{\kappa}u_t}{u_n'} = O(\delta^2)$ as well as

$\frac{\bar{\kappa}(u'_t - \bar{\kappa}u_n)}{u''_n} = O(\delta^2)$, therefore, the smaller terms can be neglected. So that, amidst the error of $O(\delta^2)$, the transverse motion is governed by the following equations,

$$\begin{aligned} (T_0 + EAe_0)u''_n + EAe_0\bar{\kappa} + \tilde{p}_n &= m\ddot{u}_n, \\ (T_0 + EAe_0)u''_b + \tilde{p}_b &= m\ddot{u}_b, \\ e_0 &= -\frac{\bar{\kappa}}{l} \int_{s_A}^{s_B} u_n ds + \frac{1}{2l} \int_{s_A}^{s_B} (u_n'^2 + u_b'^2) ds. \end{aligned} \quad (3.41)$$

The first two equations are the integro-differential equations in the transverse displacements $u_n(s, t)$ and $u_b(s, t)$, with the geometric boundary conditions,

$$u_{nA} = u_{nB} = 0 \quad \text{and} \quad u_{bA} = u_{bB} = 0 \quad \forall t. \quad (3.42)$$

For the case of small amplitude around the pretension configuration of the shallow flexible cable, we study linearized theory. Ignoring the nonlinear terms, and taking the linear part of the unit extension, we can rewrite the equation (3.41):

$$\begin{aligned} T_0 u''_n + EAe_0 \bar{\kappa} + \tilde{p}_n &= m\ddot{u}_n, \\ T_0 u''_b + \tilde{p}_b &= m\ddot{u}_b, \\ e_0 &= -\frac{\bar{\kappa}}{l} \int_{s_A}^{s_B} u_n ds, \end{aligned} \quad (3.43)$$

with the boundary conditions:

$$u_{nA} = u_{nB} = 0 \quad \text{and} \quad u_{bA} = u_{bB} = 0 \quad \forall t. \quad (3.44)$$

A CONTINUUM APPROACH TO THE NONLINEAR IN-PLANE GALLOPING OF SHALLOW FLEXIBLE CABLES

4.1 Introduction

In this chapter, we have considered the model and associated investigations following the scientific research done in [21] by M. Ferretti, D. Zulli and A. Luongo. We have considered a continuum mechanical cable model to analyze its galloping phenomenon, caused by the interaction of wind and non-circular cross-section of ice-coated cable, resulting large amplitude of oscillations at small frequencies. The contribution of an internal damping related to viscous effects and the classical external damping caused by medium resistance is introduced. The internal damping is employed in the model taking proportional to the linear stiffness operator on the basis of the Rayleigh model of damping. The aerodynamic forces are modeled according to the quasi-steady theory of aerodynamic damping of the galloping mechanism. The critical conditions in the form of wind velocity and modal frequency of the first mode of galloping are obtained in the linear field when the cable is far from the cross-over point [42]. Next, we analyzed a nonlinear problem with the help of the multiple scale method (MSM), a perturbation analysis, to investigate the postcritical behavior of cable, the amplitude of vibration and the shape of the limit-cycle. Two finite dimensional models, namely, the finite difference method and the multimodal Galerkin method are used to integrate the equations numerically and to compare the obtained results.

4.2 Continuum Model

4.2.1 Governing Equations

Here an ice-coated, shallow horizontal cable is considered to study the galloping instability phenomenon. The cable is hanging under its self-weight from the same level, at points A and B in the $(\bar{\mathbf{a}}_x, \bar{\mathbf{a}}_y)$ - vertical plane, depicted in Figure 4.1, presenting equilibrium configuration \bar{C} . A local triad $(\bar{\mathbf{a}}_t, \bar{\mathbf{a}}_n, \bar{\mathbf{a}}_b)$, formed of tangential, normal and binormal unit vectors, is defined to express the equilibrium configuration. Then we assume a uniform wind $\mathbf{U} = U\bar{\mathbf{a}}_z$ is blowing, results a time-dependent configuration C (thick line in Figure 4.1) with a displacement $\mathbf{u} = u\bar{\mathbf{a}}_t + v\bar{\mathbf{a}}_n + w\bar{\mathbf{a}}_b$, consisting of tangential $u(s, t)$, normal $v(s, t)$, binormal $w(s, t)$ components, from the configuration \bar{C} .

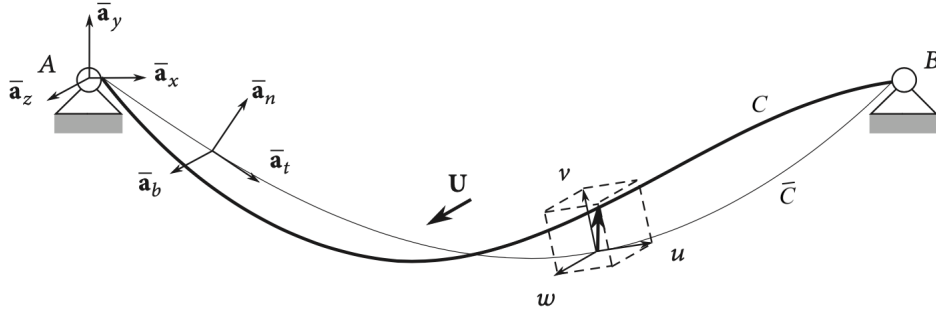


Figure 4.1: Shallow horizontal cable under normal wind flow. Thin line: in-plane equilibrium position under self-weight; thick line: current configuration under the action of both self-weight and wind.

The governing equations of motion of the cable, developed in the literature of [53] for the transverse motion $v(s, t), w(s, t)$, where the flexural and torsional stiffness are ignored, and the tangential displacement $u(s, t)$ is condensed under the dependable hypothesis, that states the speed of propagation of longitudinal waves is much larger comparing with the associated transversal waves [35, 42, 44, 71, 85, 91], also discussed in chapter 3. Taking in consideration of weakly affected galloping phenomenon, the out-of-plane displacement $w(s, t)$ is ignored in this model. The governing equations for the in-plane motion then take the form [21]:

$$\begin{aligned}
 (T_0 + EAe)v'' + EA\bar{\kappa}e - m\ddot{v} + f_n^d + f_n^a &= 0, \\
 e &= -\frac{\bar{\kappa}}{l} \int_0^l v ds + \frac{1}{2l} \int_0^l v'^2 ds, \\
 v_A &= 0, \\
 v_B &= 0,
 \end{aligned} \tag{4.1}$$

where, T_0 is prestress, constant on the abscissa $s \in [0, l]$; l is the length of the cable, chosen close (almost equal) to the chord; EA is the axial stiffness; m is the mass per unit length of cable (can be included of iced-coating); $\bar{\kappa} := \frac{mg}{T_0}$ is the uniform prestress curvature; $e(t)$ is the dynamic unitary extension, constant on s , using this, the dynamic tension is obtained as $\tilde{T} = EAe$; f_n^d and f_n^a are damping and aerodynamic forces, respectively, acting in normal direction per unit length of cable. Here the subscripts A and B is used to express the evaluation of the variable at the points A and B , i.e., at $s = 0$ and $s = l$, respectively; the prime denotes the space-differentiation and the dots are used for expressing the time-derivatives.

4.2.2 Damping Model

Damping restrains the vibratory motion, for example, mechanical oscillations by dissipating energy, and for such reasons, it is obligatory to take in consideration of damping to deal with a galloping problem. There are two types of damping, one is external damping, which is the result of the resistance of surrounding medium, and second is internal damping, caused by various dissipative occurrences in material of the structure. The linear external damping force is modeled by taking proportional to velocities, that is, $f_n^{d_{external}} = -c_e \dot{v}$, where $c_e > 0$ is an external damping coefficient. In accordance with the rheological Kelvin-Voigt model and Rayleigh model of damping (described in details by the authors of [21]), the internal damping force components become $f_n^{d_{internal}} = \zeta \left(\dot{v}'' + \frac{EA}{T_0} \bar{\kappa} \dot{e} \right)$, with ζ an internal damping coefficient.

Therefore, the total damping force takes the form,

$$f_n^d = -c_e \dot{v} + \zeta \left(\dot{v}'' + \frac{EA}{T_0} \bar{\kappa} \dot{e} \right). \quad (4.2)$$

The equations of motion (4.1) then read,

$$\begin{aligned} T_0 \left(1 + \frac{\zeta}{T_0} \partial_t \right) v'' + EA \bar{\kappa} \left(1 + \frac{\zeta}{T_0} \partial_t \right) e + EA e v'' - m \ddot{v} - c_e \dot{v} + f_n^a &= 0, \\ e &= -\frac{\bar{\kappa}}{l} \int_0^l v ds + \frac{1}{2l} \int_0^l v'^2 ds, \\ v_A &= 0, \\ v_B &= 0. \end{aligned} \quad (4.3)$$

To model the aerodynamic force f_n^a , the small curvature of the cable is neglected [16, 24, 114, 115], that is, a curved cable element is assumed to be subjected to the same aerodynamic forces acting on a long cylinder oriented as the local triad. We have,

$$f_z^a = \frac{1}{2} \rho U^2 b \left(A_0 - A_1 \left(\frac{\dot{z}}{U} \right) - A_2 \left(\frac{\dot{z}}{U} \right)^2 - A_3 \left(\frac{\dot{z}}{U} \right)^3 + \dots \right), \quad (4.4)$$

where ρ is the density of air, b is a characteristic cross-section length, and A_i are aerodynamic coefficients which depend on the iced cross-section's shape, assumed constant along the span in average. We have $A_0 = 0$, according to the hypothesis of static response to wind, is zero.

4.2.3 The Linear Problem

To obtain the critical galloping conditions, namely, the critical velocity U_c and modal frequency ω_c , we introduce the related linear problem of (4.3), which takes the form:

$$\begin{aligned} T_0 \left(1 + \frac{\zeta}{T_0} \partial_t \right) v'' + EA\bar{\kappa} \left(1 + \frac{\zeta}{T_0} \partial_t \right) e - m\ddot{v} - (c_e + U_c \hat{c}_{a1}) \dot{v} &= 0, \\ e &= -\frac{\bar{\kappa}}{l} \int_0^l v ds, \\ v_A &= 0, \\ v_B &= 0, \end{aligned} \tag{4.5}$$

where, the aerodynamic coefficient is defined as, $\hat{c}_{a1} := \frac{1}{2} \rho b A_1$.

4.2.4 The Space Eigenvalue Problem

Concerning the periodicity of motion at bifurcation point, we separate the variables in space and time by applying

$$\begin{aligned} v(s, t) &= \hat{v}(s) \exp(i\omega_c t), \\ e(t) &= \hat{e} \exp(i\omega_c t), \end{aligned} \tag{4.6}$$

where ω_c is the unknown modal frequency. Using equations (4.6), we have from the 1st equation of (4.5),

$$\begin{aligned} T_0 \left(1 + i\omega_c \frac{\zeta}{T_0} \right) \hat{v}'' \exp(i\omega_c t) + EA\bar{\kappa} \left(1 + i\omega_c \frac{\zeta}{T_0} \right) \hat{e} \exp(i\omega_c t) + m\omega_c^2 \hat{v} \exp(i\omega_c t) \\ - i\omega_c (c_e + U_c \hat{c}_{a1}) \hat{v} \exp(i\omega_c t) &= 0, \\ \Rightarrow T_0 \left(1 + i\omega_c \frac{\zeta}{T_0} \right) \left(\hat{v}'' + \frac{EA\bar{\kappa}}{T_0} \hat{e} + \frac{m\omega_c^2 - i\omega_c (c_e + U_c \hat{c}_{a1})}{T_0 \left(1 + i\omega_c \frac{\zeta}{T_0} \right)} \hat{v} \right) &= 0, \\ \Rightarrow \hat{v}'' + \frac{EA\bar{\kappa}}{T_0} \hat{e} + \beta^2 \hat{v} &= 0, \end{aligned}$$

and from the 2nd equation of (4.5),

$$\begin{aligned} \hat{e} \exp(i\omega_c t) + \frac{\bar{\kappa}}{l} \int_0^l \hat{v} \exp(i\omega_c t) ds &= 0, \\ \Rightarrow \hat{e} + \frac{\bar{\kappa}}{l} \int_0^l \hat{v} ds &= 0. \end{aligned}$$

Collecting both from the above calculation, we obtain an eigenvalue problem as follows,

$$\begin{aligned} \hat{v}'' + \frac{EA\bar{\kappa}}{T_0} \hat{e} + \beta^2 \hat{v} &= 0, \\ \hat{e} + \frac{\bar{\kappa}}{l} \int_0^l \hat{v} ds &= 0, \\ \hat{v}_A &= 0, \\ \hat{v}_B &= 0, \end{aligned} \tag{4.7}$$

where β is defined as,

$$\beta^2 := \frac{m\omega_c^2 - i\omega_c(c_e + U_c \hat{c}_{a1})}{T_0 \left(1 + i \left(\frac{\zeta}{T_0}\right) \omega_c\right)}. \tag{4.8}$$

The problem (4.7) is likely similar with that one in [42] for the linear natural vibrations of cable. Therefore, the solutions of equation (4.7) are the natural modes, we denote

$$(\hat{v}(s), \hat{e}) = (\hat{v}_j(s), \hat{e}_j), \quad j = 1, 2, \dots$$

the j th natural mode (symmetric or anti-symmetric), and the relevant wave number $\beta = \beta_j$ solves the obtained characteristic equation, which is for the antisymmetric case, $\sin\left(\frac{\beta l}{2}\right) = 0$, or for the symmetric case, the transcendental Irvine equation [42]:

$$\tan\left(\frac{\beta l}{2}\right) = -\left(\frac{\beta l}{2}\right)^3 \frac{4}{\lambda^2} + \left(\frac{\beta l}{2}\right) \tag{4.9}$$

with $\lambda = \sqrt{\frac{EA(\bar{\kappa}l)^2}{T_0}}$. We have, from equation (4.8),

$$\begin{aligned} \beta_j^2 T_0 \left(1 + i\omega_{cj} \frac{\zeta}{T_0}\right) &= m\omega_{cj}^2 - i\omega_{cj}(c_e + U_{cj} \hat{c}_{a1}), \\ \Rightarrow \beta_j^2 T_0 + i\omega_{cj} \zeta \beta_j^2 &= m\omega_{cj}^2 - i\omega_{cj}(c_e + U_{cj} \hat{c}_{a1}). \end{aligned}$$

Separating real and imaginary parts, we obtain

$$\begin{aligned} U_{cj} &= \frac{c_e + \zeta \beta_j^2}{|\hat{c}_{a1}|}, \quad \hat{c}_{a1} < 0 \\ \omega_{cj} &= \beta_j \sqrt{\frac{T_0}{m}}, \end{aligned} \tag{4.10}$$

where the suffix j indicates the j th root. Since we have $U_c := \min_j U_{cj} = U_{c1}$, in accordance with this model, the cable gallops in its first natural mode.

We can figure out the role of the internal damping ζ , appears in the equation (4.10). It divides the critical velocity into infinitely many parts, each of them is related to a different natural mode. If the cable is internally undamped, various natural modes can appear simultaneously. This is relatively an unrealistic case because of the reduction of damping ratio to $\frac{1}{\omega_j}$. For the case of discrete models, this type of situation is unclear and various damping ratios of the natural modes are obtained by experimental studies, instead of deriving it from a relevant model.

4.2.5 The Adjoint Eigenvalue Problem and the Solvability Condition

Concerning the nonlinear perturbation analysis, we require to construct an adjoint problem of (4.7) along with the solvability condition for the subsequent nonhomogeneous problem,

$$\begin{aligned} \hat{v}'' + \frac{EA\bar{\kappa}}{T_0}\hat{e} + \beta^2\hat{v} &= f(s), \\ \hat{e} + \frac{\bar{\kappa}}{l}\int_0^l \hat{v}ds &= v, \\ \hat{v}_A &= 0, \\ \hat{v}_B &= 0, \end{aligned} \tag{4.11}$$

where $f(s)$ and v are known. Now, we rewrite the equation (4.11) in the integrodifferential form, substituting \hat{e} in the first equation of it and by defining $\phi := \hat{v}(s)$ for the favor of notation,

$$\begin{aligned} \phi'' + \beta^2\phi - \frac{EA\bar{\kappa}^2}{T_0l}\int_0^l \phi ds &= f(s) - \frac{EA\bar{\kappa}}{T_0}v, \\ \phi_A &= 0, \\ \phi_B &= 0. \end{aligned} \tag{4.12}$$

We have the relevant ‘‘Extended Green Identity’’ :

$$\begin{aligned} \int_0^l \psi \left[\phi'' + \beta^2\phi - \frac{EA\bar{\kappa}^2}{T_0l}\int_0^l \phi(\tilde{s})d\tilde{s} \right] ds &= \int_0^l \phi \left[\psi'' - \frac{EA\bar{\kappa}^2}{T_0l}\int_0^l \psi(\tilde{s})d\tilde{s} + \beta^2\psi \right] ds \\ &\quad + [\phi'\psi + \phi\psi']_0^l. \end{aligned} \tag{4.13}$$

From which, we can see that the eigenvalue problem (4.7) is self-adjoint, when $\psi \equiv \phi$. Then, the solvability condition becomes,

$$\int_0^l \phi(s) \left(f(s) - \frac{EA\bar{\kappa}}{T_0} v \right) ds = 0. \quad (4.14)$$

4.3 The Nonlinear Problem

A nonlinear analysis is developed with the help of multiple scale method (MSM) to study the vibration characteristics of the cable in the nonlinear field and in the neighborhood to the dynamic bifurcation. We have the equation of motion in the nonlinear form,

$$\begin{aligned} T_0 \left(1 + \frac{\zeta}{T_0} \partial_t \right) v'' + EA\bar{\kappa} \left(1 + \frac{\zeta}{T_0} \partial_t \right) e - m\ddot{v} - (c_e + U\hat{c}_{a1})\dot{v} \\ + EAev'' - \hat{c}_{a2}\dot{v}^2 - \frac{\hat{c}_{a3}}{U}\dot{v}^3 = 0, \\ e = -\frac{\bar{\kappa}}{l} \int_0^l v ds + \frac{1}{2l} \int_0^l v'^2 ds, \\ v_A = 0, \\ v_B = 0, \end{aligned} \quad (4.15)$$

where the aerodynamic coefficients, $\hat{c}_{ak} := \frac{1}{2}\rho b A_k$, for $k = 1, 2, 3$.

4.3.1 Multiple Scale Analysis

An asymptotic multiple scale method [77, 78, 80] is employed to solve the equation (4.15). The dependent variables are expanded in a formal series via a small perturbation parameter ϵ , which will be reabsorbed at the end of the analysis, we have also introduced independent time scales (fast, slow, slowest). Expanding the dependent variables in series with respect to ϵ , we have

$$\begin{aligned} v &= \epsilon v_1 + \epsilon^2 v_2 + \epsilon^3 v_3, \\ e &= \epsilon e_1 + \epsilon^2 e_2 + \epsilon^3 e_3, \\ U &= U_c + \epsilon^2 U_2, \end{aligned} \quad (4.16)$$

where U_c denotes the critical velocity. The time scales and the related differentiation rules are introduced as follows:

$$\begin{aligned} t_0 &:= t, \\ t_2 &:= \epsilon^2 t, \\ \partial_t &= \partial_0 + \epsilon^2 \partial_2, \\ \partial_t^2 &= \partial_0^2 + 2\epsilon^2 \partial_0 \partial_2, \end{aligned} \quad (4.17)$$

with $\partial_j := \frac{\partial}{\partial t_j}$, $j = 0, 2$. Substituting equation (4.16) in 1st equation of (4.15), and using equation (4.17), we have

$$\begin{aligned}
& T_0 \left(1 + \frac{\zeta}{T_0} (\partial_0 + \epsilon^2 \partial_2) \right) (\epsilon v_1'' + \epsilon^2 v_2'' + \epsilon^3 v_3'') + EA \bar{\kappa} \left(1 + \frac{\zeta}{T_0} (\partial_0 + \epsilon^2 \partial_2) \right) (\epsilon e_1 + \epsilon^2 e_2 + \epsilon^3 e_3) \\
& - m (\partial_0^2 + 2\epsilon^2 \partial_0 \partial_2) (\epsilon v_1 + \epsilon^2 v_2 + \epsilon^3 v_3) - (c_e + U_c \hat{c}_{a1} + \epsilon^2 U_2 \hat{c}_{a1}) (\partial_0 + \epsilon^2 \partial_2) (\epsilon v_1 + \epsilon^2 v_2 + \epsilon^3 v_3) \\
& + EA (\epsilon e_1 + \epsilon^2 e_2 + \epsilon^3 e_3) (\epsilon v_1'' + \epsilon^2 v_2'' + \epsilon^3 v_3'') - \hat{c}_{a2} [(\partial_0 + \epsilon^2 \partial_2) (\epsilon v_1 + \epsilon^2 v_2 + \epsilon^3 v_3)]^2 \\
& - \frac{\hat{c}_{a3}}{(U_c + \epsilon^2 U_2)} [(\partial_0 + \epsilon^2 \partial_2) (\epsilon v_1 + \epsilon^2 v_2 + \epsilon^3 v_3)]^3 = 0, \\
\Rightarrow & \epsilon T_0 \left(1 + \frac{\zeta}{T_0} \partial_0 \right) v_1'' + \epsilon^2 T_0 \left(1 + \frac{\zeta}{T_0} \partial_0 \right) v_2'' + \epsilon^3 T_0 \left(1 + \frac{\zeta}{T_0} \partial_0 \right) v_3'' + \epsilon^3 \zeta \partial_2 v_1'' \\
& + \epsilon EA \bar{\kappa} \left(1 + \frac{\zeta}{T_0} \partial_0 \right) e_1 + \epsilon^2 EA \bar{\kappa} \left(1 + \frac{\zeta}{T_0} \partial_0 \right) e_2 + \epsilon^3 EA \bar{\kappa} \left(1 + \frac{\zeta}{T_0} \partial_0 \right) e_3 \\
& + \epsilon^3 \frac{EA \bar{\kappa}}{T_0} \zeta \partial_2 e_1 - \epsilon m \partial_0^2 v_1 - \epsilon^2 m \partial_0^2 v_2 - \epsilon^3 m \partial_0^2 v_3 - \epsilon^3 2m \partial_0 \partial_2 v_1 - \epsilon (c_e + U_c \hat{c}_{a1}) \partial_0 v_1 \\
& - \epsilon^2 (c_e + U_c \hat{c}_{a1}) \partial_0 v_2 - \epsilon^3 (c_e + U_c \hat{c}_{a1}) \partial_0 v_3 - \epsilon^3 (c_e + U_c \hat{c}_{a1}) \partial_2 v_1 - \epsilon^3 U_2 \hat{c}_{a1} \partial_0 v_1 \\
& + \epsilon^2 EA e_1 v_1'' + \epsilon^3 EA e_1 v_2'' + \epsilon^3 EA e_2 v_1'' - \epsilon^2 \hat{c}_{a2} (\partial_0 v_1)^2 - \epsilon^3 2\hat{c}_{a2} (\partial_0 v_1) (\partial_0 v_2) \\
& - \epsilon^3 \frac{\hat{c}_{a3}}{U_c} (\partial_0 v_1)^3 + O(\epsilon^4) = 0.
\end{aligned}$$

Collecting the coefficients of ϵ at the 1st, 2nd, and 3rd orders, we have

Order ϵ :

$$\begin{aligned}
& T_0 \left(1 + \frac{\zeta}{T_0} \partial_0 \right) v_1'' + EA \bar{\kappa} \left(1 + \frac{\zeta}{T_0} \partial_0 \right) e_1 - m \partial_0^2 v_1 - (c_e + U_c \hat{c}_{a1}) \partial_0 v_1 = 0, \\
& e_1 + \frac{\bar{\kappa}}{l} \int_0^l v_1 ds = 0, \\
& v_{1A} = 0, \\
& v_{1B} = 0.
\end{aligned} \tag{4.18}$$

Order ϵ^2 :

$$\begin{aligned}
& T_0 \left(1 + \frac{\zeta}{T_0} \partial_0 \right) v_2'' + EA \bar{\kappa} \left(1 + \frac{\zeta}{T_0} \partial_0 \right) e_2 - m \partial_0^2 v_2 - (c_e + U_c \hat{c}_{a1}) \partial_0 v_2 = \hat{c}_{a2} (\partial_0 v_1)^2 - EA v_1'' e_1, \\
& e_2 + \frac{\bar{\kappa}}{l} \int_0^l v_2 ds = \frac{1}{2l} \int_0^l v_1'^2 ds, \\
& v_{2A} = 0, \\
& v_{2B} = 0.
\end{aligned} \tag{4.19}$$

Order ϵ^3 :

$$\begin{aligned}
 T_0 \left(1 + \frac{\zeta}{T_0} \partial_0 \right) v_3'' + EA \bar{\kappa} \left(1 + \frac{\zeta}{T_0} \partial_0 \right) e_3 - m \partial_0^2 v_3 - (c_e + U_c \hat{c}_{a1}) \partial_0 v_3 &= 2m \partial_0 \partial_2 v_1 \\
 - \zeta \partial_2 v_1'' - \zeta \frac{EA}{T_0} \bar{\kappa} \partial_2 e_1 + (c_e + U_c \hat{c}_{a1}) \partial_2 v_1 + U_2 \hat{c}_{a1} \partial_0 v_1 + 2 \hat{c}_{a2} (\partial_0 v_1) (\partial_0 v_2) \\
 + \frac{\hat{c}_{a3}}{U_c} (\partial_0 v_1)^3 - EA (v_2'' e_1 + v_1'' e_2), \\
 e_3 + \frac{\bar{\kappa}}{l} \int_0^l v_3 ds &= \frac{1}{l} \int_0^l v_1' v_2' ds, \\
 v_{3A} &= 0, \\
 v_{3B} &= 0.
 \end{aligned} \tag{4.20}$$

When internal resonances are excluded from the natural modes, we assume the generating (monomodal) solution to the ϵ order problem as:

$$\begin{pmatrix} v_1 \\ e_1 \end{pmatrix} = A(t_2) \begin{pmatrix} \hat{v}_c(s) \\ \hat{e}_c \end{pmatrix} \exp(i\omega_c t_0) + c.c. \tag{4.21}$$

where $A(t_2)$ is a complex modulating function, $(\hat{v}_c(s), \hat{e}_c)$ is the first in-plane natural mode of vibration of the cable, ω_c is the critical modal frequency, and c.c. represents complex conjugate.

Using solution (4.21), we have from equation (4.19)

$$\begin{aligned}
 T_0 \left(1 + \frac{\zeta}{T_0} \partial_0 \right) v_2'' + EA \bar{\kappa} \left(1 + \frac{\zeta}{T_0} \partial_0 \right) e_2 - m \partial_0^2 v_2 - (c_e + U_c \hat{c}_{a1}) \partial_0 v_2 \\
 = \hat{c}_{a2} (i\omega_c A \hat{v}_c \exp(i\omega_c t_0) - i\omega_c \bar{A} \exp(-i\omega_c t_0))^2 \\
 - EA (A \hat{e}_c \exp(i\omega_c t_0) + \bar{A} \hat{e}_c \exp(-i\omega_c t_0)) (A \hat{v}_c'' \exp(i\omega_c t_0) + \bar{A} \hat{v}_c'' \exp(-i\omega_c t_0)), \\
 = A^2 (-\omega_c^2 \hat{c}_{a2} \hat{v}_c^2 - EA \hat{v}_c'' \hat{e}_c) \exp(2i\omega_c t_0) + A \bar{A} (\hat{c}_{a2} \omega_c^2 \hat{v}_c^2 - EA \hat{v}_c'' \hat{e}_c) + c.c.
 \end{aligned}$$

and,

$$\begin{aligned}
 e_2 + \frac{\bar{\kappa}}{l} \int_0^l v_2 ds &= \frac{1}{2l} v_1'^2 ds, \\
 &= A^2 \left(\frac{1}{2l} \int_0^l \hat{v}_c'^2 ds \right) \exp(2i\omega_c t_0) + A \bar{A} \left(\frac{1}{2l} \int_0^l \hat{v}_c'^2 ds \right) + c.c.
 \end{aligned}$$

From which, the ϵ^2 -order perturbation problem (4.19) takes the solution of the form,

$$\begin{aligned}
 v_2 &= A^2 \chi_{22}(s) \exp(2i\omega_c t_0) + A \bar{A} \chi_{20}(s) + c.c. \\
 e_2 &= A^2 \eta_{22} \exp(2i\omega_c t_0) + A \bar{A} \eta_{20} + c.c.
 \end{aligned} \tag{4.22}$$

where $\chi_{20}(s), \chi_{22}(s)$ are the second order modal shape corrections, and η_{20}, η_{22} are the second order dynamic unitary extension corrections, respectively.

The (complex) function $\chi_{22}(s)$ and constant η_{22} are the solution of the following boundary value problem,

$$\begin{aligned} T_0 \left(1 + 2i\omega_c \frac{\zeta}{T_0} \right) \chi_{22}'' + EA\bar{\kappa} \left(1 + 2i\omega_c \frac{\zeta}{T_0} \right) \eta_{22} + (4m\omega_c^2 - 2i\omega_c c_e - 2i\omega_c U_c \hat{c}_{a1}) \chi_{22} \\ = -\omega_c^2 \hat{c}_{a2} \hat{v}_c^2 - EA \hat{v}_c'' \hat{e}_c, \\ \eta_{22} + \frac{\bar{\kappa}}{l} \int_0^l \chi_{22} ds = \frac{1}{2l} \int_0^l \hat{v}_c'^2 ds, \\ \chi_{22A} = 0, \\ \chi_{22B} = 0, \end{aligned} \tag{4.23}$$

and the (real) function $\chi_{20}(s)$ and constant η_{20} are the solution of the following boundary value problem,

$$\begin{aligned} T_0 \chi_{20}'' + EA\bar{\kappa} \eta_{20} = -EA \hat{v}_c'' \hat{e}_c + \omega_c^2 \hat{c}_{a2} \hat{v}_c^2, \\ \eta_{20} + \frac{\bar{\kappa}}{l} \int_0^l \chi_{20} ds = \frac{1}{2l} \int_0^l \hat{v}_c'^2 ds, \\ \chi_{20A} = 0, \\ \chi_{20B} = 0. \end{aligned} \tag{4.24}$$

For approaching to the solution of ϵ^3 -order problem (4.20), we must be verified the solvability condition (4.14). Next, we substitute the 2nd equation of (4.20) in the 1st equation to get the integrodifferential equation, as follows:

$$\begin{aligned} T_0 \left(1 + \frac{\zeta}{T_0} \partial_0 \right) v_3'' - \frac{EA\bar{\kappa}^2}{l} \left(1 + \frac{\zeta}{T_0} \partial_0 \right) \int_0^l v_3 ds - m \partial_0^2 v_3 - (c_e + U_c \hat{c}_{a1}) \partial_0 v_3 \\ = \left(i \hat{c}_{a1} U_2 \omega_c A \hat{v}_c + \frac{3i \hat{c}_{a3}}{U_c} \omega_c^3 A^2 \bar{A} \hat{v}_c^3 + 4 \hat{c}_{a2} \omega_c^2 A^2 \bar{A} \hat{v}_c \chi_{22} - \frac{EA \hat{e}_c \bar{\kappa} \zeta}{T_0} A' \right. \\ \left. + (c_e + \hat{c}_{a1} U_c + 2im\omega_c) A' \hat{v}_c - \zeta A' \hat{v}_c'' - EA (2\eta_{20} + \eta_{22}) A^2 \bar{A} \hat{v}_c'' \right. \\ \left. - EA \hat{e}_c A^2 \bar{A} (2\chi_{20}'' + \chi_{22}'') - EA\bar{\kappa} \left(1 + i\omega_c \frac{\zeta}{T_0} \right) \frac{A^2 \bar{A}}{l} \int_0^l \hat{v}_c' (2\chi_{20}' + \chi_{22}') ds \right) \exp(i\omega_c t_0) \\ + NRT + c.c. \end{aligned} \tag{4.25}$$

where NRT stands for nonresonant terms. The solvability condition for equation (4.20) requires that the known term is orthogonal to $\hat{v}_c(s)$, i.e.,

$$\begin{aligned} \int_0^l \hat{v}_c \left(i \hat{c}_{a1} U_2 \omega_c A \hat{v}_c + \frac{3i \hat{c}_{a3}}{U_c} \omega_c^3 A^2 \bar{A} \hat{v}_c^3 + 4 \hat{c}_{a2} \omega_c^2 A^2 \bar{A} \hat{v}_c \chi_{22} - \frac{EA \hat{e}_c \bar{\kappa} \zeta}{T_0} A' \right. \\ \left. + (c_e + \hat{c}_{a1} U_c + 2im\omega_c) A' \hat{v}_c - \zeta A' \hat{v}_c'' - EA (2\eta_{20} + \eta_{22}) A^2 \bar{A} \hat{v}_c'' \right. \\ \left. - EA \hat{e}_c A^2 \bar{A} (2\chi_{20}'' + \chi_{22}'') - EA\bar{\kappa} \left(1 + i\omega_c \frac{\zeta}{T_0} \right) \frac{A^2 \bar{A}}{l} \int_0^l \hat{v}_c' (2\chi_{20}' + \chi_{22}') ds \right) ds = 0. \end{aligned} \tag{4.26}$$

Now, we lead the calculation to go back to the true time, which gives the following ordinary differential equation (bifurcation equation) for amplitude, as follows:

$$\dot{A} = -U_2 c_1 A + (c_{3R} + i c_{3I}) A^2 \bar{A}, \quad (4.27)$$

and this is the (well-known) normal form of Hopf bifurcation [32], where,

$$\begin{aligned} c_1 &= \frac{\hat{c}_{a1}}{2m}, \\ c_{3R} &= -\frac{1}{2m\omega_c \int_0^l \hat{v}_c^2 ds} \left[\frac{3\hat{c}_{a3}\omega_c^3}{U_c} \int_0^l \hat{v}_c^4 ds + 4\hat{c}_{a2}\omega_c^2 \int_0^l \hat{v}_c^2 \chi_{22I} ds - \frac{EA\bar{\kappa}}{l} \int_0^l \hat{v}_c ds \right. \\ &\quad \cdot \left(\frac{\zeta\omega_c}{T_0} \int_0^l \hat{v}_c' (2\chi'_{20} + \chi'_{22R}) ds + \int_0^l \hat{v}_c' \chi'_{22I} ds \right) - EA\eta_{22I} \int_0^l \hat{v}_c \hat{v}_c'' ds \\ &\quad \left. - EA\hat{e}_c \int_0^l \hat{v}_c \chi''_{22I} ds \right], \\ c_{3I} &= \frac{1}{2m\omega_c \int_0^l \hat{v}_c^2 ds} \left[4\hat{c}_{a2}\omega_c^2 \int_0^l \hat{v}_c^2 \chi_{22R} ds - \frac{EA\bar{\kappa}}{l} \int_0^l \hat{v}_c ds \left(\frac{\zeta\omega_c}{T_0} \int_0^l \hat{v}_c' \chi'_{22I} ds \right. \right. \\ &\quad \left. \left. - \int_0^l \hat{v}_c' (\chi'_{22R} + 2\chi'_{20}) ds \right) - EA(\eta_{22R} + 2\eta_{20}) \int_0^l \hat{v}_c \hat{v}_c'' ds \right. \\ &\quad \left. - EA\hat{e}_c \int_0^l \hat{v}_c (\chi''_{22R} + 2\chi''_{20}) ds \right], \end{aligned}$$

and $\chi_{22}(s) = \chi_{22R}(s) + i\chi_{22I}(s)$, $\eta_{22} = \eta_{22R} + i\eta_{22I}$.

Let us consider, $A(t) = \frac{1}{2}a(t)\exp(i\varphi(t))$, and substitute in equation (4.27), we have

$$\frac{1}{2}\dot{a}(t)e^{i\varphi(t)} + i\frac{1}{2}a(t)\dot{\varphi}(t)e^{i\varphi(t)} = -\frac{1}{2}U_2 c_1 a(t)e^{i\varphi(t)} + \frac{1}{8}(c_{3R} + i c_{3I})a^3(t)e^{i\varphi(t)}.$$

Separating real and imaginary parts, the bifurcation equation in real form is derived, as follows:

$$\begin{aligned} \dot{a} &= -u_2 c_1 a + \frac{c_{3R}}{4} a^3, \\ a\dot{\varphi} &= \frac{c_{3I}}{4} a^3. \end{aligned} \quad (4.28)$$

Solving the above equation (4.28), we get the equilibrium solutions $a_0 = 0$, a trivial solution, and other two as $a_{1,2} = \pm 2\sqrt{\frac{c_1}{c_{3R}}}$, limit-cycle amplitudes. With an eigenvalue analysis, it shows that when $U_2 < 0$, a_0 is stable and unstable when $U_2 > 0$. The bifurcation curves $a_{1,2}$, rising from $U_2 = 0$ and becomes stable for the values $U_2 > 0$, results, the Hopf bifurcation is supercritical.

Then we get the solution as the motion on the limit-cycle of the cable,

$$\begin{aligned} v(s, t) &= a(t)\hat{v}_c(s)\cos(\omega_c t + \varphi(s)) + \frac{1}{2}a(t)^2 \\ &\quad \cdot [\chi_{20}(s) + \chi_{22R}\cos(2(\omega_c t + \varphi(t))) - \chi_{22I}(s)\sin(2(\omega_c t + \varphi(t)))] , \\ e(t) &= a(t)\hat{e}_c\cos(\omega_c t + \varphi(t)) + \frac{1}{2}a(t)^2 \\ &\quad \cdot [\eta_{20} + \eta_{22R}\cos(2(\omega_c t + \varphi(t))) - \eta_{22I}\sin(2(\omega_c t + \varphi(t)))] . \end{aligned} \quad (4.29)$$

The χ 's functions express the complex behavior of the nonlinear normal mode of vibration, that is, the deformed shape of the mode of cable changes while completing a period.

4.4 Finite-Dimensional Models

To analyze the galloping mechanism and compare the results for numerical studies, two finite-dimensional numerical models: (1) the finite difference method and (2) the Galerkin method, are developed.

4.4.1 Finite Difference Method

We divide the space interval $[0, l]$ into $N_s > 2$ sub-intervals with equal spaced having amplitude $\Delta = \frac{l}{N_s}$. Let us define,

$$\begin{aligned} s_j &:= j\Delta, & j &= 0, 1, 2, \dots, N_s, \\ v_j &:= v(s_j, t), & j &= 0, 1, 2, \dots, N_s, \\ v'_j &:= v'(s_j, t), & j &= 0, 1, 2, \dots, N_s. \end{aligned} \quad (4.30)$$

and, the following second ordered central finite difference rules,

$$\begin{aligned} v' &= \frac{v_{j+1} - v_{j-1}}{2\Delta}, \\ v'' &= \frac{v_{j+1} - 2v_j + v_{j-1}}{\Delta^2}. \end{aligned} \quad (4.31)$$

Also, the integral is evaluated using the Trapezoidal rule

$$\int_0^l v ds = \Delta \left(\sum_{j=1}^{N_s-1} v_j + \frac{v_0 + v_{N_s}}{2} \right). \quad (4.32)$$

By using equations (4.30), (4.31) and (4.32), the equations in (4.15) read,

$$\begin{aligned} m\ddot{v}_j + (c_e + U\hat{c}_{a1})\dot{v}_j - \zeta \frac{\dot{v}_{j+1} - 2\dot{v}_j + \dot{v}_{j-1}}{\Delta^2} + \hat{c}_{a2}\dot{v}_j^2 + \frac{\hat{c}_{a3}}{U}\dot{v}_j^3 \\ = (T_0 + EAe) \frac{v_{j+1} - 2v_j + v_{j-1}}{\Delta^2} + EA\bar{\kappa} \left(e + \frac{\zeta}{T_0}\dot{e} \right), \quad j = 1, 2, \dots, N_s - 1, \end{aligned} \quad (4.33)$$

where,

$$\begin{aligned} e &= -\frac{\Delta\bar{\kappa}}{l} \sum_{k=1}^{N_s-1} v_k + \frac{1}{4l\Delta} \left[v_1^2 + v_{N_s-1}^2 + \frac{1}{2} \sum_{k=1}^{N_s-1} (v_{k+1} - v_{k-1})^2 \right], \\ \dot{e} &= -\frac{\Delta\bar{\kappa}}{l} \sum_{k=1}^{N_s-1} \dot{v}_k + \frac{1}{2l\Delta} \left(v_1\dot{v}_1 + v_{N_s-1}\dot{v}_{N_s-1} + \frac{1}{2} \sum_{k=1}^{N_s-1} [(v_{k+1} - v_{k-1})(\dot{v}_{k+1} - \dot{v}_{k-1})] \right), \\ v_0 &= v_{N_s} = 0. \end{aligned} \quad (4.34)$$

In the calculation of e and \dot{e} , the space derivatives at $s = 0, l$ of the displacements, are followed the forward and backward finite differences, are as follows:

$$\begin{aligned} v'_0 &= \frac{v_1}{\Delta}, \\ v'_{N_s} &= -\frac{v_{N_s-1}}{\Delta}. \end{aligned} \quad (4.35)$$

The equations (4.33) are a set of $N_s - 1$ ordinary differential equations of the unknown nodal displacements $v_j(t)$ with $j = 1, 2, \dots, N_s - 1$. They are solved by using mathematica programming.

4.4.2 Galerkin Method

The displacement field $v(s, t)$ is defined as the truncated series, as follows:

$$v(s, t) = \sum_{j=1}^{N_s} \phi_j(s) q_j(t), \quad (4.36)$$

where, q_j are the generalized coordinates, and ϕ_j are the trial functions, defined as

$$\phi_j(s) = \sqrt{\frac{2}{ml}} \sin\left(\frac{j\pi}{l}s\right), \quad (4.37)$$

which satisfy

$$\begin{aligned} \int_0^l \phi_i \phi_j ds &= \frac{1}{m} \delta_{ij}, \\ \int_0^l \phi'_i \phi'_j ds &= \frac{1}{m} \left(\frac{j\pi}{l}\right)^2 \delta_{ij}, \end{aligned} \quad (4.38)$$

in which δ_{ij} is the Kronecker delta.

Substituting equation (4.36) into the first equation of (4.15) and using equations (4.37) and (4.38), we have the residual,

$$\begin{aligned} R &= T_0 \sum_{j=1}^{N_e} \phi_j'' q_j + \zeta \sum_{j=1}^{N_e} \phi_j' \dot{q}_j + EA\bar{\kappa} \left(1 + \frac{\zeta}{T_0} \partial_t\right) e - m \sum_{j=1}^{N_e} \phi_j \ddot{q}_j - (c_e + U \hat{c}_{a1}) \sum_{j=1}^{N_e} \phi_j \dot{q}_j \\ &\quad + EAe \sum_{j=1}^{N_e} \phi_j'' q_j - \hat{c}_{a2} \sum_{j=1}^{N_e} \sum_{h=1}^{N_e} \phi_j \phi_h \dot{q}_j \dot{q}_h - \frac{\hat{c}_{a3}}{U} \sum_{j=1}^{N_e} \sum_{h=1}^{N_e} \sum_{k=1}^{N_e} \phi_j \phi_h \phi_k \dot{q}_j \dot{q}_h \dot{q}_k, \\ &= -T_0 \frac{\pi^2}{l^2} \sum_{j=1}^{N_e} j^2 \phi_j q_j - \zeta \frac{\pi^2}{l^2} \sum_{j=1}^{N_e} j^2 \phi_j \dot{q}_j + EA\bar{\kappa} \left(1 + \frac{\zeta}{T_0} \partial_t\right) e - m \sum_{j=1}^{N_e} \phi_j \ddot{q}_j \\ &\quad - (c_e + U \hat{c}_{a1}) \sum_{j=1}^{N_e} \phi_j \dot{q}_j - EAe \frac{\pi^2}{l^2} \sum_{j=1}^{N_e} j^2 \phi_j q_j - \hat{c}_{a2} \sum_{j=1}^{N_e} \sum_{h=1}^{N_e} \phi_j \phi_h \dot{q}_j \dot{q}_h \\ &\quad - \frac{\hat{c}_{a3}}{U} \sum_{j=1}^{N_e} \sum_{h=1}^{N_e} \sum_{k=1}^{N_e} \phi_j \phi_h \phi_k \dot{q}_j \dot{q}_h \dot{q}_k. \end{aligned}$$

We force the following integral to vanish over the solution domain by using the weighted residual approach, that is,

$$\begin{aligned}
& \int_0^l \phi_i R ds = 0, \\
\Rightarrow & -\frac{T_0 \pi^2}{l^2} \sum_{j=1}^{N_e} j^2 q_j \int_0^l \phi_i \phi_j ds - \frac{\zeta \pi^2}{l^2} \sum_{j=1}^{N_e} j^2 \dot{q}_j \int_0^l \phi_i \phi_j ds + EA \bar{\kappa} \left(1 + \frac{\zeta}{T_0} \partial_t\right) \int_0^l \phi_i ds \\
& - m \sum_{j=1}^{N_e} \ddot{q}_j \int_0^l \phi_i \phi_j ds - (c_e + U \hat{c}_{a1}) \sum_{j=1}^{N_e} \dot{q}_j \int_0^l \phi_i \phi_j ds - EA e \frac{\pi^2}{l^2} \sum_{j=1}^{N_e} j^2 q_j \int_0^l \phi_i \phi_j ds \\
& - \hat{c}_{a2} \sum_{j=1}^{N_e} \sum_{h=1}^{N_e} \dot{q}_j \dot{q}_h \int_0^l \phi_i \phi_j \phi_h ds - \frac{\hat{c}_{a3}}{U} \sum_{j=1}^{N_e} \sum_{h=1}^{N_e} \sum_{k=1}^{N_e} \dot{q}_j \dot{q}_h \dot{q}_k \int_0^l \phi_i \phi_j \phi_h \phi_k ds = 0, \\
\Rightarrow & -\frac{T_0 \pi^2}{l^2} \sum_{j=1}^{N_e} j^2 q_j \frac{1}{m} \delta_{ij} - \frac{\zeta \pi^2}{l^2} \sum_{j=1}^{N_e} j^2 \dot{q}_j \frac{1}{m} \delta_{ij} + EA \bar{\kappa} \left(e + \frac{\zeta}{T_0} \dot{e}\right) \frac{l}{i\pi} \sqrt{\frac{2}{ml}} \left(1 + (-1)^{i+1}\right) \\
& - m \sum_{j=1}^{N_e} \ddot{q}_j \frac{1}{m} \delta_{ij} - (c_e + U \hat{c}_{a1}) \sum_{j=1}^{N_e} \dot{q}_j \frac{1}{m} \delta_{ij} - EA e \frac{\pi^2}{l^2} \sum_{j=1}^{N_e} j^2 q_j \frac{1}{m} \delta_{ij} \\
& - \frac{2}{ml} \sqrt{\frac{2}{ml}} \hat{c}_{a2} \sum_{j=1}^{N_e} \sum_{h=1}^{N_e} \dot{q}_j \dot{q}_h \int_0^l \sin\left(\frac{i\pi}{l}s\right) \sin\left(\frac{j\pi}{l}s\right) \sin\left(\frac{h\pi}{l}s\right) ds \\
& - \frac{4}{m^2 l^2} \frac{\hat{c}_{a3}}{U} \sum_{j=1}^{N_e} \sum_{h=1}^{N_e} \sum_{k=1}^{N_e} \dot{q}_j \dot{q}_h \dot{q}_k \int_0^l \sin\left(\frac{i\pi}{l}s\right) \sin\left(\frac{j\pi}{l}s\right) \sin\left(\frac{h\pi}{l}s\right) \sin\left(\frac{k\pi}{l}s\right) ds = 0, \\
\Rightarrow & -\frac{T_0 \pi^2}{l^2} \sum_{j=1}^{N_e} j^2 q_j \frac{1}{m} \delta_{ij} - \frac{\zeta \pi^2}{l^2} \sum_{j=1}^{N_e} j^2 \dot{q}_j \frac{1}{m} \delta_{ij} + EA \bar{\kappa} \left(e + \frac{\zeta}{T_0} \dot{e}\right) \frac{l}{i\pi} \sqrt{\frac{2}{ml}} \left(1 + (-1)^{i+1}\right) \\
& - m \sum_{j=1}^{N_e} \ddot{q}_j \frac{1}{m} \delta_{ij} - (c_e + U \hat{c}_{a1}) \sum_{j=1}^{N_e} \dot{q}_j \frac{1}{m} \delta_{ij} - EA e \frac{\pi^2}{l^2} \sum_{j=1}^{N_e} j^2 q_j \frac{1}{m} \delta_{ij} \\
& - \frac{1}{2m\pi} \sqrt{\frac{2}{ml}} \hat{c}_{a2} \sum_{j=1}^{N_e} \sum_{h=1}^{N_e} \dot{q}_j \dot{q}_h \left(\frac{(-\cos(h+i-j)\pi + 1)}{(h+i-j)} + \frac{(-\cos(h-i+j)\pi + 1)}{(h-i+j)} \right) \\
& + \frac{(\cos(h+i+j)\pi - 1)}{(h+i+j)} + \frac{(\cos(h-i-j)\pi - 1)}{(h-i-j)} \Big) \\
& - \frac{1}{m^2 l} \frac{\hat{c}_{a3}}{U} \sum_{j=1}^{N_e} \sum_{h=1}^{N_e} \sum_{k=1}^{N_e} \dot{q}_j \dot{q}_h \dot{q}_k \left[\frac{\sin(i-j+h-k)\pi}{(i-j+h-k)\pi} + \frac{\sin(i-j-h+k)\pi}{(i-j-h+k)\pi} \right. \\
& - \frac{\sin(i+j+h-k)\pi}{(i+j+h-k)\pi} - \frac{\sin(i+j-h+k)\pi}{(i+j-h+k)\pi} - \frac{\sin(i-j+h+k)\pi}{(i-j+h+k)\pi} - \frac{\sin(i-j-h-k)\pi}{(i-j-h-k)\pi} \\
& \left. + \frac{\sin(i+j+h+k)\pi}{(i+j+h+k)\pi} + \frac{\sin(i+j-h-k)\pi}{(i+j-h-k)\pi} \right] = 0.
\end{aligned}$$

Using the definition of Kronecker delta, and performing some simple calculations,

we get the following set of equations:

$$\begin{aligned}
 \ddot{q}_i + \frac{1}{m} \left[\zeta \left(\frac{i\pi}{l} \right)^2 + c_e + U \hat{c}_{a1} \right] \dot{q}_i + \frac{(T_0 + EAe)}{m} \left(\frac{i\pi}{l} \right)^2 q_i \\
 - \left(\frac{1 + (-1)^{i+1}}{i} \right) \frac{1}{\pi} \sqrt{\frac{2}{ml}} EA \bar{\kappa} \left(e + \frac{\zeta}{T_0} \dot{e} \right) + \hat{c}_{a2} \sum_{j=1}^{N_e} \sum_{h=1}^{N_e} (\Gamma_{ijh} \dot{q}_j \dot{q}_h) \\
 + \frac{\hat{c}_{a3}}{U} \sum_{j=1}^{N_e} \sum_{h=1}^{N_e} \sum_{k=1}^{N_e} (\Gamma_{ijhk} \dot{q}_j \dot{q}_h \dot{q}_k) = 0, \quad i = 1, 2, \dots, N_e
 \end{aligned} \tag{4.39}$$

where,

$$\begin{aligned}
 e &= -\frac{\bar{\kappa}}{\pi} \sqrt{\frac{2}{ml}} \sum_{h=1}^{N_e} \left(\frac{1 + (-1)^{h+1}}{h} q_h \right) + \frac{\pi^2}{2ml^3} \sum_{h=1}^{N_e} (h^2 q_h^2), \\
 \dot{e} &= -\frac{\bar{\kappa}}{\pi} \sqrt{\frac{2}{ml}} \sum_{h=1}^{N_e} \left(\frac{1 + (-1)^{h+1}}{h} \dot{q}_h \right) + \frac{\pi^2}{ml^3} \sum_{h=1}^{N_e} (h^2 q_h \dot{q}_h), \\
 \Gamma_{ijh} &= \begin{cases} 0 & i = j + h, \\ & \text{or } j = i + h, \\ & \text{or } h = i + j \\ \frac{4}{\pi} \sqrt{\frac{2}{m^3 l}} \frac{[(-1)^{i+j+h} - 1] ijh}{(i+j+h)(i-j+h)(i+j-h)(i-j-h)} & \text{otherwise} \end{cases}
 \end{aligned} \tag{4.40}$$

$$\Gamma_{ijhk} = \begin{cases} \frac{3}{2m^2 l} & i = j = h = k \\ -\frac{1}{2m^2 l} & i = j + h + k, \text{ or } j = i + h + k, \text{ or } h = i + j + k, \\ & \text{or } k = i + j + h \\ \frac{1}{2m^2 l} & i + j = h + k, j \neq h, j \neq k \\ & \text{or } i + h = j + k, h \neq j, h \neq k \\ & \text{or } j + h = i + k, h \neq i, h \neq k \\ \frac{1}{m^2 l} & i = j, h = k, \text{ or } i = h, j = k, \text{ or } i = k, j = h \\ 0 & \text{otherwise} \end{cases}$$

The equations (4.39) are a set of N_e ordinary differential equations for the generalized coordinates $q_j(t)$, $j = 1, 2, \dots, N_e$.

4.5 Numerical Results

We have considered a sample of cable having the geometrical and mechanical properties as follows: the mass per unit length (of iced-cable), $m = 1.80$ kg/m; length, $l = 267$ m; axial stiffness, $EA = 2.97 \times 10^7$ N. The mass density of the cable is $\rho = 1.25$ kg/m³ and the mean diameter is $b = 0.0281$ m. The damping coefficients are as: external damping coefficient, $\zeta = 48.939$ kgm/s and the internal damping coefficient, $c_e = 0.022$ kg/(ms). Here, we consider two different case studies on the basis of initial sag, $d \simeq \frac{mgl^2}{8T_0}$; one is, when the initial sag $d = 5$ m, results $\lambda = 4.602 < 2\pi$, i.e., the cable is under the first cross-over point; and second initial sag $d = 7$ m, with $\lambda = 7.624 > 2\pi$, i.e., the cable is above of the first cross-over point. We have considered the aerodynamic parameters from the references [114, 115], concerning with an U-shaped conductor with a symmetric portion, which have the maximum ice eccentricity against the mean wind flow. The standardized drag and lift coefficients are as follows:

$$\begin{aligned} c_d(\alpha) &= 1.08334 + 0.735935\alpha^2 \\ c_l(\alpha) &= -1.5979\alpha + 4.77362\alpha^3 \end{aligned} \quad (4.41)$$

where α is the angle of attack, at which the relative wind flow meets the cross-sectional plane of the cable. The angle is formed in between the unit vector \mathbf{a}_b and wind axis \mathbf{a}_z . The values of α is taken valid in the range $-0.6 < \alpha < 0.6$ radian.

In Figure 4.2, the initial approximation of first linear modal in-plane displacement is presented.

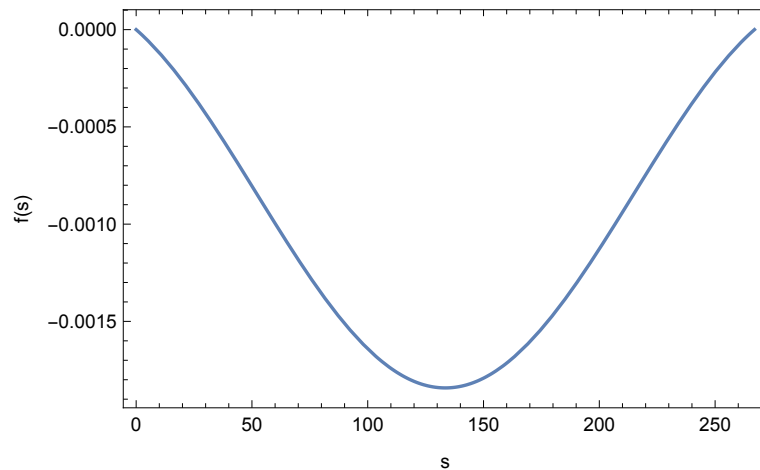


Figure 4.2: Case study 1: Approximated initial first linear mode

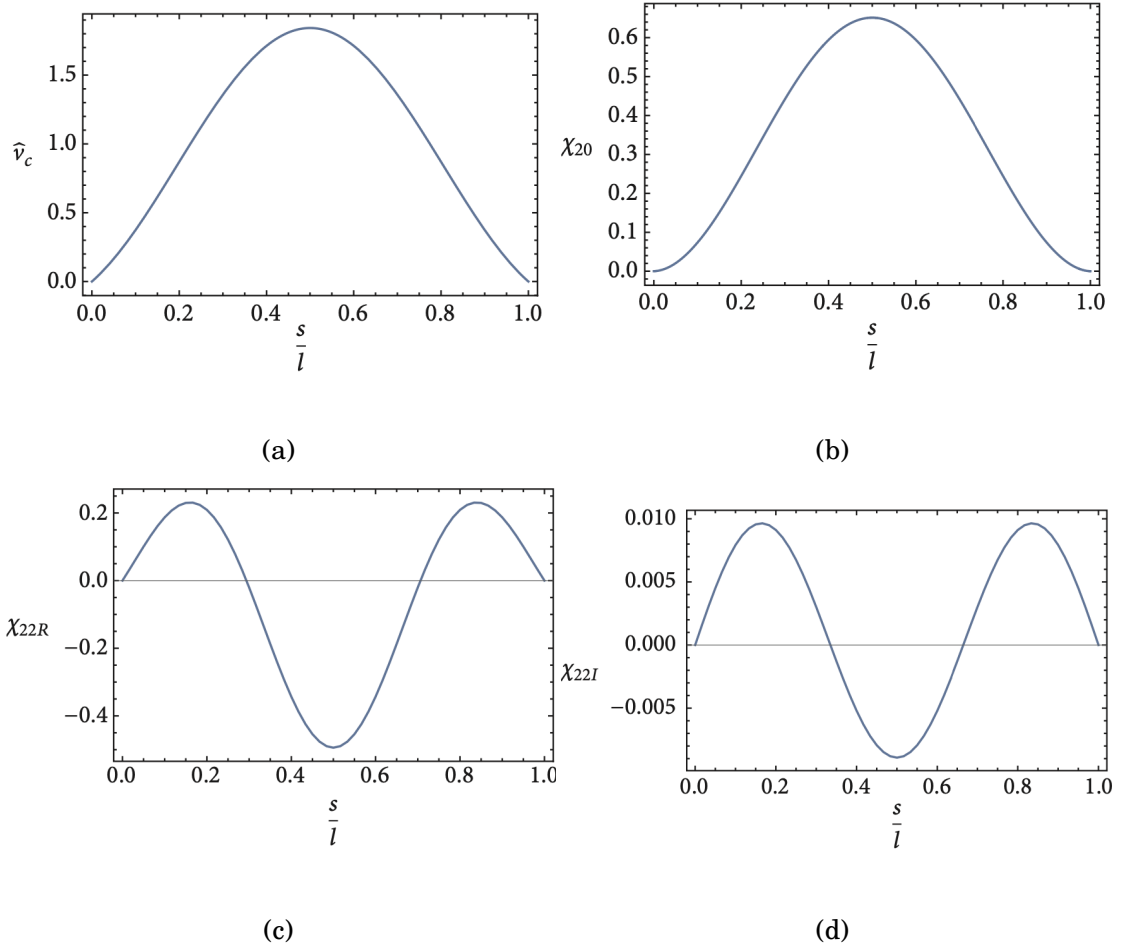


Figure 4.3: Case study 1: (a) First linear symmetric mode; (b, c, d) Second order corrections; figures are taken from [21].

In the first case, Figure 4.3 represents the mode shapes and their second order corrections. The first linear mode is symmetric, depicted in Figure 4.3(a), the dynamic unitary extension $\hat{e}_c = -5.901 \times 10^{-4}$, and critical velocity $U_c = 4.465$ m/s and modal frequency $\omega_c = 2.547$ rad/s are obtained. The corrections for the second order of modal shape $\chi_{20}(s)$, $\chi_{22R}(s)$, and $\chi_{22I}(s)$ are presented in Figures 4.3(b), 4.3(c) and 4.3(d) respectively, with the dynamic unitary extension corrections $\eta_{20} = -7.939 \times 10^{-5}$, $\eta_{22R} = 1.314 \times 10^{-4}$, and $\eta_{22I} = 1.255 \times 10^{-6}$.

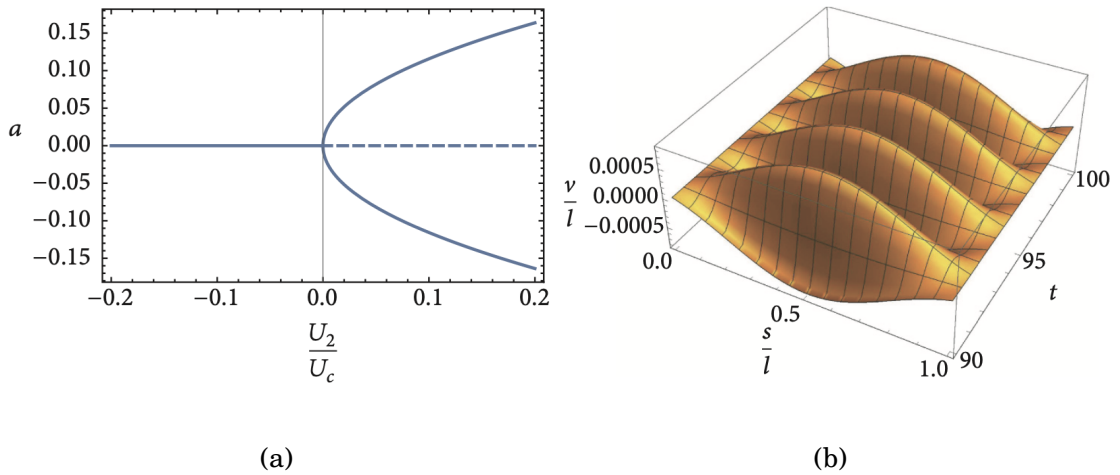


Figure 4.4: Case study 1: (a) Bifurcation diagram, solid line: stable, dashed line: unstable; (b) Reconstituted displacement $v(s, t)$ of the cable for $\frac{U_2}{U_c} = 0.11$, taken from [21].

Figure 4.4(a) depicts the bifurcation diagram, which shows the behavior of classical supercritical Hopf bifurcation, and Figure 4.4(b) displays the post-critical evolution of the time and space of the cable with the value of postcritical condition, $U_2/U_c = 0.11$.

Taking the same value of post-critical condition $U_2/U_c = 0.11$, the evolution of time of the cable is presented in Figure 4.5, comparing the results with multiple scale method, Galerkin method with nodes $N_e = 20$ and finite difference method with nodes $N_S = 100$. Figure 4.5(a) displays the half-span displacement, whereas Figure 4.5(b) shows quarter-span displacement. The MSM, Galerkin method and finite difference method are showed with green, blue and orange lines respectively, and a good agreement has been reached among the results, i.e., the asymptotic analysis is dependable.

Phase plots for the half-span and quarter-span have drawn in Figure 4.6, where they have shown a small modification in elliptical form. Also they are showing a small alteration of the shape of vibration over a period, caused by nonlinear contributions.

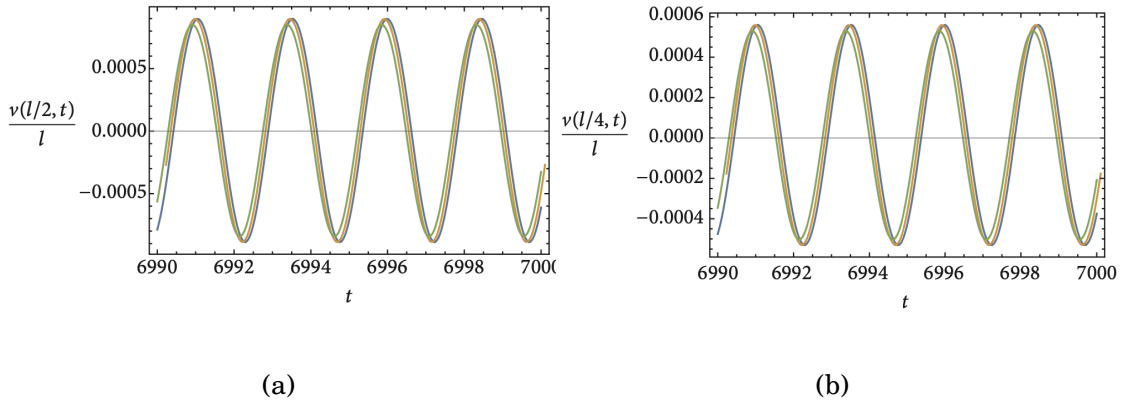


Figure 4.5: Case study 1: reconstituted time evolution of the displacement $v(s,t)$ for $\frac{U_2}{U_c} = 0.11$ at (a) half-span; (b) quarter-span (green line: multiple scale method; blue line: Galerkin method; orange line: finite difference method) [21].

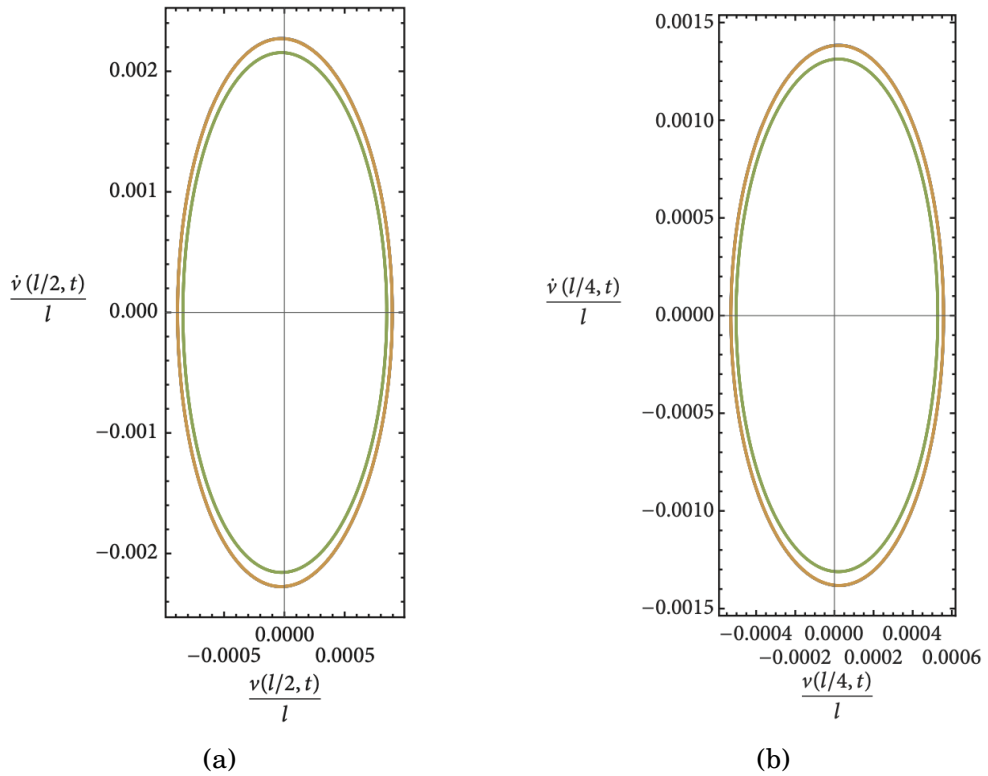


Figure 4.6: Case study 1: reconstituted phase plot (v, \dot{v}) for $\frac{U_2}{U_c} = 0.11$ at (a) half-span; (b) quarter-span (green line: multiple scale method; blue line: Galerkin method; orange line: finite difference method)[21].

In the following, Figure 4.7 represents the initial approximation of the first linear mode in the case 2. Figure 4.8 represents the mode shapes and their second order corrections for the second case, where the first linear mode is antisymmetric, depicted in Figure 4.8(a), the values of dynamic unitary extension $\hat{e}_c = 0$, and

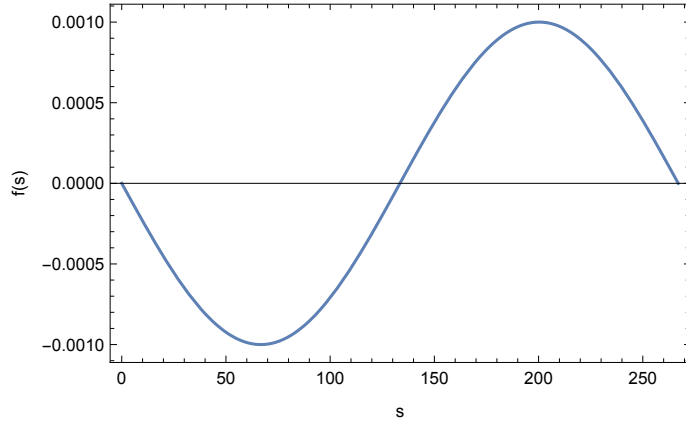


Figure 4.7: Case study 2: Approximated initial first linear mode.

critical velocity $U_c = 5.454$ m/s and modal frequency $\omega_c = 2.630$ rad/s are obtained. The corrections for the second order of modal shape $\chi_{20}(s)$, $\chi_{22R}(s)$, and $\chi_{22I}(s)$ are presented in Figures 4.8(b), 4.8(c) and 4.8(d) respectively, with the dynamic unitary extension corrections $\eta_{20} = 2.369 \times 10^{-5}$, $\eta_{22R} = 2.191 \times 10^{-4}$, and $\eta_{22I} = 1.643 \times 10^{-6}$.

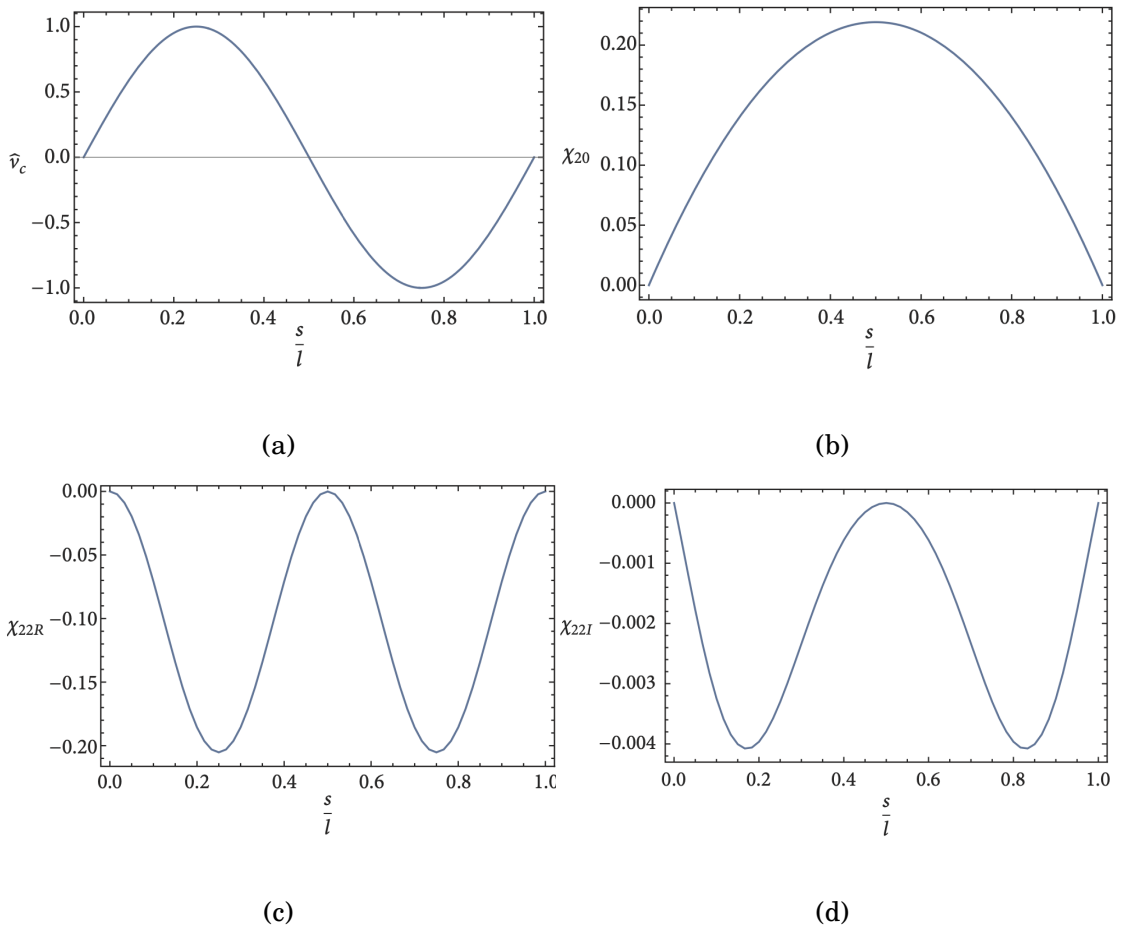


Figure 4.8: Case study 2: (a) Anti-symmetric mode; (b, c, d) Second order corrections [21].

Figure 4.9(a) depicts the bifurcation diagram for the 2nd case, which still shows the behavior of classical Hopf bifurcation, and Figure 4.9(b) displays the post-critical evolution of the time and space of the cable with the value of postcritical condition, $U_2/U_c = 0.09$.

The evolution of time of the cable is presented in Figure 4.10 by using the post-critical condition $U_2/U_c = 0.09$ and comparing the results with multiple scale method, Galerkin method with nodes $N_e = 20$ and finite difference method with nodes $N_S = 100$. Figure 4.10(a) displays the half-span displacement, whereas Figure 4.10(b) shows quarter-span displacement. The MSM, Galerkin method and finite difference method are showed with green, blue and orange lines respectively, and a good agreement has been reached in this case as well, i.e., the asymptotic analysis is reliable as discussed in the 1st case. The stationary drift in the Figure 4.10(a), shows an obvious dominant contribution of nonlinearities.

Phase plot for the quarter-span have displayed in Figure 4.11, where for the nonlinear effects, it is showing a small alteration of the shape of vibration over a period.

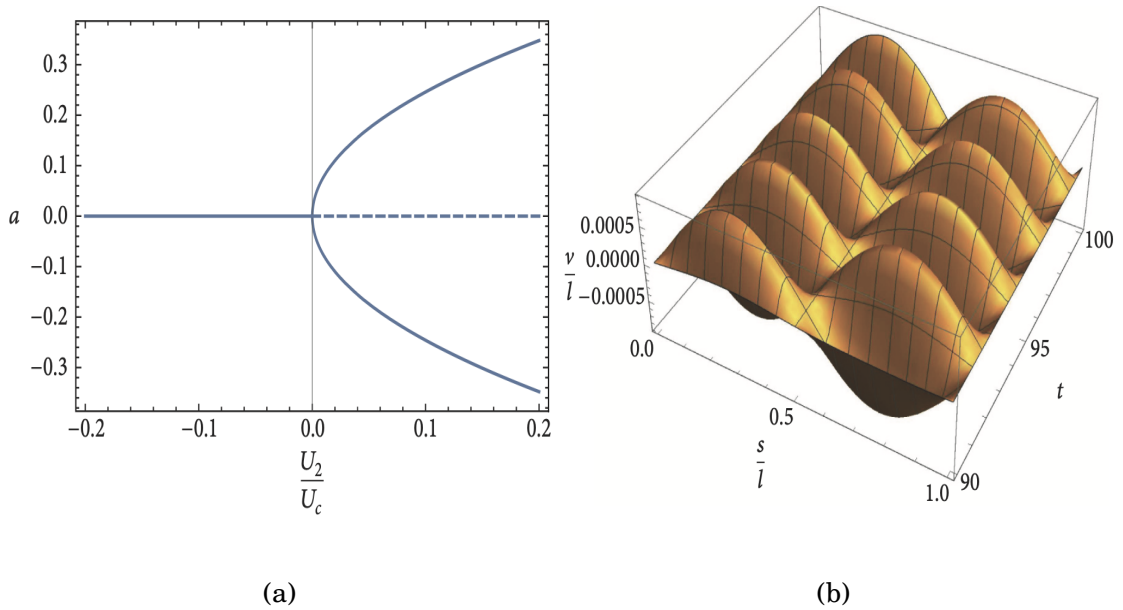


Figure 4.9: Case study 2: (a) Bifurcation diagram, solid line: stable, dashed line: unstable; (b) Reconstituted displacement $v(s, t)$ of the cable for $\frac{U_2}{U_c} = 0.09$, taken from [21].

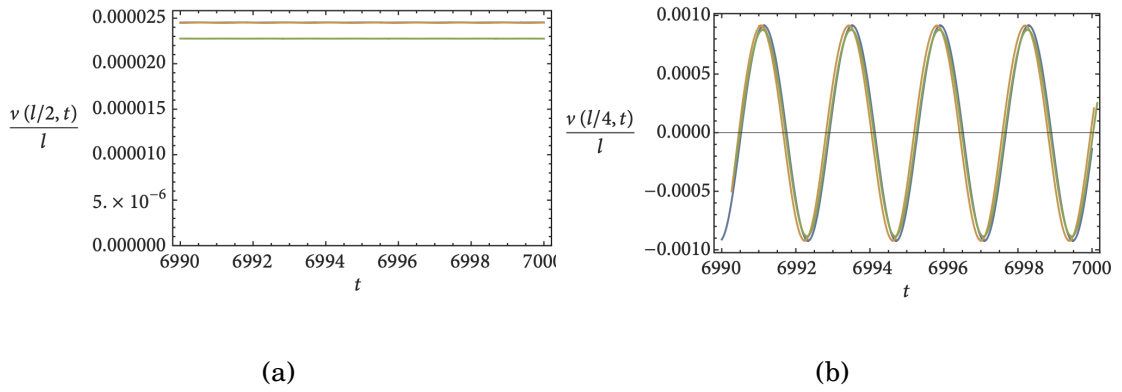


Figure 4.10: Case study 2: reconstituted time evolution of the displacement $v(s, t)$ for $\frac{U_2}{U_c} = 0.09$ at (a) half-span; (b) quarter-span (green line: multiple scale method; blue line: Galerkin method; orange line: finite difference method) [21].

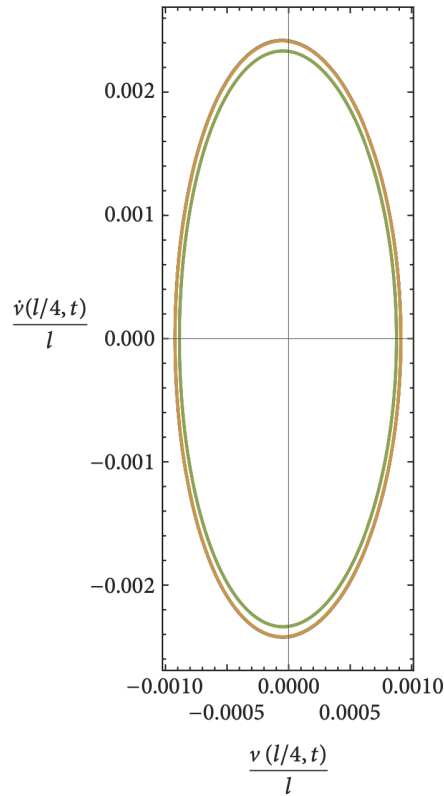


Figure 4.11: Case study 2: reconstituted phase plot (v, \dot{v}) for $\frac{U_2}{U_c} = 0.09$ at quarter-span (green line: multiple scale method; blue line: Galerkin method; orange line: finite difference method) [21].

4.6 Conclusion

A continuum approach is employed to analyze the in-plane galloping phenomenon of a horizontally suspended flexible cable. The aerodynamic forces are modeled via quasi-steady theory. On the basis of Rayleigh model of damping, the contribution of the both external and internal damping is taken into account. The study of pre- and post-critical analyses are presented. A perturbation method is employed to evaluate the modifications of the shape of critical mode and limit-cycle's magnitude. For two case-studies, numerical results in terms of finite difference and Galerkin method are presented, and they show a good agreement with the results found in analytical approach.

SPATIAL GALLOPING ANALYSIS OF SHALLOW CABLES VIA A LINEAR CONTINUUM MODEL

5.1 Introduction

A shallow flexible suspended cable, subjected to its self-weight, is modeled assuming it as a self-excited dynamical system in the linear field, taking in consideration of aerodynamic and damping forces. In accordance with the quasi-steady theory, the aerodynamic forces are developed in the model. Both the internal and external damping forces are considered simultaneously, on the basis of the Kelvin-Voigt rheological model. An exact analysis accompanied with an asymptotic and two numerical methods are performed to study the model in critical condition. The obtained outcomes are compared with different methods, as mentioned above, and presented with some tables and figures.

5.2 Mathematical Modeling

A horizontal shallow flexible cable is considered, suspended under the effect of gravity at the vertical points A and B . As long it hangs under its self-weight and no wind effects, the cable hangs in the vertical plane- $(\bar{\mathbf{a}}_x, \bar{\mathbf{a}}_y)$, by assuming an equilibrium configuration, taken as reference configuration presented by \tilde{C} (thin line in Figure 5.1). This is here approximated by a parabola, while more refined perturbation analyses are discussed in [77, 78, 80]. An orthonormal triad of unit vectors $(\bar{\mathbf{a}}_x, \bar{\mathbf{a}}_y, \bar{\mathbf{a}}_z)$ is introduced, with $\bar{\mathbf{a}}_x$ horizontal, $\bar{\mathbf{a}}_y$ vertical and $\bar{\mathbf{a}}_z$ normal to the plane. A second, intrinsic basis $(\bar{\mathbf{a}}_t(s), \bar{\mathbf{a}}_n(s), \bar{\mathbf{a}}_b(s))$ is also considered, where indexes denote the tangential, normal (in-plane) and binormal (out-of-plane) directions at the abscissa s (with $\bar{\mathbf{a}}_b \equiv \bar{\mathbf{a}}_z$). An orthogonal uniform wind flow $\mathbf{U} = U\bar{\mathbf{a}}_z$ is assumed to act on the cable, which pushes the body to a current, time-dependent, configuration (thick line in Figure 5.1), described by the displacement

field $\mathbf{u} = u(s, t)\bar{\mathbf{a}}_t(s) + v(s, t)\bar{\mathbf{a}}_n(s) + w(s, t)\bar{\mathbf{a}}_b$.

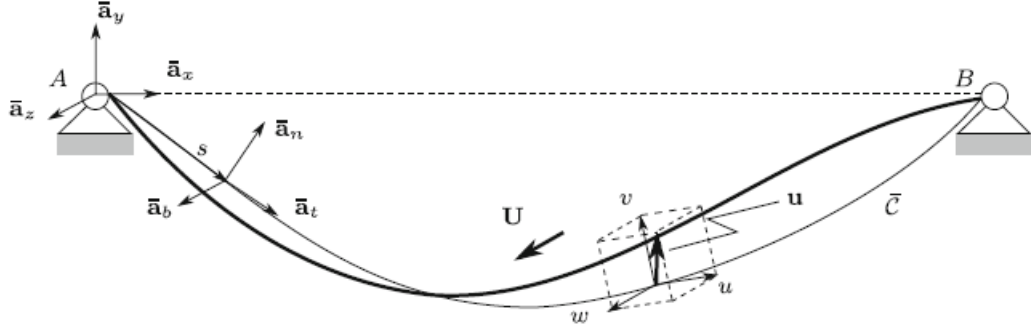


Figure 5.1: Shallow horizontal cable under normal wind flow. Thin line: in-plane equilibrium position under self-weight; thick line: current configuration under the action of both self-weight and wind.

5.2.1 Equation of Motion

The equation of motion of the cable, with the tangential displacement $u(s, t)$ condensed, and flexural and torsional stiffnesses ignored, have been derived in chapter 3, following [42, 54, 58, 91], for the transverse motion $v(s, t)$, $w(s, t)$. When nonlinearities are neglected, they read:

$$\begin{aligned}
 T_0 v'' + EA \bar{\kappa} e - m \ddot{v} + f_n^d + f_n^a &= 0, \\
 T_0 w'' - m \ddot{w} + f_b^d + f_b^a &= 0, \\
 e &= -\frac{\bar{\kappa}}{l} \int_0^l v ds, \\
 v_A &= 0, \quad v_B = 0, \\
 w_A &= 0, \quad w_B = 0.
 \end{aligned} \tag{5.1}$$

where, T_0 is the pretension, constant on s ; EA is the axial stiffness; m is the mass per unit length of the iced cable; l is the length of the cable, nearly equal to the chord; $\bar{\kappa} := \frac{mg}{T_0}$ is the initial curvature; $e(t)$ is the dynamic unit extension, constant on s ; f_n^d , f_b^d are damping forces and f_n^a , f_b^a are aerodynamic forces, all per unit length, acting in the normal and binormal direction, respectively; finally, the dot and dashes denote differentiation with respect to time and space, respectively.

5.2.2 Damping Model

Damping of the vibration of suspended iced cable emerges with the loss of energy by dissipative forces. For the reason of aerodynamic instability, the iced cable tends to gallop by a self excited vibration with low frequencies and high amplitudes. In

such problems, we need to take account the damping of the oscillation. To control the high amplitude vibrations, damping plays an important role in the steady-state excitations, albeit the damping forces are small compared to elasticity and inertia forces in many structural applications. In many dynamical systems, damping plays a critical role in defining the boundary between stability and instability by significantly affecting the response amplitudes and phases around resonance. There are two forms of damping [21, 120] namely, external and internal, both are considered in this study.

It includes the aerodynamic drag and dissipation of support motion of structures while accounting external damping. The drag force can be linear or nonlinear. It was observed that aerodynamic damping had a considerable impact on the high-amplitude vibrations of cables with low damping and high elastic modulus. The cause of external damping is due to resistance of medium of the system. The external damping is modeled as proportional to velocities, mathematically, $f_n^{d_e} = -c_e \dot{v}$, $f_b^{d_e} = -c_e \dot{w}$, where $c_e > 0$ is a damping coefficient. Which implies that an external damping operator is taken as proportional to the mass operator.

On the other hand, internal damping, accounting for various dissipation sources in material are modeled via an ‘equivalent’ viscous mechanism. Since the stiffness of the cable is of mixed nature, namely, elastic and geometric [21]. Taking in consideration of the elastic stiffness, according to Kelvin-Voigt model, we consider a local force $\eta A \bar{\kappa} \dot{e}$, where η is a coefficient of viscosity. By following the damping model proposed in [21], we have the damping forces:

$$\begin{aligned} f_n^d &= -c_e \dot{v} + \zeta \left(\frac{EA}{T_0} \kappa \dot{e} + \dot{v}'' \right), \\ f_b^d &= -c_e \dot{w} + \zeta \dot{w}'' . \end{aligned} \tag{5.2}$$

Substituting equation (5.2) into equation (5.1), we have

$$\begin{aligned} T_0 v'' + EA \bar{\kappa} e - m \ddot{v} - c_e \dot{v} + \zeta \left(\frac{EA}{T_0} \bar{\kappa} \dot{e} + \dot{v}'' \right) + f_n^a &= 0, \\ T_0 w'' - m \ddot{w} - c_e \dot{w} + \zeta \dot{w}'' + f_b^a &= 0, \\ e &= -\frac{\bar{\kappa}}{l} \int_0^l v ds, \\ v_A &= 0, \quad v_B = 0, \\ w_A &= 0, \quad w_B = 0. \end{aligned}$$

Rearranging the first two equations of the above system, the equations of motion read:

$$\begin{aligned}
 T_0 \left(1 + \frac{\zeta}{T_0} \partial_t \right) v'' + EA \bar{\kappa} \left(1 + \frac{\zeta}{T_0} \partial_t \right) e - m\ddot{v} - c_e \dot{v} + f_n^a &= 0, \\
 T_0 \left(1 + \frac{\zeta}{T_0} \partial_t \right) w'' - m\ddot{w} - c_e \dot{w} + f_b^a &= 0, \\
 e &= -\frac{\bar{\kappa}}{l} \int_0^l v ds, \\
 v_A &= 0, \quad v_B = 0, \\
 w_A &= 0, \quad w_B = 0.
 \end{aligned} \tag{5.3}$$

5.2.3 Aerodynamic Forces

In this study, the formulation of aerodynamic forces are followed by adopting the quasi-steady theory [1, 66]. According to the quasi-steady assumption, unsteady aerodynamic forces can be modeled with defining an identical steady aerodynamic situation. The theory actually is the complementary of two assumptions, are as: (1) By knowing the instanteneous motion, orientation and position of the structure, it can be completely determined the aerodynamic forces, as the oscillatory motion influences the unsteady consequence at a very low frequency. Since the 2nd and higher order derivatives of the motion are omitted, this assumption is identical to neglect inertia effect. (2) A steady system is possible to assume, which is identical to the corresponding unsteady system.

On the basis of the above assumption, we model the aerodynamic forces by neglecting the small curvatures of the cable. Because of the ice accretion, the cable's cross-sections become non-circular, and hence affected by aerodynamic forces. In the linear case, they are as follows:

$$\begin{pmatrix} f_n^a \\ f_b^a \end{pmatrix} = -U \begin{bmatrix} \hat{c}_{22}^a & \hat{c}_{23}^a \\ \hat{c}_{32}^a & \hat{c}_{33}^a \end{bmatrix} \begin{pmatrix} \dot{v} \\ \dot{w} \end{pmatrix}, \tag{5.4}$$

where,

$$\hat{c}_{22}^a := \frac{1}{2} \rho b (C_{d0} + C'_{l0}), \quad \hat{c}_{23}^a := -\rho b C_{l0}, \quad \hat{c}_{32}^a := \frac{1}{2} \rho b (C_{l0} - C'_{d0}), \quad \hat{c}_{33}^a := \rho b C_{d0},$$

and, $C_{d0}, C_{l0}, C'_{d0}, C'_{l0}$ are drag and lift aerodynamic coefficients and their derivatives with respect to the attack angle, evaluated at the origin. Here, the static

component of the aerodynamic force has been ignored. Now, the model (5.3) reads:

$$\begin{aligned}
 T_0 \left(1 + \frac{\zeta}{T_0} \partial_t\right) v'' + EA \bar{\kappa} \left(1 + \frac{\zeta}{T_0} \partial_t\right) e - m \ddot{v} - c_e \dot{v} - U (\hat{c}_{22}^a \dot{v} + \hat{c}_{23}^a \dot{w}) &= 0, \\
 T_0 \left(1 + \frac{\zeta}{T_0} \partial_t\right) w'' - m \ddot{w} - c_e \dot{w} - U (\hat{c}_{32}^a \dot{v} + \hat{c}_{33}^a \dot{w}) &= 0, \\
 e = -\frac{\bar{\kappa}}{l} \int_0^l v ds, & \\
 v_A = 0, \quad v_B = 0, & \\
 w_A = 0, \quad w_B = 0. &
 \end{aligned} \tag{5.5}$$

5.3 The “Exact” Galloping Analysis

We can rewrite the equation (5.5) as:

$$\begin{aligned}
 T_0 \begin{pmatrix} 1 + \frac{\zeta}{T_0} \partial_t \\ 0 \end{pmatrix} \begin{pmatrix} v'' \\ w'' \end{pmatrix} + \begin{pmatrix} EA \bar{\kappa} \left(1 + \frac{\zeta}{T_0} \partial_t\right) \\ 0 \end{pmatrix} e - m \begin{pmatrix} \ddot{v} \\ \ddot{w} \end{pmatrix} \\
 - \begin{bmatrix} c_e + U \hat{c}_{22}^a & U \hat{c}_{23}^a \\ U \hat{c}_{32}^a & c_e + U \hat{c}_{33}^a \end{bmatrix} \begin{pmatrix} \dot{v} \\ \dot{w} \end{pmatrix} &= \begin{pmatrix} 0 \\ 0 \end{pmatrix}, \\
 e = -\frac{\bar{\kappa}}{l} \int_0^l v ds, & \\
 v_A = 0, \quad v_B = 0, & \\
 w_A = 0, \quad w_B = 0. &
 \end{aligned} \tag{5.6}$$

It should be noticed that the linearized field equations, which are uncoupled in the motionless air, are instead coupled by the wind flow, producing aerodynamic damping.

By separating the variables according to,

$$\begin{pmatrix} v(s, t) \\ w(s, t) \\ e(t) \end{pmatrix} = \begin{pmatrix} \hat{v}(s) \\ \hat{w}(s) \\ \hat{e} \end{pmatrix} \exp(\lambda t), \tag{5.7}$$

where λ is complex.

Using equation (5.7), we have,

$$\begin{aligned}
 v'' &= \hat{v}'' \exp(\lambda t) \\
 \dot{v}'' &= \lambda \hat{v}'' \exp(\lambda t) \\
 \dot{v} &= \lambda \hat{v} \exp(\lambda t) \\
 \ddot{v} &= \lambda^2 \hat{v} \exp(\lambda t)
 \end{aligned}$$

and,

$$\begin{aligned}
 w'' &= \hat{w}'' \exp(\lambda t) \\
 \dot{w}'' &= \lambda \hat{w}'' \exp(\lambda t) \\
 \dot{w} &= \lambda \hat{w} \exp(\lambda t) \\
 \ddot{w} &= \lambda^2 \hat{w} \exp(\lambda t)
 \end{aligned}
 \tag{5.8}$$

Substituting equations (5.8) into first equation of (5.6), we have

$$\begin{aligned}
 T_0 \left(1 + \lambda \frac{\zeta}{T_0} \right) \begin{pmatrix} \hat{v}'' \\ \hat{w}'' \end{pmatrix} + \begin{pmatrix} EA\bar{\kappa} \left(1 + \lambda \frac{\zeta}{T_0} \right) \\ 0 \end{pmatrix} \hat{e} - m\lambda^2 \begin{pmatrix} \hat{v} \\ \hat{w} \end{pmatrix} \\
 - \begin{bmatrix} c_e + U\hat{c}_{22}^a & U\hat{c}_{23}^a \\ U\hat{c}_{32}^a & c_e + U\hat{c}_{33}^a \end{bmatrix} \lambda \begin{pmatrix} \hat{v} \\ \hat{w} \end{pmatrix} = \begin{pmatrix} 0 \\ 0 \end{pmatrix},
 \end{aligned}$$

and then, substitute (5.8) into the 2nd equation of (5.6), we obtain an eigenvalue problem in space as follows, namely:

$$\begin{aligned}
 \mathbf{A}(\lambda) \hat{\mathbf{u}}'' + \mathbf{B}(\lambda, U) \hat{\mathbf{u}} + \mathbf{b}(\lambda) \hat{e} &= 0, \\
 \hat{e} &= -\frac{\bar{\kappa}}{l} \int_0^l \hat{v} ds, \\
 \hat{v}_A &= 0, \quad \hat{v}_B = 0, \\
 \hat{w}_A &= 0, \quad \hat{w}_B = 0,
 \end{aligned}
 \tag{5.9}$$

where, we define

$$\begin{aligned}
 \mathbf{A}(\lambda) &:= T_0 \left(1 + \lambda \frac{\zeta}{T_0} \right) I, \\
 \mathbf{B}(\lambda, U) &:= -m\lambda^2 I - \lambda \begin{bmatrix} c_e + U\hat{c}_{22}^a & U\hat{c}_{23}^a \\ U\hat{c}_{32}^a & c_e + \hat{c}_{33}^a \end{bmatrix}, \\
 \mathbf{b}(\lambda) &:= \begin{pmatrix} EA\bar{\kappa} \left(1 + \lambda \frac{\zeta}{T_0} \right) \\ 0 \end{pmatrix}, \\
 \hat{\mathbf{u}} &:= \begin{pmatrix} \hat{v} \\ \hat{w} \end{pmatrix},
 \end{aligned}
 \tag{5.10}$$

and I is the 2×2 identity matrix. Since the problem has to be solved in the complex range, the *galloping modes are complex*, differently from what happens for a

simplified in-plane model, where they are real [21].

Solution to the field equation assumes the form,

$$\hat{\mathbf{u}} = (C_1 \exp(\beta_1 s) + C_2 \exp(\beta_2 s)) \boldsymbol{\phi}_1 + (C_3 \exp(\beta_3 s) + C_4 \exp(\beta_4 s)) \boldsymbol{\phi}_2 + \hat{e} \hat{\mathbf{u}}^*. \quad (5.11)$$

In solution (5.11), $\beta_1, \beta_2, \beta_3, \beta_4$ are the eigenvalues and $\boldsymbol{\phi}_1, \boldsymbol{\phi}_2$ are eigenvectors of the following 2×2 algebraic problem:

$$[\mathbf{B}(\lambda, U) + \beta^2 \mathbf{A}(\lambda)] \boldsymbol{\phi} = 0. \quad (5.12)$$

Moreover, $\hat{\mathbf{u}}^* := -\mathbf{B}^{-1}(\lambda, U) \mathbf{b}(\lambda)$ is a particular solution to the non-homogeneous problem (considering \hat{e} as a ‘known’ term), and C_1, C_2, C_3, C_4 are arbitrary constants.

Now,

$$\hat{\mathbf{u}}^* = -\frac{1}{\det \mathbf{B}} \begin{bmatrix} (-m\lambda^2 - \lambda(c_e + U\hat{c}_{22}^a)) EA\bar{\kappa} \left(1 + \lambda \frac{\zeta}{T_0}\right) \\ \lambda U \hat{c}_{32}^a EA\bar{\kappa} \left(1 + \lambda \frac{\zeta}{T_0}\right) \end{bmatrix},$$

and, from the solution (5.11), the in-plane and out-of-plane displacements takes the form

$$\begin{pmatrix} \hat{v} \\ \hat{w} \end{pmatrix} = \left((C_1 \exp(\beta_1 s) + C_2 \exp(\beta_2 s)) \begin{pmatrix} \phi_{11} \\ \phi_{12} \end{pmatrix} + (C_3 \exp(\beta_3 s) + C_4 \exp(\beta_4 s)) \begin{pmatrix} \phi_{21} \\ \phi_{22} \end{pmatrix} \right) - \hat{e} \frac{1}{\det \mathbf{B}} \begin{bmatrix} (-m\lambda^2 - \lambda(c_e + U\hat{c}_{22}^a)) EA\bar{\kappa} \left(1 + \lambda \frac{\zeta}{T_0}\right) \\ \lambda U \hat{c}_{32}^a EA\bar{\kappa} \left(1 + \lambda \frac{\zeta}{T_0}\right) \end{bmatrix}.$$

By substituting \hat{v} in the equation for \hat{e} , this latter is drawn in terms of the arbitrary constants. Finally, from the boundary conditions, a 4×4 homogeneous algebraic problem follows:

$$\begin{aligned} C_1 \phi_{11} + C_2 \phi_{11} + C_3 \phi_{21} + C_4 \phi_{21} - \frac{\hat{e}}{\det \mathbf{B}} (-m\lambda^2 - \lambda(c_e + U\hat{c}_{22}^a)) EA\bar{\kappa} \left(1 + \lambda \frac{\zeta}{T_0}\right) &= 0, \\ C_1 \phi_{11} \exp(\beta_1 l) + C_2 \phi_{11} \exp(\beta_2 l) + C_3 \phi_{21} \exp(\beta_3 l) + C_4 \phi_{21} \exp(\beta_4 l) \\ &\quad - \frac{\hat{e}}{\det \mathbf{B}} (-m\lambda^2 - \lambda(c_e + U\hat{c}_{22}^a)) EA\bar{\kappa} \left(1 + \lambda \frac{\zeta}{T_0}\right) = 0, \\ C_1 \phi_{12} + C_2 \phi_{12} + C_3 \phi_{22} + C_4 \phi_{22} - \frac{\hat{e}}{\det \mathbf{B}} \lambda U \hat{c}_{32}^a EA\bar{\kappa} \left(1 + \lambda \frac{\zeta}{T_0}\right) &= 0, \\ C_1 \phi_{12} \exp(\beta_1 l) + C_2 \phi_{12} \exp(\beta_2 l) + C_3 \phi_{22} \exp(\beta_3 l) + C_4 \phi_{22} \exp(\beta_4 l) \\ &\quad - \frac{\hat{e}}{\det \mathbf{B}} \lambda U \hat{c}_{32}^a EA\bar{\kappa} \left(1 + \lambda \frac{\zeta}{T_0}\right) = 0. \end{aligned} \quad (5.13)$$

In the critical condition (Hopf bifurcation), the motion is harmonic, i.e., $\lambda = i\omega_c$; the corresponding (unknown) wind velocity is the critical velocity $U = U_c$. By splitting the characteristic equations in the real and imaginary parts, two real equations for ω_c and U_c are derived.

5.4 The Asymptotic Galloping Analysis

To obtain qualitative (and hopefully, quantitative) information on the role of the out-of-plane component on galloping, we will solve equation (5.9) by a perturbation method. In such an analysis, we will follow the procedure applied in [60], where a sectional model of cable or beam was studied, by expanding it to the continuous problem discussed here, and accounting also for more complicated resonances not considered before.

The basic idea of the perturbation analysis consists in assuming that all the damping forces, external, internal and aerodynamic, are small, so that the damped aeroelastic system can be considered as a perturbation of the undamped elastic system in the void. This hypothesis is founded on the consideration that internal and external damping are small for physical reasons, and the aeroelastic forces, close to bifurcation, are of the same order of magnitude of damping. On the other hand, *a-posteriori* numerical checks of the results will confirm the reliability of such conjecture.

By rescaling all damping forces via a perturbation parameter ϵ , the equation (5.9a) read:

$$T_0 \left(1 + \epsilon \lambda \frac{\zeta}{T_0} \right) \begin{pmatrix} \hat{v}'' \\ \hat{w}'' \end{pmatrix} - [m\lambda^2 I + \epsilon \lambda \mathbf{C}(U)] \begin{pmatrix} \hat{v} \\ \hat{w} \end{pmatrix} + \begin{pmatrix} EA\bar{\kappa} \\ 0 \end{pmatrix} \left(1 + \epsilon \lambda \frac{\zeta}{T_0} \right) \hat{e} = \begin{pmatrix} 0 \\ 0 \end{pmatrix}.$$

We can re-write the eigenvalue problem (5.9) as,

$$\begin{aligned} T_0 \left(1 + \epsilon \lambda \frac{\zeta}{T_0} \right) \begin{pmatrix} \hat{v}'' \\ \hat{w}'' \end{pmatrix} - [m\lambda^2 I + \epsilon \lambda \mathbf{C}(U)] \begin{pmatrix} \hat{v} \\ \hat{w} \end{pmatrix} + \begin{pmatrix} EA\bar{\kappa} \\ 0 \end{pmatrix} \left(1 + \epsilon \lambda \frac{\zeta}{T_0} \right) \hat{e} &= \begin{pmatrix} 0 \\ 0 \end{pmatrix}, \\ \hat{e} + \frac{\bar{\kappa}}{l} \int_0^l \hat{v} ds &= 0, \\ \hat{v}_A = 0, \quad \hat{v}_B = 0, \\ \hat{w}_A = 0, \quad \hat{w}_B = 0, \end{aligned} \tag{5.14}$$

where,

$$\mathbf{C}(U) := \begin{bmatrix} c_e + U\hat{c}_{22}^a & U\hat{c}_{23}^a \\ U\hat{c}_{32}^a & c_e + U\hat{c}_{33}^a \end{bmatrix}. \tag{5.15}$$

We solve this equation by the strained parameter method [64], by introducing the following expansions with the same perturbation parameter:

$$\begin{aligned} \hat{v} &= \hat{v}_0 + \epsilon \hat{v}_1 + \dots \\ \hat{w} &= \hat{w}_0 + \epsilon \hat{w}_1 + \dots \\ \hat{e} &= \hat{e}_0 + \epsilon \hat{e}_1 + \dots \\ \lambda &= i\omega_0 + \epsilon \lambda_1 + \dots \end{aligned} \tag{5.16}$$

in which we accounted for $\lambda_0 = i\omega_0$. By substituting these expansions in equation (5.14a), we have

$$\begin{aligned}
& T_0 \left(1 + \epsilon(i\omega_0 + \epsilon\lambda_1 + \dots) \frac{\zeta}{T_0} \right) \begin{bmatrix} \hat{v}_0'' + \epsilon\hat{v}_1'' + \dots \\ \hat{w}_0'' + \epsilon\hat{w}_1'' + \dots \end{bmatrix} - [m(i\omega_0 + \epsilon\lambda_1 + \dots)^2 \mathbf{I} \\
& \quad + \epsilon(i\omega_0 + \epsilon\lambda_1 + \dots) \mathbf{C}(U)] \begin{bmatrix} \hat{v}_0 + \epsilon\hat{v}_1 + \dots \\ \hat{w}_0 + \epsilon\hat{w}_1 + \dots \end{bmatrix} \\
& \quad + \begin{pmatrix} EA\bar{\kappa} \\ 0 \end{pmatrix} \left(1 + \epsilon(i\omega_0 + \epsilon\lambda_1 + \dots) \frac{\zeta}{T_0} \right) (\hat{e}_0 + \epsilon\hat{e}_1 + \dots) = \begin{pmatrix} 0 \\ 0 \end{pmatrix}, \\
\Rightarrow & T_0 \left(1 + \epsilon i\omega_0 \frac{\zeta}{T_0} + \epsilon^2 \lambda_1 \frac{\zeta}{T_0} + \dots \right) \begin{bmatrix} \hat{v}_0'' + \epsilon\hat{v}_1'' + \dots \\ \hat{w}_0'' + \epsilon\hat{w}_1'' + \dots \end{bmatrix} - [m(i^2\omega_0^2 + \epsilon^2\lambda_1^2 + 2\epsilon i\omega_0\lambda_1 + \dots) \mathbf{I} \\
& \quad + \epsilon i\omega_0 \mathbf{C}(U) + \epsilon^2 \lambda_1 \mathbf{C}(U) + \dots] \begin{bmatrix} \hat{v}_0 + \epsilon\hat{v}_1 + \dots \\ \hat{w}_0 + \epsilon\hat{w}_1 + \dots \end{bmatrix} + \begin{pmatrix} EA\bar{\kappa} \\ 0 \end{pmatrix} (\hat{e}_0 + \epsilon\hat{e}_1 \\
& \quad + \epsilon i\omega_0 \hat{e}_0 \frac{\zeta}{T_0} + \epsilon^2 i\omega_0 \hat{e}_1 \frac{\zeta}{T_0} + \epsilon^2 \lambda_1 \hat{e}_0 \frac{\zeta}{T_0} + \dots) = \begin{pmatrix} 0 \\ 0 \end{pmatrix}, \\
\Rightarrow & T_0 \begin{pmatrix} \hat{v}_0'' \\ \hat{w}_0'' \end{pmatrix} \epsilon T_0 \begin{pmatrix} \hat{v}_1'' \\ \hat{w}_1'' \end{pmatrix} + \epsilon i\omega_0 \zeta \begin{pmatrix} \hat{v}_0'' \\ \hat{w}_0'' \end{pmatrix} - [(-m\omega_0^2 + \epsilon 2mi\omega_0\lambda_1) \mathbf{I} + \epsilon i\omega_0 \mathbf{C}(U)] \begin{bmatrix} \hat{v}_0 + \epsilon\hat{v}_1 + \dots \\ \hat{w}_0 + \epsilon\hat{w}_1 + \dots \end{bmatrix} \\
& \quad + \begin{pmatrix} EA\bar{\kappa} \\ 0 \end{pmatrix} \left(\hat{e}_0 + \epsilon \left(i\omega_0 \hat{e}_0 \frac{\zeta}{T_0} + \hat{e}_1 \right) \right) + \text{higher ordered terms of } \epsilon = \begin{pmatrix} 0 \\ 0 \end{pmatrix}, \\
\Rightarrow & T_0 \begin{pmatrix} \hat{v}_0'' \\ \hat{w}_0'' \end{pmatrix} + \epsilon \left(T_0 \begin{pmatrix} \hat{v}_1'' \\ \hat{w}_1'' \end{pmatrix} + i\omega_0 \zeta \begin{pmatrix} \hat{v}_0'' \\ \hat{w}_0'' \end{pmatrix} \right) + m\omega_0^2 \begin{pmatrix} \hat{v}_0 \\ \hat{w}_0 \end{pmatrix} \epsilon m\omega_0^2 \begin{pmatrix} \hat{v}_1 \\ \hat{w}_1 \end{pmatrix} \\
& \quad - \epsilon (i\omega_0 \mathbf{C}(U) + 2mi\omega_0\lambda_1 \mathbf{I}) \begin{pmatrix} \hat{v}_0 \\ \hat{w}_0 \end{pmatrix} + \begin{pmatrix} EA\bar{\kappa} \\ 0 \end{pmatrix} \hat{e}_0 \\
& \quad + \epsilon \begin{pmatrix} EA\bar{\kappa} \\ 0 \end{pmatrix} \left(i\omega_0 \hat{e}_0 \frac{\zeta}{T_0} + \hat{e}_1 \right) + \text{higher ordered terms of } \epsilon = \begin{pmatrix} 0 \\ 0 \end{pmatrix}.
\end{aligned}$$

From the 2nd equation of (5.14),

$$(\hat{e}_0 + \epsilon\hat{e}_1 + \dots) + \frac{\bar{\kappa}}{l} \int_0^l (\hat{v}_0 + \epsilon\hat{v}_1 + \dots) ds = 0.$$

Separating the coefficients with different orders of ϵ , we have the perturbation equations are as follows:

Order ϵ^0 :

$$\begin{aligned}
 T_0 \begin{pmatrix} \hat{v}_0'' \\ \hat{w}_0'' \end{pmatrix} + m\omega_0^2 \begin{pmatrix} \hat{v}_0 \\ \hat{w}_0 \end{pmatrix} + \begin{pmatrix} EA\bar{\kappa} \\ 0 \end{pmatrix} \hat{e}_0 &= \begin{pmatrix} 0 \\ 0 \end{pmatrix}, \\
 \hat{e}_0 + \frac{\bar{\kappa}}{l} \int_0^l \hat{v}_0 ds &= 0, \\
 \hat{v}_{0A} = 0, \quad \hat{v}_{0B} = 0, \\
 \hat{w}_{0A} = 0, \quad \hat{w}_{0B} = 0.
 \end{aligned} \tag{5.17}$$

Order ϵ^1 :

$$\begin{aligned}
 T_0 \begin{pmatrix} \hat{v}_1'' \\ \hat{w}_1'' \end{pmatrix} + m\omega_0^2 \begin{pmatrix} \hat{v}_1 \\ \hat{w}_1 \end{pmatrix} + \begin{pmatrix} EA\bar{\kappa} \\ 0 \end{pmatrix} \hat{e}_1 &= 2im\omega_0\lambda_1 \begin{pmatrix} \hat{v}_0 \\ \hat{w}_0 \end{pmatrix} - i\omega_0\zeta \begin{pmatrix} \hat{v}_0'' \\ \hat{w}_0'' \end{pmatrix} \\
 &+ i\omega_0\mathbf{C}(U) \begin{pmatrix} \hat{v}_0 \\ \hat{w}_0 \end{pmatrix} - i\omega_0\zeta \begin{pmatrix} \frac{EA}{T_0}\bar{\kappa} \\ 0 \end{pmatrix} \hat{e}_0, \\
 \hat{e}_1 + \frac{\bar{\kappa}}{l} \int_0^l \hat{v}_1 ds &= 0, \\
 \hat{v}_{1A} = 0, \quad \hat{v}_{1B} = 0, \\
 \hat{w}_{1A} = 0, \quad \hat{w}_{1B} = 0.
 \end{aligned} \tag{5.18}$$

Since the ϵ^0 -order equations (5.17) govern the undamped motion of the cable, its solutions are the natural modes. Namely: (i) $(\hat{v}_0(s), \hat{e}_0) = (\hat{v}_{0j}(s), \hat{e}_{0j})$ is the j th (symmetric, with $\hat{e}_{0j} \neq 0$; or anti-symmetric, with $\hat{e}_{0j} = 0$) in-plane mode, of frequency ω_{0j} ; (ii) $\hat{w}_0(s) = \hat{w}_{0k}(s)$ is the k th (symmetric or anti-symmetric) out-of-plane mode, of frequency ω_{0k} . Depending on the Λ^2 , Irvine parameter [42], several circumstances can occur, in which: (i) an eigenvalue is simple, (ii) an eigenvalue is double and semi-simple, or even (iii) an eigenvalue is triple and semi-simple. All these occurrences call for a specific perturbation algorithm.

By superimposing to the spectrum of the planar and out-of-plane frequencies [42], we obtain the plot in Figure 5.2.

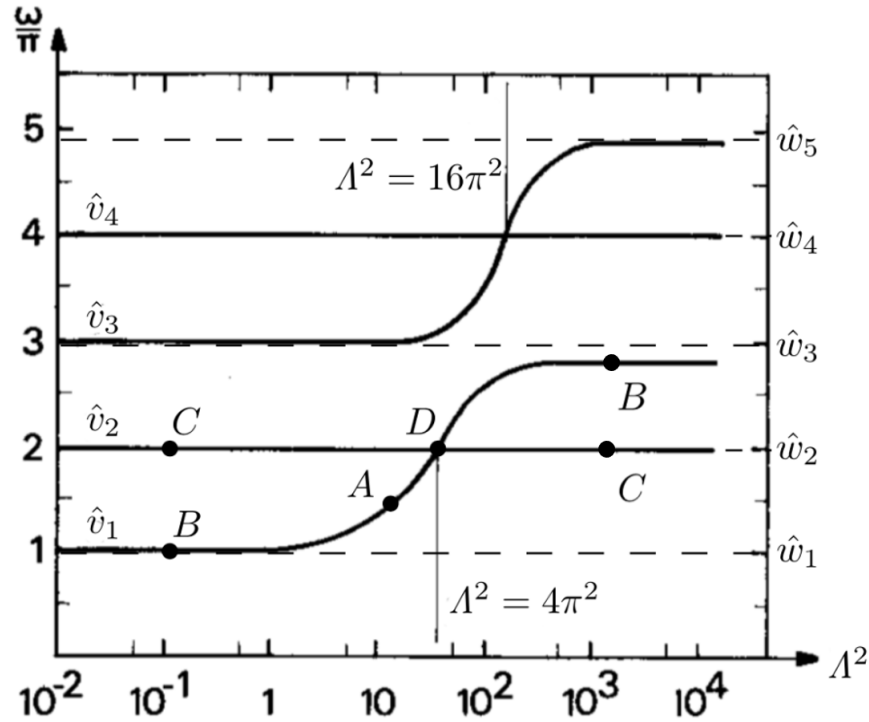


Figure 5.2: Spectrum of the planar \hat{v}_j (continuous lines) and out-of-plane \hat{w}_k (dashed lines) frequencies of the cable as function of the Irvine parameter. Odd indexes denote symmetric modes, even indexes antisymmetric modes. Points A to D are representative of different resonance conditions, taken from [42].

There, typical resonance conditions are marked at points A to D; namely:

- At (generic) points like A, i.e., falling in the transition phase in which a symmetric mode is changing its shape, a symmetric in-plane mode \hat{v}_j is nonresonant (i.e., ω_{0j} is a single eigenvalue); we will refer to such case as *nonresonant*.
- At (generic) points like B, i.e., far from the cross-over points, a symmetric in-plane mode \hat{v}_j is in 1:1 resonance with a symmetric out-of-plane mode \hat{w}_j (both sinusoidal of the same wave-number, having the same frequency); we will refer to this case as *symmetric 1:1 resonance case*;
- At (generic) points like C, i.e., still far from cross-over points, an anti-symmetric in-plane mode \hat{v}_j is in 1:1 resonance with an anti-symmetric out-of-plane mode \hat{w}_j (both sinusoidal of the same wave-number, having the same frequency); we will refer to this as *anti-symmetric 1:1 resonance case*;
- At (special) points like D, i.e., at crossover, two planar modes, one symmetric \hat{v}_j and one anti-symmetric \hat{v}_{j+1} , are in 1:1:1 resonance with an anti-symmetric out-of-plane mode \hat{w}_j ; such a degenerate resonance condition

persists in a neighborhood of points D , in which only the symmetric mode slightly change its frequency; we will refer to this as the 1:1:1 resonant case.

An additional nonresonant case, in principle, exists, concerning the first out-of-plane mode \hat{w}_1 on the left of crossover. However, this case can be proved to be meaningful, since the cable cannot gallop in a shape which, at the leading order, is out-of-plane only, since in this direction the aerodynamic force is stabilizing for any cross-section shape (i.e., $\hat{c}_{33}^a > 0$).

We will study separately (i) the nonresonant case, (ii) the two 1 : 1 resonant cases, and (iii) the 1 : 1 : 1 resonant case.

5.4.1 The Non-resonant Case

We take a generating solution to equation (5.17) made of just one planar mode, i.e.,

$$\begin{pmatrix} \hat{v}_0 \\ \hat{w}_0 \\ \hat{e}_0 \end{pmatrix} = \begin{pmatrix} \hat{v}_{0j}(s) \\ 0 \\ \hat{e}_{0j} \end{pmatrix}, \quad (5.19)$$

in which, $\hat{e}_{0j} \neq 0$ if the mode is symmetric, and $\hat{e}_{0j} = 0$ if anti-symmetric. Then the properties of the natural mode,

$$\int_0^l \begin{pmatrix} \hat{v}_{0j} \\ 0 \end{pmatrix} \left[T_0 \begin{pmatrix} \hat{v}_{0j}'' \\ 0 \end{pmatrix} + m\omega_{0j}^2 \begin{pmatrix} \hat{v}_{0j} \\ 0 \end{pmatrix} + \begin{pmatrix} EA\bar{\kappa} \\ 0 \end{pmatrix} \hat{e}_{0j} \right] ds = \begin{pmatrix} 0 \\ 0 \end{pmatrix}.$$

We get,

$$\int_0^l \hat{v}_{0j} \hat{v}_{0j}'' ds + \frac{m\omega_{0j}^2}{T_0} \int_0^l \hat{v}_{0j}^2 ds + \frac{EA}{T_0} \bar{\kappa} \int_0^l \hat{v}_{0j} \hat{e}_{0j} ds = 0. \quad (5.20)$$

The solvability condition for Eq. (5.18) requires the known term is orthogonal to the eigenvector, i.e.,

$$\int_0^l \begin{pmatrix} \hat{v}_{0j} \\ 0 \end{pmatrix}^T \left[2m\lambda_{1j} \begin{pmatrix} \hat{v}_{0j} \\ 0 \end{pmatrix} - \zeta \begin{pmatrix} \hat{v}_{0j}'' \\ 0 \end{pmatrix} + \mathbf{C}(U) \begin{pmatrix} \hat{v}_{0j} \\ 0 \end{pmatrix} - \zeta \begin{pmatrix} EA \\ T_0 \end{pmatrix} \bar{\kappa} \hat{e}_{0j} \right] ds = 0. \quad (5.21)$$

From which we have,

$$\begin{aligned} & 2m\lambda_{1j} \int_0^l \hat{v}_{0j}^2 ds - \zeta \int_0^l \hat{v}_{0j} \hat{v}_{0j}'' ds + (c_e + U\hat{c}_{22}^a) \int_0^l \hat{v}_{0j}^2 ds - \zeta \frac{EA}{T_0} \bar{\kappa} \int_0^l \hat{v}_{0j} \hat{e}_{0j} ds = 0, \\ \Rightarrow & [2m\lambda_{1j} + (c_e + U\hat{c}_{22}^a)] \int_0^l \hat{v}_{0j}^2 ds - \zeta \left(\int_0^l \hat{v}_{0j} \hat{v}_{0j}'' ds + \frac{EA}{T_0} \bar{\kappa} \int_0^l \hat{v}_{0j} \hat{e}_{0j} ds \right) = 0. \end{aligned}$$

By accounting for the properties of the mode (5.20),

$$\begin{aligned} & (2m\lambda_{1j} + c_e + U\hat{c}_{22}^a) \int_0^l \hat{v}_{0j}^2 ds + \zeta \frac{m\omega_{0j}^2}{T_0} \int_0^l \hat{v}_{0j}^2 ds = 0 \\ \Rightarrow & 2m\lambda_{1j} + c_e + U\hat{c}_{22}^a + \zeta \frac{m\omega_{0j}^2}{T_0} = 0. \end{aligned}$$

The frequency correction is derived:

$$\lambda_{1j} = -\frac{1}{2m} \left[c_e + U\hat{c}_{22}^a + \zeta \frac{m\omega_{0j}^2}{T_0} \right]. \quad (5.22)$$

This result shows that all the forms of damping add a real contribution to the purely imaginary eigenvalue $i\omega_{0j}$. While $c_e > 0$ and $\zeta > 0$ (i.e., they are stabilizing), $\hat{c}_{22}^a \geq 0$ (i.e., it can be stabilizing or instabilizing). The equilibrium is stable when the square bracket is positive, and unstable when negative. The bifurcation condition then occurs when $\lambda_{1i} = 0$, i.e., at the critical wind velocity:

$$U_{cj} = \frac{c_e + \zeta \frac{m\omega_{0j}^2}{T_0}}{|\hat{c}_{22}^a|}, \quad \hat{c}_{22}^a < 0. \quad (5.23)$$

This expression coincides with that one found in [60] for the simplified in-plane galloping model.

From the above outcome, we can summarize, in the non-resonant case, *the added out-of-plane degree-of-freedom* does not change, at the leading order, the critical wind velocity evaluated by accounting according to the Den-Hartog criterion. As only significant effect, it adds an out-of-plane component of motion, described by the solution $\hat{w}_1(s)$ to equation (5.18b); since this component is in quadrature with respect to the planar mode (all the known terms of the equations being affected by the imaginary unit), the galloping mode is complex. On the other hand, since $\frac{\|\hat{w}(s)\|}{\|\hat{v}(s)\|} = O(\epsilon)$, any material point of the cable describes trajectories whose projection in the cross-section plane are very narrow ellipses. We conclude that the rougher model is quite accurate in the nonresonant case.

5.4.2 The 1:1 Resonant Case

We consider a bi-modal generating solution to equation (5.18), made of a planar and an out-of-plane mode, either symmetric or anti-symmetric, namely:

$$\begin{pmatrix} \hat{v}_0 \\ \hat{w}_0 \\ \hat{e}_0 \end{pmatrix} = a_1 \begin{pmatrix} \hat{v}_{0j}(s) \\ 0 \\ \hat{e}_{0j} \end{pmatrix} + a_2 \begin{pmatrix} 0 \\ \hat{w}_{0j} \\ 0 \end{pmatrix}, \quad (5.24)$$

where $\hat{v}_{0j} \equiv \hat{w}_{0j} = \sin\left(\frac{j\pi s}{l}\right)$, with \hat{e}_{0j} different from zero only when j is odd, and where a_1, a_2 are arbitrary constants. We denote by $\omega_{0j} = \frac{j\pi}{l} \sqrt{\frac{T_0}{m}}$ the common frequency.

Properties of eigenmodes,

$$\int_0^l \begin{pmatrix} \hat{v}_{0j} \\ 0 \end{pmatrix}^T \left[T_0 \begin{pmatrix} a_1 \hat{v}_{0j}'' \\ a_2 \hat{w}_{0j}'' \end{pmatrix} + m\omega_{0j}^2 \begin{pmatrix} a_1 \hat{v}_{0j} \\ a_2 \hat{w}_{0j} \end{pmatrix} + \begin{pmatrix} EA\bar{\kappa} \\ 0 \end{pmatrix} a_1 \hat{e}_{0j} \right] ds$$

$$\int_0^l \begin{pmatrix} 0 \\ \hat{w}_{0j} \end{pmatrix}^T \left[T_0 \begin{pmatrix} a_1 \hat{v}_{0j}'' \\ a_2 \hat{w}_{0j}'' \end{pmatrix} + m\omega_{0j}^2 \begin{pmatrix} a_1 \hat{v}_{0j} \\ a_2 \hat{w}_{0j} \end{pmatrix} + \begin{pmatrix} EA\bar{\kappa} \\ 0 \end{pmatrix} a_1 \hat{e}_{0j} \right] ds$$

which implies,

$$\int_0^l \hat{v}_{0j} \hat{v}_{0j}'' ds + \frac{m\omega_{0j}^2}{T_0} \int_0^l \hat{v}_{0j}^2 ds + \frac{EA}{T_0} \bar{\kappa} \int_0^l \hat{v}_{0j} \hat{e}_{0j} ds = 0 \quad (5.25a)$$

$$T_0 \int_0^l \hat{w}_{0j} \hat{w}_{0j}'' ds + m\omega_{0j}^2 \int_0^l \hat{w}_{0j}^2 ds = 0 \quad (5.25b)$$

The solvability conditions of the 1st equation of (5.18) require the known term is orthogonal to both the eigenvectors associated with the semi-simple eigenvalue ω_{0j} , i.e.,

$$\int_0^l \begin{pmatrix} \hat{v}_{0j} \\ 0 \end{pmatrix}^T \left[(2m\lambda_{1j} + \mathbf{C}(U)) \begin{pmatrix} a_1 \hat{v}_{0j} \\ a_2 \hat{w}_{0j} \end{pmatrix} - \zeta \begin{pmatrix} a_1 \hat{v}_{0j}'' \\ a_2 \hat{w}_{0j}'' \end{pmatrix} - \zeta \begin{pmatrix} EA \\ T_0 \end{pmatrix} \bar{\kappa} a_1 \hat{e}_{0j} \right] ds = 0 \quad (5.26a)$$

$$\int_0^l \begin{pmatrix} 0 \\ \hat{w}_{0j} \end{pmatrix}^T \left[(2m\lambda_{1j} + \mathbf{C}(U)) \begin{pmatrix} a_1 \hat{v}_{0j} \\ a_2 \hat{w}_{0j} \end{pmatrix} - \zeta \begin{pmatrix} a_1 \hat{v}_{0j}'' \\ a_2 \hat{w}_{0j}'' \end{pmatrix} - \zeta \begin{pmatrix} EA \\ T_0 \end{pmatrix} \bar{\kappa} a_1 \hat{e}_{0j} \right] ds = 0 \quad (5.26b)$$

From the equation (5.26a),

$$(2m\lambda_{1j} + c_e + U\hat{c}_{22}^a) a_1 \int_0^l \hat{v}_{0j}^2 ds + U\hat{c}_{23}^a a_2 \int_0^l \hat{v}_{0j} \hat{w}_{0j} ds - \zeta a_1 \int_0^l \hat{v}_{0j} \hat{v}_{0j}'' ds$$

$$- \zeta \frac{EA}{T_0} \bar{\kappa} a_1 \int_0^l \hat{v}_{0j} \hat{e}_{0j} ds = 0.$$

Using the properties (5.25a) of the eigenmodes, we get

$$\left(2m\lambda_{1j} + c_e + U\hat{c}_{22}^a + \zeta \frac{m\omega_{0j}^2}{T_0} \right) a_1 + U\hat{c}_{23}^a a_2 = 0. \quad (5.27)$$

From the equation (5.26b) and by using properties (5.25b), we get

$$U \hat{c}_{32}^a a_1 + \left(2m \lambda_{1j} + c_e + U \hat{c}_{33}^a + \zeta \frac{m \omega_{0j}^2}{T_0} \right) a_2 = 0. \quad (5.28)$$

Equations (5.27) and (5.28) can be written in the following matrix form:

$$(\mathbf{B}(U) + \lambda_{1j} \mathbf{I}) \begin{pmatrix} a_1 \\ a_2 \end{pmatrix} = \begin{pmatrix} 0 \\ 0 \end{pmatrix}, \quad (5.29)$$

where, by accounting for the modal shapes and frequency,

$$\begin{aligned} \mathbf{B}(U) &:= \frac{1}{2m} (\mathbf{B}^d + U \mathbf{B}^a), \\ &= \frac{1}{2m} \left(\begin{bmatrix} c_e + \zeta \left(\frac{j\pi}{l} \right)^2 & 0 \\ 0 & c_e + \zeta \left(\frac{j\pi}{l} \right)^2 \end{bmatrix} + U \begin{bmatrix} \hat{c}_{22}^a & \hat{c}_{23}^a \\ \hat{c}_{32}^a & \hat{c}_{33}^a \end{bmatrix} \right), \end{aligned} \quad (5.30)$$

and where \mathbf{B}^d accounts for external and internal damping, and \mathbf{B}^a for the aerodynamic damping.

Equation (5.29) is an eigenvalue problem in λ_{1j} , whose characteristic equation reads,

$$\lambda_{1j}^2 + \lambda_{1j} \text{tr} \mathbf{B}(U) + \det \mathbf{B}(U) = 0, \quad (5.31)$$

where $\text{tr} \mathbf{B} := B_{11} + B_{22}$, $\det \mathbf{B} := B_{11} B_{22} - B_{12} B_{21}$ are the invariants of the total (damping plus aerodynamic) modal damping matrix $\mathbf{B} = \mathbf{B}(U)$. The roots $\lambda_{1j}^{(1)}$, $\lambda_{1j}^{(2)}$ of Equation (5.31) rule the stability of equilibrium. From the characteristic equation (5.31),

$$\begin{aligned} \lambda_{1j}^{(1)} &= \frac{-\text{tr} \mathbf{B} + \sqrt{\text{tr}^2 \mathbf{B} - 4 \det \mathbf{B}}}{2}, \\ \lambda_{1j}^{(2)} &= \frac{-\text{tr} \mathbf{B} - \sqrt{\text{tr}^2 \mathbf{B} - 4 \det \mathbf{B}}}{2}. \end{aligned} \quad (5.32)$$

By following [60], an exhaustive description of the bifurcation scenario is depicted in Figure 5.3(a) on the invariant plane, where the four eigenvalues $\lambda_j = \pm i \omega_{0j} + \epsilon \lambda_{1j}^{(1,2)}$ are sketched in each of the regions bounded by two half-axes and the parabola $\text{tr}^2 \mathbf{B} = 4 \det \mathbf{B}$ (on which the eigenvalues coalesce in pair). It is seen that the first quadrant of the plane is stable, and bounded by two half-axes, on which two different bifurcation occur, namely:

- when $\det \mathbf{B} = 0$ and $\text{tr} \mathbf{B} > 0$, we have

$$\lambda_{1j}^{(1)} = \frac{-\text{tr} \mathbf{B} + \text{tr} \mathbf{B}}{2} = 0$$

and,

$$\lambda_{1j}^{(2)} = \frac{-\text{tr}\mathbf{B} - \text{tr}\mathbf{B}}{2} = -\text{tr}\mathbf{B} < 0$$

so that, $\lambda_j = \pm i\omega_{0j} + \epsilon\lambda_{1j}^{(2)}$, with $\lambda_{1j}^{(1)} = 0$ and $\lambda_{1j}^{(2)} < 0$ i.e., just a pair of complex conjugate eigenvalues is on the imaginary axis, which implies that a simple Hopf bifurcation occurs.

- when $\text{tr}\mathbf{B} = 0$ and $\det\mathbf{B} > 0$, we have

$$\lambda_{1j}^{(1,2)} = \pm i\sqrt{|\det\mathbf{B}|}$$

so that, $\lambda_j = \pm i\omega_{0j} + \epsilon\lambda_{1j}^{(1,2)}$, with $\lambda_{1j}^{(1,2)} = \pm i\sqrt{|\det\mathbf{B}|}$ i.e., two pairs of complex conjugate eigenvalues are on the imaginary axis, which implies that a double Hopf bifurcation occurs.

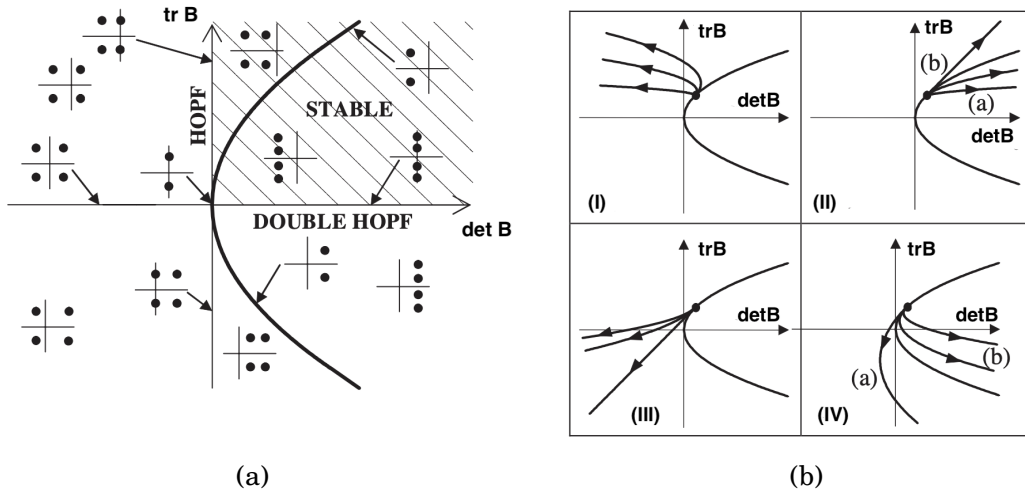


Figure 5.3: Eigenvalues $\lambda_{1j} = \pm i\omega_{0j} + \epsilon\lambda_{1j}^{(1,2)}$ in the plane of the invariants of the modal damping matrix \mathbf{B} : (a) eigenvalue sketches in each region, (b) eigenvalue paths for increasing wind velocity U , according to the signs of $\text{tr}\mathbf{B}^a$, $\det\mathbf{B}^a$; the parabola has equation $\text{tr}^2\mathbf{B} = 4\det\mathbf{B}$, taken from [60].

Figure 5.3(b) describes the paths followed by the system when U increases from zero. When $U = 0$, the damping matrix is made of the damping part only, for which all the eigenvalues have real and negative parts and coalesce in pair on the parabola. When, however, U increases from zero, depending on the aerodynamic properties of the cross-section (described by $\text{tr}\mathbf{B}^a$, $\det\mathbf{B}^a$), a pair, or both pairs of eigenvalue can cross the imaginary axis, thus entailing loss of stability. Namely,

- if $\text{tr}\mathbf{B}^a > 0$, $\det\mathbf{B}^a < 0$ (case I in Figure 4.3(b)), a *simple Hopf bifurcation* occurs at a sufficiently high wind velocity U_c ;

- if $\text{tr}\mathbf{B}^a > 0$, $\det\mathbf{B}^a \geq 0$ (case II in Figure 4.3(b)), the *equilibrium remain stable* for any wind velocity U_c ;
- if $\text{tr}\mathbf{B}^a < 0$, $\det\mathbf{B}^a \leq 0$ (case III in Figure 4.3(b)), a *simple Hopf bifurcation* again occurs at a sufficiently high wind velocity U_c ;
- if $\text{tr}\mathbf{B}^a < 0$, $\det\mathbf{B}^a > 0$ (case IV in Figure 4.3(b)), either *two successive Hopf bifurcations* (curve (a)) or a *double Hopf bifurcation* (curve (b)) occur at a sufficiently high wind velocity U_c .

Therefore, once the invariants of the aerodynamic matrix \mathbf{B}^a are known, it is a priori known the mechanism of galloping (if any) the cable will undergo.

Concerning the value assumed by critical wind velocity, it is determined by requiring either: (i) $\det\mathbf{B} = 0$ and $\text{tr}\mathbf{B} > 0$ for simple Hopf bifurcation, or, (ii) $\text{tr}\mathbf{B} = 0$ and $\det\mathbf{B} > 0$ for double Hopf bifurcation.

From the 1st case:

$$\begin{aligned}
 & -\frac{1}{2m} \left(2 \left(c_e + \zeta \left(\frac{j\pi}{l} \right)^2 \right) + U (\hat{c}_{22}^a + \hat{c}_{33}^a) \right) + \left(\frac{1}{4m^2} \left(4 \left(c_e + \zeta \left(\frac{j\pi}{l} \right)^2 \right)^2 \right. \right. \\
 & \quad \left. \left. + 4 \left(c_e + \zeta \left(\frac{j\pi}{l} \right)^2 \right) U (\hat{c}_{22}^a + \hat{c}_{33}^a) + U^2 (\hat{c}_{22}^a + \hat{c}_{33}^a) \right) - \frac{1}{4m^2} \left(4 \left(c_e + \zeta \left(\frac{j\pi}{l} \right)^2 \right)^2 \right. \right. \\
 & \quad \left. \left. + 4 \left(c_e + \zeta \left(\frac{j\pi}{l} \right)^2 \right) U (\hat{c}_{22}^a + \hat{c}_{33}^a) + 4U^2 (\hat{c}_{22}^a \hat{c}_{33}^a - \hat{c}_{23}^a \hat{c}_{32}^a) \right) \right)^{1/2} = 0, \\
 \Rightarrow & U \sqrt{(\hat{c}_{22}^a + \hat{c}_{33}^a) - 4(\hat{c}_{22}^a \hat{c}_{33}^a - \hat{c}_{23}^a \hat{c}_{32}^a)} - U (\hat{c}_{22}^a + \hat{c}_{33}^a) = 2 \left(c_e + \zeta \left(\frac{j\pi}{l} \right)^2 \right), \\
 \Rightarrow & U \left(\sqrt{\text{tr}\mathbf{B}^a - 4\det\mathbf{B}^a} - \text{tr}\mathbf{B}^a \right) = 2 \left(c_e + \zeta \left(\frac{j\pi}{l} \right)^2 \right), \\
 \Rightarrow & U = \frac{2 \left(c_e + \zeta \left(\frac{j\pi}{l} \right)^2 \right)}{\sqrt{\text{tr}^2\mathbf{B}^a - 4\det\mathbf{B}^a} - \text{tr}\mathbf{B}^a}.
 \end{aligned}$$

It follows that, a simple Hopf bifurcation occurs (in I, III or IV-a) at:

$$U_c = 2 \frac{\left(c_e + \zeta \left(\frac{j\pi}{l} \right)^2 \right)}{\sqrt{\text{tr}^2\mathbf{B}^a - 4\det\mathbf{B}^a} - \text{tr}\mathbf{B}^a}, \quad (5.33)$$

and from the 2nd case,

$$\begin{aligned}
 & \left(c_e + \zeta \left(\frac{j\pi}{l} \right)^2 + U \hat{c}_{22}^a \right) + \left(c_e + \zeta \left(\frac{j\pi}{l} \right)^2 + U \hat{c}_{33}^a \right) = 0, \\
 \Rightarrow & 2 \left(c_e + \zeta \left(\frac{j\pi}{l} \right)^2 \right) + U \text{tr}\mathbf{B}^a = 0, \\
 \Rightarrow & U = -\frac{2 \left(c_e + \zeta \left(\frac{j\pi}{l} \right)^2 \right)}{\text{tr}\mathbf{B}^a},
 \end{aligned}$$

which follows that, a double Hopf bifurcation occurs (in case IV-b) at:

$$U_c = -2 \frac{\left(c_e + \zeta \left(\frac{j\pi}{l} \right)^2 \right)}{\text{tr} \mathbf{B}^a}. \quad (5.34)$$

It can be checked, by numerical experiments carried out ahead on data relevant to real iced cross-sections that, such critical velocities at the resonance can be either higher or lower than the critical Den-Hartog velocity. This means that the coupling between the in-plane and out-of-plane motion can have a beneficial as well as detrimental effect with respect to the single-component motion, occurring in conditions of non-resonance.

As a significant example, let us consider the case $\hat{c}_{22}^a > 0$ which occurs for the so-called aerodynamically stable cross-sections (according to the one degree-of-freedom model). Since it is $\hat{c}_{33}^a > 0$ for any cross-sections, results $\text{tr} \mathbf{B}^a > 0$, so that double Hopf bifurcation cannot occur (since equation (5.34) gives a negative value). However, if $\det \mathbf{B}^a < 0$ (i.e., if the case I occurs), then a simple Hopf bifurcation takes place (since equation (5.33) supplies a positive value). Hence, coupling makes unstable a cable that would be stable in non-resonance conditions.

Once the critical wind velocity has been evaluated, we could be interested in finding the galloping mode. To face this problem, we have to find the eigenvector $(\mathbf{a}_1, \mathbf{a}_2)$ of equation (5.29). We distinguish two cases:

- In the simple Hopf bifurcation case, it is $\lambda_{1j}^{(1)} = 0$ at criticality; therefore a real $(\mathbf{a}_1^{(1)}, \mathbf{a}_2^{(1)})$ eigenvector is found. This entails that the galloping mode, as in the nonresonant case, is real at the leading order, i.e., the material points describe straight lines in the cross-section plane. If, however, we account for higher-order corrections, the motion become (weakly) complex.
- In the double Hopf bifurcation case, $\lambda_{1j}^{(1,2)} = \pm i \sqrt{|\det \mathbf{B}^a|}$, so that two complex $(\mathbf{a}_1^{(1,2)}, \mathbf{a}_2^{(1,2)})$ eigenvectors are found. This entails that galloping manifests itself via the superposition of two complex modes. In each mode, a material point describes an ellipse whose axis lengths are of the same order of magnitude.

5.4.3 The 1:1:1 Resonant Case

We consider a three-modal solution to equation (5.18), involving all the three resonant modes, a planar symmetric mode $\hat{v}_j(s)$, a planar anti-symmetric mode $\hat{v}_k(s)$, and an out-of-plane anti-symmetric mode $\hat{w}_k(s)$, with $k = j + 1$, $\hat{v}_k = \hat{w}_k =$

$\sin\left(\frac{k\pi s}{l}\right)$. Close to the cross-over point, it is:

$$\omega_{0k} = \frac{k\pi}{l} \sqrt{\frac{T_0}{m}}, \quad \omega_{0j} = \omega_{0k} + \epsilon\sigma, \quad (5.35)$$

where σ is a detuning parameter.

The generating solution reads:

$$\begin{pmatrix} \hat{v}_0 \\ \hat{w}_0 \\ \hat{e}_0 \end{pmatrix} = a_1 \begin{pmatrix} \hat{v}_{0j}(s) \\ 0 \\ \hat{e}_{0j} \end{pmatrix} + a_2 \begin{pmatrix} \hat{v}_{0k}(s) \\ 0 \\ 0 \end{pmatrix} + a_3 \begin{pmatrix} 0 \\ \hat{w}_{0k}(s) \\ 0 \end{pmatrix}, \quad (5.36)$$

where a_1, a_2, a_3 are arbitrary amplitudes. Then, the properties of eigenmodes,

$$\begin{aligned} \int_0^l \begin{pmatrix} \hat{v}_{0j} \\ 0 \end{pmatrix}^T \left[T_0 \begin{pmatrix} a_1 \hat{v}_{0j}'' + a_2 \hat{v}_{0k}'' \\ a_3 \hat{w}_{0k}'' \end{pmatrix} + m\omega_{0j}^2 \begin{pmatrix} a_1 \hat{v}_{0j} + a_2 \hat{v}_{0k} \\ a_3 \hat{w}_{0k} \end{pmatrix} + \begin{pmatrix} EA\bar{\kappa} \\ 0 \end{pmatrix} a_1 \hat{e}_{0j} \right] ds &= \begin{pmatrix} 0 \\ 0 \end{pmatrix} \\ \int_0^l \begin{pmatrix} \hat{v}_{0k} \\ 0 \end{pmatrix}^T \left[T_0 \begin{pmatrix} a_1 \hat{v}_{0j}'' + a_2 \hat{v}_{0k}'' \\ a_3 \hat{w}_{0k}'' \end{pmatrix} + m\omega_{0j}^2 \begin{pmatrix} a_1 \hat{v}_{0j} + a_2 \hat{v}_{0k} \\ a_3 \hat{w}_{0k} \end{pmatrix} + \begin{pmatrix} EA\bar{\kappa} \\ 0 \end{pmatrix} a_1 \hat{e}_{0j} \right] ds &= \begin{pmatrix} 0 \\ 0 \end{pmatrix} \\ \int_0^l \begin{pmatrix} 0 \\ \hat{w}_{0k} \end{pmatrix}^T \left[T_0 \begin{pmatrix} a_1 \hat{v}_{0j}'' + a_2 \hat{v}_{0k}'' \\ a_3 \hat{w}_{0k}'' \end{pmatrix} + m\omega_{0j}^2 \begin{pmatrix} a_1 \hat{v}_{0j} + a_2 \hat{v}_{0k} \\ a_3 \hat{w}_{0k} \end{pmatrix} + \begin{pmatrix} EA\bar{\kappa} \\ 0 \end{pmatrix} a_1 \hat{e}_{0j} \right] ds &= \begin{pmatrix} 0 \\ 0 \end{pmatrix} \end{aligned}$$

We get the followings respectively,

$$\begin{aligned} a_1 \int_0^l \hat{v}_{0j} \hat{v}_{0j}'' ds + a_2 \int_0^l \hat{v}_{0j} \hat{v}_{0k}'' ds + \frac{m\omega_{0j}^2}{T_0} a_1 \int_0^l \hat{v}_{0j}^2 ds \\ + a_1 \frac{EA}{T_0} \bar{\kappa} \int_0^l \hat{v}_{0j} \hat{e}_{0j} ds + \frac{m\omega_{0j}^2}{T_0} a_2 \int_0^l \hat{v}_{0j} \hat{v}_{0k} ds = 0, \end{aligned} \quad (5.37)$$

$$\begin{aligned} a_1 \int_0^l \hat{v}_{0k} \hat{v}_{0j}'' ds + a_2 \int_0^l \hat{v}_{0k} \hat{v}_{0k}'' ds + \frac{m\omega_{0j}^2}{T_0} a_1 \int_0^l \hat{v}_{0k} \hat{v}_{0j} ds \\ + a_1 \frac{EA}{T_0} \bar{\kappa} \int_0^l \hat{v}_{0k} \hat{e}_{0j} ds + \frac{m\omega_{0j}^2}{T_0} a_2 \int_0^l \hat{v}_{0k}^2 ds = 0, \end{aligned} \quad (5.38)$$

and,

$$\int_0^l \hat{w}_{0k} \hat{w}_{0k}'' ds + \frac{m\omega_{0j}^2}{T_0} \int_0^l \hat{w}_{0k}^2 ds = 0. \quad (5.39)$$

When the solution (5.36) is substituted in equation (5.18), the known term must be rendered orthogonal to the three eigenvectors which span the null space. Therefore, the following three algebraic conditions must hold simultaneously:

$$\int_0^l \begin{pmatrix} \hat{v}_{0j} \\ 0 \end{pmatrix}^T \left[(2m\lambda_{1j} + \mathbf{C}(U)) \begin{pmatrix} a_1\hat{v}_{0j} + a_2\hat{v}_{0k} \\ a_3\hat{w}_{0k} \end{pmatrix} - \zeta \begin{pmatrix} a_1\hat{v}_{0j}'' + a_2\hat{v}_{0k}'' \\ a_3\hat{w}_{0k}'' \end{pmatrix} - \zeta \begin{pmatrix} \frac{EA}{T_0}\bar{\kappa} \\ 0 \end{pmatrix} a_1\hat{e}_{0j} \right] ds = 0. \quad (5.40a)$$

$$\int_0^l \begin{pmatrix} \hat{v}_{0k} \\ 0 \end{pmatrix}^T \left[(2m\lambda_{1j} + \mathbf{C}(U)) \begin{pmatrix} a_1\hat{v}_{0j} + a_2\hat{v}_{0k} \\ a_3\hat{w}_{0k} \end{pmatrix} - \zeta \begin{pmatrix} a_1\hat{v}_{0j}'' + a_2\hat{v}_{0k}'' \\ a_3\hat{w}_{0k}'' \end{pmatrix} - \zeta \begin{pmatrix} \frac{EA}{T_0}\bar{\kappa} \\ 0 \end{pmatrix} a_1\hat{e}_{0j} \right] ds = 0. \quad (5.40b)$$

$$\int_0^l \begin{pmatrix} 0 \\ \hat{w}_{0k} \end{pmatrix}^T \left[(2m\lambda_{1j} + \mathbf{C}(U)) \begin{pmatrix} a_1\hat{v}_{0j} + a_2\hat{v}_{0k} \\ a_3\hat{w}_{0k} \end{pmatrix} - \zeta \begin{pmatrix} a_1\hat{v}_{0j}'' + a_2\hat{v}_{0k}'' \\ a_3\hat{w}_{0k}'' \end{pmatrix} - \zeta \begin{pmatrix} \frac{EA}{T_0}\bar{\kappa} \\ 0 \end{pmatrix} a_1\hat{e}_{0j} \right] ds = 0. \quad (5.40c)$$

From the equation (5.40a),

$$\begin{aligned} & \int_0^l \begin{pmatrix} \hat{v}_{0j} \\ 0 \end{pmatrix}^T \left[\left((2m\lambda_{1j} + c_e + U\hat{c}_{22}^a) (a_1\hat{v}_{0j} + a_2\hat{v}_{0k}) + U\hat{c}_{23}^a a_3\hat{w}_{0k} \right) \right. \\ & \quad \left. - \zeta \begin{pmatrix} a_1\hat{v}_{0j}'' + a_2\hat{v}_{0k}'' \\ a_3\hat{w}_{0k}'' \end{pmatrix} - \zeta \begin{pmatrix} \frac{EA}{T_0}\bar{\kappa} \\ 0 \end{pmatrix} a_1\hat{e}_{0j} \right] ds = \begin{pmatrix} 0 \\ 0 \end{pmatrix}, \\ \Rightarrow & (2m\lambda_{1j} + c_e + U\hat{c}_{22}^a) a_1 \int_0^l \hat{v}_{0j}^2 ds + (2m\lambda_{1j} + c_e + U\hat{c}_{22}^a) a_2 \int_0^l \hat{v}_{0j}\hat{v}_{0k} ds \\ & + U\hat{c}_{23}^a a_3 \int_0^l \hat{v}_{0j}\hat{w}_{0k} ds - \zeta a_1 \int_0^l \hat{v}_{0j}\hat{v}_{0j}'' ds - \zeta a_2 \int_0^l \hat{v}_{0j}\hat{v}_{0k}'' ds - \zeta \frac{EA}{T_0}\bar{\kappa} a_1 \int_0^l \hat{v}_{0j}\hat{e}_{0j} ds = 0. \end{aligned}$$

By taking into account the properties of eigenmode (5.37), we get from the above

equation

$$\begin{aligned} & \left(2m\lambda_{1j} + c_e + U\hat{c}_{22}^a + \zeta \frac{m\omega_{0j}^2}{T_0} \right) a_1 \int_0^l \hat{v}_{0j}^2 ds \\ & + \left(2m\lambda_{1j} + c_e + U\hat{c}_{22}^a + \zeta \frac{m\omega_{0j}^2}{T_0} \right) a_2 \int_0^l \hat{v}_{0j} \hat{v}_{0k} ds + U\hat{c}_{23}^a a_3 \int_0^l \hat{v}_{0j} \hat{w}_{0k} ds = 0, \\ \Rightarrow & \left[2m\lambda_{1j} + \left(c_e + U\hat{c}_{22}^a + \zeta \frac{m\omega_{0j}^2}{T_0} \right) \right] a_1 = 0, \end{aligned}$$

by accounting for symmetry/ anti-symmetry of the modal shapes, some integrals of products disappear. From the equation (5.40b), we have

$$\begin{aligned} & (2m\lambda_{1j} + c_e + U\hat{c}_{22}^a) a_1 \int_0^l \hat{v}_{0j} \hat{v}_{0k} ds + (2m\lambda_{1j} + c_e + U\hat{c}_{22}^a) a_2 \int_0^l \hat{v}_{0k}^2 ds \\ & + U\hat{c}_{23}^a a_3 \int_0^l \hat{v}_{0k} \hat{w}_{0k} ds - \zeta a_1 \int_0^l \hat{v}_{0k} \hat{v}_{0j}'' ds - \zeta a_2 \int_0^l \hat{v}_{0k} \hat{v}_{0k}'' ds - \zeta \frac{EA}{T_0} \bar{\kappa} a_1 \int_0^l \hat{v}_{0k} \hat{e}_{0j} ds = 0, \\ \Rightarrow & \left(2m\lambda_{1j} + c_e + U\hat{c}_{22}^a + \zeta \frac{m\omega_{0j}^2}{T_0} \right) a_1 \int_0^l \hat{v}_{0j} \hat{v}_{0k} ds \\ & + \left(2m\lambda_{1j} + c_e + U\hat{c}_{22}^a + \zeta \frac{m\omega_{0j}^2}{T_0} \right) a_2 \int_0^l \hat{v}_{0k}^2 ds + U\hat{c}_{23}^a a_3 \int_0^l \hat{v}_{0k} \hat{w}_{0k} ds = 0, \\ \Rightarrow & \left[2m\lambda_{1j} + \left(c_e + U\hat{c}_{22}^a + \zeta \left(\frac{k\pi}{l} \right)^2 \right) \right] a_2 + U\hat{c}_{23}^a a_3 = 0. \end{aligned}$$

From the equation (5.40c), we get

$$\begin{aligned} & U\hat{c}_{32}^a a_1 \int_0^l \hat{v}_{0j} \hat{w}_{0k} ds + U\hat{c}_{32}^a a_2 \int_0^l \hat{v}_{0k} \hat{w}_{0k} ds \\ & + (2m\lambda_{1j} + c_e + U\hat{c}_{33}^a) a_3 \int_0^l \hat{w}_{0k}^2 ds - \zeta a_3 \int_0^l \hat{w}_{0k} \hat{w}_{0k}'' ds = 0, \\ \Rightarrow & [U\hat{c}_{32}^a a_2 + (2m\lambda_{1j} + c_e + U\hat{c}_{33}^a) a_3] \int_0^l \hat{w}_{0k}^2 ds + \zeta a_3 \frac{m\omega_{0j}^2}{T_0} \int_0^l \hat{w}_{0k}^2 ds = 0, \\ \Rightarrow & U\hat{c}_{32}^a a_2 + \left[2m\lambda_{1j} + c_e + U\hat{c}_{33}^a + \zeta \left(\frac{k\pi}{l} \right)^2 \right] a_3 = 0. \end{aligned}$$

Collecting all equations, we obtain:

$$\left[2m\lambda_{1j} + \left(c_e + U\hat{c}_{22}^a + \zeta \frac{m\omega_{0j}^2}{T_0} \right) \right] a_1 = 0. \quad (5.41a)$$

$$\left[2m\lambda_{1j} + \left(c_e + U\hat{c}_{22}^a + \zeta \left(\frac{k\pi}{l} \right)^2 \right) \right] a_2 + U\hat{c}_{23}^a a_3 = 0. \quad (5.41b)$$

$$\left[2m\lambda_{1j} + \left(c_e + U\hat{c}_{33}^a + \zeta \left(\frac{k\pi}{l} \right)^2 \right) \right] a_3 + U\hat{c}_{23}^a a_2 = 0. \quad (5.41c)$$

Since the equation (5.41a) is uncoupled from the remaining two, and identical to that derived in the non-resonant case, the symmetric mode is not involved into the resonance, but behaves as it were non-resonant. The remaining two anti-symmetric modes, instead, interact; however, since the relevant equations are identical to that determined in the 1 : 1 resonance, the same results discussed here hold. Therefore, this case add nothing of new to the previous ones.

5.5 Numerical Results

A horizontal shallow flexible cable is considered as a sample to study its geometrical and mechanical properties. In this study, we considered the length of the cable is $l = 267\text{m}$, the mass per unit length is $m = 4.4\text{kg/m}$, the axial stiffness is $EA = 4.0 \times 10^8\text{N}$. Our study corresponds for the two different sags, $d = 3\text{m}$, which is denoted by S, for this case the internal damping $c_e = 0.056\text{kg}\times\text{s/m}$ and the external damping $\zeta = 239.4\text{kg}\times\text{m}\times\text{s}$, the curvature $\kappa = 3.37 \times 10^{-4}\text{m}^{-1}$ and the pretension $T_0 = 128.213\text{kN}$. The larger sag is taken as $d = 26\text{m}$, the case is denoted by L and for which the initial curvature is $\kappa = 2.92 \times 10^{-3}\text{m}^{-1}$, pretension $T_0 = 14.734\text{kN}$. The aerodynamic parameters, taken from [76], refers to the galloping for the ice-coated cable, they are, air mass per unit volume $\rho = 1.25\text{kg/m}^3$, radius $b = 0.102\text{m}$. The aerodynamic coefficients as drag coefficient $C_d(\alpha)$ and lift coefficient $C_l(\alpha)$ are plotted in Figure 5.4. Figure 5.4(b) is drawn to study the initial angle of ice-coating comparing the configuration with Den-Hartog criterion [16], which is $C_d(\alpha) + C_l'(\alpha) > 0$, and the initial attack angle is taken $\alpha_0 = \frac{\pi}{25} = 7.2^\circ$. Here, the numerical result are described for the cases S and L, where S stands for smaller sag, L for larger sag respectively.

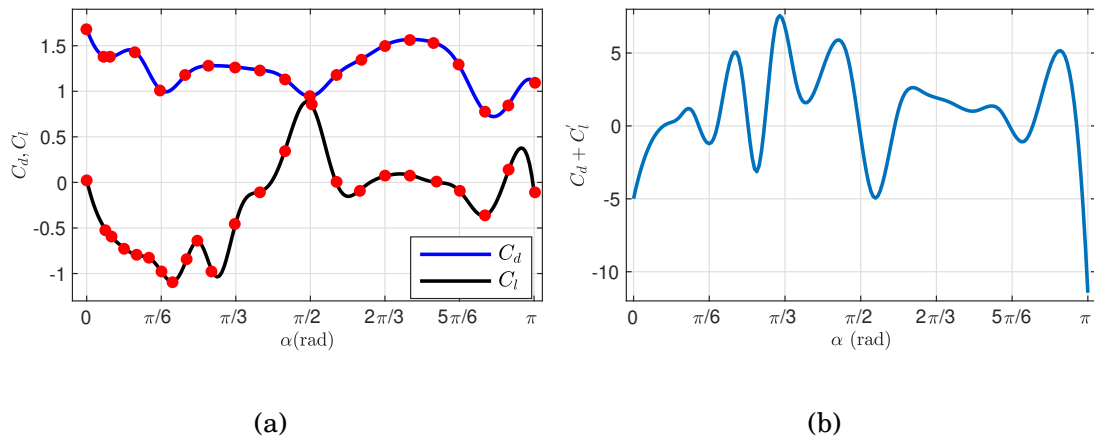


Figure 5.4: Aerodynamic coefficients, taken from [9, 120]: (a) Drag and lift coefficients; (b) Values of $C_d + C_l'$

The solution of the system (5.9) in terms of the critical modes with respect to velocity and modal frequency of the oscillation are investigated as exact galloping analysis comparing with analytical and numerical studies. In table 5.1 and table 5.2, the critical velocity and modal frequencies are compared between exact and numerical solutions in two different cases. The results of exact galloping analysis and numerical treatment with two methods are showing a good agreement. Particularly, the errors in modal frequencies between different approaches, in both cases, are practically zero.

Table 5.1: Critical modal conditions for exact and numerical solutions: velocity (ms^{-1})

Case	U_c exact.	U_c FDM	err. %	U_c GM	err. %
S	2.781	2.809	1.00	2.859	2.72
L	0.891	0.917	2.83	0.893	0.22

Table 5.2: Critical modal conditions for exact and numerical solutions: frequency (rad/s)

Case	ω_c exact.	ω_c FDM	err. %	ω_c GM	err. %
S	4.017	4.017	0.0	4.016	0.02
L	1.361	1.361	0.0	1.361	0.0

The numerical representation of modal shapes of the exact galloping analysis comparing with numerical methods are depicted in Figure 5.5 - Figure 5.8. Figure 5.5 and Figure 5.6 represent the normal (\hat{v}) and binormal (\hat{w}) components of displacement respectively, for the case S. The modal shape is anti-symmetric and complex with the same magnitude. The modal shape for the larger sag case (L) are

shown in Figure 5.7 and Figure 5.8; where the critical mode is anti-symmetric and complex. The numeric results are in good agreement with exact analysis.

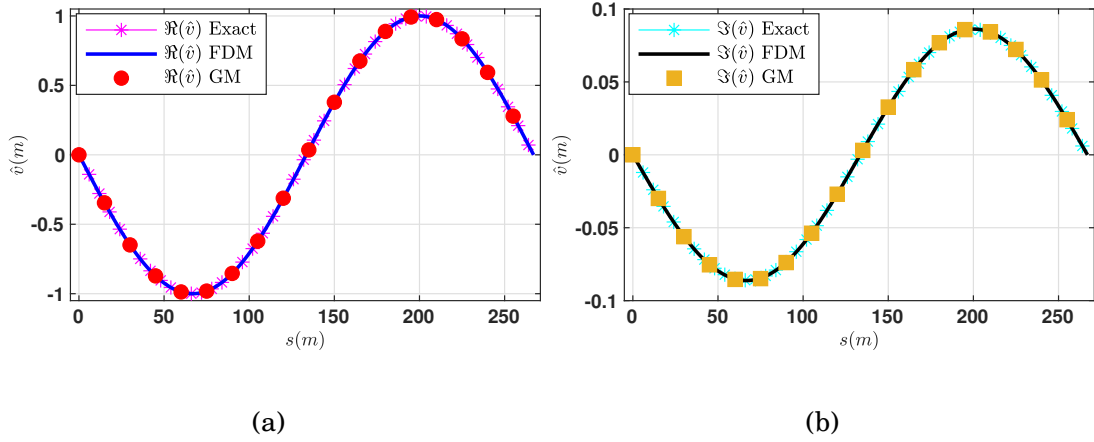


Figure 5.5: critical mode for case S: (a) Real parts of \hat{v} ; (b) imaginary parts of \hat{v}

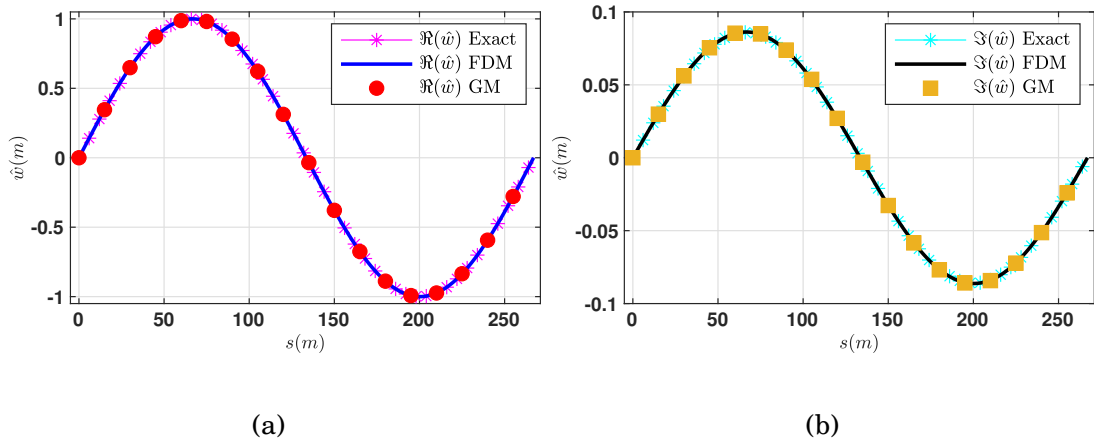


Figure 5.6: critical mode for case S: (a) real parts of \hat{w} ; (b) imaginary parts of \hat{w}

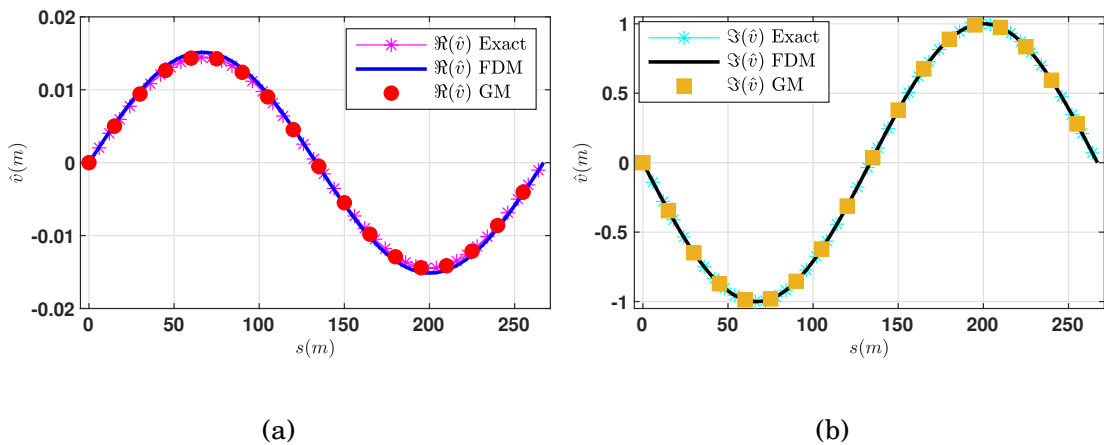


Figure 5.7: critical mode for case L: (a) real parts of \hat{v} ; (b) imaginary parts of \hat{v}

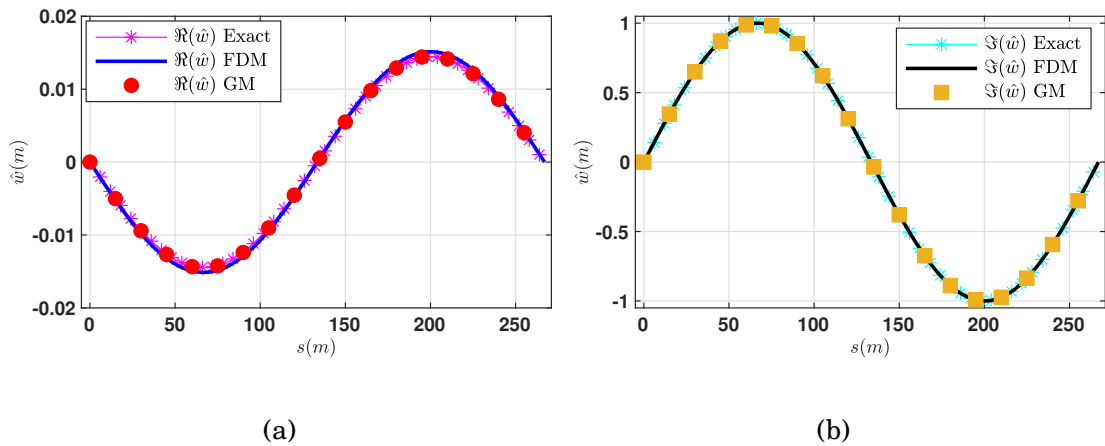


Figure 5.8: critical mode for case L: (a) real parts of \hat{w} ; (b) imaginary parts of \hat{w}

5.5.1 The non-resonant case

For the non-resonant case, we have the configuration having only planar displacement. Table 5.3 and Table 5.4 display the comparison of the wind speed between the asymptotic analysis and the numerical analysis with the corresponding modal frequencies.

Table 5.3: Critical modal conditions for analytical and numerical solutions: velocity (ms^{-1})

Case	U_c non-res.	U_c FDM	err. %	U_c GM	err. %
S	2.3159	2.3161	0.008	2.3180	0.09
L	1.5595	1.5760	1.04	1.5800	1.29

Table 5.4: Critical modal conditions for analytical and numerical solutions: frequency (rad/s)

Case	ω_c non-res.	ω_c FDM	err. %	ω_c GM	err. %
S	3.426	3.426	0.0	3.426	0.0
L	1.947	1.947	0.0	1.947	0.0

From the above table 5.3 and table 5.4, the critical wind velocities and modal frequencies for two different cases, in analytical analysis, are agreed well with the finite difference and Galerkin's methods, specially the modal frequencies. The numerical solution as critical velocity and modal frequency for the non-resonant case are drawn in the Figure 5.9 and Figure 5.10 for the cases S and L, respectively. For the small sag (S) and larger sag (L) cases, the critical mode is symmetric and

complex. The two numerical methods are fitted well with the same amplitude. For the case S, along the span, the mode shape has one semi-wave ; and for the case L, it has three semi-wave shapes.

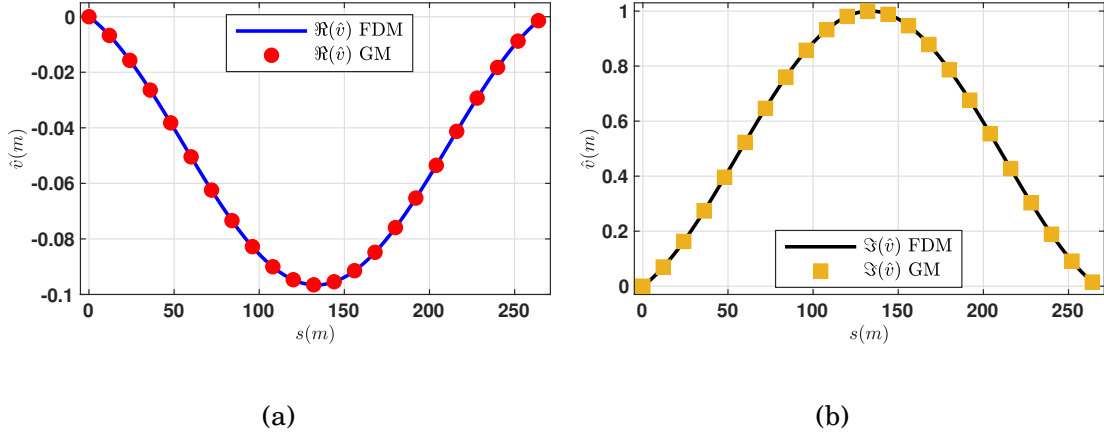


Figure 5.9: critical mode for case S: (a) real parts of \hat{v} ; (b) imaginary parts of \hat{v}

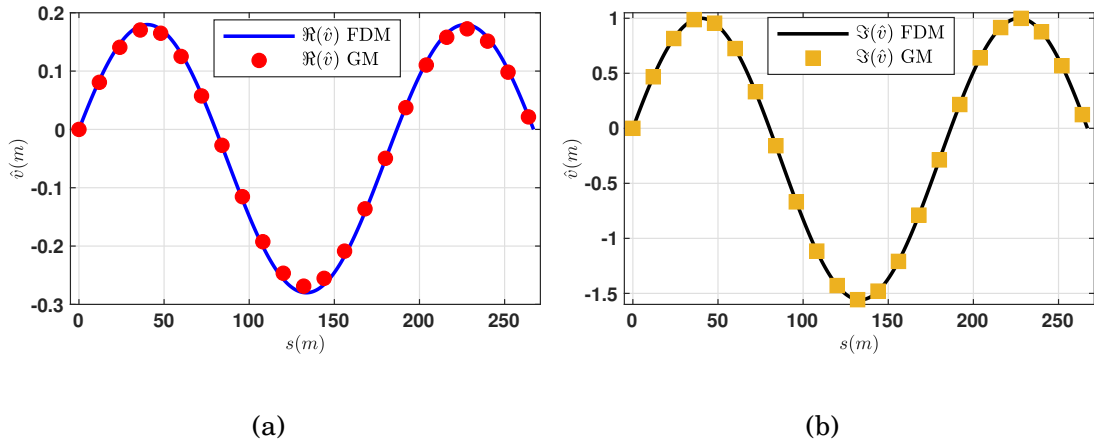


Figure 5.10: critical mode for case L: (a) real parts of \hat{v} ; (b) imaginary parts of \hat{v}

5.5.2 One - One resonant case

For the smaller sag (S) case: with different initial attack angles and aerodynamic coefficients, the stability conditions of equilibrium are analyzed, are as follows:

- at initial attack angle, $\alpha = \frac{\pi}{20} = 9^\circ$, $\text{tr}\mathbf{B}^a = 0.141 > 0$, $\det\mathbf{B}^a = -0.0028 < 0$, a simple Hopf bifurcation occurs at wind velocity $U_c = 5.011\text{m/s}$ with a real eigenvector $(\mathbf{a}_1^{(1)}, \mathbf{a}_2^{(1)}) = (4.718, 1)$.

- at initial attack angle, $\alpha = \frac{3\pi}{50} = 10.8^\circ$, $\text{tr}\mathbf{B}^a = 0.251 > 0$, $\det\mathbf{B}^a = 0.0041 > 0$, with the eigenvector $(\mathbf{a}_1^{(1)}, \mathbf{a}_2^{(1)}) = (-1.76, 1)$, the wind velocity $U_c = -5.001\text{m/s}$, i.e., the equilibrium remains stable.
- at initial attack angle, $\alpha = \frac{27\pi}{100} = 48.6^\circ$, $\text{tr}\mathbf{B}^a = -0.037 < 0$, $\det\mathbf{B}^a = -0.026 < 0$, a simple Hopf bifurcation occurs at wind velocity $U_c = 0.488\text{m/s}$ with eigenvector $(\mathbf{a}_1^{(1)}, \mathbf{a}_2^{(1)}) = (5.84, 1)$.
- for the aerodynamic coefficients, $c_{22}^a = -0.5$, $c_{23}^a = -0.2$, $c_{32}^a = 0.6$, and $c_{33}^a = 0.2$, $\text{tr}\mathbf{B}^a = -0.3 < 0$, $\det\mathbf{B}^a = 0.02 > 0$, a single Hopf bifurcation occurs at $U_c = 0.445\text{m/s}$ with a real eigenvector $(\mathbf{a}_1^{(1)}, \mathbf{a}_2^{(1)}) = (-0.666, 1)$, and a double Hopf bifurcation occurs at $U_c = 0.594\text{m/s}$ with two complex eigenvectors $(\mathbf{a}_1^{(1,2)}, \mathbf{a}_2^{(1,2)}) = (-0.56 \pm 0.079i, 1)$.

All the cases are described in the following table 5.5, where $IV(a)$ and $IV(b)$ indicates single Hopf and double Hopf bifurcation cases, respectively.

Table 5.5: Critical modal conditions for analytical and numerical solutions: velocity (ms^{-1})

Case	U_c analyt.	U_c FDM	err. %	U_c GM	err. %
I	5.011	5.011	0.0	4.827	3.81
II	-5.001	-5.002	0.02	-5.076	1.47
III	0.488	0.477	2.3	0.487	0.20
IV(a)	0.445	0.437	1.8	0.438	1.59
IV(b)	0.594	0.597	0.5	0.588	1.02

The following figures, Figure 5.11 to Figure 5.20, are representing the modal shapes of normal and binormal displacements, discussed in the above table 5.5. The results are showing good agreement with the two different numerical methods.

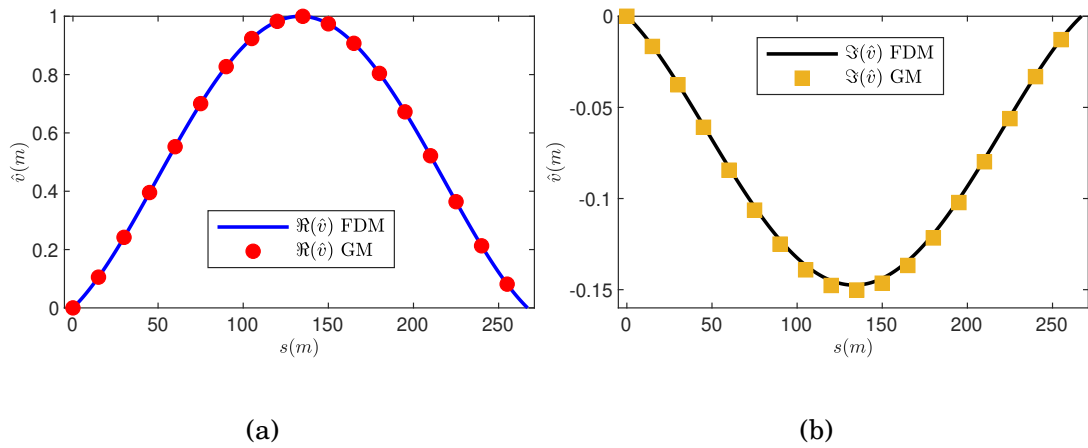


Figure 5.11: modal shapes for (case I in Figure 5.3-(b)): (a) real parts of \hat{v} ; (b) imaginary parts of \hat{v}

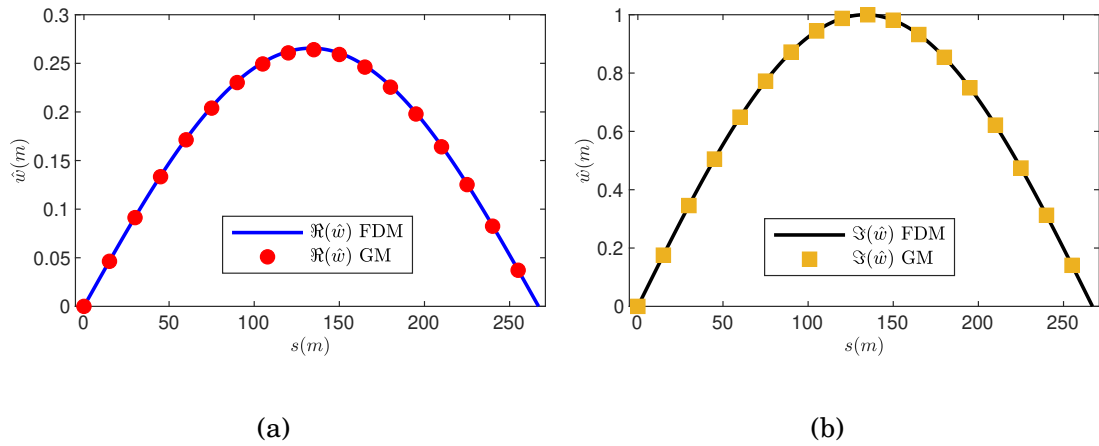


Figure 5.12: modal shapes for (case I in Figure 5.3-(b)): (a) real parts of \hat{w} ; (b) imaginary parts of \hat{w}

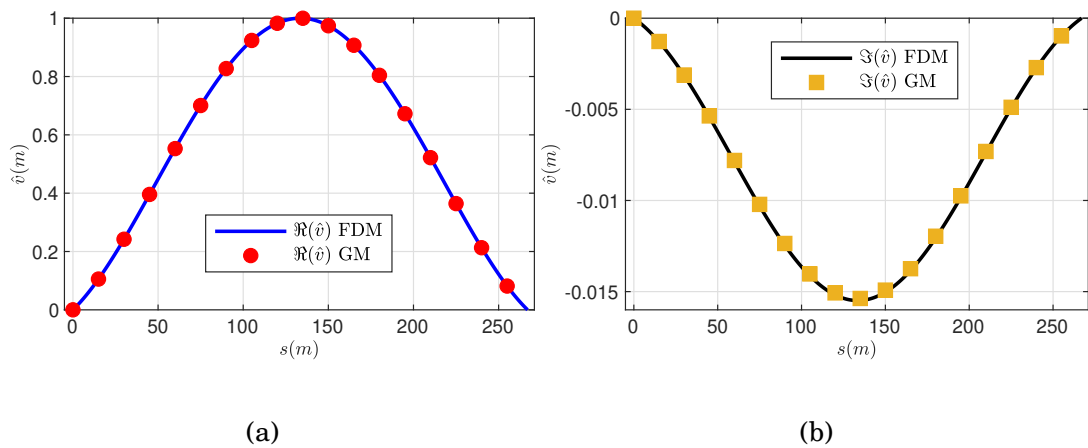


Figure 5.13: modal shapes for (case II in Figure 5.3-(b)): (a) real parts of \hat{v} ; (b) imaginary parts of \hat{v}

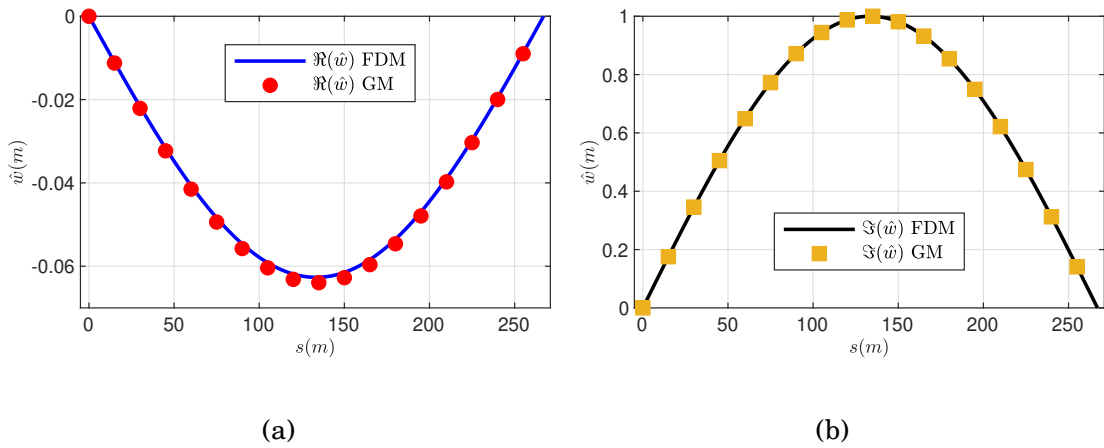


Figure 5.14: modal shapes for (case II in Figure 5.3-(b)): (a) real parts of \hat{w} ; (b) imaginary parts of \hat{w}

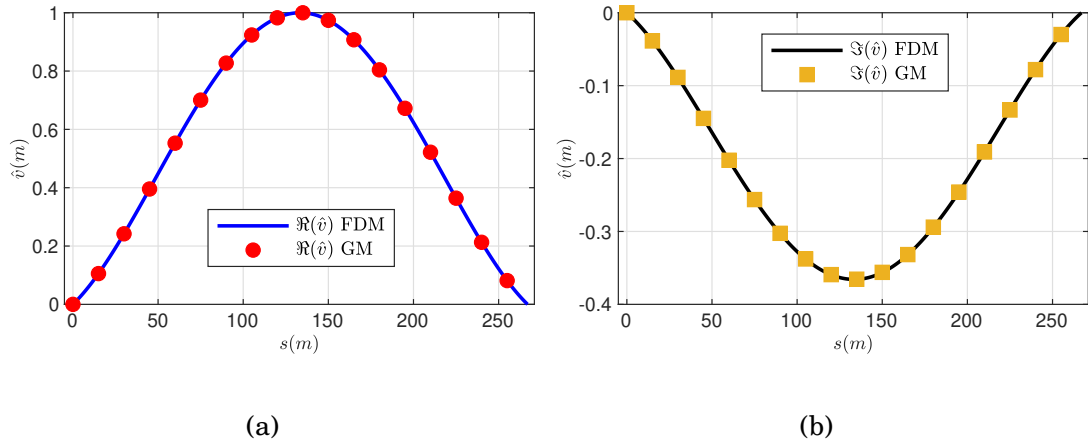


Figure 5.15: modal shapes for (case III in Figure 5.3-(b)): (a) real parts of \hat{v} ; (b) imaginary parts of \hat{v}

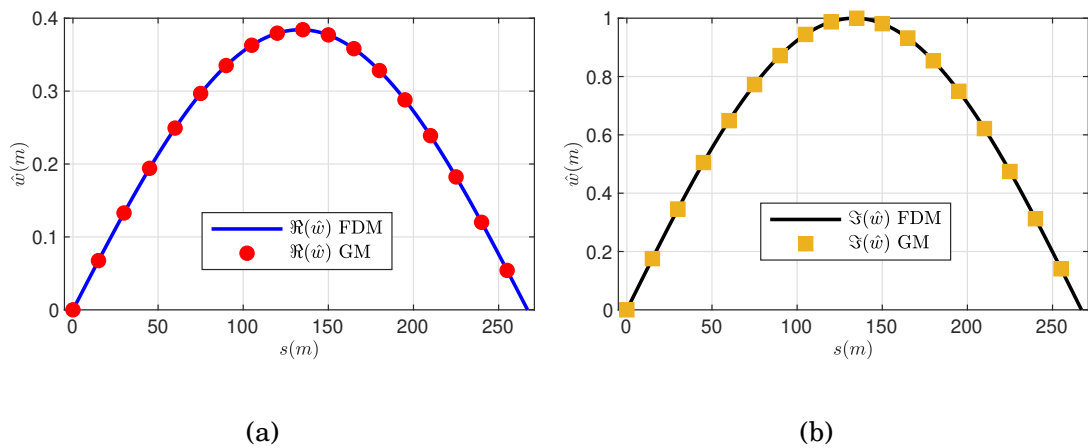


Figure 5.16: modal shapes for (case III in Figure 5.3-(b)): (a) real parts of \hat{w} ; (b) imaginary parts of \hat{w}

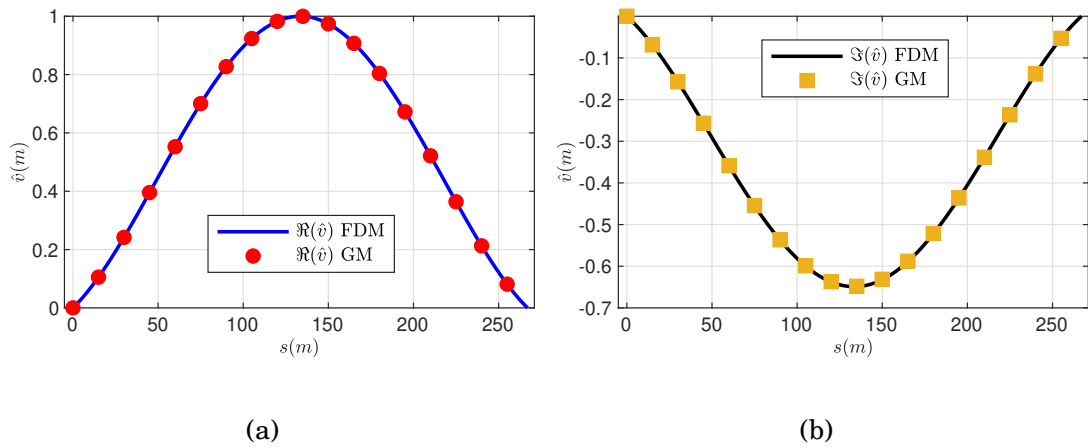


Figure 5.17: modal shapes for (case IV, curve (a), in Figure 5.3-(b)): (a) real parts of \hat{v} ; (b) imaginary parts of \hat{v}

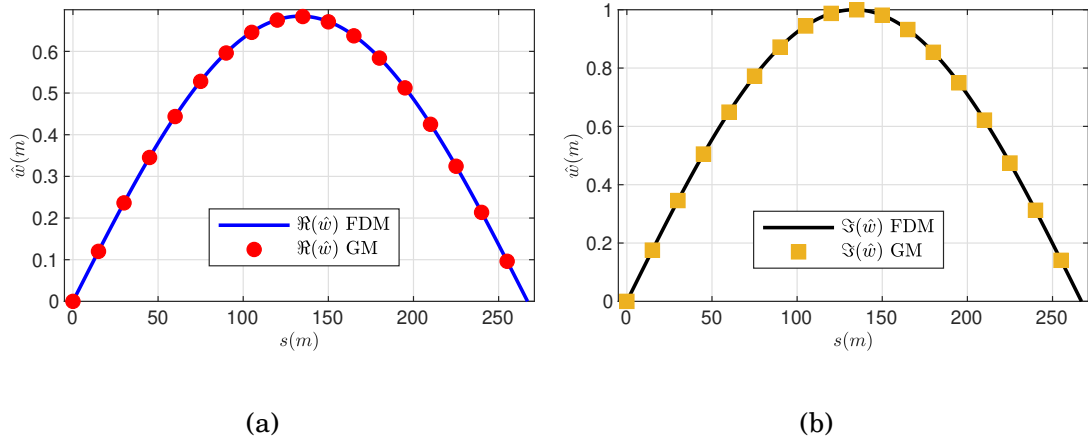


Figure 5.18: modal shapes for (case IV, curve (a), in Figure 5.3-(b)): (a) real parts of \hat{w} ; (b) imaginary parts of \hat{w}

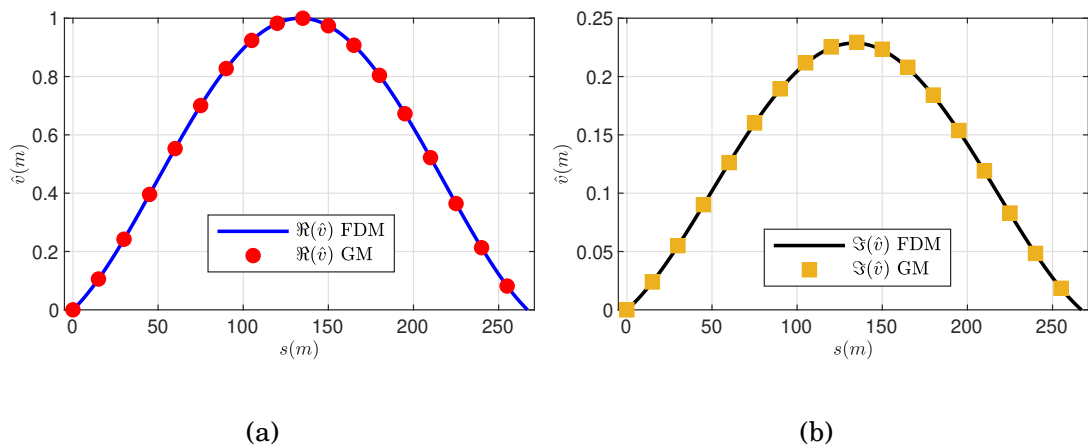


Figure 5.19: modal shapes for (case IV, curves (b), in Figure 5.3-(b)): (a) real parts of \hat{v} ; (b) imaginary parts of \hat{v}

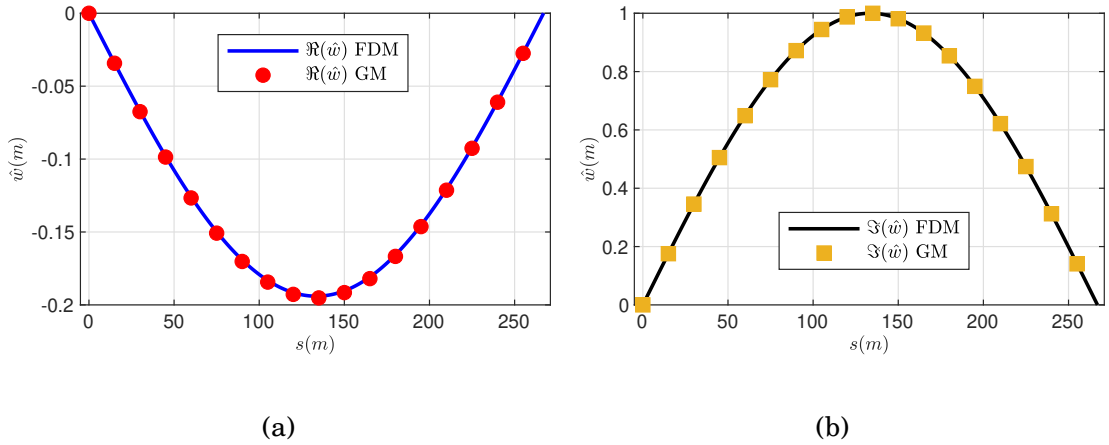


Figure 5.20: modal shapes for (case IV, curves (b), in Figure 5.3-(b)): (a) real parts of \hat{w} ; (b) imaginary parts of \hat{w}

For the larger sag (L) case, with the same aerodynamic coefficients, the outcomes of the analysis are described below:

- for $\text{tr}\mathbf{B}^a = 0.141 > 0, \det\mathbf{B}^a = -0.0028 < 0$, a simple Hopf bifurcation occurs at wind velocity $U_c = 1.692\text{ms}^{-1}$ with eigenvector $(\mathbf{a}_1^{(1)}, \mathbf{a}_2^{(1)}) = (4.71, 1)$.
- for $\text{tr}\mathbf{B}^a = 0.251 > 0, \det\mathbf{B}^a = 0.0041 > 0$, with the eigenvector $(\mathbf{a}_1^{(1)}, \mathbf{a}_2^{(1)}) = (-1.76, 1)$, the wind velocity $U_c = -1.689\text{ms}^{-1}$, i.e., the equilibrium remains stable.
- for $\text{tr}\mathbf{B}^a = -0.037 < 0, \det\mathbf{B}^a = -0.026 < 0$, a simple Hopf bifurcation occurs at wind velocity $U_c = 0.165\text{ms}^{-1}$ with eigenvector $(\mathbf{a}_1^{(1)}, \mathbf{a}_2^{(1)}) = (5.84, 1)$.
- for $\text{tr}\mathbf{B}^a = -0.3 < 0, \det\mathbf{B}^a = 0.02 > 0$, a single Hopf bifurcation occurs at $U_c = 0.150\text{ms}^{-1}$ with a real eigenvector $(\mathbf{a}_1^{(1)}, \mathbf{a}_2^{(1)}) = (-0.666, 1)$, and a double Hopf bifurcation occurs at $U_c = 0.200\text{ms}^{-1}$ with two complex eigenvectors $(\mathbf{a}_1^{(1,2)}, \mathbf{a}_2^{(1,2)}) = (-0.56 \pm 0.08i, 1)$.

Like above, the following table 5.6 depicts all the bifurcation conditions for the larger sag case with common frequency $\omega_c = 0.680\text{rad/s}$.

Table 5.6: Critical modal conditions for analytical and numerical solutions: velocity (ms^{-1})

Case	U_c analyt.	U_c FDM	err. %	U_c GM	err. %
I	1.692	1.73	2.24	1.75	3.31
II	-1.689	-1.63	3.62	-1.71	1.22
III	0.165	0.161	2.48	0.169	2.36
IV(a)	0.150	0.154	2.59	0.156	3.8
IV(b)	0.200	0.198	1.01	0.200	0.0

Figure 5.21 to Figure 5.30, depict the modal shapes of normal and out-of-normal displacements, discussed in the above table 5.6. The results are showing good agreement with the two different numerical methods.

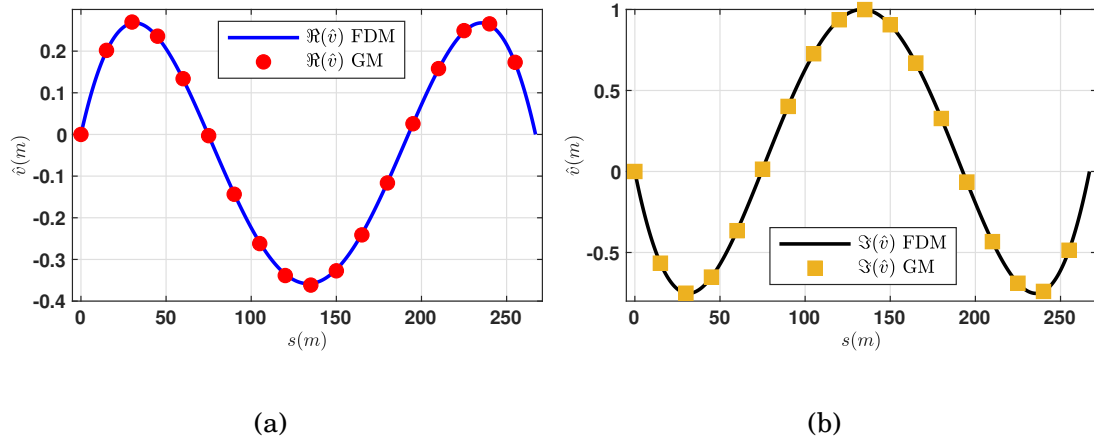


Figure 5.21: modal shapes for (case I in Figure 5.3-(b)): (a) real parts of \hat{v} ; (b) imaginary parts of \hat{v}

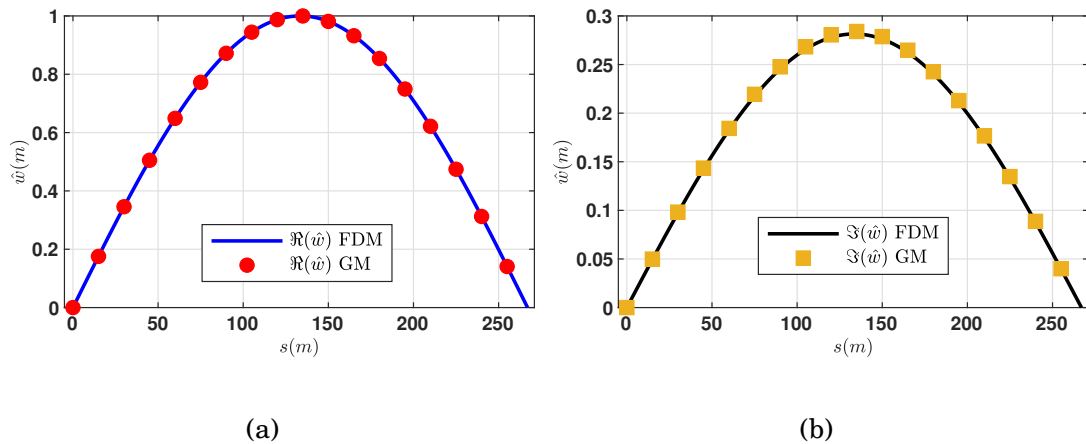


Figure 5.22: modal shapes for (case I in Figure 5.3-(b)): (a) real parts of \hat{w} ; (b) imaginary parts of \hat{w}

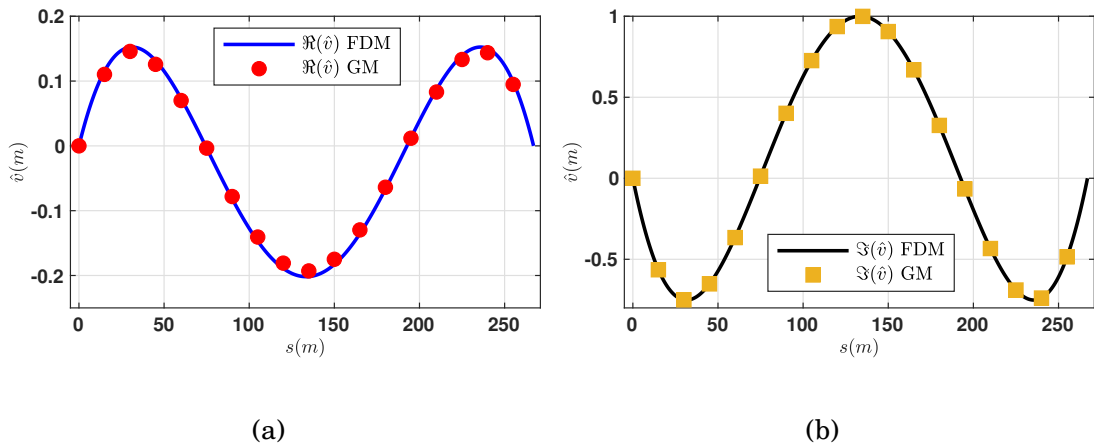


Figure 5.23: modal shapes for (case II in Figure 5.3-(b)): (a) real parts of \hat{v} ; (b) imaginary parts of \hat{v}

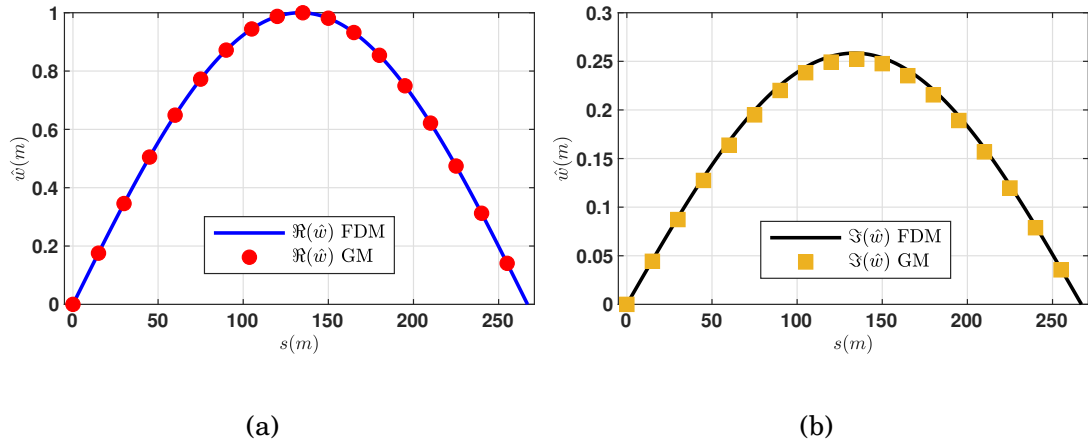


Figure 5.24: modal shapes for (case II in Figure 5.3-(b)): (a) real parts of \hat{w} ; (b) imaginary parts of \hat{w}

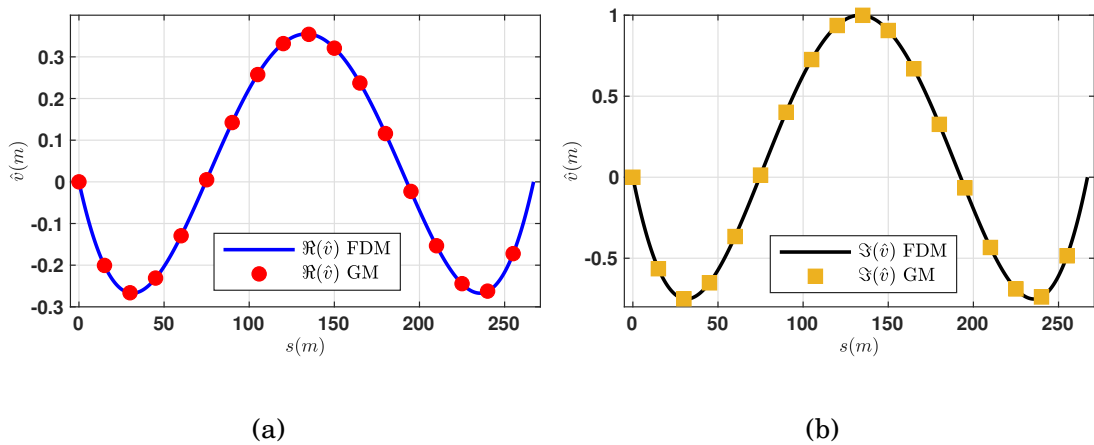


Figure 5.25: modal shapes for (case III in Figure 5.3-(b)): (a) real parts of \hat{v} ; (b) imaginary parts of \hat{v}

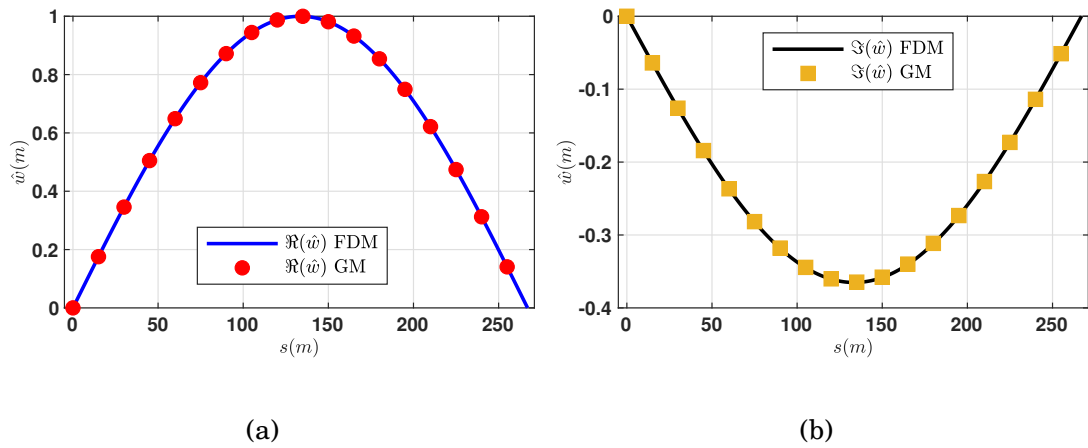


Figure 5.26: modal shapes for (case III in Figure 5.3-(b)): (a) real parts of \hat{w} ; (b) imaginary parts of \hat{w}

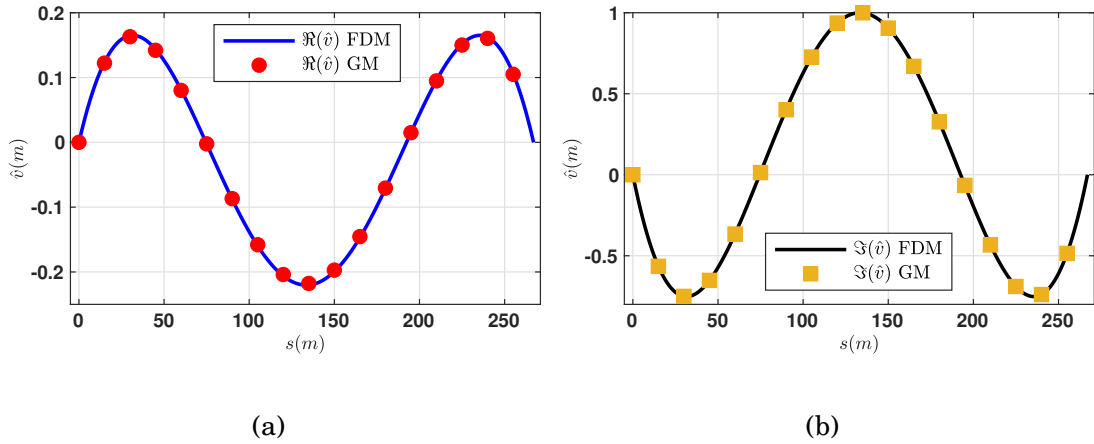


Figure 5.27: modal shapes for (case IV, curve (a), in Figure 5.3-(b)): (a) real parts of \hat{v} ; (b) imaginary parts of \hat{v}

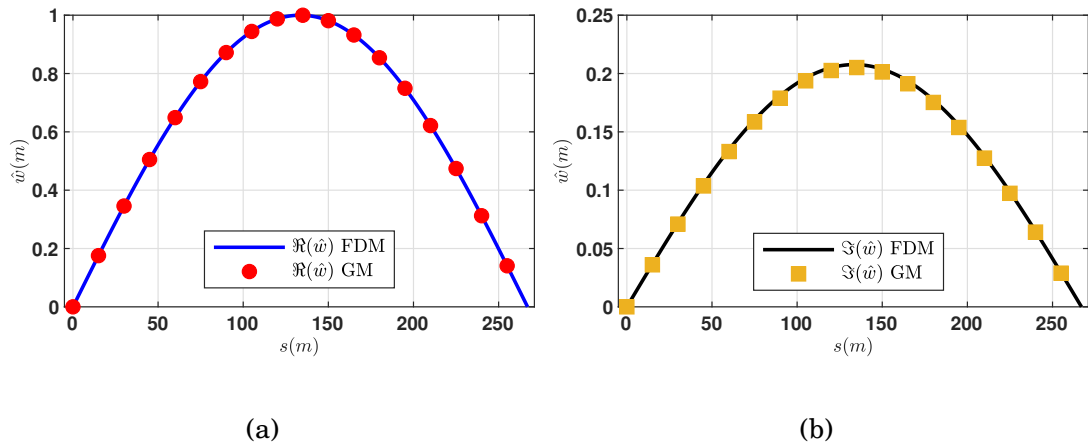


Figure 5.28: modal shapes for (case IV, curve (a), in Figure 5.3-(b)): (a) real parts of \hat{w} ; (b) imaginary parts of \hat{w}

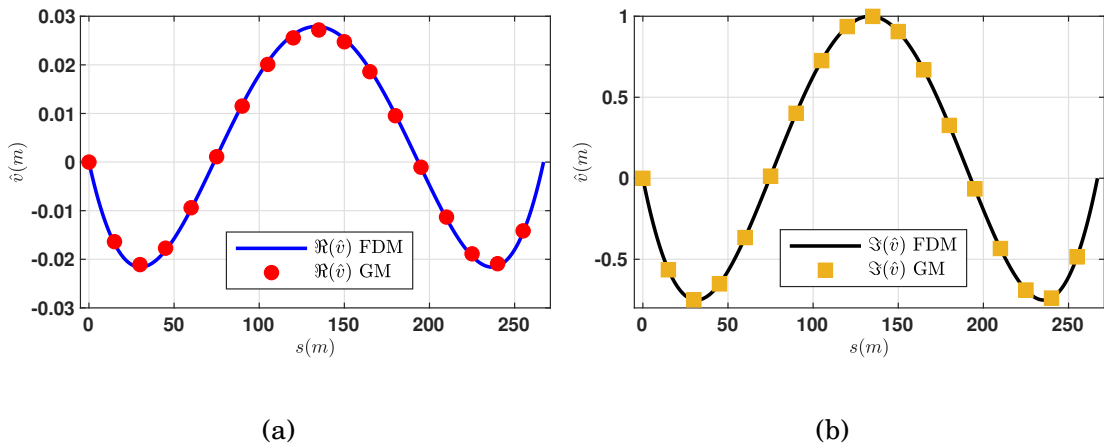


Figure 5.29: modal shapes for (case IV, curves (b), in Figure 5.3-(b)): (a) real parts of \hat{v} ; (b) imaginary parts of \hat{v}

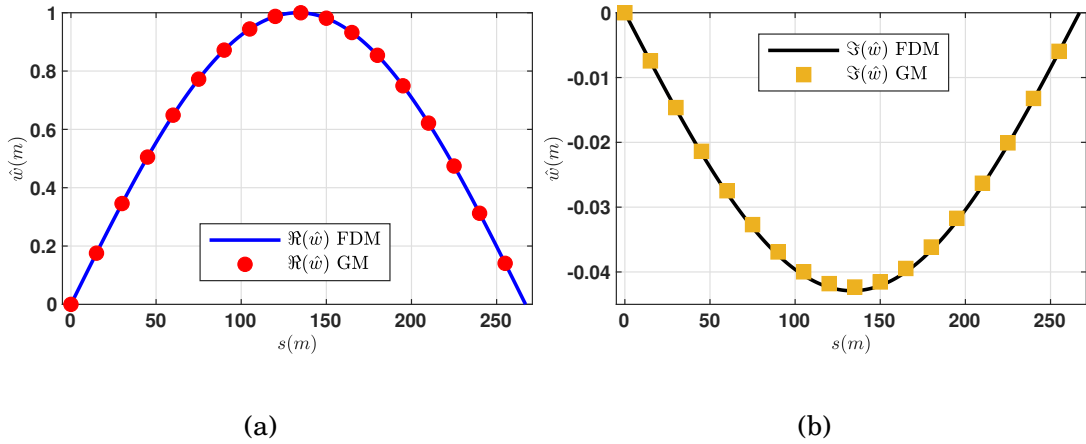


Figure 5.30: modal shapes for (case IV, curves (b), in Figure 5.3-(b)): (a) real parts of \hat{w} ; (b) imaginary parts of \hat{w}

5.5.3 The 1:1:1 resonant case

From the system of equations 5.41, the study of the non-resonant and 1:1 resonant cases hold here.

Bifurcation occurs at the critical wind velocity,

$$U_c = \frac{c_e + \zeta \frac{m\omega_{0j}^2}{T_0}}{|\hat{c}_{22}^a|}, \quad \hat{c}_{22}^a < 0 \quad (5.42)$$

with a real eigenvector $(\mathbf{a}_1, 0)$.

As analyzed above, the single Hopf bifurcation occurs for $\det \mathbf{B} = 0$ and $\text{tr} \mathbf{B} > 0$, or, double Hopf bifurcation occurs for $\text{tr} \mathbf{B} = 0$ and $\det \mathbf{B} > 0$. It follows that, a simple

Hopf bifurcation occurs (in cases I, III or IV-a) at:

$$U_c = 2 \frac{\left(c_e + \zeta \left(\frac{k\pi}{l} \right)^2 \right)}{-\text{tr}\mathbf{B}^a + \sqrt{\text{tr}^2\mathbf{B}^a - 4\det\mathbf{B}^a}}, \quad (5.43)$$

and, a double Hopf bifurcation occurs (in case IV-b) at:

$$U_c = -2 \frac{\left(c_e + \zeta \left(\frac{k\pi}{l} \right)^2 \right)}{\text{tr}\mathbf{B}^a}. \quad (5.44)$$

For the smaller sag (S) case:

- at initial attack angle, $\alpha = \frac{\pi}{20} = 9^\circ$, $\text{tr}\mathbf{B}^a = 0.141 > 0$, $\det\mathbf{B}^a = -0.0028 < 0$, bifurcation condition occurs at the critical velocity $U_c = 4.60\text{ms}^{-1}$ and a simple Hopf bifurcation occurs at wind velocity $U_c = 10.60\text{ms}^{-1}$ with a real eigenvector $(\mathbf{a}_1^{(1)}, \mathbf{a}_2^{(1)}) = (4.718, 1)$.
- at initial attack angle, $\alpha = \frac{3\pi}{50} = 10.8^\circ$, $\text{tr}\mathbf{B}^a = 0.251 > 0$, $\det\mathbf{B}^a = 0.0041 > 0$, bifurcation condition occurs at $U_c = -2.0\text{ms}^{-1}$ and with the eigenvector $(\mathbf{a}_1^{(1)}, \mathbf{a}_2^{(1)}) = (-1.76, 1)$, and the critical wind velocity is found $U_c = -10.58\text{ms}^{-1}$, i.e., the equilibrium remains stable.
- at initial attack angle, $\alpha = \frac{27\pi}{100} = 48.6^\circ$, $\text{tr}\mathbf{B}^a = -0.037 < 0$, $\det\mathbf{B}^a = -0.026 < 0$, bifurcation condition occurs at $U_c = 0.759\text{ms}^{-1}$, and a simple Hopf bifurcation occurs at wind velocity $U_c = 1.033\text{ms}^{-1}$ with eigenvector $(\mathbf{a}_1^{(1)}, \mathbf{a}_2^{(1)}) = (5.84, 1)$.
- for the aerodynamic coefficients, $c_{22}^a = -0.5$, $c_{23}^a = -0.2$, $c_{32}^a = 0.6$, and $c_{33}^a = 0.2$, $\text{tr}\mathbf{B}^a = -0.3 < 0$, $\det\mathbf{B}^a = 0.02 > 0$, bifurcation condition occurs at $U_c = 0.304\text{ms}^{-1}$, a single Hopf bifurcation occurs at $U_c = 0.942\text{ms}^{-1}$ with a real eigenvector $(\mathbf{a}_1^{(1)}, \mathbf{a}_2^{(1)}) = (-0.666, 1)$, and a double Hopf bifurcation occurs at $U_c = 1.257\text{ms}^{-1}$ with two complex eigenvectors $(\mathbf{a}_1^{(1,2)}, \mathbf{a}_2^{(1,2)}) = (-0.56 \pm 0.079i, 1)$.

All the cases are described in the following table 5.7 and 5.8, where $IV(a)$ and $IV(b)$ indicates single Hopf and double Hopf bifurcation cases, respectively.

Table 5.7: Critical modal conditions for analytical and numerical solutions with common modal frequency $\omega_{0j} = 3.42\text{rad/s}$: velocity (ms^{-1}); (Non-resonant part)

Case	U_c analyt.	U_c FDM	err. %	U_c GM	err. %
I	4.60	4.46	3.13	4.60	0.0
II	-2.00	-2.09	4.30	-2.03	1.47
III	0.759	0.757	0.26	0.753	0.79
IV	0.304	0.305	0.32	0.304	0.0

Table 5.8: Critical modal conditions for analytical and numerical solutions with common frequency $\omega_{0j} = 4.017\text{rad/s}$: velocity (ms^{-1})

Case	U_c analyt.	U_c FDM	err. %	U_c GM	err. %
I	10.60	10.66	0.56	10.67	0.65
II	-10.58	-10.59	0.09	-10.60	0.18
III	1.033	1.035	0.19	1.035	0.19
IV(a)	0.942	0.944	0.21	0.946	0.42
IV(b)	1.257	1.262	0.39	1.265	0.63

with the corresponding mode shapes, presented in the following figures:

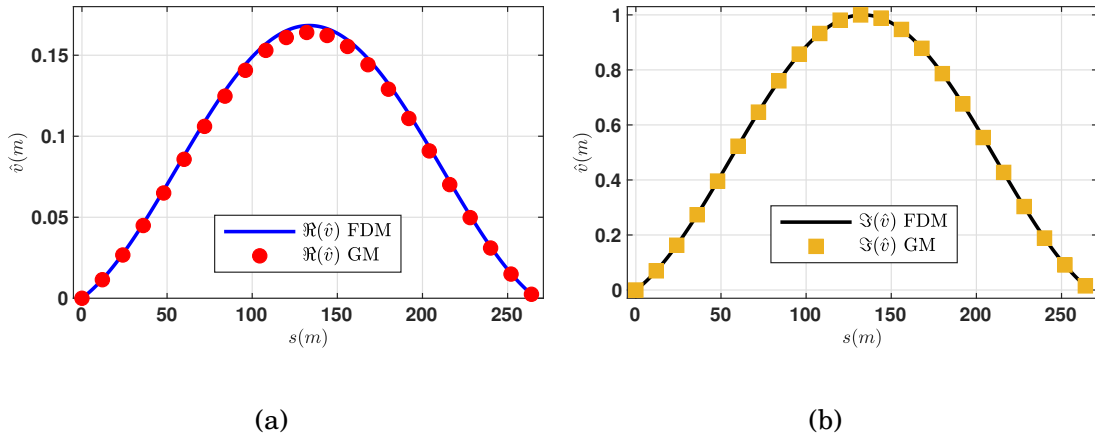


Figure 5.31: modal shapes for the non-resonant part of (case I in Figure 5.3-(b)): (a) real and (b) imaginary parts of \hat{v}

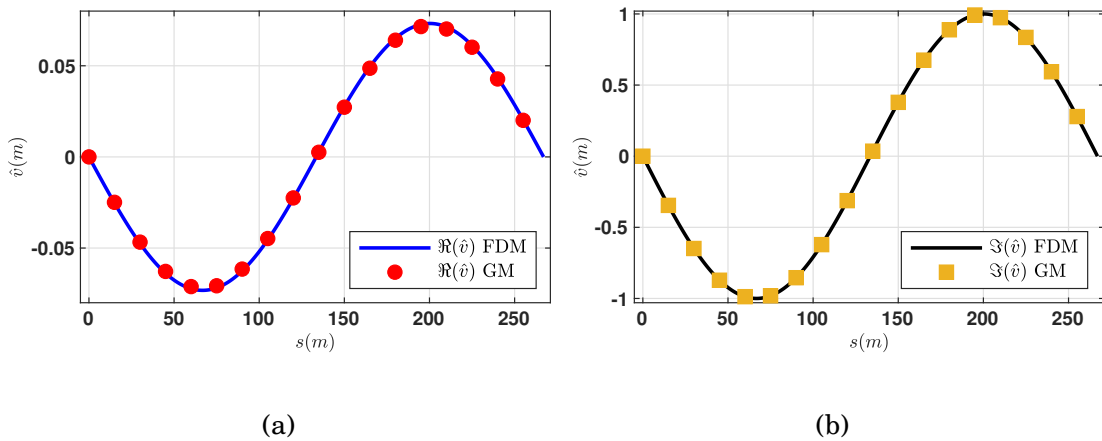


Figure 5.32: modal shapes for (case I in Figure 5.3-(b)): (a) real parts of \hat{v} ; (b) imaginary parts of \hat{v}

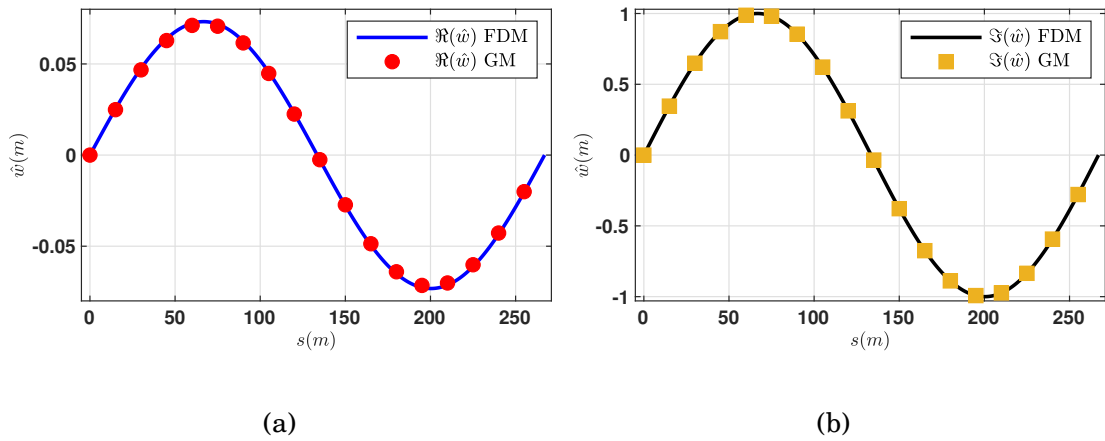


Figure 5.33: modal shapes for (case I in Figure 5.3-(b)): (a) real parts of \hat{w} ; (b) imaginary parts of \hat{w}

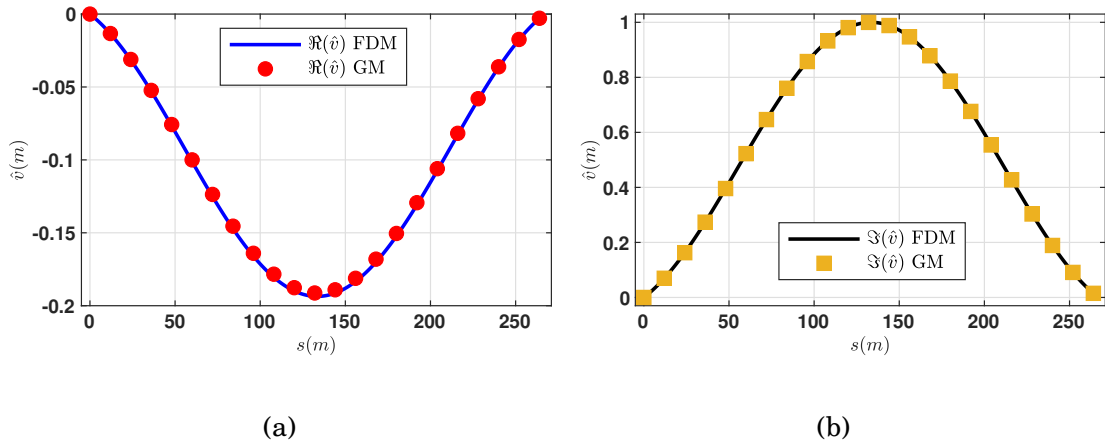


Figure 5.34: modal shapes for the non-resonant part of (case II in Figure 5.3-(b)): (a) real and (b) imaginary parts of \hat{v}

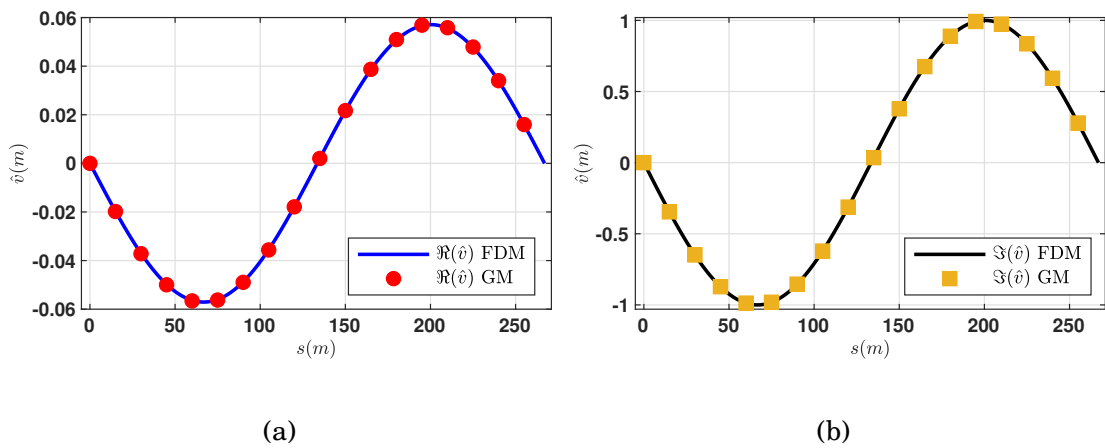


Figure 5.35: modal shapes for (case II in Figure 5.3-(b)): (a) real parts of \hat{v} ; (b) imaginary parts of \hat{v}

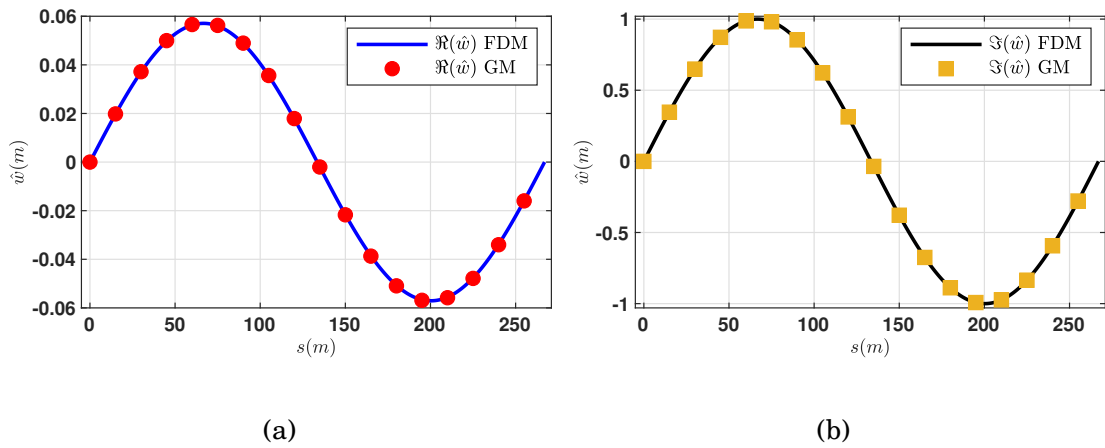


Figure 5.36: modal shapes for (case II in Figure 5.3-(b)): (a) real parts of \hat{w} ; (b) imaginary parts of \hat{w}

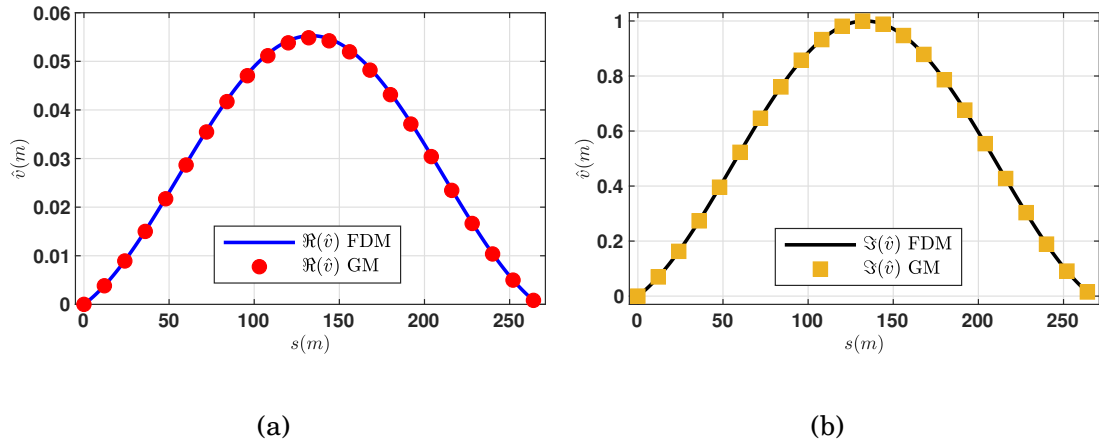


Figure 5.37: modal shapes for non-resonant part of (case III in Figure 5.3-(b)): (a) real and (b) imaginary parts of \hat{v}

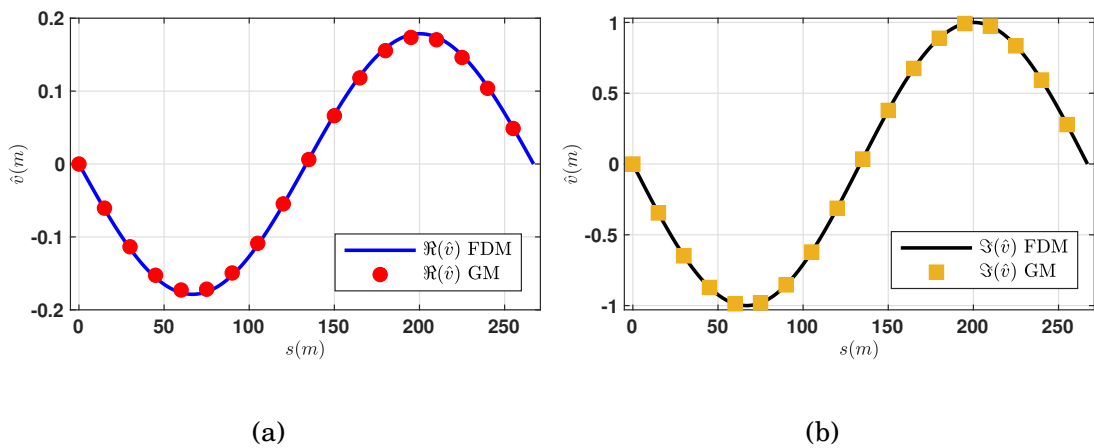


Figure 5.38: modal shapes for (case III in Figure 5.3-(b)): (a) real parts of \hat{v} ; (b) imaginary parts of \hat{v}

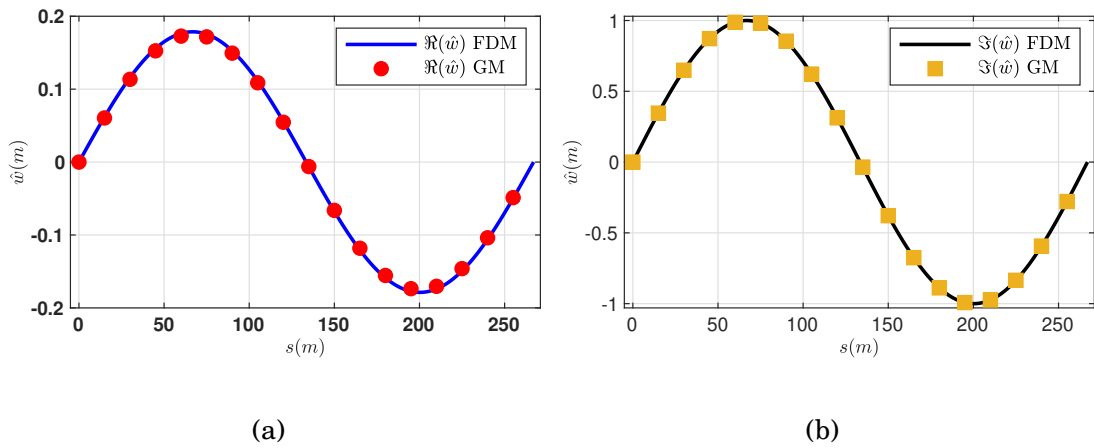


Figure 5.39: modal shapes for (case III in Figure 5.3-(b)): (a) real parts of \hat{w} ; (b) imaginary parts of \hat{w}

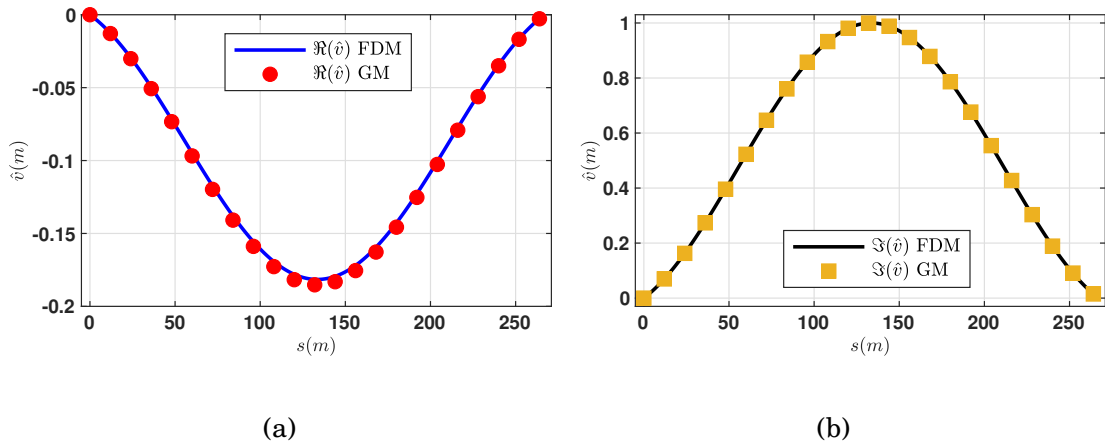


Figure 5.40: modal shapes for non-resonant part of (case IV in Figure 5.3-(b)): (a) real and (b) imaginary parts of \hat{v}

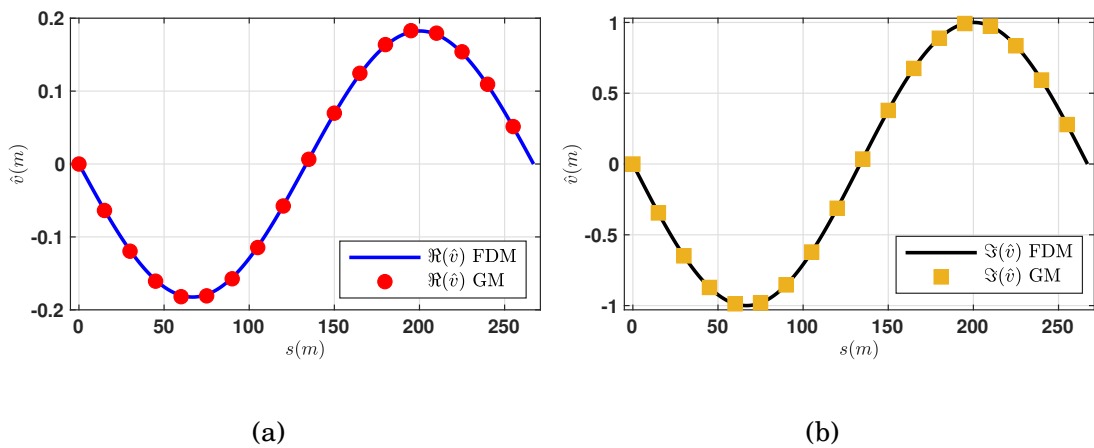


Figure 5.41: modal shapes for (case IV, curve (a), in Figure 5.3-(b)): (a) real parts of \hat{v} ; (b) imaginary parts of \hat{v}

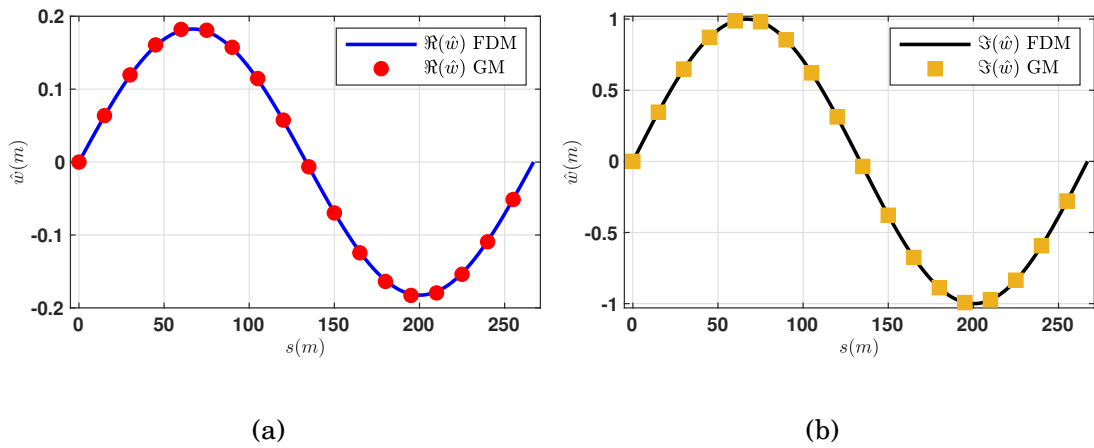


Figure 5.42: modal shapes for (case IV, curve (a), in Figure 5.3-(b)): (a) real parts of \hat{w} ; (b) imaginary parts of \hat{w}

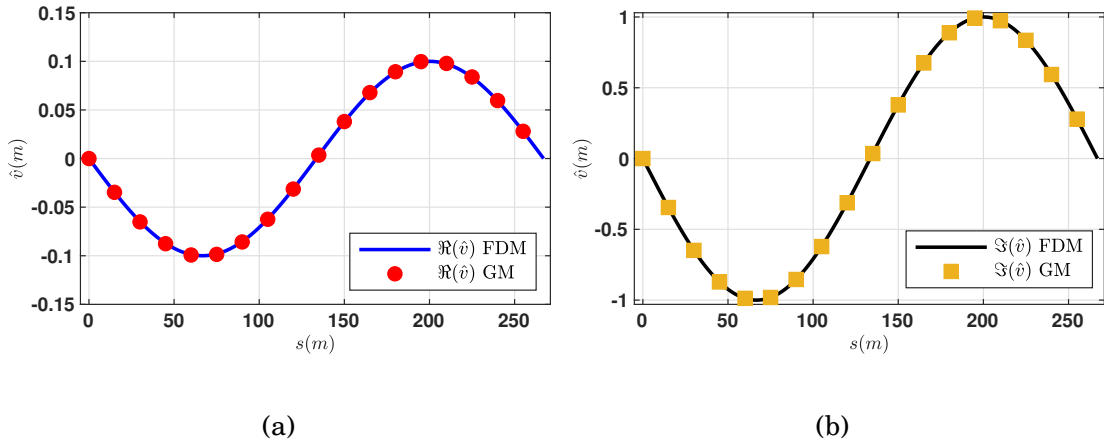


Figure 5.43: modal shapes for (case IV, curves (b), in Figure 5.3-(b)): (a) real parts of \hat{v} ; (b) imaginary parts of \hat{v}

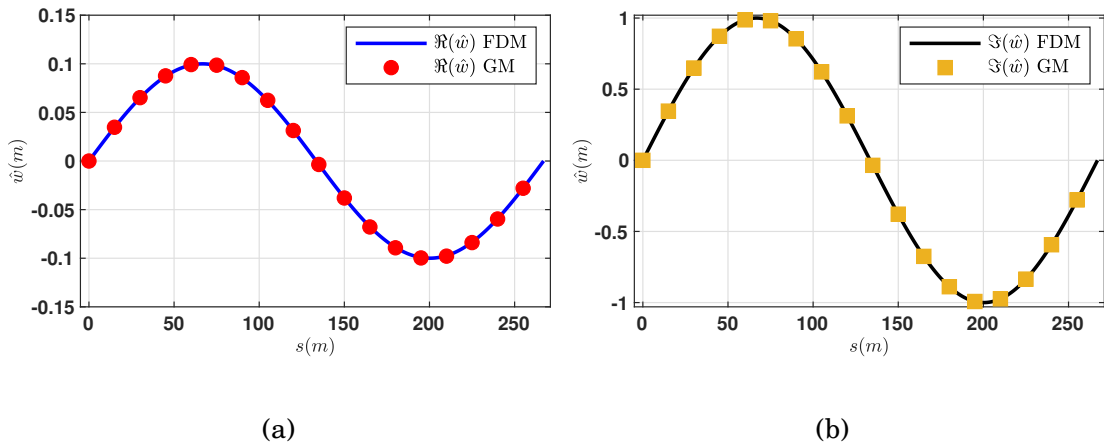


Figure 5.44: modal shapes for (case IV, curves (b), in Figure 5.3-(b)): (a) real parts of \hat{w} ; (b) imaginary parts of \hat{w}

For the larger sag (L) case with the same aerodynamic coefficients,

- for $\text{tr}\mathbf{B}^a = 0.141 > 0, \det\mathbf{B}^a = -0.0028 < 0$, bifurcation condition occurs at $U_c = 3.09\text{ms}^{-1}$, and a simple Hopf bifurcation occurs at wind velocity $U_c = 3.39\text{ms}^{-1}$ with eigenvector $(\mathbf{a}_1^{(1)}, \mathbf{a}_2^{(1)}) = (4.71, 1)$.
- for $\text{tr}\mathbf{B}^a = 0.251 > 0, \det\mathbf{B}^a = 0.0041 > 0$, for the non-resonant case, the wind velocity $U_c = -1.34\text{ms}^{-1}$ and for the 1:1 resonance, with the eigenvector $(\mathbf{a}_1^{(1)}, \mathbf{a}_2^{(1)}) = (-1.76, 1)$ the wind velocity $U_c = -3.39\text{ms}^{-1}$, i.e., the equilibrium remains stable.
- for $\text{tr}\mathbf{B}^a = -0.037 < 0, \det\mathbf{B}^a = -0.026 < 0$, bifurcation condition occurs at $U_c = 0.510\text{ms}^{-1}$, and a simple Hopf bifurcation occurs at wind velocity $U_c = 0.331\text{ms}^{-1}$ with eigenvector $(\mathbf{a}_1^{(1)}, \mathbf{a}_2^{(1)}) = (5.84, 1)$.
- for $\text{tr}\mathbf{B}^a = -0.3 < 0, \det\mathbf{B}^a = 0.02 > 0$, bifurcation occurs at $U_c = 0.205\text{ms}^{-1}$, and a single Hopf bifurcation occurs at $U_c = 0.302\text{ms}^{-1}$ with a real eigenvector $(\mathbf{a}_1^{(1)}, \mathbf{a}_2^{(1)}) = (-0.666, 1)$, and a double Hopf bifurcation occurs at $U_c = 0.402\text{ms}^{-1}$ with two complex eigenvectors $(\mathbf{a}_1^{(1,2)}, \mathbf{a}_2^{(1,2)}) = (-0.56 \pm 0.08i, 1)$.

Like above, the following table 5.9 and 5.10 depict all the bifurcation conditions for the larger sag case (L) with the corresponding common frequencies.

Table 5.9: Critical modal conditions for analytical and numerical solutions with common modal frequency $\omega_{0j} = 1.94\text{rad/s}$: velocity (ms^{-1}); (Non-resonant part)

Case	U_c analyt.	U_c FDM	err. %	U_c GM	err. %
I	3.09	3.06	0.98	3.10	0.32
II	-1.34	-1.36	1.47	-1.36	1.47
III	0.510	0.514	0.77	0.508	0.39
IV	0.205	0.198	3.53	0.208	1.44

Table 5.10: Critical modal conditions for analytical and numerical solutions with common frequency $\omega_{0j} = 1.361\text{rad/s}$: velocity (ms^{-1})

Case	U_c analyt.	U_c FDM	err. %	U_c GM	err. %
I	3.39	3.37	0.59	3.31	2.41
II	-3.39	-3.45	1.73	-3.43	1.16
III	0.331	0.334	0.89	0.337	1.78
IV(a)	0.302	0.306	1.30	0.305	0.98
IV(b)	0.402	0.403	0.24	0.407	1.22

With the corresponding mode shapes, presented in the following figures:

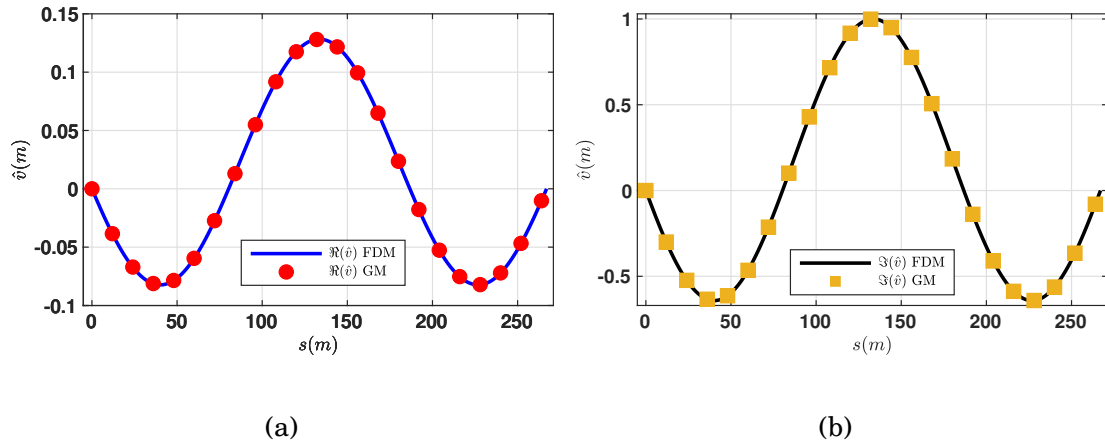


Figure 5.45: modal shapes for the non-resonant part of (case I in Figure 5.3-(b)): (a) real and (b) imaginary parts of \hat{v}

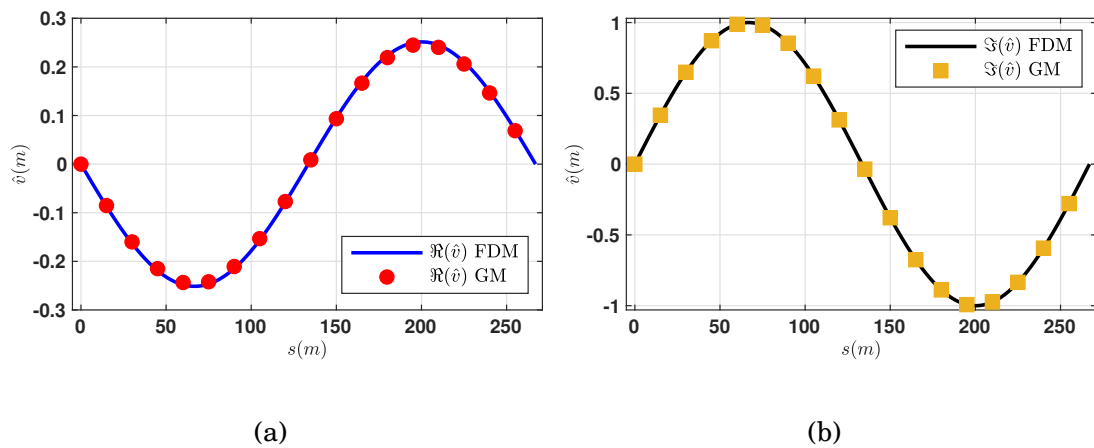


Figure 5.46: modal shapes for (case I in Figure 5.3-(b)): (a) real parts of \hat{v} ; (b) imaginary parts of \hat{v}

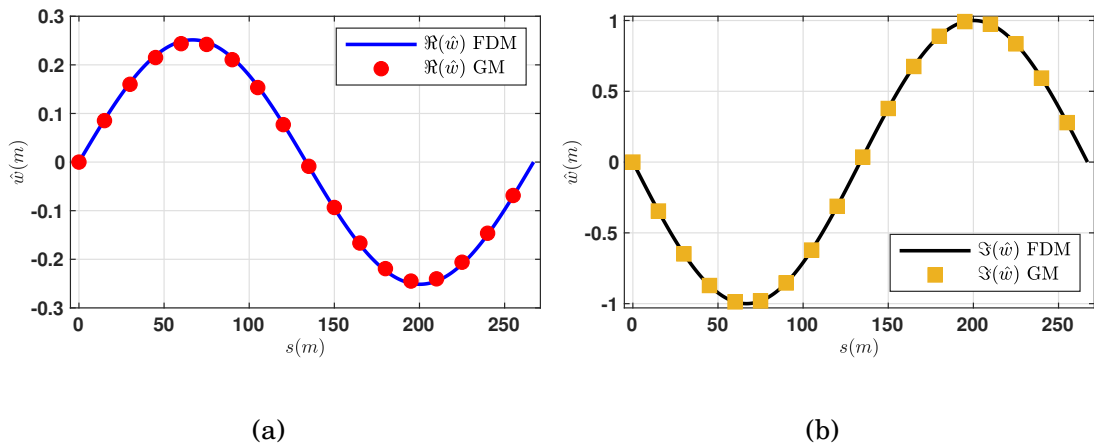


Figure 5.47: modal shapes for (case I in Figure 5.3-(b)): (a) real parts of \hat{w} ; (b) imaginary parts of \hat{w}

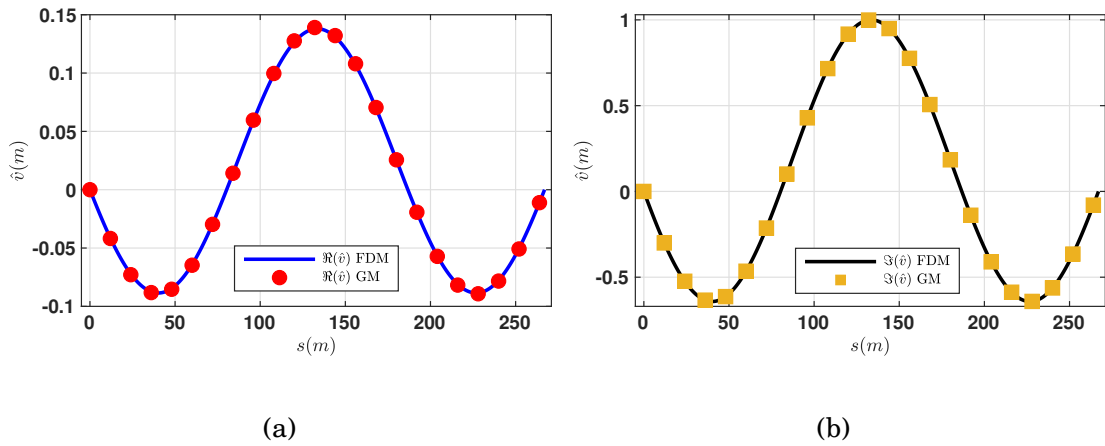


Figure 5.48: modal shapes for the non-resonant part of (case II in Figure 5.3-(b)): (a) real and (b) imaginary parts of \hat{v}

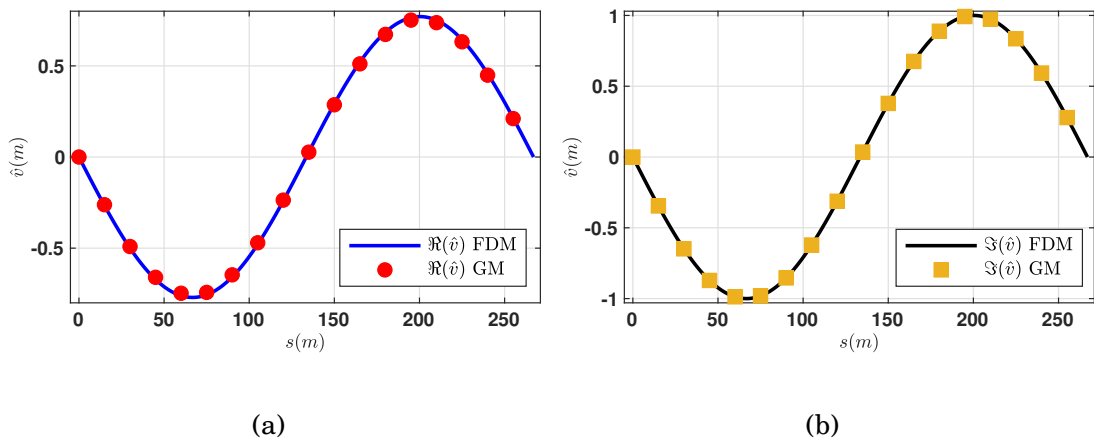
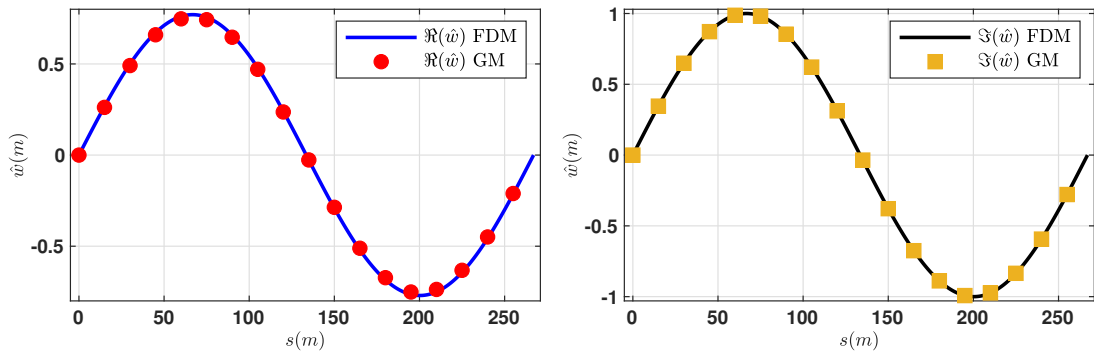


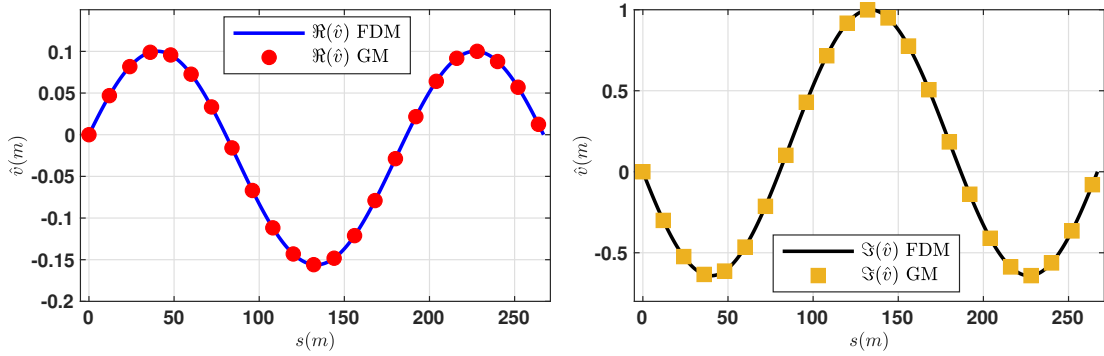
Figure 5.49: modal shapes for (case II in Figure 5.3-(b)): (a) real parts of \hat{v} ; (b) imaginary parts of \hat{v}



(a)

(b)

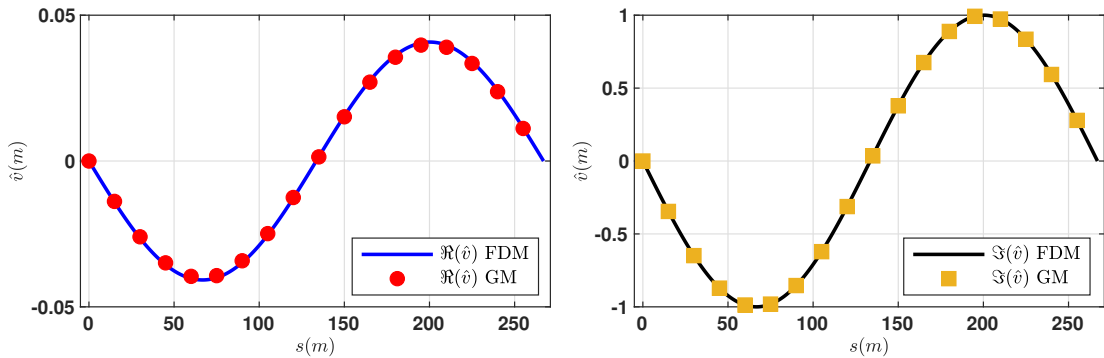
Figure 5.50: modal shapes for (case II in Figure 5.3-(b)): (a) real parts of \hat{w} ; (b) imaginary parts of \hat{w}



(a)

(b)

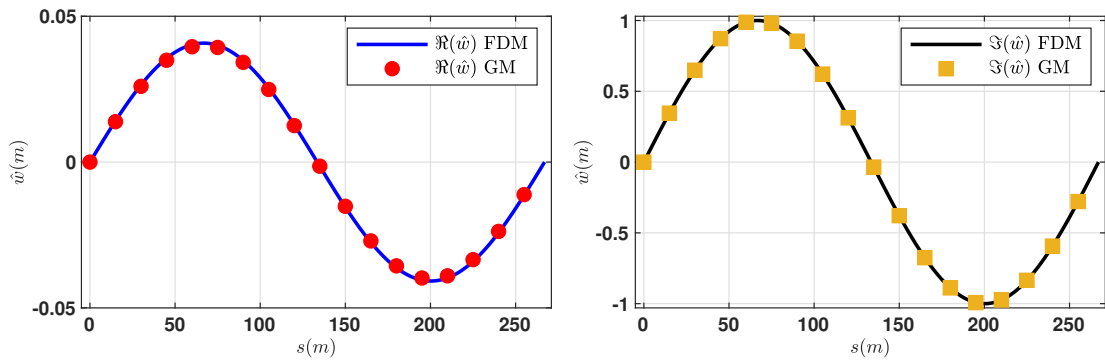
Figure 5.51: modal shapes for non-resonant part of (case III in Figure 5.3-(b)): (a) real and (b) imaginary parts of \hat{v}



(a)

(b)

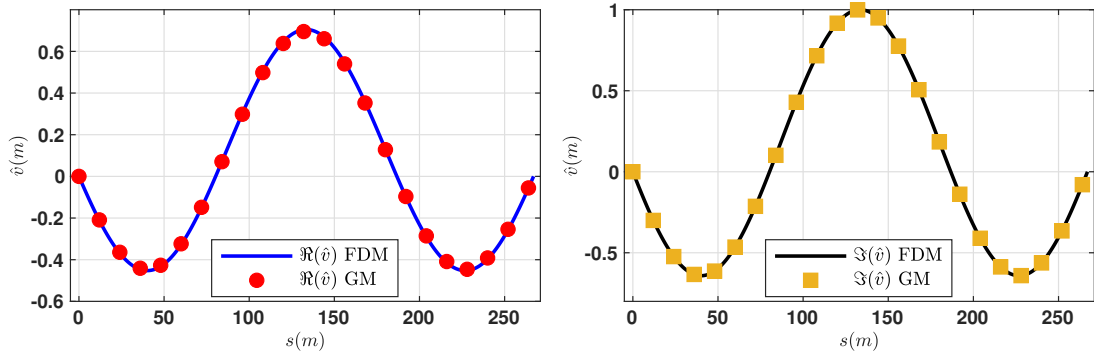
Figure 5.52: modal shapes for (case III in Figure 5.3-(b)): (a) real parts of \hat{v} ; (b) imaginary parts of \hat{v}



(a)

(b)

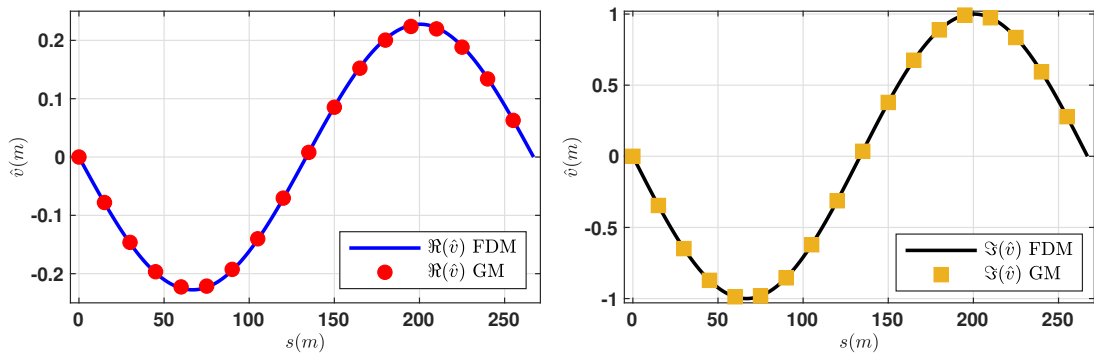
Figure 5.53: modal shapes for (case III in Figure 5.3-(b)): (a) real parts of \hat{w} ; (b) imaginary parts of \hat{w}



(a)

(b)

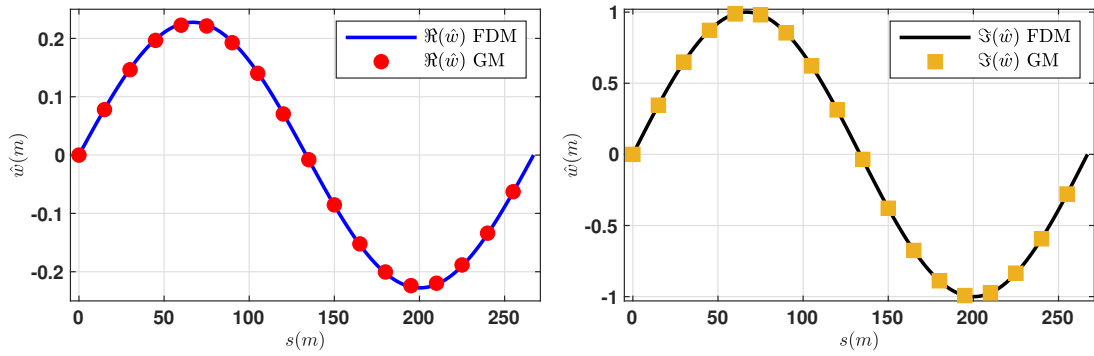
Figure 5.54: modal shapes for non-resonant part of (case IV in Figure 5.3-(b)): (a) real and (b) imaginary parts of \hat{v}



(a)

(b)

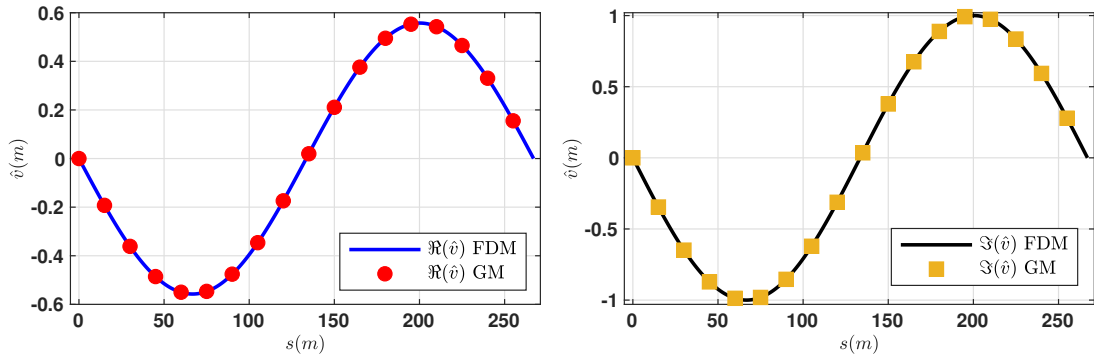
Figure 5.55: modal shapes for (case IV, curve (a), in Figure 5.3-(b)): (a) real parts of \hat{v} ; (b) imaginary parts of \hat{v}



(a)

(b)

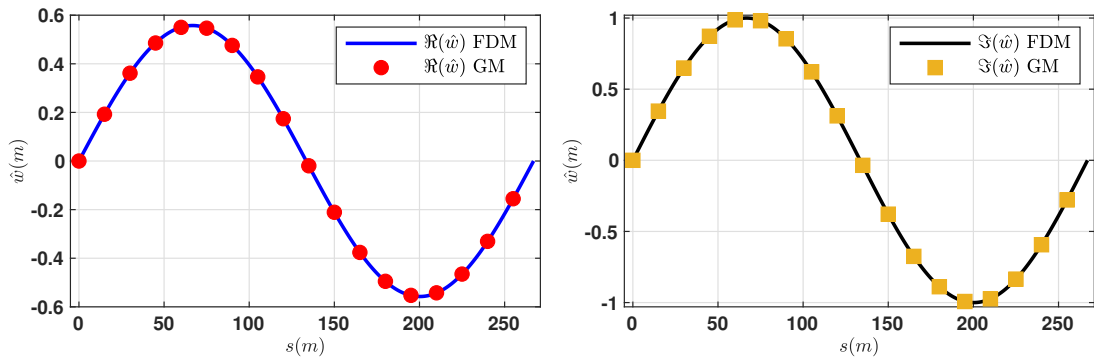
Figure 5.56: modal shapes for (case IV, curve (a), in Figure 5.3-(b)): (a) real parts of \hat{w} ; (b) imaginary parts of \hat{w}



(a)

(b)

Figure 5.57: modal shapes for (case IV, curves (b), in Figure 5.3-(b)): (a) real parts of \hat{v} ; (b) imaginary parts of \hat{v}



(a)

(b)

Figure 5.58: modal shapes for (case IV, curves (b), in Figure 5.3-(b)): (a) real parts of \hat{w} ; (b) imaginary parts of \hat{w}

Summarizing the above analysis, all the results at the critical condition, have a good agreement with exact, analytical and numerical studies.

5.6 Conclusions

Coupled in-plane and out-of-plane galloping of shallow horizontal cable has been studied via a continuous approach, in the linear field. The structural model, taken from literature, consists of two coupled integro-differential equations in the transverse displacement components, where the integral term derives from condensation of the longitudinal component. Damping has been included according to the Rayleigh model, consisting in an external part, proportional to the mass algebraic operator, and an internal part, proportional to the differential stiffness operator. Aerodynamic forces have been described according to the quasi-static theory. An exact differential boundary value problem has been obtained, from which the critical wind velocity is derived. Both exact and numerical solutions, based on Finite Differences and Galerkin Methods, have been worked out.

Aimed at obtaining simpler analytical expressions, the boundary value problem has been also tackled by asymptotic methods, based on perturbations of mono-modal or multi-modal solutions to the undamped and not-self-excited problem. The analysis of the spectrum of the natural frequencies of the cable has revealed the occurrence of some peculiar circumstances, depending on the value of the Irvine's parameter. namely: (i) non-resonance, (ii) 1 : 1 resonance, and (iii) 1 : 1 : 1 resonances, involving one, two or three modes, respectively, each calling for a devoted analysis. This has shown that galloping of horizontal cables manifests via two different mechanisms:

- Non-resonant (almost) planar mono-modal oscillations: these involve a symmetric mode only, and occurs in the transition regions of the spectrum, where the mode is fastly changing its shape. The non-resonant behavior is well captured by the simpler planar model of galloping, since coupling only triggers small out-of-plane displacements, which, being in quadrature, lead the material points to describe narrow elliptical trajectories.
- Resonant in-plane and out-of-plane bi-modal oscillations: these involve two modes, one in-plane and the other out-of-plane, of the same wavelength, either symmetric or anti-symmetric, whose amplitudes are of the same order of magnitude. The resonant behavior occurs in any region far from the transition, but including the cross-over. The relevant critical wind velocity can be either lower or higher than that predicted by the planar model. Coupling,

under some circumstances, can induce motions in which the trajectories of the material points are wide ellipses.

- For symmetry reasons, three-modal coupled oscillations do not occur, since they break into a planar symmetric mono-modal motion and a spatial antisymmetric-antisymmetric bi-modal motion.

Numerical results, concerning (i) exact analytical solution, the (ii) Finite Difference and the (iii) Galerkin solutions have validated the findings of the asymptotic analysis. The solution with the four different methods (exact, analytical, and two numerical) are fitted well.

VIBRATION CONTROL OF A CABLE STRUCTURE VIA A FLEXIBLE PIEZOELECTRIC DAMPER AND ENERGY HARVESTING

6.1 Introduction

Piezoelectricity or piezoelectric effect in general, literally means the electricity originated by pressure, which is found in our nature environment in many materials. Two French scientists Pierre and Jacque Curie, more than a century ago, discovered the ability of some materials to metamorphose the mechanical energy into electrical energy and vice-versa by deforming the body of the materials. They noticed that there are a class of materials, produce electricity when pressure is given and also when they are placed in an electric field, they strain mechanically. Some materials found naturally as tourmaline, quartz, topaz and etc. are the class of monocrystalline materials which have the piezoelectric properties. But these materials cannot be used directly as actuators or sensors for controlling vibrations of structures. On the other hand, artificially made polycrystalline ceramic materials are suitable to use as sensors and actuators. These materials includes lead zirconate (PZT), polyvinylidene fluoride (PVDF) and others, can be made in a way that can show remarkable piezoelectric properties. These elements are the most used piezoelectric transducers, because of their ease production and powerful coupling behavior of electrical and mechanical energies. There are different types of piezoelectric devices with different forms and different shapes. Day by day these devices have become most popular among the relevant fields and industries in the application of vibration control and harvesting energy.

6.1.1 Piezoelectric devices to control vibration of structures

Piezoelectric devices have been widely used in many applications, such as, controlling the structural vibrations. Due to their perfect sensing and actuation capabilities, which arises from their exceptional non-intrusiveness behavior and high electro-mechanical coupling coefficient, they are extensively utilized materials in this particular application of vibration control.

Piezoelectric devices are embedded in a structure, possibly flexible in nature, to which vibration needs to control or harvesting energy from vibration. In general, the structural system is lightly damped and their transfer functions are of higher orders [88]. The problem arises with controlling vibration of these systems are always complicated. The vibration control problems include aircrafts, satellites, sport products and many structural systems. Suspended cables, suspension bridges, cable nets, stay-cables, structural beams, transmission lines are examples of structural problems where piezoelectric devices can be attached for the purpose of controlling vibration.

Many researchers are currently working on this subject to diminish vibration of structures and to harvest energy from it [14, 107]. Researchers and structural designers have a lot of options when using so called smart materials such as, piezoelectric material, in structural construction and different machines, as these materials have the capability to generate control functions, exalted integrating detection, sensing and actuation in engineering systems [88]. The widely use of piezoelectric materials to suppress vibration are found in the following studies. Xie et al. [111] have formulated and designed a shunted flexible piezoelectric damping system with a single cable structure and solved numerically in the purpose of controlling vibration of deployable space cable structures. They used a tube-shaped PVDF piezoelectric material with different layers and attached at one end of a single cable to absorb the energy arises as a result of vibration. They employed LR and NC-R shunt circuits and compared the outcomes with the control free structure. Li and Ma [72] developed a robust controller named μ -synthesis controller that can effectively suppress the effects of external and mixed uncertainties on flexible cable structures. Their results indicated that the controller can meet the performance requirements while maintaining the stability of the system. However, it can introduce unnecessary conservativeness and cannot acheive the desired results. In order to control the vibration in a partially covered surface of a compressed shell, Zhang and colleagues [121] have studied the effects of the increasing number of layers in a laminated PVDF actuator on the voltage distribution in the cavity. They found that the number of layers can be decrease the resistance

voltage in the active vibration control of the shell. To create a more effective and efficient mechanism for wave filtering, Ouisse et al. [81] developed a kirigami based piezo-shunted structure with an auxetic core. The structure is composed of a pyramidal core and a series of piezoelectric patches. Crawley with Luis [14] developed a theoretical formulation to introduce controlling vibration of structures by utilizing piezoelectric materials. They used analytical techniques to develop an intelligent structure with a PZT actuator concerning static and dynamic stresses. They attached the PZT actuator with a composite laminated cantilever beam. On the other study, Hagood and Crawley [37] used an electrical inductance in series to investigate the damping performance of space structures experimentally. A technique to attenuate vibration, called positive position feedback (PPF), was proposed by Fanson and Caughey [26]. They performed experimental investigation in laboratory on a cantilever beam by attaching piezoelectric material with it as actuator and sensor.

Bailey and Hubbard [3], first time, studied by analytical approach the active vibration control of a smart beam, where piezoelectric actuators and sensors were distributed along the beam. They used polyvinylidene fluoride as the piezoelectric material. As active vibration control phenomena is much more complex, it needs complicated algorithms and highly advanced hardwares [111], where in a actuator, the piezoelectric material supplies conducting force, whereas in a sensor, piezoelectric material provides the information about the amplitude and phase of the vibrations.

On the other hand, passive control of vibration generally depends on the modification of some basic properties of the system without any external supply of electrical energy. The ability of a resonant shunt circuit to suppress the vibration of a system at tuning frequency, is not constraint by its dependence on external electrical energy, variations in vibration or on its geometrical properties. There are several types of shunt circuits, such as inductive-resistive (LR), inductive (L), resistive-inductive-capacitive (RLC), and capative-inductive (LC). First time, the piezoelectric shunt damping was introduced by Forward [27]. By experimental investigation, he illustrated the feasibility to attach exterior electric circuits to suppress the mechanical vibrations in optical structures. He also designed the resistance-negative capacitance (NC-R) shunt [28]. Hagood and Flotow [38] forwarded the theoretical base of shunt circuit by introducing resistive shunt and resonant shunt techniques. These circuits need to connect with the structure as a mechanical vibration absorber. A detailed description of piezoelectric transducers for controlling structural vibration can be found in [74]. Generally, a piezoelectric shunt circuit composed of piezoelectric transducer by connecting it with an electric impedance, and by attaching them on a smart structure, for example, cables,

beams.

Several researchers have emphasized on the optimal design of shunt circuits [4, 39, 40, 99, 102, 116]. Berardengo et al. [18] studied optimal shunt circuit design with negative capacitance. Theoretical and experimental observations were performed to design optimal LR shunt by Thomas et al. [102]. Researchers also investigated multimodal vibration control mechanism with the smart material using as actuator [5, 8, 9, 41, 108, 117]. By using only a single piezoelectric device, Hollkamp [41] described a method to attenuate multiple mode vibration. Wu [108] used a single piezoelectric transducer, Behrens et al. [8] used shunt circuits with negative capacitance controller on piezoelectric laminated structures to propose a technique to control the multimode vibrations. The use of negative capacitance in shunt circuits for damping vibration of piezoactuated structures are discussed in [6, 7, 10, 11, 75, 103]. Bisegna and Caruso [10] performed theoretical investigation by connecting a negative capacitance in two electric circuits to suppress single-mode and multi-mode vibration of piezoactuated structures. Theoretical as well as experimental investigations on damping vibration by using negative capacitance shunts with effective suppression performances were reported in [6, 7, 75].

As above, researchers also emphasized on the vibration control phenomenon of flexible structures like, flexible cables, strings. In general, most of the piezoelectric materials have a higher stiffness than flexible structures, and the fragility nature of piezoelectric ceramics, it is difficult to transfer any deformation in the flexible structure to piezoelectric material in the purpose of controlling vibration or harvesting energy. But hopefully, there are some flexible piezoelectric materials, and they have been used in flexible structures to suppress vibration and in devices of energy harvesters [112, 119], flexible sensors [15, 18, 118]. These flexible piezoelectric materials are attracted by researchers in recent years, where they are used as dampers, actuators, sensors, or energy harvesters, connecting with resonant shunt circuits [10, 111, 121]. Here, we consider piezoelectric polymer polyvinylidene fluoride (PVDF) thin film as its flexible nature, high piezoelectric coefficient, high frequency bandwidth response and above all for high performance [29, 51, 89].

6.1.2 Piezoelectric devices for harvesting energy

Researchers are also interested to develop wireless systems and electronic devices with extremely low power, which is intended as an aspect of possible interest for the energy sectors, where the suppliers are looking for renewable source of energies. The research on this field is growing day by day as the world is experiencing the scarcity of different source of energies. Most often these piezoelectric devices are

cheap to produce and maintain, and widely used in generating power in sensors, wireless communication systems, and electric signals. The main limitations of power harvesting field are due to the fact that the power produced by piezoelectric energy harvesters is insufficient to power the majority of modern electronics [122]. A crucial part of designing energy harvesters is selecting the compatible piezoelectric material. For cable structures, it is not possible to transfer the total deformation from flexible cable elements to the rigid piezoelectric materials such as, piezoelectric ceramics and single crystals. Since PVDF material is flexible polymer, it is possible to transfer the deformation from cable to the PVDF piezoelectric polymer. Due to high polarisations inside their crystalline formations, piezoelectric ceramics and single crystals have substantially stronger piezoelectric capabilities than piezoelectric polymers [123]. Besides, a certain amount of electrical energy dissipates when the harvester is tuned with electrical circuits. As a result, the power generation of cable harvesters with PVDF polymer is small compared to that of harvesters made with rigid ceramics and single crystals.

In this chapter, we have designed a tube-shaped damper with PVDF material and connect it with electric shunt circuits, and lastly, attached them in flexible straight cable to control its vibration passively and compared the obtained results with [111]. After that, we harvested energy from this composite structure as electricity.

6.2 Modeling

To design a control system, the first step is to develop a mathematical model of the system by taking into account the disturbances that responsible for the unbesought vibrations. The analytical model of the structure can be developed by using finite element (FE) method. We have here, developed a smart cable to control the vibration, whose one end is encircled by PVDF tube, as described in the Figure 6.1.

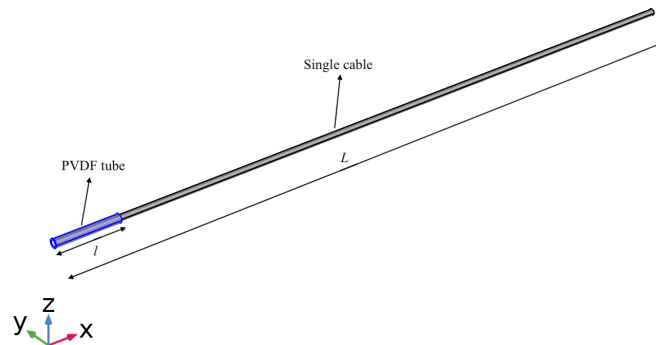
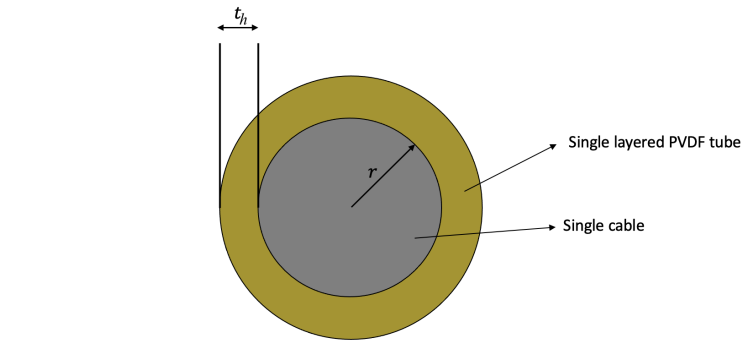


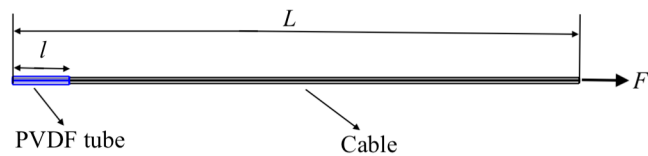
Figure 6.1: The smart cable: a single cable of length L , left end of which encircled by piezoelectric PVDF tube of length l .

6.2.1 Finite element modeling of the smart cable

The representation of the developed FE model of the smart cable must be done reliably that the model can be used in later applications, such as control applications, energy harvesting. We need to select the type of elements and sizes optimally to get the best FE model. A detailed description of the geometry of the smart cable is depicted in Figure 6.1 and Figure 6.2. For FE model, we have employed COMSOL Multiphysics to model the structure and solving the model. A smart cable is designed using a single cable of length L , whose left end is encircled by polyvinylidene fluoride (PVDF) thin film as tube of length l , and neglecting the gaps between the cable and the tube. We have the characteristics of the model: number of elements: domains 10360, boundaries 6036, edges 1016 and DOF 60981.



(a)



(b)

Figure 6.2: Geometry of the smart cable.

6.2.2 Tube-shaped PVDF damping component modeling and design

Introducing a piezoelectric PVDF damping component in the structure implies the use of a suitable electric impedance controlling the vibrations. The damper as a tube-shaped PVDF thin film is rolled up along one end of a vibrating cable in a way that the gap between the curved surfaces of the tube and cable can be neglected, see Figures 6.1, 6.2. As the PVDF tube is flexible and wide frequency bandwidth response, the deformation in the cable can be transmitted upon vibration to the PVDF tube and that causes charge on the both surfaces, inner and outer of it due to the effect of piezoelectricity. When a resonant shunt circuit is connected with the

PVDF tube, the electric current produces due to the charges of the surfaces, and some of the electrical energy dissipated in the circuit via electric resonance. The major deformation in the PVDF tube can be happened when cable experienced axial tension and pure bending. Taking all these in mind, the PVDF tube is designed on the basis of the relation of deformation in the cable with the surface charges in PVDF tube.

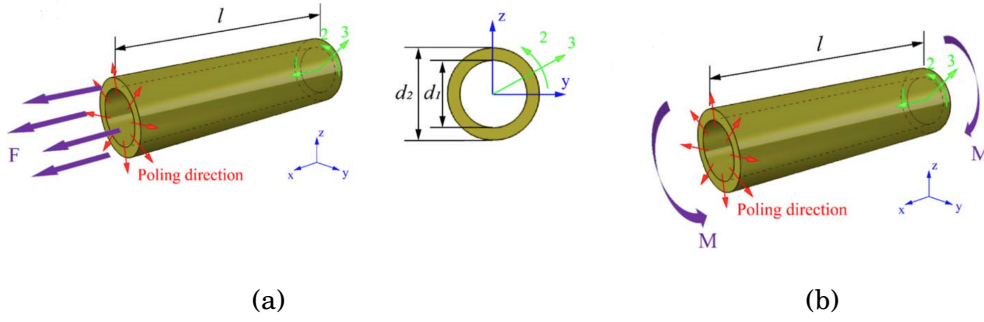


Figure 6.3: A schematic of the PVDF tube [111]: (a) under longitudinal tension; (b) under pure bending

6.2.2.1 Deformation and surface charges

The concept of design of the PVDF tube is followed by Xie et al. [111], where the deformation regarding tension and bending are considered. The characteristics of the PVDF tube is considered linear throughout the study. The thickness of the tube is taken uniform, denoted by $t_h := \frac{d_2 - d_1}{2}$, where d_1 and d_2 are the inner and outer diameter of the tube with length l . A uniform axial force F acts on x -direction, the axial normal stress,

$$\sigma_1 = \frac{F}{A_c}, \quad (6.1)$$

with A_c , the cross-sectional area. The relative piezoelectric displacement [88],

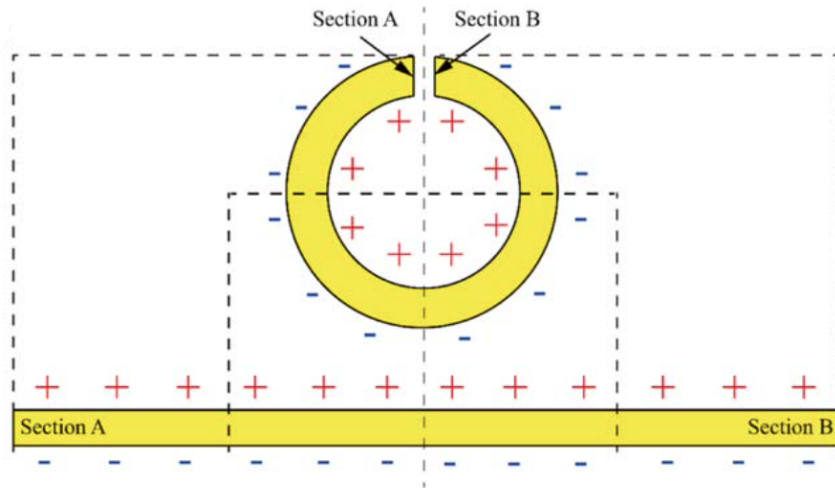
$$D_i = d_{ij}\sigma_j, \quad (6.2)$$

where d_{ij} ($i = 1, 2, 3; j = 1, 2, 3, 4, 5, 6$) are piezoelectric coefficients. The total surface charge,

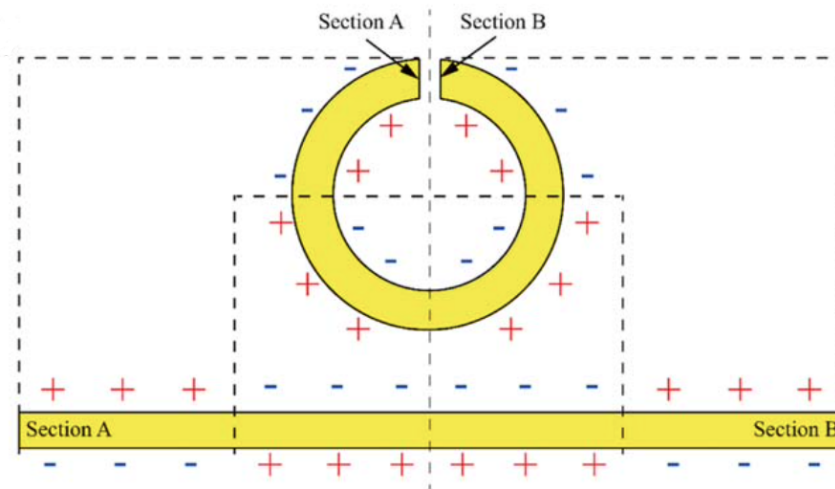
$$\begin{aligned} Q &= \int D_3 dA, \\ &= \int d_{31}\sigma_1 dA, \end{aligned} \quad (6.3)$$

where A is the average circumferential area of the tube. Using equation (6.1) into equation (6.3), we get

$$Q = \int_0^{2\pi} \frac{2d_{31}Fl(d_1 + d_2)}{\pi(d_2^2 - d_1^2)} d\theta. \quad (6.4)$$



(a)



(b)

Figure 6.4: Charge distribution in the PVDF tube [111]: (a) under an axial tension; (b) under a pure bending

The polarization direction of the tube is in thickness direction, as a result the outer surface charge and inner surface charge acts opposite direction to each other. When an axial force acts, then the polarization direction at all positions directed from inner surface to outer surface. Upon vibration, a voltage difference produces by axial tension, between the surfaces of inner and outer of the tube, see Figure 6.4, by which the mechanical energy can be transformed into electrical energy. Accounting pure bending, the normal stress in the axial direction,

$$\sigma_1 = \frac{Mz}{I_y}, \quad (6.5)$$

with M is the bending moment and I_y is the cross-sectional moment of inertia with respect to y -axis, and $z = \text{sign}(z)$, which determines the stress in tension or in compression. Using equation (6.5), equation (6.3) becomes

$$Q = \int_0^{2\pi} \frac{d_{31} M l (d_1 + d_2) \sin \theta}{2I_y} d\theta. \quad (6.6)$$

The aggregated charges on the tension and compression sides are of same value with opposite sign to each other, as a result the total surface charge vanishes. To get rid of this phenomena, the PVDF tube cut into several sectors while bending, and connect each of them with different electrodes. We need such a design for the transversal vibration, but not for the longitudinal one.

6.2.3 Geometric parameters optimization

The attachment of the PVDF tube cohesively with the cable regarded as a combined load carrying structure. The cross-sectional area and the normal stress of the PVDF tube depend on the thickness of the tube, and the thickness has an impact on the tube's capacitance, and consequently, the overall quantity of charge stored. For the optimal performance of damping, we need to calculate the accurate thickness of the tube. The optimization procedure is performed on the basis of maximizing mechanical vibration's modal electromechanical coupling factor, as the shunt is tuned with the mechanical vibration mode of the structure. Combined with PVDF tube, structure's left end is fixed and right end is under a tensile force F_0 . It is assumed that along the length of PVDF tube, the axial force is uniform; we neglect: the change in radius, capacitance change of the tube, gaps between PVDF sectors and change in inner diameter.

By assumption of the PVDF tube a capacitor with capacitance c of a single layer, the electrical energy generates in the tube [88, 111],

$$W_0 = \frac{Q^2}{2c}, \quad (6.7)$$

where Q is the total electrical charge on the circumferential surface of the PVDF tube. Using equation (6.3),

$$Q = d_{31} \frac{F_0}{A_t} A, \quad (6.8)$$

with A_t is the entire cross-sectional area of the composite structure. We have the capacitance [88],

$$c = \frac{\varepsilon_r \varepsilon_0 A}{t_0}, \quad (6.9)$$

where ε_r is the PVDF tube's relative dielectric permittivity, ε_0 is the free space's dielectric permittivity, t_0 is the thickness of a layer of PVDF tube. Using equations (6.8), (6.9) into equation (6.7), we get

$$W_0 = \frac{d_{31}^2 F_0^2 t_0 A}{2\varepsilon_r \varepsilon_0 A_t^2}. \quad (6.10)$$

Total energy of the n -layered tube is,

$$W = n \cdot W_0 = \frac{d_{31}^2 F_0^2}{2\varepsilon_r \varepsilon_0 A_t^2} (n t_0 A), \quad (6.11)$$

where $t_0 A$ is the volume of a layer of PVDF tube and $n t_0 A$ is the total volume V_{tube} of the n -layered tube. Accounting the cross-sectional geometry, we have the relation as follows:

$$V_{tube} = t_h \left(2\pi \left(r + \frac{t_h}{2} \right) \right) l, \quad (6.12a)$$

$$A_t = \pi (r + t_h)^2. \quad (6.12b)$$

Using equations (6.12) into equation (6.11), we get

$$W = \frac{d_{31}^2 F_0^2 t_h \left(2\pi \left(r + \frac{t_h}{2} \right) \right) l}{2\varepsilon_r \varepsilon_0 (\pi (r + t_h)^2)^2}. \quad (6.13)$$

For the maximum value of W with respect to t_h , we have

$$\frac{dW}{dt_h} = \frac{\pi d_{31}^2 F_0^2 l}{\varepsilon_r \varepsilon_0 \pi^2} \cdot \frac{r^2 - 2rt_h - t_h^2}{(r + t_h)^5} = 0, \quad (6.14)$$

which implies,

$$t_h = (\sqrt{2} - 1)r. \quad (6.15)$$

Hence, the PVDF tube's optimal thickness is, $t_h \approx 0.4r$. Figure 6.5 shows the relationship between the normalized electrical energy and thickness of the tube. From the equation (6.15) and the figure, when the thickness is about 0.4 times of the inner radius, the total electrical energy is generated, and when the thickness is 0.2 times of inner radius, the maximum electrical energy 1.19 times of reference energy, is generated.

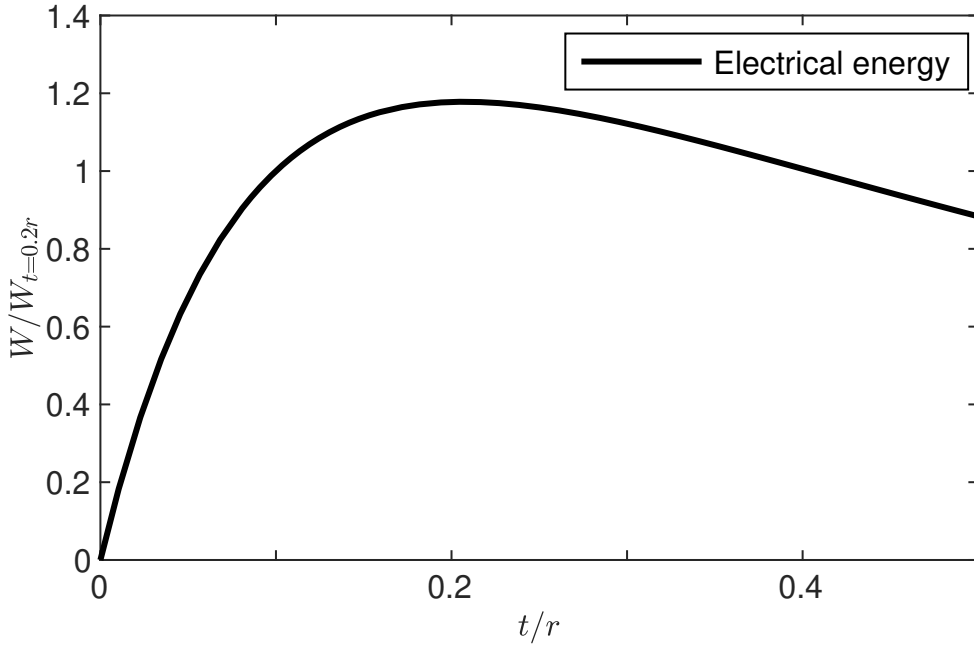


Figure 6.5: Relationship between the electrical energy and the thickness.

6.2.4 Positioning of the PVDF tube

Here, we have calculated the optimal position of the PVDF tube under *transverse vibration*. For the best performance, it is needed to place the tube in a position of the cable that can produce maximum electrical energy to damp maximum vibration of the cable. We consider here, a 1D free transverse vibration problem of a string following [109, 111], whose initial displacement is $f(x)$ and initial velocity is $g(x)$. The solution is given by,

$$v(x, t) = \sum_{k=1}^{\infty} \sin \frac{n\pi x}{l} \left(\frac{2}{\omega_k l} \int_0^l g(x) \sin \frac{k\pi x}{l} dx \sin \omega_k t + \frac{2}{l} \int_0^l f(x) \sin \frac{k\pi x}{l} dx \cos \omega_k t \right), \quad (6.16)$$

with $v(x, t)$, the transverse displacement of the string at time t and position x ; ω_k is the k -th order natural frequency, dx is the infinitesimal section of the string. The axial strain,

$$\begin{aligned} \varepsilon &= \frac{ds - dx}{dx} \\ &= \sqrt{1 + v_x^2(x, t)} - 1, \end{aligned} \quad (6.17)$$

with ds , the infinitesimal length of the section after deformation; v_x represents rotational angle, a partial derivative of $v(x, t)$ with respect to x . To evaluate the

optimal position, we have taken an initial displacement $f(x)$ with zero initial velocity, as follows:

$$f(x) = v(x, 0) = \begin{cases} \frac{2hx}{l}, & \text{when } x \leq 0.5l, \\ \frac{2h(l-x)}{l}, & \text{when } x > 0.5l, \end{cases} \quad (6.18a)$$

$$g(x) = \frac{\partial v}{\partial t}(x, 0) = 0, \quad (6.18b)$$

where h is an initial lateral displacement. Now using equations (6.18), (6.16) into equation (6.17), we can represent the time histories of displacement and the strain in Figure 6.6 for the positions of 2m and 0.01m, respectively. From the figures, the axial strain at 0.01m is larger than at 2m, under the vibration of cable. So, the optimal position should be very close to the fixed end of the cable.

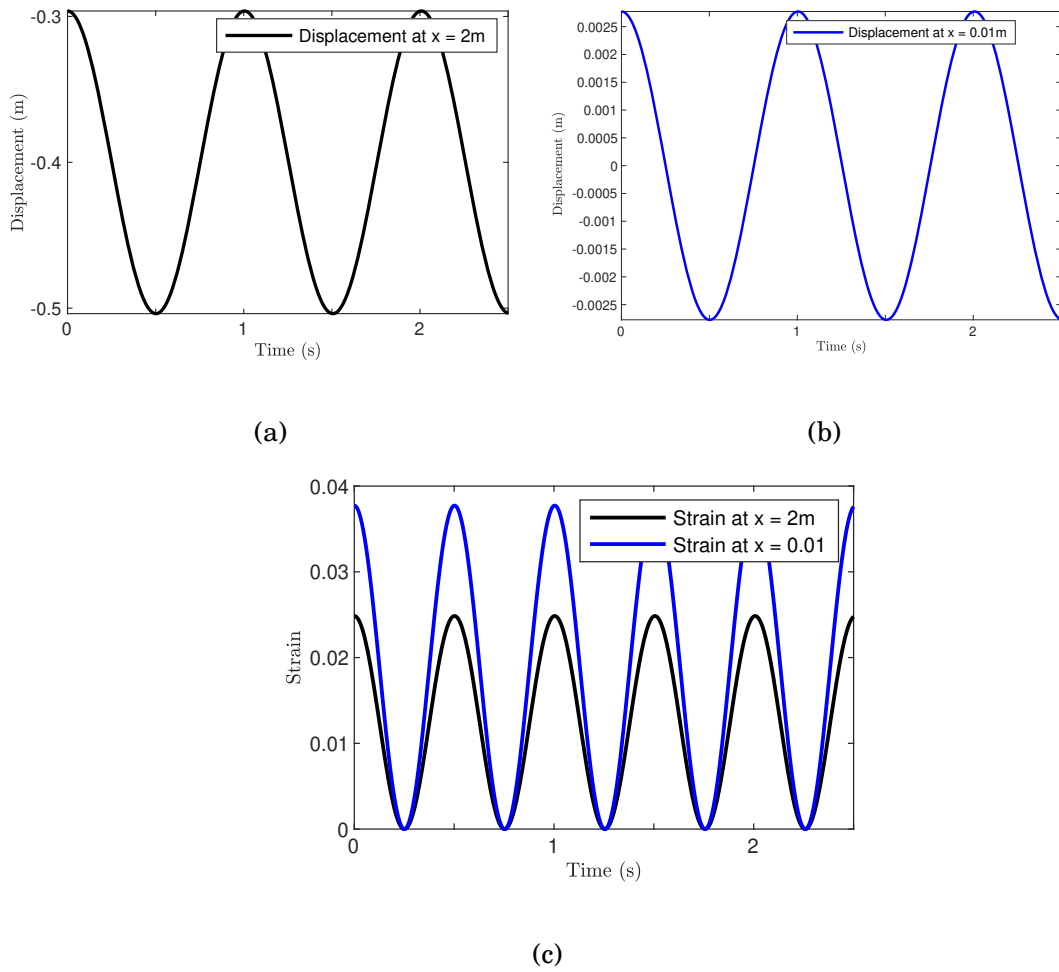


Figure 6.6: Transverse displacement and strain

6.3 Shunt circuit design

In this section, we consider two types of shunt circuits, LR (series resistance-inductance) shunt and NC-R (series resistance-negative) shunt circuits. The PVDF tube is considered as capacitor and voltage source, are connected in series.

6.3.1 The LR shunt circuit

The design of LR shunt is presented in Figure 6.7, and the optimal value of R and L is given by [38],

$$R_{opt} = \frac{\sqrt{2}k_i}{\omega_i^{sc} C_p (1 + k_i^2)}, \quad (6.19a)$$

and

$$L_{opt} = \frac{1}{(\omega_i^{sc})^2 (1 + k_i^2) C_p}, \quad (6.19b)$$

where, $k_i := \frac{(\omega_i^{oc})^2 - (\omega_i^{sc})^2}{(\omega_i^{sc})^2}$ is the i -th effective coupling factor, C_p is the capacitance of the tube, ω_i^{oc} and ω_i^{sc} are the natural frequencies in the open circuit and short circuit, respectively.

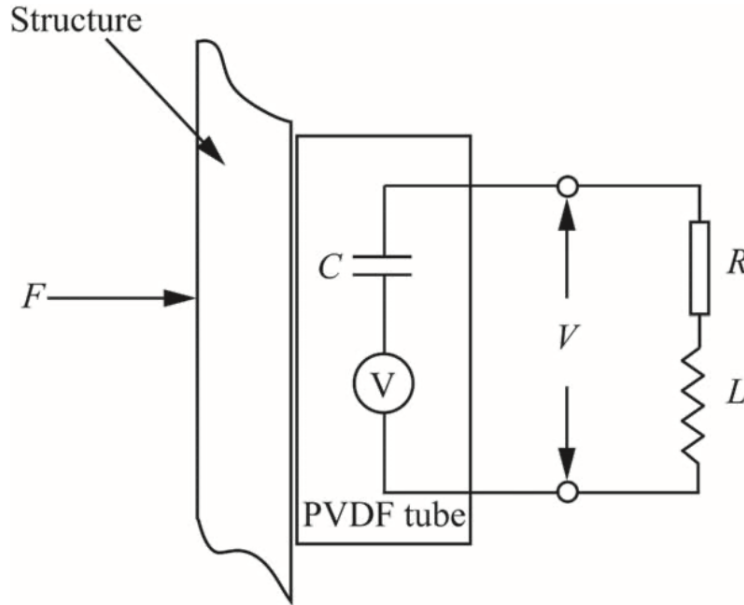


Figure 6.7: LR shunt circuit system taken from [111].

6.3.2 The NC-R shunt circuit

As the NC-R shunt can dissipate the generated energy by the stretching and bending deformations simultaneously, we have taken into account the negative

capacitance (NC) to control vibration. In general, the NC is used for improving the suppress performance by increasing modal coupling factor. The NC-R shunt circuit system is shown in Figure 6.8. In this study, the NC-R shunt circuit as well as the stability condition of the negative capacitance and the related optimal resistance followed by [6]:

$$C_n > C_p \left(1 + \sum_{i=1}^N k_i^2 \right), \quad (6.20a)$$

and

$$R_n = \frac{1}{\omega_F C_{eq}}, \quad (6.20b)$$

where, $\omega_F := \sqrt{\frac{(\omega_i^{sc})^2 + (\omega_i^{oc})^2}{2}} = \sqrt{(\omega_i^{sc})^2 + \frac{C_n - 2C_p}{2(C_n - C_p)} ((\omega_i^{oc})^2 - (\omega_i^{sc})^2)}$,

and $C_{eq} = \frac{C_p C_n}{C_n - C_p}$, with ω_i^{sc} , ω_i^{oc} are natural frequencies of the structure when the NC-R circuit is connected with PVDF tube with the conditions of short circuit and open circuit.

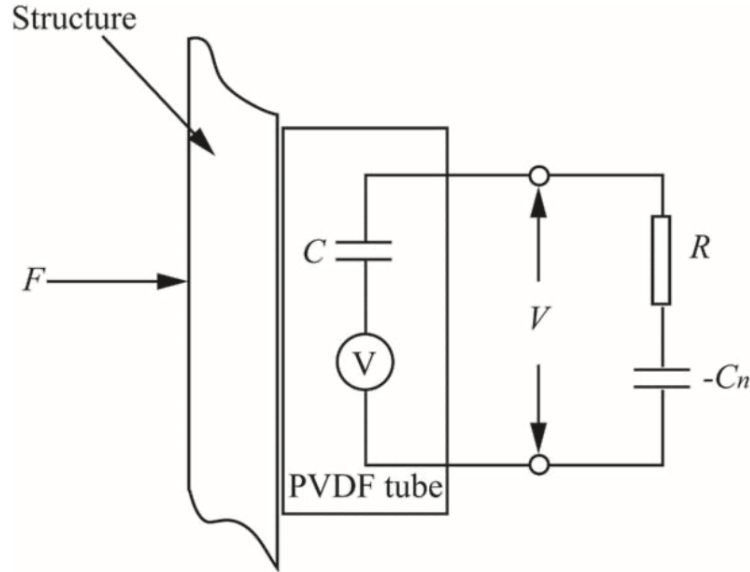


Figure 6.8: NC-R shunt circuit system taken from [111].

6.4 Numerical Results

We have modeled the structure as described above, the cable of length $L = 1\text{m}$ of which the left end is encircled by PVDF thin film as a tube of length $l = 0.1\text{m}$, and using the other optimized parameter values given in Table 6.1 and 6.2, we have studied the model via finite element analysis in COMSOL Multiphysics. We have investigated the cable structure's frequency response, time-history response under forced condition. For the PVDF tube, we consider: the piezoelectric constant $d_{31} = 23 \text{ pCN}^{-1}$; electromechanical coupling factor $k_{31} = 0.12$; Young's modulus $E_p = 2 \times 10^9 \text{ Nm}^{-2}$; Poisson's ratio $\nu_p = 0.3$; density $\rho_p = 1780 \text{ kgm}^{-3}$; relative dielectric constant $\epsilon_r/\epsilon_0 = 12$, and for the cable, the Young's modulus $E_s = 2 \times 10^9 \text{ Nm}^{-2}$; Poisson's ratio $\nu_s = 0.3$; mass density $\rho_s = 800 \text{ kgm}^{-3}$.

6.4.1 Damping characteristics

Modeling of damping parameters are of remarkable significance to determine dynamical response of the structures. We are assumed viscous damping and dependent on frequency. A specific type of viscous damping is known as Rayleigh damping. Under Rayleigh damping, we assumed the structure's modal damping ratio is 0.005.

6.4.2 Analysis of the longitudinal vibration of a single cable structure

We have studied here, the axial deformation only and for this, we have used a single-layered PVDF tube without cutting it different sectors. When the structure is subjected to longitudinal vibration, the configuration of the structure is illustrated in Figure 6.9. All degrees of freedom at the left end of the cable structure are constrained and a constant axial pretension 0.5 MPa acts on the right end. The radius of the cable is taken $r = 0.005 \text{ m}$, and the thickness of the PVDF tube $t_h = 0.002 \text{ m}$.

Under the short circuit condition with the PVDF tube, we have evaluated the natural frequency of the structure using the optimized values of the circuit components as described in Table 6.1.

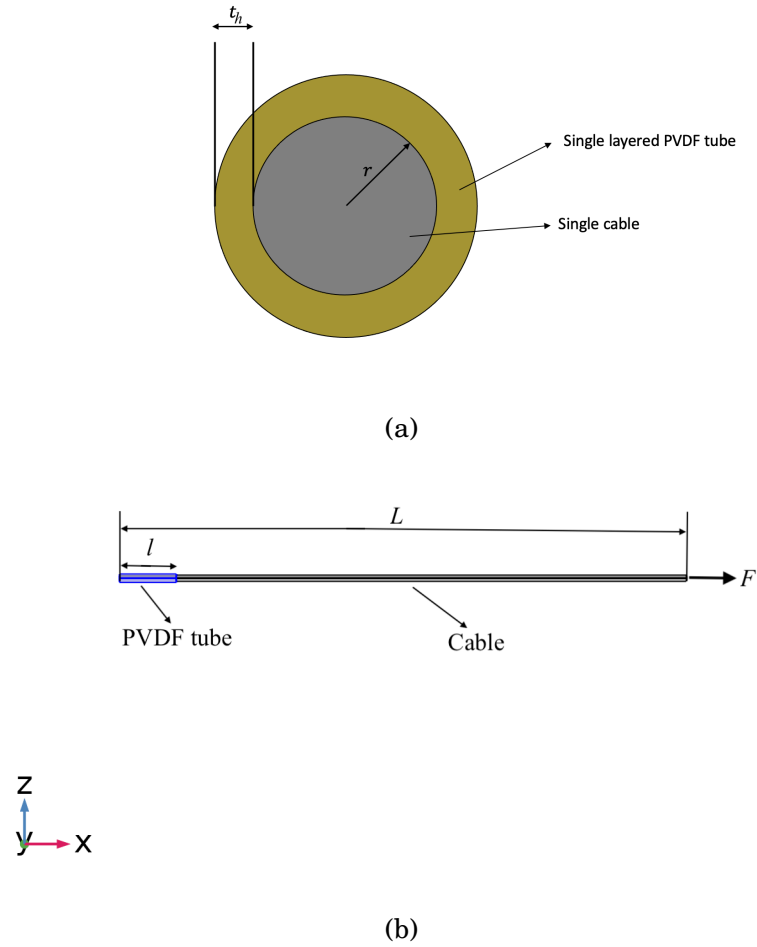


Figure 6.9: Single cable structure with the tube shaped PVDF damping system.

Table 6.1: The natural frequency of the longitudinal vibrating structure and the parameters for the shunt circuits

Natural frequency (short circuit)	ω_{short} (Hz)	414.84
LR shunt circuit	R_{opt} (Ω)	7.52×10^4
	L_{opt} (H)	733.23
NC-R shunt circuit	R_n (Ω)	5.65×10^6
	C_n (F)	2.1×10^{-10}

For the purpose of numerical simulations, we have applied a small axial force $F = 1$ N for analyzing frequency response and time-history response for the forced

vibration analysis. For the forced vibration analysis, we have used the first order resonance frequency of the structure.

The obtained results are depicted in Figure 6.10. The frequency response under frequency domain analysis is presented in Figure 6.10(a), describing the responses under control-free, LR shunt connected and NC-R shunt connected structure. The response amplitude of the frequency at resonance dropped by 87.45% with LR shunt and 63.44% with NC-R shunt, comparing with the control free response.

In the forced vibration analysis, the amplitude of response suppressed by 90.52% with LR shunt and 77.98% with NC-R shunt with the comparison of control-free response, shown in Figure 6.10(b).

From the above discussion of the outcomes, we can conclude that the design with LR shunt damping system gives better performance to reduce vibration comparing with NC-R shunt in the case of right end point displacement.

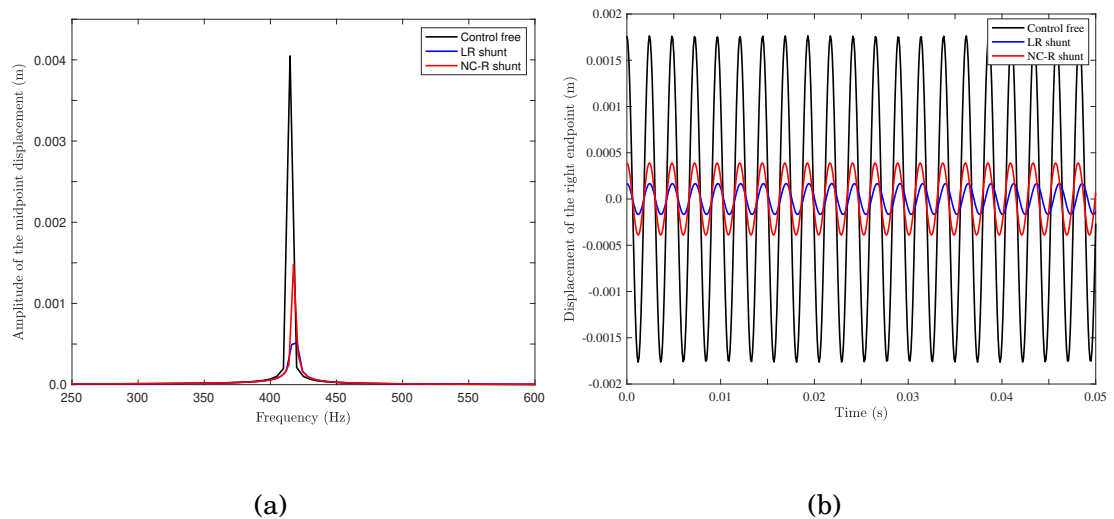


Figure 6.10: The longitudinal vibration response of the single cable structure with the tube-shaped PVDF damping system: (a) Frequency response of the right endpoint; (b) time-history response of the right endpoint under forced vibration.

6.4.3 Analysis of the transverse vibration of a single-cable structure

To study the transverse vibration response of the cable structure, we cut the PVDF tube into two sectors and bonded them at the left end and an initial constant axial pretension 0.5 MPa is applied to the cable. The configuration of the structure is shown in Figure 6.11. The left and right end of the cable are fixed. We have applied a small force $F = 1$ N at the midpoint of the cable on transverse direction,

as described in the figure, for the cases of amplitude response of the frequency analysis and forced vibration analysis.

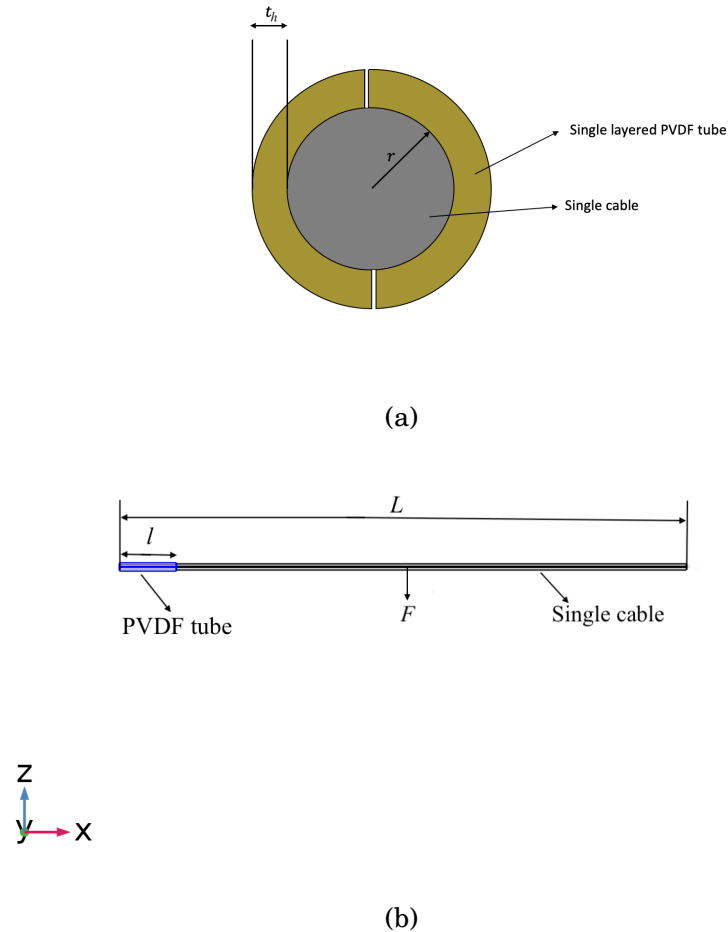


Figure 6.11: Single cable structure with the tube shaped PVDF damping system.

Here, we have only considered in the Z -direction's displacement. The optimal value of the corresponding geometric parameters are in Table 6.2. If the frequency for the transverse vibration is ω , then the frequency for the stretching will be 2ω (twice of the transverse vibration) [111]. The annexed PVDF tube, in the case of transverse vibration, experiences bending and stretching deformations. Because of high frequency dependence of LR shunt circuit to model the damper, depending on the frequency difference for the bending and stretching deformation, here, two optimization schemes are followed. The composite structure's natural frequency is obtained in the cases of short circuit or open circuit and presented in Table 6.2.

Table 6.2: The natural frequency of transverse vibrating structure and the parameters for the shunt circuits

Natural frequency (short circuit)	ω_{short} (Hz)	16.0
LR shunt circuit for bending	R_{opt} (Ω)	5.09×10^5
	L_{opt} (H)	6.62×10^5
LR shunt circuit for stretching	R_{opt} (Ω)	2.69×10^5
	L_{opt} (H)	1.65×10^5
NC-R shunt circuit	R_n (Ω)	1.69×10^7
	C_n (F)	1.05×10^{-10}

The numerical representation of the transverse vibration amplitude response is shown in Figure 6.12. In Figure 6.12(a), the amplitude response of the frequency decreased by 64.95% with LR shunt for bending, 77.76% with LR shunt for stretching and 72.73% with NC-R shunt damping system.

From Figure 6.12(b), the amplitude is dropped by 44.05% with LR shunt for bending, 67.68% with LR shunt for stretching and 65.07% with NC-R shunt for the forced vibration analysis.

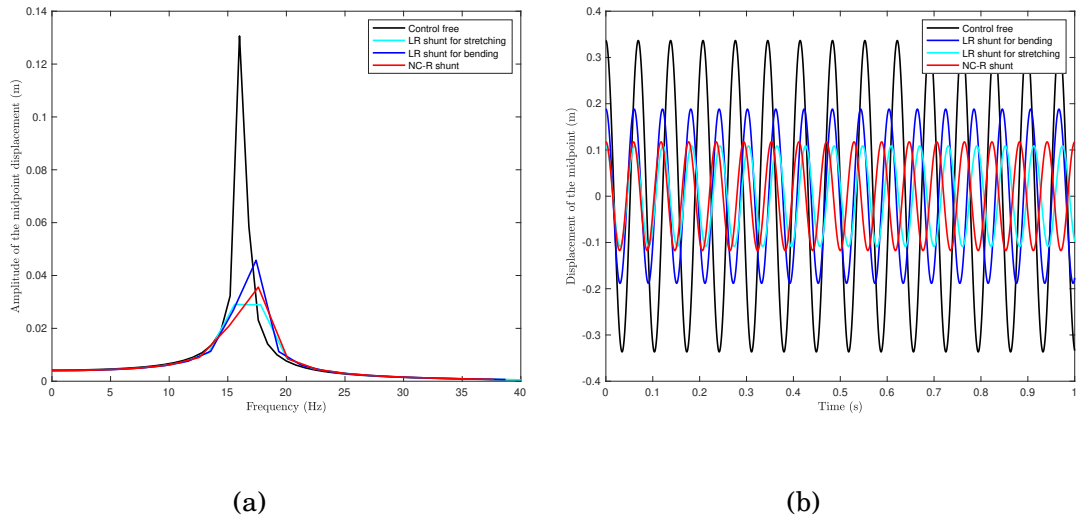


Figure 6.12: The transverse vibration response of the single cable structure with the tube-shaped PVDF damping system: (a) Frequency response of the midpoint; (b) time-history response of the midpoint under forced vibration.

From the above outcomes for the both cases of longitudinal and transverse vibrations, an axial strain is caused by the stretching deformation. By assuming the induced maximum voltage in damping as U_{max} , in the case of longitudinal vibration, it varies from $-U_{max}$ to U_{max} , and for the transverse vibration, it varies

from 0 to U_{max} . Thus, it is more fruitful the energy transformation procedure in the design of damping system with longitudinal vibration. As a result, LR shunt has a lesser performance in the transverse vibration control. On the other hand, NC-R shunt has less remarkable performance for longitudinal vibration case than LR shunt.

6.5 Configuration of the model for energy harvester

Here, the geometry of the energy harvester is shown in Figure 6.1, where we consider the same composite structure, constructed by attaching a piezoelectric tube at one end of a straight cable. The left end of the structure is fixed in all degrees of freedom and the right end is free to move. We have taken into account only the body load of the structure. The harvester is analyzed in a reference frame which is vibrating, as it is modeled in COMSOL Multiphysics with applying a sinusoidal body load.

6.6 Discussion of results

A straight cable of length $L = 1\text{m}$ and a PVDF tube of length $l = 0.1\text{m}$ is taken into account to design the composite structure to harvest energy when the harvester excites with a sinusoidal acceleration. The electrical load is considered $R_{load} = 5.09 \times 10^5 \Omega$. The input of mechanical energy by the excitation of the harvester by acceleration, the harvested energy from the input energy, and the induced voltage in the PVDF tube, all are presented as functions of frequency in figures 6.13 (a) - 6.13 (c). Figure 6.13 (a) shows the peak of induced voltage across the piezoelectric tube. The maximum voltage 0.2015 V is produced at 11.5 Hz. At the same frequency, the peak of input mechanical power is $5.447 \times 10^{-3} \text{ W}$, presented in Figure 6.13 (b), and the harvested energy as electric power $3.988 \times 10^{-8} \text{ W}$ from the mechanical power input, is drawn in Figure 6.13 (c). As it is discussed above that it is difficult to transform the total deformation of a flexible structure to the piezoelectric material and the attachment of electrical circuits with the piezoelectric harvester, the amount of input mechanical energy is small which results a low amount of energy extraction from the harvester.

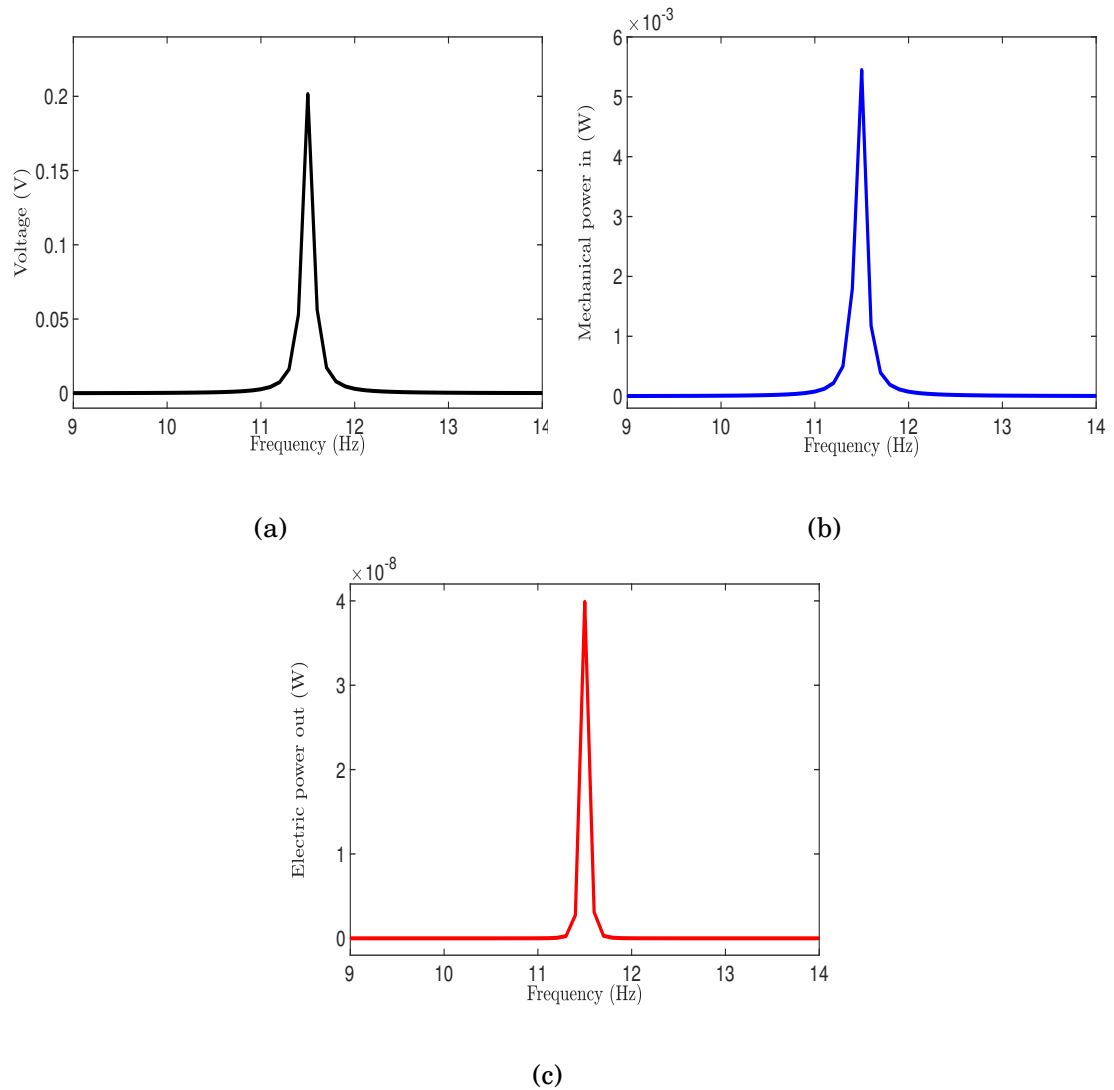


Figure 6.13: Energy harvester: (a) The peak of induced voltage across the PVDF tube; (b) The mechanical power input in the harvester; (c) The harvested power from the mechanical power input.

The harvester's performance depending on the resistance of electrical load is drawn in Figure 6.14 . Figure 6.14 (a) shows the induced voltage in the PVDF harvester, Figure 6.14 (b) depicts the mechanical power input to the harvester, and the harvested energy from the PVDF harvester is presented in Figure 6.14 (c) at 1g acceleration when the cable is oscillating at 11.5 Hz. The outcomes are presented in logarithmic scale for x -axis. The peak of harvested energy as electric power is 3.78×10^{-6} W.

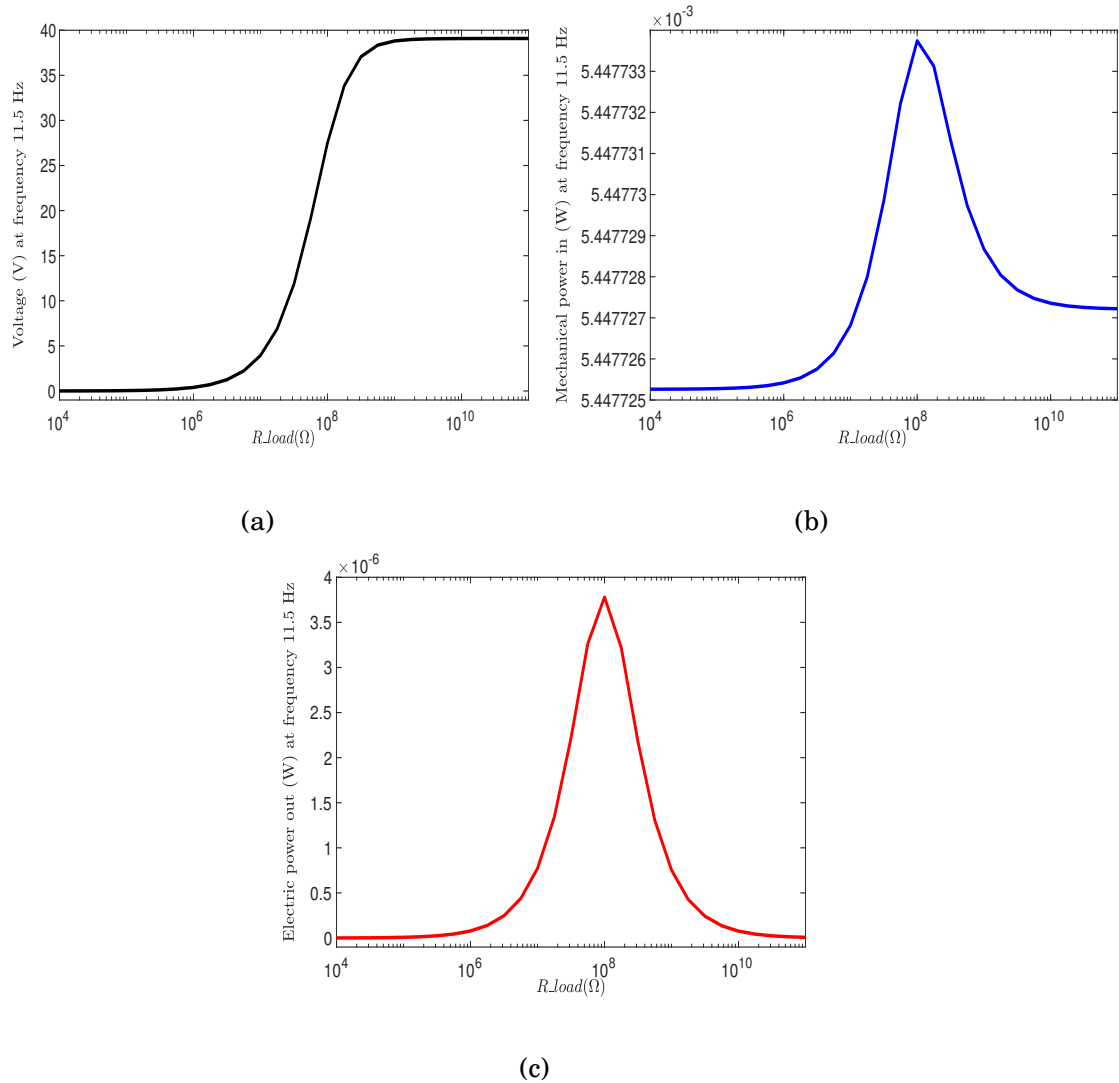


Figure 6.14: Energy harvested depending on electrical load resistance: (a) Induced voltage across the PVDF tube; (b) The mechanical power input in the harvester; (c) The harvested power from the mechanical power input.

In Figure 6.15 (a), the voltage induced across the harvester; in Figure 6.15 (b), the input mechanical power, and in Figure 6.15 (c), the output electrical power, all are depicted against the mechanical acceleration when the frequency of the oscillation is 11.5 Hz. The voltage is linearly increased with acceleration with an applied load impedance of $5.09 \times 10^5 \Omega$, and the mechanical power input and the output harvested electric power are increasing quadratically with the acceleration.

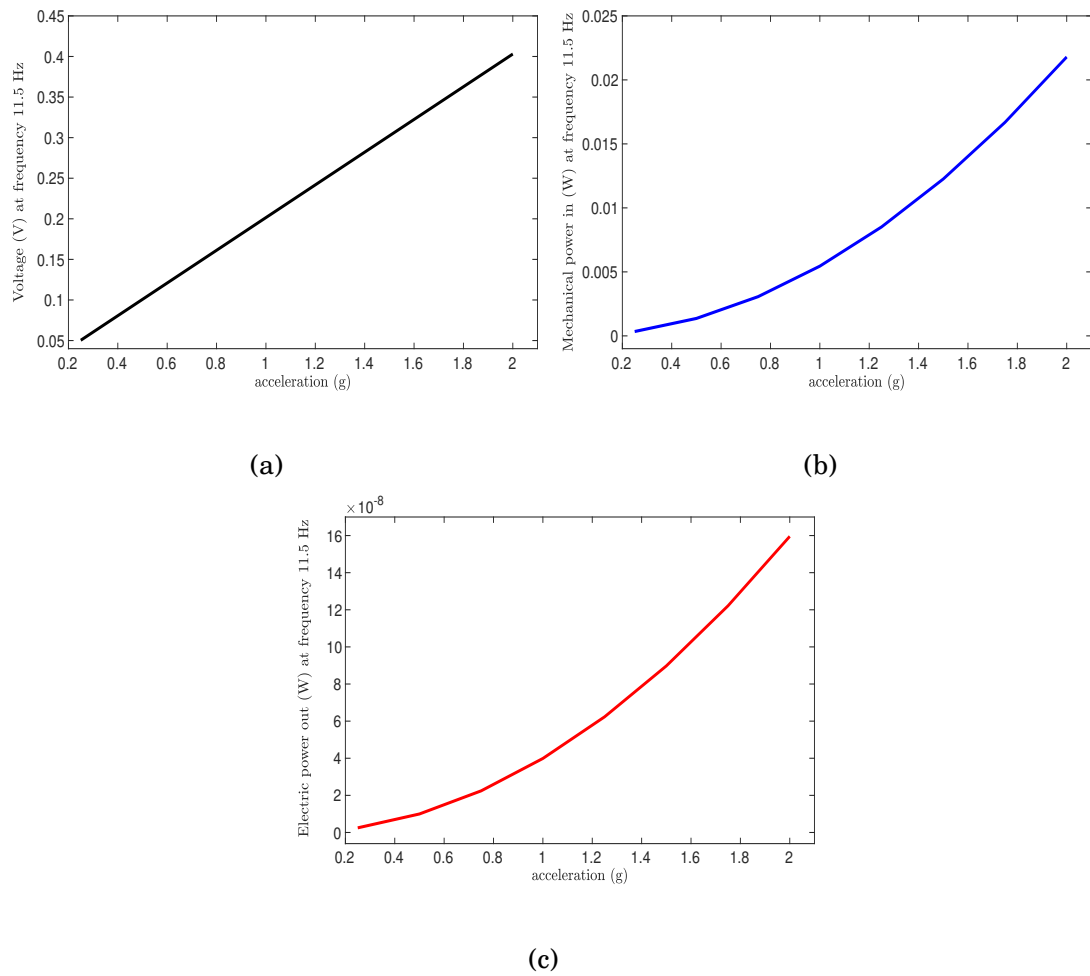


Figure 6.15: Energy harvested dependence on mechanical acceleration: (a) Induced voltage across the PVDF tube; (b) The mechanical power input in the harvester; (c) The harvested power from the mechanical power input.

6.7 Conclusion

A smart cable structure is designed with a shunted piezoelectric tube-shaped damper to suppress vibration of the cable when subjected to an axial or a transverse load. Flexible piezoelectric polymer, polyvinylidene fluoride (PVDF) thin film is used to model such a damper. The optimal placement and thickness of the PVDF damper are determined. Two shunt circuits, LR and NC-R shunts are taken into account to observe the performances of controlling vibration. The geometrical parameters and the parameters for shunt circuits are also determined optimally. We are in conclusion that, for the axial vibration, LR shunt shows a better performance than that of designed with NC-R shunt circuit. On the other hand, for the transverse vibration, LR and and NC-R shunts more or less equally work. Also, energy is harvested from the harvester, showing the dependence of electric load resistance and acceleration when the structure is oscillating at a certain frequency.

CONCLUSIONS AND FUTURE DEVELOPMENT

In this thesis paper, the presented research works deal with the outcomes of my studies and research conducted under the supervision of my professors during the PhD period of last three years. The in-plane and out-of-plane galloping of an iced suspended cable is analyzed in the first part of this research work via a continuum model. Various methods of solutions are employed to analyze the model for studying the mechanical behavior of the structure. By exact analysis, the critical wind velocity and modal frequencies are determined. In order to get the qualitative as well as quantitative information on the role of the out-of-plane component on galloping, we have addressed analytical method to solve the space eigenvalue problem. Three resonance cases are illustrated by the analytical analysis; where, in non-resonant case, the planar (mono-modal) mode is symmetric and happens in the transition phase of the spectrum. At the leading order, the additional degree-of-freedom has no effect on the critical wind velocity as determined by accounting the use of Den-Hartog criterion. Only significant consequence is that, it adds the bi-normal component of the motion, which makes the galloping mode complex as it is in quadrature with the planar mode. Besides, every material point of the cable specifies trajectories that project as extremely small ellipses in the cross-section plane. In the one-one resonant case, a planar mode and an out-of-plane mode with same magnitude of wavelength, symmetric or antisymmetric, occurs far from the transition region. In one-one-one resonant case, a symmetric planar mode and a spatial antisymmetric-antisymmetric bi-mode occur. Regarding the numerical results, the obtained results e.g., the vibration modes, critical solutions as critical wind velocities and modal frequencies at different cases are of good agreement with the exact and analytical solutions.

In the reduced order model i.e., in the planar model, the governing integro-differential equation was solved by exact analysis in the linear field, and solved asymptotically in nonlinear field. At the resonance, by the numerical analysis, the critical velocities either higher (one-one resonance) or lower (non-resonance) than

the critical Den-Hartog velocity. This indicates that, when occurring under non-resonance conditions, the coupling between the in-plane and out-of-plane motion can have both a positive as well as a negative impact on the single-component motion. A cable that would be stable in non-resonance case can be unstable due to the coupling.

More specifically, from the linear in-plane model, it reveals that: the critical wind velocities are split into each associated mode by internal damping; the critical mode can be symmetric or anti-symmetric. A stable Hopf bifurcation occurs in the planar cable, and it changes its shape along the limit-cycle by a drift and a small out-of-plane component which makes the nonlinear normal mode complex. On the other hand, the linear spatial model expresses the coupling between planar and out-of-plane displacements due to the aerodynamics forces.

In the second part, a smart cable is designed and mathematically formulated to control vibration of the structures, and to harvest energy due to the oscillation of the cable. A single straight cable is attached with a PVDF tube and is tuned with electrical shunt circuits, one is LR shunt and other one is NC-R shunt circuits. Design with LR shunt shows remarkable performance when studying longitudinal vibration suppression of the cable. For transverse vibration control, LR shunt and NC-R shunt, both are equally performed. On the other hand, the energy in the form of electrical power is extracted from the designed cable harvester, and the extracted energy is compatible to power small electronic devices.

I would like to devote my future work to extend the research by accounting swing angle and thermal effects on the cable structures. One of my further interest is to develop a smart long curved cable by attaching piezoelectric devices when the structure is subjected to wind force.

BIBLIOGRAPHY

- [1] R. D. Blevins, *Flow-induced vibration*, second ed., Krieger Publishing Company, Florida, 2001.
- [2] F. Bleich, C. B. McCullough, R. Rosecrans and G. S. Vincent, *The Mathematical Theory of Vibration in Suspension Bridges*. Washington, D. C.: US Government Printing Office, 1950.
- [3] T. Bailey and J. E. Hubbard, "Distributed piezoelectric-polymer active vibration control of a cantilever beam," *J. Guid. Control Dyn*, 8, pp. 605-611, 1985.
- [4] M. Berardengo, S. Manzoni, O. Thomas and M. Vanali, "Piezoelectric resonant shunt enhancement by negative capacitances: optimization, performance and resonance cancellation," *J. Intelligent Mater. Syst. Struct.*, 29, pp. 2581-2606, 2018.
- [5] M. Berardengo, S. Manzoni and A. M. Conti, "Multi-mode passive piezoelectric shunt damping by means of matrix inequalities," *J. Sound Vib.*, 405, pp. 287-305, 2017.
- [6] M. Berardengo, S. Manzoni, O. Thomas and C. Giraud-Audine, "A new electrical circuit with negative capacitances to enhance resistive shunt damping," *Proc. ASME 2015 Conf. on Smart Materials, Adaptive Structures and intelligent Systems-SMASIS*, 2015.
- [7] M. Berardengo, O. Thomas, C. Giraud-Audine and S. Manzoni, "Improved resistive shunt by means of negative capacitance: new circuit, performances and multi-mode control," *Smart Mater. Struct.*, 25, 075033, 2016.
- [8] S. Behrens, A. J. Fleming and S. O. R. Moheimani, "A broadband controller for shunt piezoelectric damping of structural vibration," *Smart Mater. Struct.*, 12, pp. 18-28, 2003.
- [9] S. Behrens, S. O. R. Moheimani and A. J. Fleming, "Multiple mode current flowing passive piezoelectric shunt controller," *J. Sound Vib.*, 266, pp. 929-942, 2003.

- [10] P. Bisegna and G. Caruso, "On the use of negative capacitances for vibration damping of piezoactuated structures," *Proc. SPIE*, 5760, pp. 317-328, 2005.
- [11] B. S. Beck, K. A. Cunefare and M. Collet, "The power output and efficiency of a negative capacitance shunt for vibration control of a flexural system," *Smart Mater. Struct.*, 22, 065009, 2013.
- [12] A. Carpinteri, *Structural Mechanics Fundamentals* (1st ed.). CRC Press, 2013.
- [13] R. W. Clough and J. Penzien, *Dynamics of structures*, Comput. Struct., Inc, Berkeley, Calif, USA, 3rd edition, 2003.
- [14] E. F. Crawley and J. D. Luis, "Use of piezoelectric actuators as elements of intelligent structures," *J. AIAA J.*, 25, pp. 1373 - 1385, 1987.
- [15] X. Chen, J. Shao, H. Tian, X. Li, Y. Tian and C. Wang, "Flexible three-axial tactile sensors with microstructure-enhanced piezoelectric effect and specially-arranged piezoelectric arrays," *Smart Mater. Struct.*, 27, 025018, 2018.
- [16] J. P. Den Hartog, *Mechanical Vibrations*, Dover Publications, 1985.
- [17] J. P. Den Hartog, "Transmission line vibration due to sleet" in *Transactions of the American Institute of Electrical Engineers*, vol. 51, no. 4, pp. 1074-1076, 1932.
- [18] C. Dagdeviren et al., "Recent progress in flexible and stretchable piezoelectric devices for mechanical energy harvesting, sensing and actuation," *Extreme Mechanics Letters*, 9, pp. 269-281, 2016.
- [19] F. D'Annibale, G. Rosi and A. Luongo, "On the failure of the 'Similar Piezoelectric Control' in preventing loss of stability by nonconservative positional forces" *Zeitschrift für angewandte Mathematik und Physik*, 66, pp. 1949-1968, 2015.
- [20] F. D'Annibale, "Basic perturbation analysis & Multiple scale analysis for single- and multi-degree of freedom systems" *Lecture notes*.
- [21] M. Ferretti, D. Zulli, and A. Luongo, "A continuum approach to the nonlinear in-plane galloping of shallow flexible cables" *Advances in Mathematical Physics*, vol. 2019, Art. ID. 6865730, 2019.
- [22] M. Ferretti, G. Piccardo, and A. Luongo, "Semi-analytical approaches for the nonlinear dynamics of a taut string subject to a moving load," *Nonlinear Dyn*, 2019.

- [23] M. Ferretti, G. Piccardo, and A. Luongo, "Weakly nonlinear dynamics of taut strings traveled by a single moving force," *Meccanica*, 2017.
- [24] F. Foti and L. Martinelli, "A unified analytical model for the self-damping of stranded cables under aeolian vibrations," *Journal of Wind Engineering & Industrial Aerodynamics*, vol. 176, pp. 225-238, 2017.
- [25] I. Fried, "Large deformation static and dynamic finite element analysis of extensible cables," *Comput. Struct.*, 15, pp. 315-319, 1982.
- [26] J. L. Fanson and T. K. Caughey, "Positive position feedback control for large space structures," *J. AIAA J.*, 28, pp. 717 - 724, 1990.
- [27] R. L. Forward, "Electronic damping of vibrations in optical structures," *J. Appl. Opt.*, 18, pp. 690-697, 1979.
- [28] R. L. Forward, "Electromechanical transducer-coupled mechanical structure with negative capacitance compensation circuit," *US Patent*, 4, pp. 158, 787, 1979.
- [29] E. Fukada et al, "Sound isolation by piezoelectric polymer films connected to negative capacitance circuits," *IEEE Trans. Electr. Insulat.*, 11, pp. 328-333, 2004.
- [30] M. Gu, C. J. Liu, Y. L. Xu, and H. F. Xiang, "Response characteristics of wind excited cable with artificial rivulet," *Applied Mathematics and Mechanics*, vol. 23, no. 10, pp. 1176-1187, 2002.
- [31] W. J. Goodey, "On the natural modes and frequencies of a suspended chain," *Quarterly Journal of Mechanics and Applied Mathematics*, vol. 14, no. 1, pp. 118-127, 1961.
- [32] J. Guckenheimer and P. Holmes, *Nonlinear Oscillations, Dynamical Systems, and Bifurcation of Vector Fields*, Springer, New York, NY, USA, 1983.
- [33] P. Guo, S. Li, and D. Wang, "Analysis of wind attack angle increments in wind tunnel tests for the aerodynamic coefficients of iced hangers," *Advances in Structural Engineering*, pp. 1-11, 2019.
- [34] H. J. Hopkins, *A Span of Bridges: An illustrated History*, Newton Abbot, England: David and Charles, ch 1, 1970.
- [35] P. Hagedorn and B. Schäfer, "On non-linear free vibrations of an elastic cable," *International Journal of Non-Linear Mechanics*, vol. 15, pp. 333-340.

- [36] W. M. Henghold, J. J. Russel and J. D. Morgan, "Free vibrations of cable in three dimensions," *Journal of Struct. Div. ASCE*, 101, pp. 2277 - 2291, 1977.
- [37] N. W. Hagood and E. F. Crawley, "Experimental investigation into passive damping enhancement for space structures," *J. Guid. Control Dyn.*, 14, pp. 1100-1109, 1991.
- [38] N. W. Hagood and A. Von Flotow, "Damping of structural vibrations with piezoelectric materials and passive electrical networks," *J. Sound Vib.*, 146, pp. 243-268, 1991.
- [39] J. Høgsberg and S. Krenk, "Balanced calibration of resonant piezoelectric RL shunts with quasi-static background flexibility correction," *J. Sound Vib.*, 341, pp. 16-30, 2015.
- [40] J. Høgsberg and S. Krenk, "Calibration of piezoelectric RL shunts with explicit residual mode correction," *J. Sound Vib.*, 386, pp. 65-81, 2017.
- [41] J. J. Hollkamp, "Multimodal passive vibration suppression with piezoelectric materials and resonant shunts," *J. Intelligent Mater. Syst. Struct.*, 5, pp. 49-57, 1994.
- [42] H. M. Irvine, *Cable Structures*, MiT Press, Cambridge, UK, 1981.
- [43] H. M. Irvine and J. H. Griffin, "On the dynamic response of a suspended cable," *Earthquake Engineering and Structural Dynamics*, vol. 4, pp. 389-402, 1976.
- [44] H. M. Irvine and T. K. Caughey, "The Linear Theory of Free Vibrations of a Suspended Cable," *Proceedings of the Royal Society A Mathematical, Physical and Engineering Sciences*, vol. 341, no. 1626, pp. 299-315, 1974.
- [45] H. M. Irvine and G. B. Sinclair, *Int. J. Sol. Struct.*, 12:309-317, 1976.
- [46] H. M. Irvine and G. B. Sinclair, *J. Eng. Mech. Div., Proc. ASCE*, 101, 1975.
- [47] K. F. Jones, "Coupled vertical and horizontal galloping," *Journal of Engineering Mechanics*, vol. 118, pp. 92-107, 1992.
- [48] S. Kmet and Z. Kokorudova, "Nonlinear analytical Solution for cable truss," *Journal of Engineering Mechanics*, vol. 132, pp. 119-123, 2006.
- [49] H. J. Kang, Y. Y. Zhao, and H. P. Zhu, "Linear and nonlinear dynamics of suspended cable considering bending stiffness," *Journal of Vibration and Control*, vol. 0, no. 0, pp. 1-19, 2013.

- [50] K. Kloppel and K. H. Lie, "Die Iotrechten Eigenschwingungen der Hangebrucken. Bauingenieur", 23, pp. 277, 1942.
- [51] A. Khan, Z. Abas, H. S. Kim and I. K. Oh, "Piezoelectric thin films: an integrated review of transducers and energy harvesting," *Smart Mater. Struct.*, 25, 053002, 2016.
- [52] A. Luongo, D. Zulli, and G. Piccardo, "Analytical and numerical approaches to nonlinear galloping of internally resonant suspended cables," *Journal of Sound and Vibration*, vol. 315, no. 3, pp. 375–393, 2008.
- [53] A. Luongo and D. Zulli, "Dynamic instability of inclined cables under combined wind flow and support motion," *Nonlinear Dyn*, vol. 67, pp. 71-87, 2012.
- [54] A. Luongo and D. Zulli, *Mathematical Models of Beams and Cables*, ISTE Ltd and John Wiley & Sons, Inc., 2013.
- [55] A. Luongo, D. Zulli, and G. Piccardo, "A linear curved-beam model for the analysis of galloping in suspended cables," *Journal of Mechanics of Materials and Structures*, vol. 2, no. 4, pp. 675-694, 2007.
- [56] A. Luongo and G. Piccardo, "Non-linear galloping of sagged cables in 1:2 internal resonance," *Journal of Sound and Vibration*, vol. 214, no. 5, pp. 915-940, 1998.
- [57] A. Luongo and D. Zulli, "Statics of shallow inclined elastic cables under general vertical loads: A perturbation approach," *Mathematics*, vol. 6, no. 2, pp. 63-72, 2018.
- [58] A. Luongo and G. Piccardo, "A continuous approach to the aeroelastic stability of suspended cables in 1:2 internal resonance," *Journal of Vibration and Control*, vol. 14, no. 1-2, pp. 135-157, 2008.
- [59] A. Luongo and D. Zulli, "Static perturbation analysis of inclined shallow elastic cables under general 3D-loads," *Curved and Layered Structures*, vol. 5, pp. 250-259, 2018.
- [60] A. Luongo and G. Piccardo, "Linear instability mechanisms for coupled translational galloping," *Journal of Sound and Vibration*, vol. 288, no. 4-5, pp. 1027-1047, 2005.
- [61] A. Luongo, A. Paolone, and G. Piccardo, "Postcritical Behavior of Cables Unndergoing Two Simultaneous Galloping Modes," *Mechanica*, Springer Verlag, vol. 33, no. 3, pp. 229-242, 1998.

- [62] A. Luongo, G. Rega, and F. Vestroni, "Monofrequent oscillations of a non-linear model of a suspended cable," *Journal of Sound and Vibration*, vol. 82, no. 2, pp. 247-259, 1982.
- [63] A. Luongo, G. Rega, and F. Vestroni, "Planar non-linear free vibrations of an elastic cable," *International Journal of Non-Linear Mechanics*, vol. 19, no. 1, pp. 39-52, 1984.
- [64] A. Luongo, D. Zulli, and G. Piccardo, "On the effect of twist angle on nonlinear galloping of suspended cables," *Computers and Structures*, vol. 87, pp. 1003-1014, 2009.
- [65] A. Luongo, G. Rega, and F. Vestroni, "Planar nonlinear free vibrations of an elastic cable," *Int. J. Non-linear Mechanics*, vol. 19, no. 1, pp. 39-52, 1984.
- [66] A. Luongo, M. Ferretti and S. Di Nino, *Stabilità e biforcazione delle strutture. Sistemi statici e dinamici*, Società Editrice Esculapio.
- [67] A. M. Loredo-Souza and A. G. Davenport, "A novel approach for wind tunnel modelling of transmission lines," *Journal of Wind Engineering and Industrial Aerodynamics*, vol. 89, pp. 1017-1029, 2001.
- [68] S. Li, T. Wu, T. Huang, and Z. Chen, "Aerodynamic stability of iced stay cables on cable-stayed bridge," *Wind and Structures*, vol. 23, no. 3, pp. 253-273, 2016.
- [69] X. Liu, M. Zou, C. Wu, B. Yan, and M. Cai, "Galloping stability and aerodynamic characteristic of iced transmission line based on 3-DOF," *Shock and Vibration*, vol. 2020, Art. ID. 8828319, 2020.
- [70] M. Lepidi and V. Gattulli, "Static and dynamic response of elastic suspended cables with thermal effects," *International Journal of Solids and Structures*, vol. 49, pp. 1103-1116, 2012.
- [71] C. L. Lee and N. C. Perkins, "Nonlinear oscillations of suspended cables containing a two-to-one internal resonance," *Nonlinear Dynamics*, vol. 3, no. 6, pp. 465-490, 1992.
- [72] T. J. Li and Y. J. Ma, "Robust vibration control of flexible cable-strut structure with mixed uncertainties," *J. Vib. Control*, 17, pp. 1407 - 1416, 2011.
- [73] A. B. Mehrabi, P. E. Associate member, ASCE, and H. Tabatabai, P. E., "Unified Finite Difference Formulation for Free Vibration of Cables," *J. Struct. Eng.*, 124, pp. 1313-1322, 1998.

-
- [74] S. O. R. Moheimani and A. J. Fleming, *Piezoelectric Transducers for Vibration Control and Damping*, London: Springer.
- [75] B. de Marneffe and A. Preumont, "Vibration damping with negative capacitance shunts: theory and experiment," *Smart Mater. Struct.*, 17, 035015, 2008.
- [76] M. Novak, A. G. Davenport, Members, ASCE, and Hiroshi Tanaka, "Vibration of towers due to galloping of iced cables," *Journal of the Engineering Mechanics Division*, vol. 104, no. 2, pp. 457-473, 1978.
- [77] A. H. Nayfeh, *Introduction to Perturbation Techniques*, John Wiley & Sons, New York, NY, USA, 2001.
- [78] A. H. Nayfeh and D. T. Mook, *Nonlinear Oscillations*, John Wiley & Sons, New York, NY, USA, 2008.
- [79] A. H. Nayfeh and P. F. Pai, *Linear and Nonlinear Structural Mechanics*, John Wiley & Sons, Inc., 2004.
- [80] A. H. Nayfeh, *Perturbation Methods*, John Wiley & Sons, New York, NY, USA, 2000.
- [81] M. Ouisse, M. Collet and F. Scarpa, "A piezo-shunted kirigami auxetic lattice for adaptive elastic wave filtering," *Smart Mater. Struct.*, 25, 115016, 2016.
- [82] L. C. Pagnini, A. Freda, and G. Piccardo, "Uncertainties in the evaluation of one degree-of-freedom galloping onset," *European Journal of Environmental and Civil Engineering*, 2016.
- [83] A. G. Pugsley, "On the natural frequencies of suspended chains," *Quarterly Journal of Mechanics and Applied Mathematics*, vol. II, Pt. 4, 1949.
- [84] G. Piccardo, "A methodology for the study of coupled aeroelastic phenomena," *Journal of Wind Engineering and Industrial Aerodynamics*, vol. 48, pp. 241-252, 1993.
- [85] N. C. Perkins, "Modal interactions in the non-linear response of elastic cables under parametric/external excitation," *International Journal of Non-Linear Mechanics*, vol. 27, no. 2, pp. 233-250, 1992.
- [86] W. B. Parsons, *Engineers and Engineering in the Renaissance*, Cambridge, Massachusetts: The MIT Press, pp. 71-72, 1976.

- [87] M. Pakdemirli, S. A. Nayfeh, and A. H. Nayfeh, "Analysis of one-to-one autoparametric resonances in cables - Discretization vs. Direct treatment," *Nonlinear Dynamics*, vol. 8, pp. 65-83, 1995.
- [88] A. Preumont, *Mechatronics-Dynamics of Electromechanical and Piezoelectric Systems*, Dordrecht: Springer, 2006.
- [89] X. Pan et al., "A self-powered vibration sensor based on electrospun poly (vinylidene fluoride) nanofibers with enhanced piezoelectric response," *Smart Mater. Struct.*, 25, 105010, 2016.
- [90] G. Rega and A. Luongo, "Natural vibrations of suspended cables with flexible supports," *Computers & Structures*, vol. 12, pp. 65-75, 1980.
- [91] G. Rega, "Nonlinear vibrations of suspended cables - Part I: Modeling and analysis," *Applied Mechanics Reviews*, vol. 57, no. 1-6, pp. 443-478, 2004.
- [92] G. Rega, W. Lacarbonara, A. H. Nayfeh, and C. M. Chin, "Multiple resonances in suspended cables: direct versus reduced-order models," *International Journal of Non-Linear Mechanics*, vol. 34, pp. 901-924, 1999.
- [93] J. H. Rohrs, *Trans. Cambridge Phil. Soc.*, 9: Part III, pp. 379 - 398, 1851.
- [94] E. J. Routh, *Advanced Dynamics of Rigid Bodies*, Dover, NY, 6th ed., 1955.
- [95] W. D. Rannie and T. Von Karman, "The Failure of the Tacoma Narrows Bridge," Federal Works Agency, appl. VI, 1941.
- [96] D. S. Saxon and A. S. Cahn, "Modes of vibration of a suspended chain," *Quarterly Journal of Mechanics and Applied Mathematics*, vol. VI, Pt. 3, 1953.
- [97] U. Starossek, "Cable Dynamics - A Review," *Structural Engineering International*, vol. 3, no. 4, pp. 171-176, 1994.
- [98] A. I. Soler, "Dynamic Response of Single Cables with Initial Sag," *Journal of the Franklin Institute*, vol. 290, Issue 4, pp. 377-387, 1970.
- [99] P. Soltani, G. Kerschen, G. Tondreau and A. Deraemaeker, "Tuning of a piezoelectric vibration absorber attached to a damped structure," *J. Intelligent Mater. Syst. Struct.*, 28, pp. 1115-1129, 2017 .
- [100] M. S. Triantafyllou and L. Grinfolgel, "Natural Frequencies and Modes of Inclined Cables," *Journal of Structural Engineering*, ASCE, 112, 1, pp. 139 - 148.

- [101] C. Truesdell, "The Rational Mechanics of Flexible or Elastic Bodies," Turici: Orell Füssli, pp.1638-1788.
- [102] O. Thomas, J. Ducarne and J-F. Deü, "Performance of piezoelectric shunts for vibration reduction," *Smart Mater. Struct.*, 21, 015008, 2012.
- [103] W. Tang, L. B. Wang, Y. M. Ren, B. Bao and J. J. Cao, "Design and experimental analysis of self-sensing SSDNC technique for semi-active vibration control," *Smart Mater. Struct.*, 27, 085028, 2018.
- [104] B. W. Van Oudheusden, "On the quasi-steady analysis of one-degree-of-freedom galloping with combined translational and rotational effects," *Nonlinear Dynamics*, vol. 8, pp. 435-451, 1995.
- [105] G. S. Vincent, *Wind Effects on Build. and Struct.*, Teddington, England, H. M. S. O., 2, pp. 512 - 522, 1965.
- [106] E. T. Whittaker, *Analytical Dynamics*, 4th ed. Cambridge: Cambridge University Press, pp. 34-177.
- [107] K. Wasa, T. Matsushima, H. Adachi, I. Kanno and H. Kotera, "Thin-film piezoelectric materials for a better energy harvesting MEMS," *J. Microelectromech. Syst.*, 21, pp. 451-457, 2012.
- [108] S. Y. Wu, "Method for multiple-mode shunt damping of structural vibration using a single PZT transducer," *Proc. SPIE*, 3327, pp. 159-168, 1998.
- [109] W. Jr. Weaver, S. P. Timoshenko and D. H. Young, *Vibration Problems in Engineering*, New York: Wiley, 1990.
- [110] H. H. West, L. F. Geschwindner and J. E. Suhoski, "Natural Vibrations of Suspension Cables," *Journal of the Structural Division, ASCE*, ST11, pp. 2277-2291, 1975.
- [111] F. Xie, Y. Su, W. Zhou and W. Z. Zhang, "Design and evaluation of a shunted flexible piezoelectric damper for vibration control of cable structures," *Smart Mater. Struct.*, 28, 085031, 2019.
- [112] M. Xie et al., "Flexible self-powered multi-functional sensor for stiffness-tunable soft robotic gripper by multimaterial 3D printing," *Nano Energy*, 79, 105438, 2021 .
- [113] H. Yamaguchi, "Fundamentals of Cable Dynamics," *Proceedings of International Seminar on Cable Dynamics*, Tokyo, pp. 81 - 94.

- [114] P. Yu, Y. M. Desai, A. H. Shah, Member, ASCE, and N. Popplewell, "Three-degree-of-freedom model for galloping. Part I: Formulation," *Journal of Engineering Mechanics*, vol. 119, no. 12, pp. 2404-2425, 1993.
- [115] P. Yu, Y. M. Desai, N. Popplewell, and A. H. Shah, Member, ASCE, "Three-degree-of-freedom model for galloping. Part II: Solutions," *Journal of Engineering Mechanics*, vol. 119, no. 12, pp. 2426-2448, 1993.
- [116] K. Yamada, H. Matsuhisa, H. Utsuno and K. Sawada, "Optimum tuning of series and parallel LR circuits for passive vibration suppression using piezoelectric elements," *J. Sound Vib.*, 329, 5036-5057, 2010.
- [117] L. Yan, B. Bao, D. Guyomar and M. Lallart, "Periodic structure with interconnected nonlinear electrical networks," *J. Intelligent Mater. Syst. Struct.*, 28, pp. 204-229, 2017.
- [118] Z. S. Yang, L. H. Tang, M. Y. Xie, S. S. Sun, W. H. Li and A. W. Kean, "Soft magneto-sensitive elastomer and polyvinylidene fluoride polymer based nonlinear piezoelectric energy harvesting: design, modeling and experiment," *Smart Mater. Struct.*, 28, 015031, 2019.
- [119] Z. Yang, S. Zhou, J. Zu and D. Inman, "High-performance piezoelectric energy harvesters and their applications," *Joule*, 2, pp. 642-697, 2018.
- [120] D. Zulli, G. Piccardo, and A. Luongo, "On the nonlinear effects of the mean wind force on the galloping onset in shallow cables," *Nonlinear Dyn*, 2020.
- [121] Y. H. Zhang, H. P. Niu and S. L. Xie, "Numerical and experimental investigation of active vibration control in a cylindrical shell partially covered by a laminated PVDF actuator," *Smart Mater. Struct.*, 17, 035024, 2008.
- [122] H. A. Sodano, D.J. Inman and G. Park, "A review of power harvesting from vibration using piezoelectric materials," *Shock Vib. Dig.*, 36, 197-206, 2004.
- [123] H. Li, C. Tian and Z. D. Deng, "Energy harvesting from low frequency applications using piezoelectric materials," *Appl. Phys. Rev.*, 1, 041301, 2014.